



HAL
open science

Mid-Infrared Detectors and THz Devices Operating in the Strong Light-Matter Coupling Regime

Pierre-Baptiste Vigneron

► **To cite this version:**

Pierre-Baptiste Vigneron. Mid-Infrared Detectors and THz Devices Operating in the Strong Light-Matter Coupling Regime. Materials Science [cond-mat.mtrl-sci]. Université Paris Saclay (COMUE), 2019. English. NNT: 2019SACLS082 . tel-02298382

HAL Id: tel-02298382

<https://theses.hal.science/tel-02298382>

Submitted on 26 Sep 2019

HAL is a multi-disciplinary open access archive for the deposit and dissemination of scientific research documents, whether they are published or not. The documents may come from teaching and research institutions in France or abroad, or from public or private research centers.

L'archive ouverte pluridisciplinaire **HAL**, est destinée au dépôt et à la diffusion de documents scientifiques de niveau recherche, publiés ou non, émanant des établissements d'enseignement et de recherche français ou étrangers, des laboratoires publics ou privés.

Mid-Infrared Detectors and THz Devices Operating in the Strong Light-Matter Coupling Regime

Thèse de doctorat de l'Université Paris-Saclay
préparée à Université Paris-Sud, Centre de Nanosciences et Nanotechnologies (C2N)

Ecole doctorale n°575 Electrical, Optical, Bio:
PHYSICS-AND-ENGINEERING (EOBE)
Spécialité de doctorat : Physique

Thèse présentée et soutenue à Palaiseau, le Avril 15th 2019, par

PIERRE-BAPTISTE VIGNERON

Composition du Jury :

Gottfried Strasser Professeur, Institut für Festkörperelektronik (TU Wien)	Rapporteur
Stefano Barbieri Directeur de recherche, Institut d'Electronique, de Microélectronique et de Nanotechnologie (IEMN, UMR 8520)	Rapporteur
Virginie Trinité Ingénieure de recherche, Thales Group	Examineur
Roland Teissier Directeur de recherche, Institut d'Electronique et des Systèmes (IES, UMR 5214)	Examineur
Raffaele Colombelli Directeur de recherche, Centre de Nanosciences et Nanotechnologies (C2N, Paris Sud, UMR 9001)	Directeur de thèse
Jean-Michel Manceau Chargé de recherche, Centre de Nanosciences et Nanotechnologies (C2N, Paris Sud, UMR 9001)	Co-encadrant
Sukhdeep Dhillon Directeur de recherche, Laboratoire Pierre-Aigrain (LPA, ENS Ulm, UMR 8551)	Examineur

*Merci à Caroline, Claudine et Jacques,
pour leur soutien quotidien.*

Contents

1	Light-Matter Interaction	5
1.1	III-V Semiconductor: GaAs	5
1.1.1	Envelope Function Formalism	5
1.1.2	Quantum Wells and Subbands	6
1.2	Intersubband Transitions	8
1.2.1	Light Matter Interaction	8
1.2.2	Absorption	9
1.2.3	Lorentz Model for Dielectrics	9
1.2.4	Highly Doped Semiconductors: Depolarization shift	13
1.3	Electromagnetic Waveguide	14
1.3.1	Drude Model for Metals	14
1.3.2	Helmholtz Equation	14
1.3.3	Parallel Plate Waveguide	16
1.3.4	Metal-Insulator-Metal Dispersive Cavity	17
1.4	Intersubband Polaritons	22
1.4.1	Two-Level Model: Jaynes-Cummings Hamiltonian	22
1.4.2	2D Electron Gas: Dark States and Bright States	25
1.4.3	Coupled Mode Theory	26
1.5	Conclusion	29
I	THz Polaritonic Dispersive Cavities, a Tool for THz Emitters	31
2	Dispersive THz Cavities for the Strong Coupling Regime	33
2.1	Key Concept: Final-State Stimulation	34
2.2	Active Region Design	35
2.2.1	Schrödinger-Poisson Simulations	35
2.2.2	Multi-pass measurements	36
2.3	Design of the Cavity: RCWA Simulations	38

2.4	Fabrication & Mounting	39
2.4.1	Cleanroom Processing	39
2.4.2	Mounting	40
2.5	Set-up for Measuring the Polaritonic Dispersion at Low-T	41
2.5.1	Fourier Transform Interferometer and Beam Condenser	41
2.5.2	Variable Angle Inset	43
2.5.3	Dispersion Measurements	46
2.6	Perspectives: Polaritonic LEDs Based on Polariton-Polariton Scattering	50
2.7	Conclusions	52
3	Initial Pump-Probe Experiment of THz Polaritonic Structures	53
3.1	Principle of the Pump and Probe Measurement	53
3.2	Main Components of a Time-Domain Spectroscopy System	55
3.2.1	THz Pulsed Broadband Source: Photo-conductive Antenna	55
3.2.2	THz Pulse Sampling	56
3.2.3	Choice of the Crystal to Study Polaritons at $3 THz$	58
3.3	Reflectivity Measurements	59
3.4	Initial Pump and Probe Measurements	60
3.4.1	Saturation of the ISB Polariton	60
3.4.2	Source Description	61
3.4.3	Pump and Probe Measurements at 45°	62
3.5	Conclusion and Perspectives	65
II	Development of Short Pulse THz Lasers	67
4	THz Quantum Cascade Laser Integration in Time-Domain Spectroscopy	69
4.1	Detecting the QCL Emission with EO Detection: Seeding	69
4.2	Optimization of the Laser Gain and Cavity	70
4.2.1	Fabry-Pérot Cavity in a Metal-Metal Waveguide	70
4.2.2	Dispersion Compensation: Gires-Tournois Interferometer (GTI)	74
4.3	ICP Etching: Recipe Development	77
4.3.1	Experiment	79
4.3.2	Reduction of Micromasking: Chemical Etching with Cl_2	80
4.3.3	Obtaining a High Etch Rate: Ar & N_2	81
4.3.4	Obtaining Vertical and Smooth Sidewalls: Resist Profile and Pressure Control	83
4.3.5	Conclusion of the Etching Development	84
4.4	Second Generation of GTI-THz-QCLs Used in this Work	86
4.4.1	The THz QCL Active Regions used in this Work	86
4.4.2	Side Absorbers Permit to Broaden the Laser Spectra	87
4.4.3	Fabrication	88

4.4.4	Sample Mounting	92
4.4.5	Characterization of GTI QCLs (ENS/LPA)	93
4.5	Conclusions	95
 III Mid-Infrared Polaritonic Detectors		97
5	Quantum Wells Infrared Detectors: Introductory Theory	99
5.1	Brief Introduction to Quantum Well Infrared Detectors	99
5.1.1	Black Body radiation	99
5.1.2	Material and Electrical Transport Properties	100
5.1.3	Detector Performance	104
5.2	Selected Developments of Mid-IR Detectors from the Literature	107
5.2.1	QWIP Developments and Recent Improvements	107
5.2.2	Infra-Red Detectors Operating in Strong Coupling	110
5.3	Motivations to Study QWIPs in Strong Coupling	113
5.4	Conclusion	115
6	Quantum Well Infrared Detectors in Strong Coupling	117
6.1	Active Region	117
6.1.1	Multipass Measurements	118
6.2	QWIP in Weak Coupling: Mesa Resonator	120
6.2.1	Mesa: Design & Fabrication	120
6.2.2	Measurements	121
6.2.3	Conclusions QWIPs Measurement in Weak Coupling	125
6.3	QWIP in Strong Coupling: Simulations, Design and Fabrication	126
6.3.1	Simulations & Cavity Optimization	126
6.3.2	Experimental Dispersion in Reflectivity	131
6.3.3	SC-QWIP: Fabrication & Design	132
6.4	SC-QWIP Measurements	135
6.4.1	Experimental Set-Up	135
6.4.2	Measurements	137
6.4.3	Interpretation of the Experimental Results	140
6.5	Conclusions & Perspectives	144
 APPENDICES		151
A	External Cavity for THz Double-Metal Waveguides	151
A.1	Anti-Reflection Coatings	151
A.1.1	Coatings Based on Transparent and Insulator Materials	152
A.1.2	Coatings Based on Thin Metallic Layers	154
B	Polariton Active Regions: Growth Sheets	159
B.1	THz Polariton	159
B.2	Mid-IR Polaritons	160

Remerciement

Je tiens tout d'abord à remercier mon directeur de thèse Raffaele Colombelli qui m'a donné l'opportunité de faire ma thèse sur un sujet qui me tient à cœur. J'ai apprécié pouvoir aborder mon projet de thèse avec une autonomie de réflexion et d'action. J'ai beaucoup appris sous sa coordination.

Au côté de Raffaele, Jean-Michel Manceau était toujours présent pour m'apporter l'aide dont j'avais besoin en salle d'expérimentation et en salle blanche. Je suis très reconnaissant pour toutes les compétences expérimentales qu'il m'a transmises.

Mes remerciements s'adressent également aux membres de mon jury qui ont partagé leur regard sur mon travail et mon manuscrit de thèse. J'ai apprécié la qualité et la rigueur de leurs remarques qui m'ont aidé à raffiner ce manuscrit.

Durant ma thèse, j'ai eu l'occasion d'enseigner pendant deux ans. Ce fut une expérience très enrichissante, à travers laquelle j'ai confirmé mon plaisir d'enseigner. J'ai également pu prendre la mesure de la charge que représente un enseignement en Université. Je remercie Adel Bousseksou, Marie Godard, Guillaume Agnus, Arnaud Bournel et Navy Yam pour la confiance qui m'a été accordée.

Aux côtés des permanents, l'expérience et la motivation des post-docs sont des aides précieuses. Thibault Laurent, ainsi que Jean-Michel, ont conçu les composants mécaniques, fabriqué à l'atelier mécanique du C2N Orsay, indispensables à la mesure en dispersion des polaritons THz. Les discussions avec Pierre Laffaille sur les structures QCL m'ont fait prendre du recul sur mon travail. Bruno Paullilo m'a transmis son expérience de la gravure ionique. Les conseils de Stefano Pirotta (et le manuscrit de Bruno) m'ont apporté les compétences nécessaires pour les mesures des détecteurs moyen infra-rouge. Enfin la créativité de Mario Malerba pour introduire de nouvelles géométries et de nouvelles étapes dans nos procédés de fabrication salle blanche est une source d'inspiration continue.

Ce fut un plaisir de partager mon quotidien avec d'autres étudiants tous plus motivés et intéressants les uns que les autres. Mes prédécesseurs Daniel Chastanet et Bruno toujours prêts à partager de leur savoir-faire et nous remonter le moral. Avec Laurent Boulley, Claire Abadie, Arnaud Jolivet, François Joint, Valerio Piazza, Lu Lu, Guillaume Marcaux, Farsane Tabataba-Vikili, Aurore Ecarnot, Omar Saket, Ludivine Emeric, Marina Yakovleva et Mathias Berciano nous avons vécu en parallèle, sur des projets différents, les mêmes étapes du processus de thèse. Les échanges que nous avons eu tout au long de notre expérience de thèse

ont été très enrichissants et parfois rassurants dans les périodes difficiles comme l'inondation du site d'Orsay ou le déménagement au plateau de Scalay.

Linh-Ngoc Tran, Paul Goulain et Oussama Ouznali représentent la prochaine génération de thésards. Leur humour et leur conversation ont été des sources quotidiennes de bonne humeur. Je leur souhaite beaucoup de réussite pour la suite de leur thèse.

Mais que serait un groupe de physique appliquée sans les ingénieures et ingénieurs qui l'accompagnent. Nathalie Isac, Jean-René Coudeville, David Bouville, Samson Edmond, François Maillard, Cédric Villebasse, Abdelhanin Aassime et Marie-Paule Planté ont été très présents dans ma progression en la salle blanche. Grâce à leur rigueur et leur patience, j'ai rapidement pu évoluer en autonomie en salle blanche.

Fabien Bayle a été d'une grande aide pour exploiter au maximum de leur capacités les outils d'imagerie par balayage électronique. Ces outils transversaux m'ont été utiles à chaque nouvelle étape de ma thèse.

Une étape inattendue de ma thèse fût la calibration de la gravure ICP après l'inondation du laboratoire. Stéphane Guillet, Nathalie et Etienne Herth ont pris le temps de m'expliquer en détails le fonctionnement de la machine de gravure et la physique des plasmas. Ils m'ont appris à développer des approches systématiques pour retrouver une recette de gravure opérationnelle.

Ma thèse a été financée grâce au projet européen Ultra-QCL. A travers ce projet, j'ai eu l'opportunité de visiter les différents laboratoires du consortium : Leeds, Ratisbonne et Pise. Ce fut avec grand intérêt que j'ai découvert la spécialité de chaque laboratoire et que j'ai pu rencontrer les chercheuses et chercheurs de grande qualité qui animent ces lieux. Je tiens tout particulièrement à remercier Sukhdeep Dhillon, qui a coordonné le projet avec détermination, patience et bienveillance.

Au cours de ma thèse, j'ai collaboré principalement avec le Laboratoire Pierre Aigrain. L'équipe de Sukhdeep m'a toujours accueilli chaleureusement, rue Lohmond, pour échanger des échantillons autant que des idées. Je souhaite plein de réussites à Jacques Hawecker et Valentino Pistore pour la fin de leur thèse et à Hanond Nong pour ses débuts en entreprise.

Mes derniers remerciements vont à mes proches qui ont cru en moi tout au long de mon projet de thèse. Caroline, Jacques et Claudine ont suivi mon projet au quotidien. Michel, Romain et Nano qui m'ont apporté leur regard extérieur aux moments décisifs de mon projet de thèse. J'ai une pensée toute particulière pour ma grand-mère qui nous a quitté en mai 2018 et qui m'a transmis son intérêt pour la connaissance et une certaine forme de détermination.

Résumé

Les dispositifs optoélectroniques quantiques en couplage faible, amplement étudiés durant ces dernières décennies, ont apporté des solutions technologiques dans de nombreux domaines : émetteurs (LED, laser), détecteurs (QWIP, QCD) ou générateur de courant (cellules photovoltaïques). Néanmoins, les performances de ces dispositifs en couplage faible atteignent leurs limites fondamentales dans certains domaines, tels que les détecteurs à puit quantique (QWIP) ou les lasers à cascade quantique (QCL). A titre d'exemples, la température maximale de fonctionnement des lasers à cascade quantique THz (THz-QCL) a très peu évolué au cours des dix dernières années. Dans ce contexte, de nouveaux concepts (nouveaux matériaux, phénomènes non-linéaires, ...) sont introduits pour tenter de dépasser les performances actuelles de certains dispositifs optoélectroniques. Dans ce manuscrit, notre approche consiste à explorer les propriétés de dispositifs en couplage fort afin d'évaluer leurs éventuelles capacités à dépasser les performances de dispositifs en couplage faible.

Le couplage fort est atteint lorsque que le taux d'échange d'énergie (oscillation de Rabi) entre deux résonateurs, dans notre cas un photon de cavité et une excitation électronique intersousbande, est supérieur au taux de relaxation de chacun des résonateurs. Dans ce cas, la dégénérescence de mode est levée. Les deux résonateurs sont alors représentés par une seule quasi-particule nommée polariton (mélange d'une onde de polarisation -polari-, et d'un photon -ton-).

Dans le domaine des transitions intersous-bandes, qui s'étend du moyen infra-rouge au THz, nous avons ciblé deux applications pour lesquels les propriétés des polaritons pourraient apporter des améliorations notables par rapport aux dispositifs existants. La première concerne les sources de lumière cohérente dans le THz. Une source de lumière cohérente largement utilisée dans le domaine du THz sont les THz-QCL qui utilisent l'inversions de populations entre niveaux électroniques. L'ingénierie des QCL utilise des niveaux d'énergies relativement proches les uns des autres ce qui rend ces systèmes sensibles à l'activation thermique des phonons. Une méthode alternative à l'inversion de population, utilisant les propriétés des polaritons, est la stimulation par l'état final. Cette seconde méthode, moins dépendante de la température, pourrait être utilisée pour générer une source de lumière cohérente. Une seconde application des polaritons intersous-bande concerne les photo-détecteurs moyen-infrarouge à puits quantiques. Ces détecteurs sont fondamentalement limités par entremêlement entre l'énergie de détection et l'énergie d'activation thermique. Des structures optimisées pour détecter en couplage fort pourraient potentiellement dissocier l'énergie de détection de l'énergie

d'activation thermique.

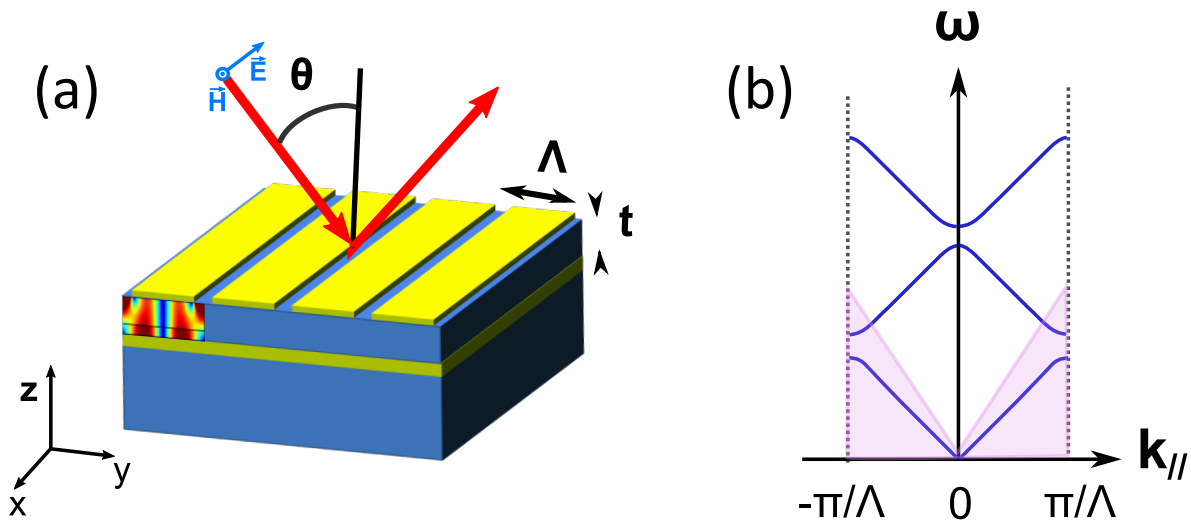


Figure 1: (a) Schéma d'une cavité dispersive Métal-Isolant-Métal avec une période Λ et une épaisseur t . (b) Diagramme de band du mode TM_{00} restreint à la première zone de Brillouin de cette cavité. En rose le cône de lumière. La géométrie de la cavité, période du réseau et épaisseur de la cavité, peuvent être adaptés à chaque région active et une ingénierie du couplage fort est dès lors envisageable.

Pour adresser ces deux problématiques nous avons choisi d'utiliser une même géométrie de cavité pour les domaines du moyen-infra-rouge et du THz : une cavité métal-insolant-métal avec un réseau sur le métal supérieur (Figure 1). Cette cavité métal-insolant-métal, dont la géométrie est adaptée à chaque domaine de fréquence, confine fortement le champ électromagnétique autour de la région active et le réseau dispersif donne accès à plusieurs états de couplage fort entre la lumière et la matière. Plus précisément, nous souhaitons travailler au-dessus du cône de lumière, sans interaction avec les modes d'ordre supérieurs et de sorte que les minimums d'énergie des deux branches polaritoniques se trouvent à $k_{//} = 0$. Ainsi nous avons choisi de coupler la transition intersousbande (Mid-IR ou THz) avec la 3^{ème} branche photonique de la cavité.

Dans le domaine du THz, les dimensions de la cavité métal-insolant-métal que nous avons étudié sont les suivantes : épaisseur $t=11 \mu m$, période $\Lambda =36 \mu m$ avec un taux de remplissage de 80% en couplage fort avec une transition à $2.7 THz$. Dans un premier temps, la dispersion en réflectivité des branches polaritoniques a été mesurée à l'aide d'un outil de mesure spécialement conçu pour ce projet. Figure 2 présente les mesures de dispersion en réflectivité de cette cavité en couplage faible (à température ambiante, purement photonique) et en couplage fort (à basse température, écartement de Rabi) obtenues à travers un spectromètre infrarouge à transformée de Fourier dont le compartiment échantillon a été poussé sous vide.

Une fois la dispersion de l'échantillon mesurée, l'échantillon a été caractérisé dans un système de spectroscopie résolue en temps (TDS) afin d'étudier les variations d'absorption de la cavité polaritonique soumise à une excitation laser (pompe THz-QCL). Les cavités dispersives donnant accès à plusieurs niveaux de couplage fort sur un même échantillon, il est alors possible d'accorder les états polaritoniques avec la fréquence du laser de pompe (fixé à $3.1 THz$) en faisant pivoter l'échantillon.

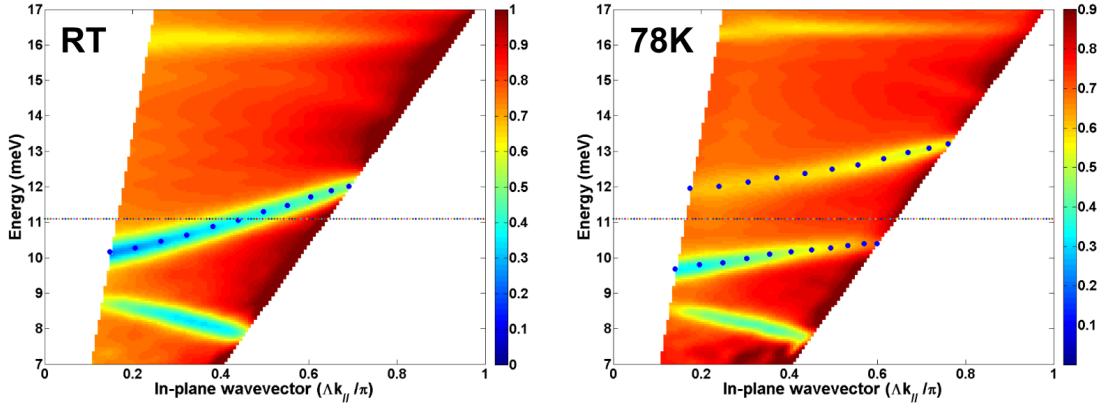


Figure 2: Mesure en dispersion à température ambiante (RT) et à 78K des polaritons inter-sous-bande THz avec un spectromètre à transformée de Fourier.

Suite au positionnement des branches polaritoniques (via la mesure en dispersion), il a été estimé que la configuration idéale pour explorer les phénomènes de relaxation polariton-polariton est d’exciter la branche polaritonique basse à 25° et de sonder cette même branche à 0° . Cette mesure est en cours au Laboratoire Pierre-Aigrain de l’ENS/Ulm.

Dans un second temps nous avons utilisé les cavités dispersives métal-isolant-métal pour étudier les propriétés de photo-détection moyen infrarouge à puit quantique opérant en couplage forte. L’objectif de cette seconde étude est double. En termes de performance du dispositif, le couplage fort pourrait être utilisé pour dissocier la fréquence de détection et de l’énergie d’activation thermique. Ainsi, la température à laquelle le dispositif en couplage fort opère en régime de limitation par le bruit de fond pourrait être augmentée par rapport au même dispositif en couplage faible. D’autre part, la génération de photo-courant à partir d’un état polaritonique pourrait répondre à certains problèmes fondamentaux sur l’interaction entre un état brillant des polaritons (état collectif) et un état électronique (état unique).

Nous avons choisi une longueur d’onde de photo-détection à $10 \mu m$ ce qui a défini la géométrie de la cavité métal-isolant-métal : d’épaisseur $t=1 \mu m$, de période $\Lambda =3.5 \mu m$ avec un taux de remplissage de 80% en couplage fort avec une transition à $2.7 THz$.

Le fonctionnement des photo-détecteurs à puit quantique est basé sur la génération de photocourant à partir de l’excitation d’électrons de l’état fondamental du puit quantique (quasi-lié) vers le continuum (au-dessus de la barrière, Figure 3, a). Dans le cadre de cette thèse, nous avons conçu, fabriqué et mesuré des détecteurs en couplage faible (mesa) et fort (SC-QWIP).

Le régime de couplage faible a été étudié sur des structures à plasmon de surface (mesa) dans lesquelles la lumière est injectée par le substrat. Les caractérisations de ces méso nous ont donné des informations sur la qualité des quatre régions actives que nous avons conçu. Il est apparu durant cette étude préliminaire que les régions actives avaient un courant d’obscurité élevé et qu’il était difficile d’extraire des informations sur les performances de ces détecteurs (réponse et T_{blip}). Néanmoins les détecteurs restent opérationnels et l’observation des propriétés polaritoniques de ces échantillons est toujours possible (Figure 3 (b)).

Une étude préliminaire du couplage fort consiste à mesurer la dispersion en réflectivité de la cavité à température ambiante (possible dans le moyen-infrarouge). Les branches polari-

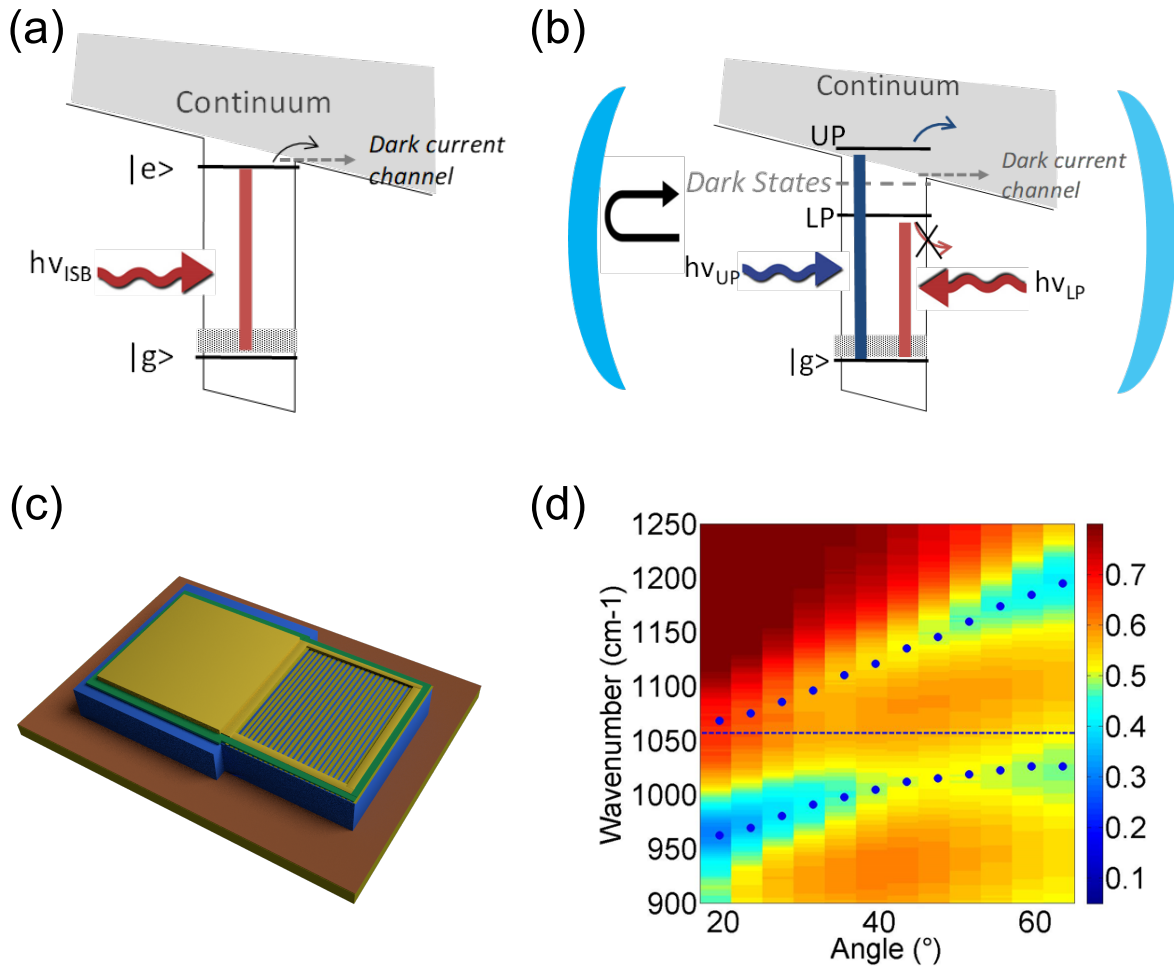


Figure 3: Schéma d'un photo-détecteur en couplage faible a) et fort b). c) Schéma d'un photodétecteur opérant en couplage fort. d) Dispersion en réflectivité et à température ambiante d'un dispositif polaritonique en couplage fort (période $3.8 \mu m$, taux de remplissage 70%)

toniques ont été observées et les simulations correspondent avec les mesures expérimentales (Figure 3) d).

Après validation en réflectivité du couplage fort entre la région active et la cavité dispersive, les dispositifs de photo-détecteur en couplage fort (SC-QWIP) ont été fabriqués dans la salle blanche du C2N-Orsay. Le schéma du dispositif de photo-détection est présenté Figure 3 (c). Il est constitué de deux plans métalliques de part et d'autre de la région active. Le métal supérieur est composé d'un réseau métallique de périodes $\Lambda = 3.2 ; 3.7$ et $4 \mu m$ et de facteur de remplissage de 80% fabriqué grâce à une étape de lithographie électronique. Le réseau métallique supérieur est ensuite connecté à l'électrode afin d'assurer le contact électrique.

Figure 4 présente les dispersions expérimentales normalisées en photo-courant pour les périodes $4 \mu m$ (a), $3.7 \mu m$ (b), $3.2 \mu m$ (c). Une nette différence entre les pics de photo-courant et les pics d'absorption attendu par les simulations (points blancs) est observable pour le polariton bas. Pour rendre compte de cet effet nous avons dû considérer que le polariton bas se trouvait à l'intérieur du puit quantique (Figure 3, (b)) de sorte qu'il ne puisse générer du photo-courant qu'à partir du moment où il est suffisamment proche de la transition nue. Ainsi nous avons introduit une fonction de transfert tenant en compte de l'effet tunnel (encart Figure 4, (d)) dans la barrière en introduisant une coupure lorsque l'énergie du po-

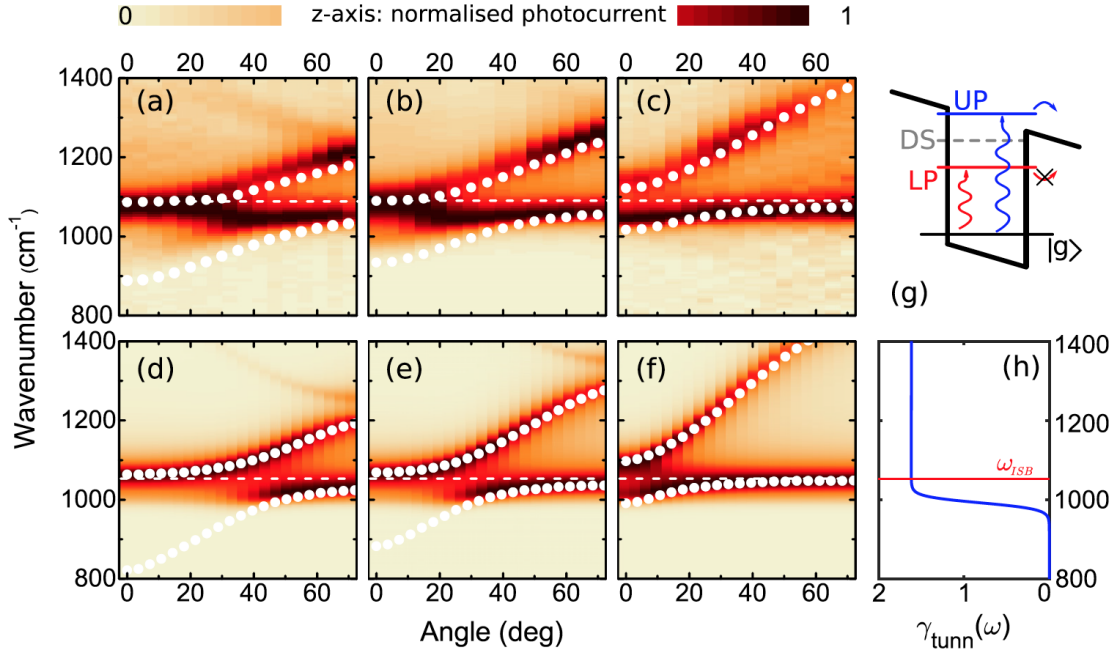


Figure 4: (a), (b), (c) dispersion en photocourant des SC-QWIP pour les période (4; 3,7 et 3,2 μm) et les pics d'absorption des polaritons (points blancs) obtenus en simulation RCWA. (d), (e) et (f) sont les simulations en tenant en compte du tunneling du polariton bas à travers la barrière (encart Figure (d)).

lariton bas se trouve sous la transition nue (ω_{eg}). Les mêmes simulations que précédemment tenant compte de cette fonction de transfert (Figure 4, (d), (e), (f)) montrent un bon accord avec les mesures expérimentales. Ce résultat nous éclaire sur les propriétés des polaritons en couplage fort qui sera intégré dans la conception de nouveaux détecteurs (SC-QWIP or SC-QCD) conçus pour fonctionner en couplage fort.

En parallèle de ces deux projets sur les polaritons ISB, nous avons participé à la conception et à la fabrication de QCLs pour la génération d'impulsions courtes THz. Les cavités Gires-Tournois ont montré leur intérêt, dans le moyen-infrarouge puis dans le THz, pour compenser la dispersion de la région active. Dans le THz les GTI-QCL ont initialement utilisé des régions actives avec un gain relativement étroit, utilisant pour mécanisme d'inversion la dépopulation par phonon LO (longitudinal optique). Afin de réduire la largeur temporelle de l'impulsion THz nous proposons d'utiliser des structures QCL large bande. Pour ce faire deux types de régions actives large bande ont été développées : l'une rassemblant deux régions actives (dépopulation LO phonon) de fréquences centrales différentes et l'autre basée sur un mécanisme de transitions intermini-bande assistées par LO phonon.

La difficulté majeure dans la fabrication de ces cavités est la gravure des cavités laser. En effet la cavité Gires-Tournois est constituée de deux miroirs séparés l'un de l'autre de seulement 3 μm . Compte tenu de l'épaisseur des régions actives ($>15 \mu\text{m}$) cela impose l'utilisation d'une gravure sèche an-isotrope et selective. Afin de pouvoir fabriquer ces cavités nous avons développé une recette de gravure ICP (Induced Coupled Plasma) dédiée à ce type d'application.

Les cavités GTI fabriquées grâce à cette recette de gravure ICP ont généré des impul-

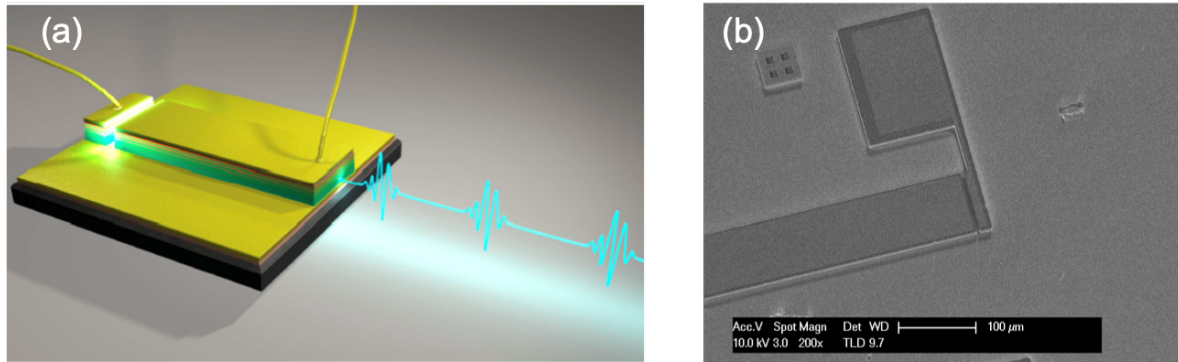


Figure 5: (a) Image 3D d'une cavité Gires-Tournois utilisée pour la génération d'impulsions THz courtes. (b) Image MEB de la cavité Gires-Tournois.

sions courtes semblables aux résultats obtenus dans la littérature. Ces dispositifs pourraient être utilisés comme pompe en régime pulsé picoseconde pour accéder au temps de vie des polaritons THz.

Introduction

The development of epitaxial growth in the 70's [1], such as molecular beam epitaxy (MBE), appeared as a revolutionary tool to explore the fields of condensed-matter, semiconductor, and opto-electronics. MBE brought an unprecedented control of material layer thickness at the nano-scale.

One of the breakthroughs that stems from the MBE development was the fabrication of quantum well (QW) structures, heterostructures and modulation doping. Inside the QW the electronic states are confined and transitions between these electronic states can be engineered between the valence and conduction bands (inter-band) or inside one band (intersub-band). In a QW, the alloy composition of a same material (AlGaAs; AlGaInP;...), the width of the QW and the doping of the material are the key elements to tune the transition energy. In the case of intersubband transitions, a wide spectral range from the near-infrared to the THz is accessible.

Optoelectronic devices typically operate in the weak coupling regime between light and matter, for example in conventional lasers which rely on population inversion to achieve optical gain. Recently, however, there has been a surge of interest in quantum systems operating instead in the *strong coupling regime*, when the coupling strength of the light-matter interaction is so strong that new states – cavity polaritons – are created, that are partially light, and partially material excitations.

In semiconductors, exciton-polaritons have been the most widely studied type of strongly coupled system. However, recently, a new phenomenon has been realized exploiting intersubband transitions. The resulting excitations are called intersubband polaritons, and they have two remarkable properties: (i) a bosonic character that is maintained up to high carrier densities since they are not restricted by the Mott transition limit; and, (ii) large Rabi splittings.

One of the main issues for intersubband polaritons is the choice of the cavity, as ISB transitions are TM polarized and therefore Bragg mirrors cannot be used. In the Mid-IR, the first strategy to observe polaritons relied on total internal reflection. In 2003, by confining the electromagnetic radiation between a doped layer and a GaAs/Air interface ISB polaritons were demonstrated for the first time [2], six years after the theoretical proposal [3]. Subsequent developments include the demonstration of ISB polariton LEDs [4] and exciton-polariton LEDs at near-IR wavelengths; polariton-based detectors/emitters [5, 6, 7]; ultra-fast switching [8].

The total internal reflection configuration has significant drawbacks: it restricts the probing incident or emission angles through the cavity, no coupling from the surface is possible, the overlap with the active region is not maximized, and the cavity is not directly scalable from one frequency range to another.

In parallel to the work in the Mid-IR, research in the THz range explored the *ultrastrong coupling* regime [9]. Because the Rabi-splitting varies as the square root of the overlap between the electromagnetic field and the QW active region, metal-insulator-metal (M-I-M) cavities have been widely employed [10], as they offer confinement close to one. One peculiarity of the patch cavities used for these studies is that they have no dispersion.

These diverse developments led to the design of a new generation of M-I-M resonators that are instead dispersive. These resonators with a periodically opened top metal have several advantages: the confinement is high, the light is coupled from the surface of the sample, the coupling can be engineered by controlling the geometry of the cavity or the angle of incidence and they are entirely scalable from the NIR to the THz [11, 12, 13]. In 2018, phonon-polariton scattering was observed by optical pumping of a dispersive M-I-M cavity Ref.[14]. This experiment proved the versatility of this type of cavity.

The goal of this work has been to take advantage of the dispersive M-I-M cavities to explore the fundamental properties of ISB polaritons *bright states* in the Mid-IR and in the THz spectral ranges.

In the Mid-IR we have explored the effect of the strong coupling on the generation of photocurrent by using a quantum well infrared photodetector in strong coupling with a dispersive M-I-M cavity [15]. This approach has a two-fold motivation. From the device point of view, the strong coupling regime could be a key technique to disentangle the frequency of detection from the thermal activation energy. From the polaritonic point of view, dispersive cavities represent an ideal platform to explore the interaction between *bright states* and electrical transport. Understanding and mastering the energy exchange between the *bright states* and the electrons - direct and reverse mechanisms - is essential for the development of detectors, but especially for electrically pumped emitters.

On the other side of the *Reststrahlen band*, the observation of THz-ISB polaritons is in their early stages. Effectively, in the THz domain, quantum devices ([16, 17], QWIP [18]) and thermal devices (bolometers) are generally limited to cryogenic operating temperatures. In the long term, strong coupling might reveal as a promising concept to reduce the temperature dependence of THz quantum devices. Nevertheless, most of the fundamental properties (lifetime, saturation levels, scattering mechanisms) of THz ISB polaritons still need to be assessed. The observation and the estimation of these structural properties would be essential to design THz quantum devices in strong coupling, for instance for a THz ISB polariton laser. Note that it is possible to observe THz polaritons at room temperature using parabolic quantum wells (PQWs) [19, 20]. However, the growth of these PQWs is still challenging and we chose to work with standard square quantum wells that are for the moment the best candidates (narrower linewidth) for ISB polariton physics in this spectral range.

In this manuscript, we have implemented dispersive M-I-M cavities in strong coupling with a THz intersubband transition. The dispersion of the cavity – measured with a specially developed set-up - will be used to access a broad set of polaritonic states offering a platform to explore the fundamental properties of THz-ISB polaritons.

One crucial peculiarity here is that the Rabi-splitting ($E_{Rabi,THz} \sim 1-2 \text{ meV}$) is much smaller than the LO-phonon energy ($E_{LO,GaAs} \approx 36 \text{ meV}$). Consequently, the phonon-polariton scattering is not permitted in the THz and alternative mechanisms have to be explored such as polariton-polariton scattering [21].

To observe these specific mechanisms a powerful source of light associated with a precise technique of spectral measurement is necessary. The quantum cascade laser demonstrated in the Mid-IR in 1994 [22] and in the THz in 2002 [23], appears as a good candidate for the excitation of the polaritonic states, especially since the demonstration of output peak powers close to 1 Watt [17, 24] in the range of 2.5 to 4 THz. An elevated output power enables to pump effectively the ISB polaritons. Furthermore, the pulse length can potentially be chosen from the μs (electrical power supply) to the ps (modelocked QC lasers [25, 26]).

THz-QC lasers can be synchronized with a photo-conductive antenna and integrated in a time-domain spectroscopy (TDS) system. The sample in strong coupling and its modifications under the intense laser electromagnetic field can then be analyzed with a THz probe. To be compatible with these two technologies (THz QCL and TDS) we engineered the ISB polariton states around 2.5-3 THz.

The manuscript is divided into three main parts and it consists of six chapters that follow almost chronologically the conduct of my Ph.D.

Part 1 concerns the work on the THz polaritons in a dispersive cavity. I first implemented the Metal-Insulator-Metal (M-I-M) dispersive cavity for THz polaritons. I specifically designed and fabricated an experimental set-up to measure the dispersion on a Fourier Transform Interferometer (FTIR). The ISB polaritons have then been studied in time-domain spectroscopy (TDS) at the LPA in the group of S.Dhillon.

In Part 2, we explore the impact of the spectral gain broadening of a QC active region to reduce the pulses width of mode-locked THz-QC lasers.

In Part 3, we implement the M-I-M dispersive cavity on a bound-to-quasi-bound Quantum Well Infrared Photodetector (QWIP) to observe the electronic behavior of ISB polaritons.

Chapter 1 serves as a general introduction describing the formalism related to: material science in III-V semiconductors and metals, the physics of quantum wells and intersubband transitions, the electromagnetism of double-metal waveguides and finally the strong-coupling regime between a cavity photon and intersubband plasmon.

Chapter 2 presents the design and the fabrication of dispersive M-I-M cavities in strong coupling with a THz intersubband transition (3 THz). A specific set-up has been fabricated to measure the dispersion of these samples in reflectivity at liquid Helium temperature. This initial study gives crucial information about the energy levels of the polaritonic states and confirms the compatibility of these samples with time-domain spectroscopy measurement performed at the LPA/ENS laboratory. Chapter 3 presents the preliminary results on these samples with TDS reflectivity and pump-probe measurements. The measurement of the polaritonic branches with and without laser pumping provides information about the potential scattering mechanisms that come into play in the THz range. Taking a long term view, this study could lead to the definition of a protocol for the development of intersubband polariton lasers in the THz domain.

In parallel to the THz polaritons, Part 2 (composed only by Chapter 4), explores tech-

niques to improve the performance of mode-locked THz-QCLs (shorten the pulse). Recent results, in which our group was involved, proposed to tailor the laser cavity with a Gires-Tournois Interferometer (GTI) to compensate the gain dispersion of the active region [27]. With this technique, stable pulses down to 4 ps were obtained. In the context of the European project *H2020-Ultra-QCL*, we investigated two methods to increase the number of lasing modes: by broadening the gain. First, the dispersion compensation of a GTI was applied to broadband active region heterostructures. The fabrication (C2N-Orsay cleanroom) of the GTI-QC lasers required the development of a specific dry-etching recipe Ref.[28] that will be described in details.

Part 3 of the thesis manuscript presents the work on quantum well infra-red detectors in strong coupling.

Chapter 5 introduces the main elements of the detection theory (responsivity, detectivity, noise equivalent power) adapted to QWIP devices. Some notable works related to QWIP technology in weak and strong coupling are discussed.

In Chapter 6 the design, the fabrication, and the characterization of the structures in weak (Mesa) and in strong-coupling (SC-QWIP) are presented. A comparative analysis of the devices in weak and strong coupling and of the dispersion in photocurrent of the devices in strong coupling confirms the polaritonic origin of the experimentally observed signal. In particular, the singular shape of the polariton dispersions has confirmed the relative positions of the polaritonic states (dressed states) compared to the single particle states that set the electronic transport. The specific behavior of the lower polariton dispersion in photocurrent required the introduction of a phenomenological model that is able to accurately reproduce the experimental data using a single transfer function summarizing the frequency dependence of the probability rate of escape from the QW for an electron in the excited state.

Light-Matter Interaction in Semiconductor Quantum Wells

This first chapter introduces the theoretical concepts of light-matter interaction. These transversal concepts valid for both THz and Mid-IR domains are essential to understand the strong coupling regime.

First, the quantum mechanics of III-V semiconductors adapted to GaAs and the inter-subband transitions will be presented. Then M-I-M cavities will be studied. Finally, we present two theoretical visions of the strong coupling regime between a cavity photon and an electronic transition.

1.1 III-V Semiconductor: GaAs

In this manuscript, we will present experimental results on THz polaritons, THz lasers and Mid-IR detectors. All these devices have used GaAs/AlGaAs heterostructures active regions. In this first section, we will apply the concepts of quantum mechanics of III-V semiconductors to this peculiar material.

Bulk GaAs crystallizes in Zinc-Blende structure (Figure 1.1) where the elements of the groups III and V stand on the nodes of two face-centered-cubic lattice offset by a quarter of diagonal. The first Brillouin zone of the reciprocal space represented Figure 1.1 is an octahedron with cut faces. The maximum of the valence band and the minimum of the conduction band are at the Γ point. The bulk GaAs has a direct gap.

The growth by molecular beam epitaxy permits to realize lattice-matched heterostructures between GaAs and AlGaAs.

1.1.1 Envelope Function Formalism

In a bulk semiconductor, electrons are subjected to the a crystalline potential $V(\mathbf{r})$, periodic in the three dimensions: $V(\mathbf{r} + \mathbf{R}) = V(\mathbf{r})$ if \mathbf{R} belongs to the Bravais lattice. The Hamiltonian, neglecting the spin-orbit interaction, is then written:

$$H_{el} = \frac{p^2}{2m_e} + V(\mathbf{r}). \quad (1.1)$$

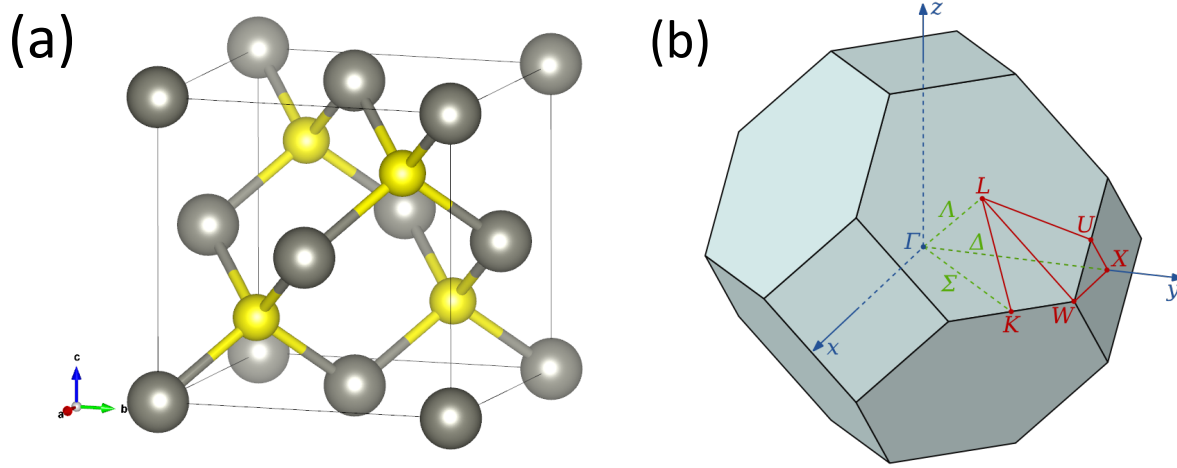


Figure 1.1: (a) Crystallographic view of the Zinc-Blend structure performed with Vesta Software with the data of *materialsproject.org*. The Gallium sites are in grey and the Arsenide sites on half of the tetrahedral sites are in yellow. (b) Brillouin zone for the Zinc-Blend structure.

According to the Bloch Theorem, the eigen states are $\psi_{n,\mathbf{k}} = \frac{e^{i\mathbf{k}\cdot\mathbf{r}}}{\sqrt{V}} u_{n,\mathbf{k}}(\mathbf{r})$ where $n \in \mathbb{N}$. These states are the product between a plane wave and a function with the same period of the crystal lattice.

In the heterostructure, the energy gap between the different materials is distributed between the valence and the conduction bands. Thus the conduction band has a profile $E_c(z)$. In this case, a similar solution can be found where the plane wave is replaced by an envelope function (f_i) which is supposed to vary over one lattice period slowly.

$$\Psi_i(\mathbf{r}) = f_i(\mathbf{r}) u_{\Gamma}^{B,W}(\mathbf{r}), \quad (1.2)$$

i represents the quantum number of the problem and $u_{\Gamma}^{B,W}(\mathbf{r})$ is the conduction band wavefunction of the barrier (well) at the Γ point of the Brillouin zone. The envelope function profile is determined by the potential $E_c(z)$ to which an external potential $V_{ext}(\mathbf{r})$ can be added.

By using this approach, it is possible to describe the electrons of the conduction band only with the envelope function. The method consists in taking into account the contribution of the crystalline potential in the calculation through the effective mass defined by $m^* = \hbar^2 \left(\frac{\partial^2 E_c(k)}{\partial k^2} \right)^{-1}$.

1.1.2 Quantum Wells and Subbands

The evaluation of the effective mass of the different subbands is not trivial. Evan O'Neill Kane was one of the main developers of the k.p model used to solve this problem. To estimate the effective masses in the different bands of the system Kane worked under the hypothesis [29] that the ratio between the eigenvalues of the n_{th} confined states and the band gap (E_n/E_g) was small compared to unity. Under these conditions, the band mixing can be neglected and the wavefunctions clearly defined.

The system is then described only by the envelope function with the appropriate effective mass

$$-\frac{\hbar^2}{2m^*}\nabla^2 f_i(\mathbf{r}) + V(\mathbf{r})f_i(\mathbf{r}) = E_i f_i(\mathbf{r}). \quad (1.3)$$

In a quantum well the artificial potential is created only along the growth direction z , meaning that $V(\mathbf{r}) = V(z)$. In this case, the free motion in the x and y directions can be separated :

$$f_{i,\mathbf{k}_{x,y}} = \frac{1}{\sqrt{S}} e^{j\mathbf{k}_{x,y}\cdot\mathbf{r}} \psi_i(z), \quad (1.4)$$

where $\mathbf{k}_{x,y} = \mathbf{k}_x + \mathbf{k}_y$ is the transverse wavevector and S is the sample area. By inserting (1.4) into Equation (1.3) we can write the Schrodinger equation in one dimension

$$-\frac{\hbar^2}{2m^*} \frac{\partial^2}{\partial z^2} \psi_i(z) + V(z)\psi_i(z) = E_i \psi_i(z), \quad (1.5)$$

with $\frac{1}{m^*} \frac{\partial}{\partial z} \psi_i(z)$ and $\psi_i(z)$ continuous at the interface between two different materials.

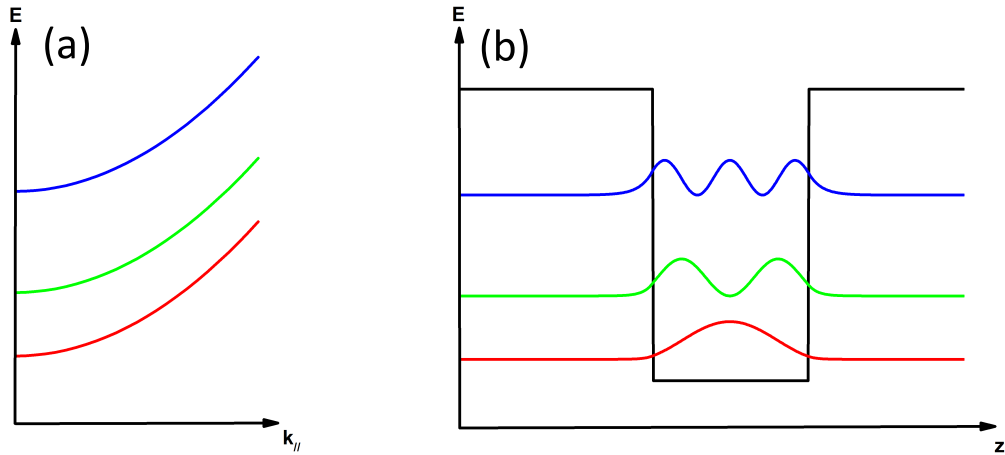


Figure 1.2: (a) Schematics of three energy levels in a GaAs/AlGaAs Quantum well. (b) Energy dispersion as a function of the in-plane wave vector.

To illustrate Equation (1.5) we consider the simplest model of an infinitely high barrier square QW [30], i.e, $V = 0$ for $0 \leq z \leq L_w$, $V = \infty$ for $z < 0$ and $z > L_w$, where L_w is the width of the QW. In this case the eigenstates and energy levels are

$$\begin{cases} \Psi_n(\mathbf{k}_{xy}) = \sqrt{\frac{2}{L_w S}} \sin\left(\frac{\pi n}{L_w} z\right) \exp(i\mathbf{k}_{xy} \cdot \mathbf{r}) \\ E_n(\mathbf{k}_{xy}) = \frac{\hbar^2}{2m} \left(\frac{\pi^2 n^2}{L_w^2} + k_{xy}^2 \right) \end{cases} \quad (1.6)$$

Where S is the normalization area in the x - y plane, n is a positive integer, \mathbf{k}_{xy} is the x - y plane wavevector and m the effective mass in the well. Equation (1.6) explains the reason for the term "subband": in a given quantized state one can add many electrons occupying different in-plane momenta.

1.2 Intersubband Transitions

In the following section, we will introduce *Fermi's Golden Rule* to calculate photon absorption inside a Quantum Well.

1.2.1 Light Matter Interaction

We consider an incident wave at frequency ω , with a wave vector \mathbf{q} such as $\omega = cq/n_s$ where c is the speed of light in vacuum and n_s is the substrate refractive index, $\hat{\mathbf{e}}$ is the light polarization. The oscillating electric field can then be written: $\vec{F} = F\hat{\mathbf{e}}\cos(\omega t - \mathbf{q}\cdot\mathbf{r})$. The corresponding vector potential according to the Coulomb Gauge is $\vec{A}(\mathbf{r}, t) = j\frac{F\hat{\mathbf{e}}}{2\omega}e^{j(\omega t - \mathbf{q}\cdot\mathbf{r})}$ [31].

The Hamiltonian of an electron, charge $-e$, progressing in an electromagnetic field is obtained from the Hamiltonian of a free electron, by replacing \vec{p} by $\vec{p} + e\vec{A}$. In the dipolar approximation, when the wavelength is far larger than the system dimensions (quantum well width), the photon wavevector \vec{q} and the spatial dependence of \vec{A} can be neglected. Under these conditions and by neglecting the term in A^2 :

$$H = H_0 + \frac{e\vec{A}\cdot\vec{p}}{m^*}, \quad (1.7)$$

where H_0 is the Hamiltonian in the absence of an electric field.

We consider the transition from an initial state $|\Phi_{i,\mathbf{k}}\rangle$ of subband i , with wavevector \mathbf{k} and energy $E_{i,\mathbf{k}} = E_i + \frac{\hbar^2\mathbf{k}^2}{2m^*}$ and a final state $|\Phi_{f,\mathbf{k}'}\rangle$ of subband f , with wavevector \mathbf{k}' and energy $E_{f,\mathbf{k}'} = E_f + \frac{\hbar^2\mathbf{k}'^2}{2m^*}$. These two states are described by

$$\begin{cases} \Psi_{i,\mathbf{k}}(\mathbf{r}) = \frac{1}{\sqrt{S}}e^{j\mathbf{k}_{xy}\cdot\mathbf{r}}\Phi_i(z) \\ \Psi_{f,\mathbf{k}'}(\mathbf{r}) = \frac{1}{\sqrt{S}}e^{j\mathbf{k}'_{xy}\cdot\mathbf{r}}\Phi_f(z) \end{cases} \quad (1.8)$$

The transition rate $\Gamma_{if}(\hbar\omega)$ between these two states is given by *Fermi's Golden Rule*

$$\Gamma_{if}(\hbar\omega) = \frac{2\pi}{\hbar}|\langle\Psi_{f,\mathbf{k}'}|V|\Psi_{i,\mathbf{k}}\rangle|^2\delta(E_{f,\mathbf{k}} - E_{i,\mathbf{k}} - \hbar\omega), \quad (1.9)$$

where $V = \frac{e\vec{A}\cdot\vec{p}}{m^*} = \frac{jeF}{2m^*\omega}\hat{\mathbf{e}}\cdot\mathbf{p}$. The transition rate is then proportional to the square of the following matrix element:

$$\langle\Psi_{f,\mathbf{k}'}|\hat{\mathbf{e}}\cdot\mathbf{p}|\Psi_{i,\mathbf{k}}\rangle = \epsilon_z\delta_{\mathbf{k},\mathbf{k}'}\langle\Phi_{f,\mathbf{k}'}|p_z|\Phi_{i,\mathbf{k}}\rangle. \quad (1.10)$$

Consequently, only an electric field with a z component (TM polarized) can couple to an intersubband transition, which occurs at a constant \mathbf{k} vector. The energy difference between the two states $E_{if} = E_{f,\mathbf{k}} - E_{i,\mathbf{k}}$ does not depend on \mathbf{k} . By introducing the oscillator strength

$$f_{if} = \frac{2}{m^*\hbar\omega_{if}}|\langle\Phi_f(z)|p_z|\Phi_i(z)\rangle|^2 = \frac{2m^*\omega_{if}}{\hbar}|\langle\Phi_f(z)|z|\Phi_i(z)\rangle|^2, \quad (1.11)$$

and the z -component of the incident beam intensity $I_z = \frac{\epsilon_0cn_sF_z^2}{2}$, we obtain finally [32]

$$\Gamma_{if}(\hbar\omega) = \frac{2\pi e^2 I_z f_{if}}{m^*\omega\epsilon_0cn_s}\delta(\hbar\omega - E_{if}). \quad (1.12)$$

In Equation (1.11) the oscillator strength is related to the dipolar matrix elements that can be calculated from the knowledge of the envelope functions.

Experimentally the Dirac function $\delta(\hbar\omega - E_{ij})$ can be replaced by a Lorentzian function taking into account the natural broadening of the energy levels. The Lorentzian function is written with a full width half maximum γ , centered around E_{if} . In addition the electron density by unit area N_i and N_j for each state can be considered. The transition rate (Equation (1.12)) is then weighted by the number of possible transitions between the states i and f $S(N_f - N_i)$. The final expression of the transition rate is then

$$\Gamma_{if}(\hbar\omega) = \frac{(N_i - N_f)S e^2 I_z f_{if}}{m^* \omega \epsilon_0 c n_s} \frac{\gamma}{(\gamma/2)^2 + (\omega - \omega_{if})^2}. \quad (1.13)$$

In the following, we consider that only the first subband is occupied ($E_F < E_2$) and focus only on the transition $1 \rightarrow 2$. Thus $N_1 - N_2 = N_1 = N_s$ where S is the surface of the sample.

1.2.2 Absorption

In any medium, the absorption coefficient ($\alpha_{3D}(\mathbf{r}, \omega)$) is defined by the ratio between the electromagnetic field energy absorbed per unit of time and volume ($\hbar\Gamma_{ij}/(S * L_{eff})$) and the intensity of the electromagnetic field ($I = \frac{\epsilon_0 c n_s F^2}{2}$). Consequently, a wave propagating in an active medium on a length L is damped by a factor $e^{-\alpha_{3D}L}$. A more convenient approach uses the absorbance, i.e., the electromagnetic energy absorbed by unit of surface, that is a dimensionless quantity related to absorption by the relation $\alpha_{2D} = \alpha_{3D}L_{eff}$ with $L_{eff} \approx L_{well}$ the effective thickness of the quantum well (quasi 2D electron gas) [33]. By using Equation (1.13) we can give the expression of the absorbance [31]

$$\alpha_{2D}(\omega) = \frac{N_s e^2 f_{12}}{m^* \epsilon_0 c n_s} \frac{\gamma}{(\gamma/2)^2 + (\omega - \omega_{12})^2} \quad (1.14)$$

Experimentally the transmission is more accessible than the absorption. Considering a TM wave with intensity I propagating through a quantum well, making an angle θ with the growth direction (z), the length of interaction with the quantum well is then $L_{eff}/\cos(\theta)$. The transmission in this situation is

$$T(\omega) = \exp(-\alpha_{3D}L_{eff}\sin^2(\theta)/\cos(\theta)) = \exp(-\alpha_{2D}\sin^2(\theta)/\cos(\theta)), \quad (1.15)$$

the factor $\sin^2(\theta)$ is because only the z component of the electric field interacts with the electron gas. By neglecting the reflectivity at the interfaces the absorption $A = 1 - T$ is proportional to α_{2D} for weak absorptions

$$A = 1 - \exp(-\alpha_{2D}\sin^2(\theta)/\cos(\theta)) \approx \alpha_{2D}\sin^2(\theta)/\cos(\theta). \quad (1.16)$$

1.2.3 Lorentz Model for Dielectrics

The Lorentz model is a semi-classical model describing the propagation of an electromagnetic wave in a dielectric. This model is the most efficient to describe the properties of insulators/semiconductors at optical frequencies from the far to the mid-Infrared. Electrons

with a mass m are described as elastically bound to the nucleus that is considered as fixed. In the case of N electrons by unit volume, there are as many oscillator eigenfrequencies [34]. The damping strength is $-m_e\gamma\frac{\partial\mathbf{r}}{\partial t}$. The fundamental equation of the dynamics of an electron of mass m_e , charge $-e$, resonant at ω_0 and driven by an electric field $\mathbf{E}(\omega) = E_0\hat{e}e^{-j\omega t}$ is

$$m_e(-\omega^2 - j\gamma\omega + \omega_0^2)\mathbf{r} = -e\mathbf{E}(\omega). \quad (1.17)$$

The induced polarization -that is proportional to the dipole moment- is then

$$\mathbf{P}_{res}(\omega) = -Ne\mathbf{r} = \frac{Ne^2}{m_e} \frac{1}{(\omega_0^2 - \omega^2 - j\gamma\omega)} \mathbf{E}(\omega). \quad (1.18)$$

The dielectric displacement of the medium is defined by $\mathbf{D} = \epsilon_0(1 + \chi)\mathbf{E} + \mathbf{P}_{res}$ where χ is the susceptibility of the material. According to Equation (1.18) we obtain $\mathbf{D} = \epsilon_0\epsilon(\omega)\mathbf{E}$ with

$$\epsilon(\omega) = 1 + \chi + \frac{Ne^2}{\epsilon_0 m_e} \frac{1}{(\omega_0^2 - \omega^2 - j\gamma\omega)}. \quad (1.19)$$

We can split (1.19) into its real and imaginary parts

$$\begin{cases} \epsilon_1(\omega) = Re[\epsilon_r] = 1 + \chi + \frac{Ne^2}{\epsilon_0 m_e} \frac{\omega_0^2 - \omega^2}{(\omega_0^2 - \omega^2)^2 + (\gamma\omega)^2} \\ \epsilon_2(\omega) = Im[\epsilon_r] = \frac{Ne^2}{\epsilon_0 m_e} \frac{\gamma\omega}{((\omega_0^2 - \omega^2)^2 + (\gamma\omega)^2)} \end{cases} \quad (1.20)$$

This form of equation leads to constant permittivities on each side of the resonance. At low frequencies (static) $\epsilon_{st} = \epsilon_r(\omega \rightarrow 0) = 1 + \chi + \frac{Ne^2}{\epsilon_0 m_e \omega_0^2}$. At high frequency the limit is $\epsilon_\infty = \epsilon_r(\omega \rightarrow \infty) = 1 + \chi$.

ϵ_1 and ϵ_2 are related to the refractive index n and the extinction coefficient κ of the medium through

$$\begin{cases} \epsilon_1 = n^2 - \kappa^2 \\ \epsilon_2 = 2n\kappa \end{cases} \quad (1.21)$$

One important aspect of a resonant Lorentzian absorption is that the effect on the refractive index occurs over a larger frequency range than the absorption.

Bulk GaAs

In III-V semiconductors, like GaAs, the atoms are arranged in a Zinc-Blende crystal structure by bonds of mainly covalent nature. The chemical bond shows a partial ionic character because the shared electrons lie slightly closer to group V atoms than to group III. This asymmetry in the electron cloud creates a dipole moment that interacts with electric fields. This polarization creates strong absorption and reflection bands in the infrared spectral range, particularly close to the *transverse optical* (TO) photon modes of the crystal.

The interaction between electro-magnetic waves and TO phonons can be modeled introducing a damped oscillator of frequency ω_{TO} in the Lorentz model, which yields a dielectric function response in the form (1.19)

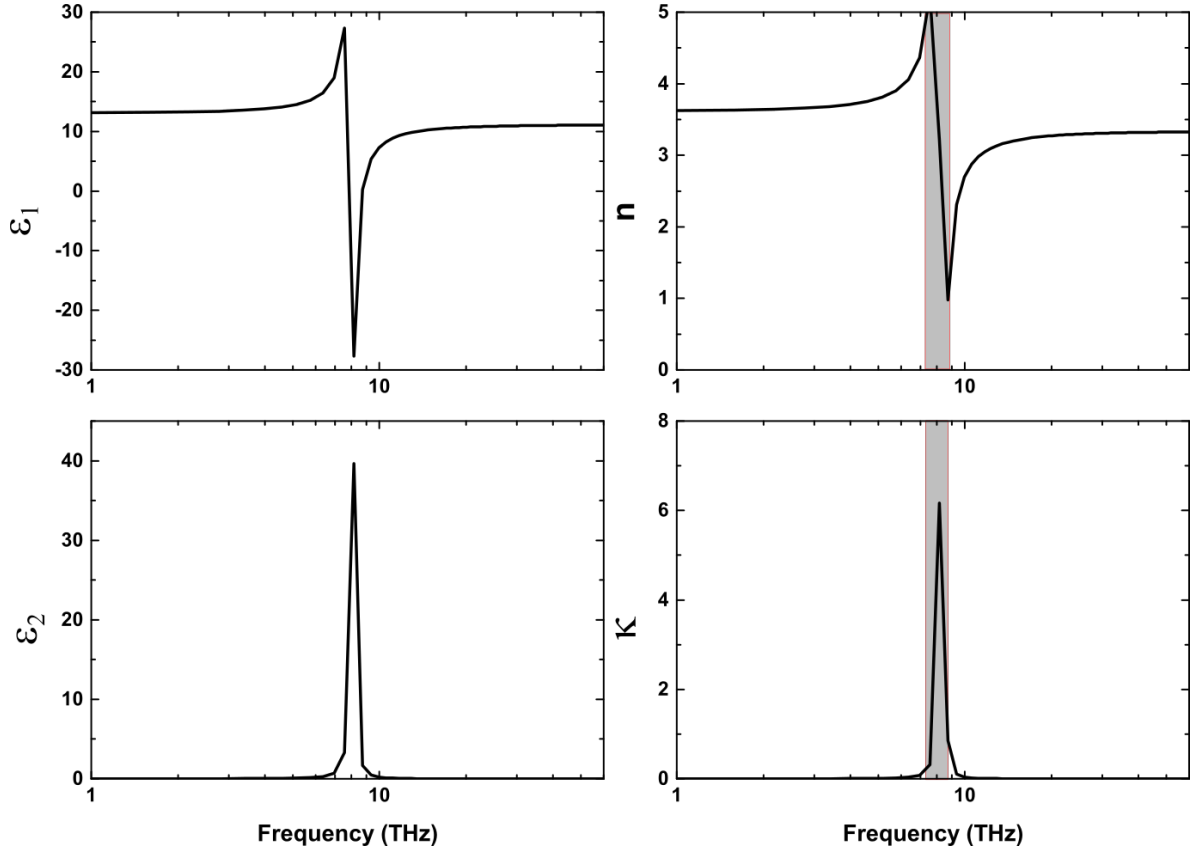


Figure 1.3: Optical constants (real and imaginary part of the permittivity ϵ_1 , ϵ_2 , index n and losses κ) derived from the Lorentz model for undoped GaAs. The grey areas represent the *Reststrahlen* band. The phonon's frequencies are $\nu_{TO} = 8.05 \text{ THz}$ for the transverse-optical phonon and $\nu_{LO} = 8.75 \text{ THz}$ for the longitudinal-optical phonon.

$$\epsilon(\omega) = 1 + \chi + \frac{Ne^2}{\epsilon_0 m_e} \frac{1}{(\omega_{TO}^2 - \omega^2 - j\gamma_{ph}\omega)} \quad (1.22)$$

$$= \epsilon_\infty + (\epsilon_{st} - \epsilon_\infty) \frac{\omega_{TO}^2}{\omega_{TO}^2 - \omega^2 - j\gamma_{ph}\omega}. \quad (1.23)$$

Where γ_{ph} is the damping of the phonon mode. If we recall the Lyddane-Sachs-Teller relation

$$\frac{\omega_{LO}^2}{\omega_{TO}^2} = \frac{\epsilon_{st}}{\epsilon_\infty}. \quad (1.24)$$

The equation (1.22) can be rewritten

$$\epsilon_r^{ph}(\omega) = \epsilon_\infty \left(1 + \frac{\omega_{LO}^2 - \omega_{TO}^2}{\omega_{TO}^2 - \omega^2 - i\gamma_{ph}\omega} \right) \quad (1.25)$$

The model parameters are experimentally extracted [35], yielding $\epsilon_\infty = 11.1$, $\nu_{TO} = 8.05 \text{ THz}$, $\nu_{LO} = 8.75 \text{ THz}$ and $\gamma_{ph} = 4.07 \cdot 10^{13} \text{ 1/s}$. The Figure 1.3 shows the real and the imaginary parts of the dielectric function, together with the refractive index and the extinction coefficient, of undoped GaAs.

Note that between ν_{LO} and ν_{TO} , ϵ_r is negative and $\sqrt{\epsilon_r}$ is imaginary. In this frequency band named *Reststrahlen band*, light cannot propagate into the medium and is completely reflected.

Dielectric Function in Multiple Quantum Wells

In a more detailed way, it has been shown [36] that a multiple quantum well behaves as an anisotropic dielectric with a Lorentz-like frequency dependence [31, 12]. Starting from the Lorentz equation (1.19), we can consider several resonances ω_k . To agree with the experiments, the oscillator strength f_k of each transition must be taken into account leading to the following

$$\epsilon(\omega) = 1 + \chi + \sum_k \frac{N_k e^2}{\epsilon_0 m_e} \frac{f_k}{(\omega_k^2 - \omega^2 - j\gamma\omega)} \quad (1.26)$$

In the case of a QW with an effective width $L_{eff} \sim L_{QW}$ when we focus mainly on the transition $1 \rightarrow 2$, we can write

$$\epsilon(\omega) = \epsilon_\infty \left(1 + \frac{N_s e^2}{\epsilon_0 m_e \epsilon_\infty L_{eff}} \frac{f_{12}}{(\omega_{12}^2 - \omega^2 - j\gamma\omega)} \right) \quad (1.27)$$

Where $N_s = N * L_{eff}$ is the number of oscillators by unit surface. We can then define the bidimensionnal conductivity of the quantum well $\sigma_{2D}(\omega) = \sigma(\omega)/L_{eff}$, in order to relate the dielectric function to the conductivity as follows:

$$\epsilon(\omega) = \epsilon_\infty + \frac{j\sigma_{2D}(\omega)}{\epsilon_0 \omega L_{eff}} \quad (1.28)$$

which gives the following expression for the conductivity

$$\sigma_{2D}(\omega) = \frac{N_s e^2 f_{12}}{m^*} \frac{\omega}{\omega_{12}^2 - \omega^2 - j\gamma\omega}. \quad (1.29)$$

At this stage it is interesting to introduce the plasma frequency associated to the transition $i \rightarrow f$

$$\omega_{Pif} = \sqrt{\frac{(N_i - N_f) e^2 f_{if}}{m^* \epsilon_0 \epsilon_\infty L_{eff}}} \quad (1.30)$$

if only two subbands are involved we can write $\omega_{P12} = \sqrt{\frac{N_s e^2 f_{12}}{m^* \epsilon_0 \epsilon_\infty L_{eff}}}$ which gives the following expression

$$\begin{cases} \sigma_{2D}(\omega) = j\omega \epsilon_0 \epsilon_\infty L_{eff} \frac{\omega_{P12}^2}{\omega_{12}^2 - \omega^2 - j\gamma\omega} \\ \epsilon(\omega) = \epsilon_\infty \left(1 + \frac{\omega_{P12}^2}{(\omega_{12}^2 - \omega^2 - j\gamma\omega)} \right) \end{cases} \quad (1.31)$$

This result is used to describe the permittivity in the Rigorous Coupled Wave Analysis algorithm. Note that the value of ϵ_∞ is different between the mid-infrared ($\epsilon_\infty = 11$) and the THz ($\epsilon_\infty = 12.96$).

The expression $\sigma_{2D}(\omega)$ in Equation (1.31) leads to a second definition of the absorption that is compatible with the Equation (1.16) at low doping level [33]

$$A = \frac{\mathcal{R}(\sigma_{2D}) \sin^2(\theta)}{\epsilon_0 c n_s \cos(\theta)}. \quad (1.32)$$

1.2.4 Highly Doped Semiconductors: Depolarization shift

For high electronic densities ($N_s > 10^{11} \text{cm}^{-2}$), i.e high absorptions, it is not possible to neglect the oscillating dipole created by the charge distribution in the quantum well. This oscillation that corresponds to the dynamical Coulomb interaction has a significant impact on the optical response of the quantum well.

In this development, we consider only the z component of the fields. The relation between the external field F_{ext} and the total field F_z is given by the conservation of the electronic displacement D_z at the interface

$$F_z^{ext} = \epsilon_{zz} F_z \quad (1.33)$$

An electron in the 2D electron gas is sensitive to the external radiation excitation as well as the oscillation of the other electrons around it. These oscillations induce an alternative current [37]

$$j_z(\omega) = \sigma_{zz} F_z = \tilde{\sigma}_{zz} F_z^{ext} \quad (1.34)$$

where $\tilde{\sigma}_{zz}$ describes the response of the medium with the external field and is expressed as

$$\tilde{\sigma}_{zz} = \frac{\sigma_{zz}(\omega)}{\epsilon_{zz}(\omega)} \quad (1.35)$$

Considering that the relation between σ_{zz} and ϵ_{zz} is defined by Equation (1.31) we can rewrite the conductivity as

$$\tilde{\sigma}_{zz} = -j\epsilon_0\epsilon_\infty\omega L_{eff} \frac{\epsilon_{zz} - 1}{\epsilon_{zz}} = j\omega\epsilon_0\epsilon_\infty L_{eff} \frac{\omega_p^2}{\omega^2 - \tilde{\omega}_{12} + j\gamma\omega} \quad (1.36)$$

where $\tilde{\omega}_{12} = \sqrt{\omega_{12}^2 + \omega_{p12}^2}$

The absorption of the quantum well is given similarly than in the previous section

$$A = \frac{\mathcal{R}(\tilde{\sigma}_{zz}) \sin^2(\theta)}{\epsilon_0 c n_s \cos(\theta)} \quad (1.37)$$

The expression of the absorption is modified only by the coefficient $\tilde{\omega}_{12}$. The absorption is blue shifted. This phenomenon is named *depolarization shift*.

1.3 Electromagnetic Waveguide

The choice of the cavity is crucial to confine the light in the active region and explore the polariton properties. In this manuscript, we mainly exploit the properties of metal-metal cavities. This section presents the electromagnetic concepts that will be used in the rest of the manuscript. Note that these theoretical concepts are also valid for the metal-metal THz-QCLs (Chapter 4).

1.3.1 Drude Model for Metals

To describe metals the model of *free electrons* is preferred. In this model the metal behaves as a plasma with fixed positive ions and moving electrons. The free electron model for metals was proposed by Drude in 1900. When an electric field is applied, the free electrons accelerate and then undergo collisions with a characteristic scattering time $\tau_{met} = \frac{1}{\gamma_{met}}$, where γ_{met} is the damping rate in the metal. Therefore the electrical conductivity is limited by scattering.

The Drude equation is similar to the Lorentz's ones except for the restoring force term because the electrons are free to move in the lattice under an applied field. The equation of motion for the displacement of a free electron of mass m_e and charge $-e$ forced by an AC field is then

$$m_0 \left(\frac{\partial^2}{\partial t^2} + \gamma_{met} \frac{\partial}{\partial t} \right) \mathbf{r} = -e\mathbf{E} \quad (1.38)$$

Considering a periodic electric field $\mathbf{E}(\omega) = E_0 \tilde{e} e^{-i\omega t}$ Equation (1.38) leads to the permittivity

$$\epsilon_r(\omega) = 1 - \frac{Ne^2}{\epsilon_0 m_0} \frac{1}{\omega^2 + j\gamma_{met}\omega} = 1 - \frac{\omega_p^2}{\omega^2 + j\gamma_{met}\omega} \quad (1.39)$$

where ω_p is the *plasma frequency*

$$\omega_p = \sqrt{\frac{Ne^2}{\epsilon_0 m_0}} \quad (1.40)$$

In a metal the optical properties are equivalently described by the AC conductivity than by the permittivity. In fact the two functions are related by

$$\epsilon_r(\omega) = 1 + \frac{j\sigma(\omega)}{\epsilon_0\omega} \quad (1.41)$$

1.3.2 Helmholtz Equation

Maxwell's curl equations in a source-free, linear and homogeneous medium under a time-harmonic field are

$$\vec{\nabla} \times \vec{E} = -j\omega\mu\vec{H} \quad (1.42)$$

$$\vec{\nabla} \times \vec{H} = j\omega\epsilon\vec{E} \quad (1.43)$$

To uncouple these two equations we take the curl on the first one and use the second one

$$\vec{\nabla} \times \vec{\nabla} \times \vec{E} = -j\omega\mu\vec{\nabla} \times \vec{H} = \omega^2\mu\epsilon\vec{E}. \quad (1.44)$$

Recalling the vector identity $\vec{\nabla} \times \vec{\nabla} \times \vec{A} = \vec{\nabla}(\vec{\nabla} \cdot \vec{A}) - \nabla^2\vec{A}$ and knowing that $\vec{\nabla} \times \vec{E} = 0$ in a source-free region, (1.44) becomes then

$$\nabla^2\vec{E} + \omega^2\mu\epsilon\vec{E} = 0 \quad (1.45)$$

This last equation is known as *Helmholtz* equation. The propagation constant in the medium is defined as $k = \omega\sqrt{\mu\epsilon} = nk_0$ where n is the refractive index of the medium and $k_0 = \omega/c$ is the free space propagation constant. In free space Helmholtz equation becomes

$$\nabla^2\vec{E} + \omega^2\mu\epsilon\vec{E} = \left(\frac{\partial^2\vec{E}}{\partial x^2} + \frac{\partial^2\vec{E}}{\partial y^2} + \frac{\partial^2\vec{E}}{\partial z^2} \right) + \omega^2\mu\epsilon\vec{E} = 0 \quad (1.46)$$

The projection of the Helmholtz equation on each component of a Cartesian reference system is then

$$\left(\frac{\partial^2 E_i}{\partial x^2} + \frac{\partial^2 E_i}{\partial y^2} + \frac{\partial^2 E_i}{\partial z^2} \right) + k_0^2 E_i = 0 \quad (i = x, y, z) \quad (1.47)$$

Equation (1.47) can be solved using the *method of separation of variables* for partial differential equations [38]

$$E_i(x, y, z) = f_i(x) * g_i(y) * h_i(z) \quad (1.48)$$

One can then separate in three ordinary 1D differential equations

$$\frac{\partial^2 f_i}{\partial x^2} + k_x^2 f_i = 0; \quad \frac{\partial^2 g_i}{\partial y^2} + k_y^2 g_i = 0; \quad \frac{\partial^2 h_i}{\partial z^2} + k_z^2 h_i = 0 \quad (i = x, y, z) \quad (1.49)$$

where the propagation constant has been separated in three components so that

$$k_x^2 = k_y^2 = k_z^2 = k_0^2 \quad (1.50)$$

The solutions of Equation (1.49) are plane waves in the form $e^{\pm jk_x x}$, $e^{\pm jk_y y}$ and $e^{\pm jk_z z}$ respectively. By convention, the - signs represent propagation in positive direction, while the + signs propagation in the negative direction.

This development leads to the expression of a plane wave

$$\vec{E} = \vec{E}_0 e^{-j\vec{k} \cdot \vec{r}} \quad (1.51)$$

This equation injected in the Maxwell-Gauss equation considering a medium without charges leads to

$$\vec{k} \cdot \vec{E}_0 = 0, \quad (1.52)$$

meaning that the electric field amplitude vector \vec{E}_0 must be orthogonal to the direction of propagation \vec{k} . Additionally if we use the *Maxwell-Faraday law*, we obtain

$$\vec{H} = \frac{1}{\omega\mu_0} \vec{k} \times \vec{E}_0 \quad (1.53)$$

This result shows that the magnetic field vector \vec{H} is simultaneously orthogonal to the direction of propagation and the electric field. Therefore the EM radiation propagates in free space as a transverse magnetic (TEM) wave.

In a medium, the electromagnetic wave can be bound in one or more directions by dielectric discontinuities or conducting boundaries. Waveguides impose specific constraints that shape the transverse mode characteristics.

1.3.3 Parallel Plate Waveguide

Waveguides are structures that confine and direct electromagnetic radiation. A simple type of waveguide is composed of two perfectly conducting infinite plates separated by a distance t between which EM waves are guided.

First, we recall the behavior of a TM wave reflected by a perfectly conducting surface located at $z=0$ in the x - y plane. The incident wave is described by a magnetic field in the form

$$\vec{H}_{inc} = H_0 e^{-j(k_x x + k_z z)} \mathbf{y} \quad (1.54)$$

Where $k_x = k_0 \cos(\theta_{inc})$ and $k_z = k_0 \sin(\theta_{inc})$. Due to the fact that the magnetic field has to be tangential to the conducting boundary the reflected field is necessarily

$$\vec{H}_{refl} = H_0 e^{-j(k_x x - k_z z)} \mathbf{y} \quad (1.55)$$

assuming a perfect reflection on the metallic plate. The total magnetic field from Eq.(1.54) and (1.55)

$$\vec{H} = \vec{H}_{refl} + \vec{H}_{inc} = 2H_0 \cos(k_z z) e^{-jk_x x} \mathbf{y} \quad (1.56)$$

The Ampère's law gives the electric field as a function of the magnetic field

$$\vec{E} = \frac{\nabla \times \vec{H}}{j\omega\epsilon} = \frac{1}{j\omega\epsilon} \left[-\mathbf{x} \frac{\partial}{\partial z} + \mathbf{z} \frac{\partial}{\partial x} \right] H_y \quad (1.57)$$

$$= 2H_0 \sqrt{\frac{\mu}{\epsilon}} \left[\frac{k_z}{k_0} \sin(k_z z) \mathbf{x} - \frac{jk_x}{k_0} \cos(k_z z) \mathbf{z} \right] e^{-jk_x x} \quad (1.58)$$

To satisfy the boundary condition at $z=0$ the tangential component of \vec{E} and the normal component of \vec{H} has to vanish, i.e. $E_x = E_y = H_z = 0$. In addition, the same conditions are satisfied on the other metal plane for $z=t$, consequently, for $\sin(k_z t) = 0$ thus $k_z t = \pi m$ with m an integer. This equation defines all the TM_m modes where $k_z = m\pi/t$. The same development gives similar sets of wavenumbers for the TE modes. Finally, both TM and TE mode guidance condition is

$$k_z = m\pi/t \quad (1.59)$$

where $m=0,1,2,\dots$ for TM modes and $m=1,2,\dots$ for TE modes. The parallel-plate waveguide is calculated using the dispersion relation $k_x^2 + k_z^2 = k_0^2 = \omega^2 \mu \epsilon$. According to equation (1.59)

$$k_x = \sqrt{\omega^2 \mu \epsilon - (m\pi/t)^2} \quad (1.60)$$

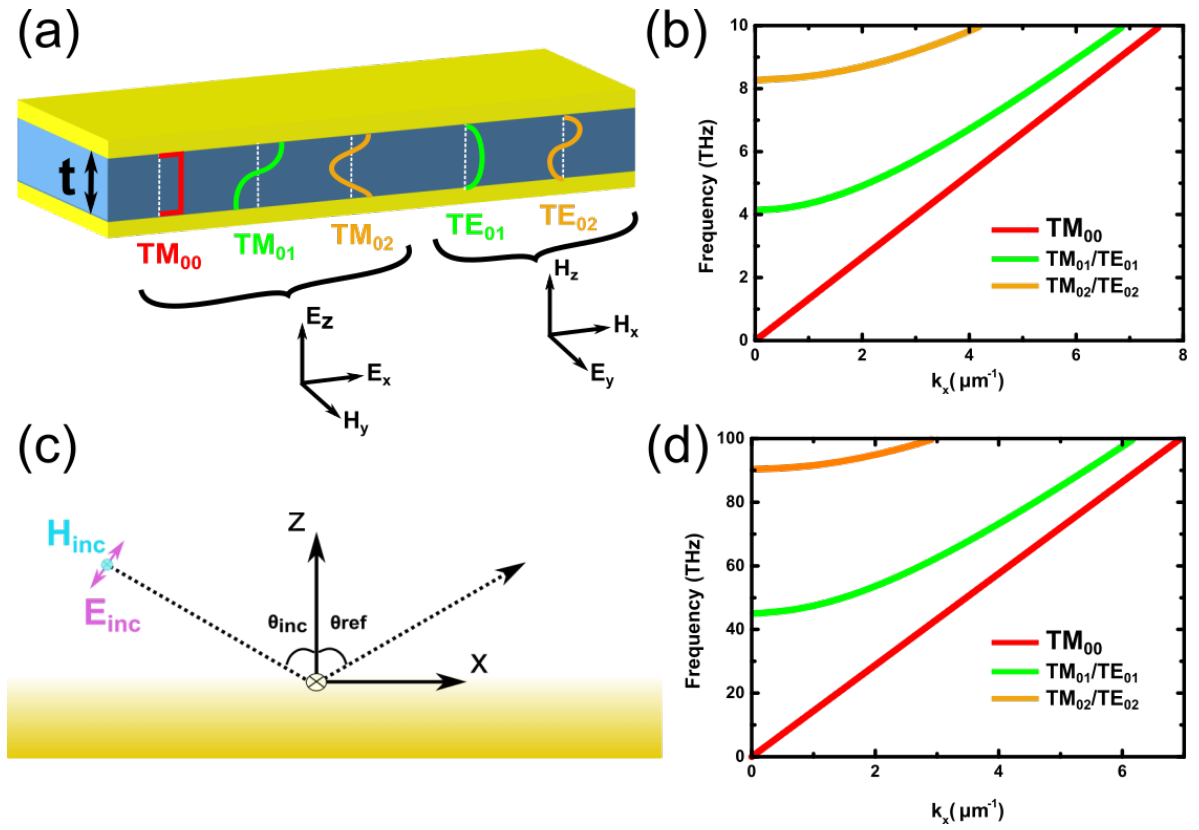


Figure 1.4: (a) Schematics of the Metal-Insulator-Metal waveguide with first TM/TE modes presented. (c) Schematics of a TM mode impinging TM mode on a metallic plane. Graphics (b) and (d) show the dispersion of these modes: in the Mid-Infra Red (d) with a cavity width of $1 \mu\text{m}$ and a permittivity $\epsilon_r = 11$; and in the THz (b) with a cavity width of $10 \mu\text{m}$ and a permittivity $\epsilon_r = 13.1$.

In the following, we will mostly operate with the TM_{00} mode (M-I-M dispersive cavity and M-I-M laser cavity). This mode ($m=0, k_z = 0$) has a linear dispersion (Figure 1.4) and it is defined by the fields

$$\begin{cases} \vec{E} = -2\sqrt{\frac{\mu}{\epsilon}} H_0 e^{-jk_x x} \mathbf{z} = -2\eta H_0 e^{-jk_x x} \mathbf{z} \\ \vec{H} = \vec{H}_{refl} + \vec{H}_{inc} = 2H_0 e^{-jk_x x} \mathbf{y} \end{cases} \quad (1.61)$$

Where $k_x = k_0$ and η is the impedance of the material.

1.3.4 Metal-Insulator-Metal Dispersive Cavity

In this section, we present the design of the dispersive metal-insulator-metal cavities. Then we introduce the basic principles of Rigorous Coupled Wave Analysis (RCWA) simulations and apply this algorithm to our study.

Concept

To reach the strong coupling regime, a high overlap between the electromagnetic field and the active medium is needed. In the near infrared, excitonic polaritons are epitaxially im-

plemented using structures with Bragg mirrors to confine the light close to the active region [39]. This solution is not directly scalable to the Mid-IR and the THz because ISB transitions only interact with TM modes. In the THz, a basic cavity with high confinement of the electromagnetic field in the active core ($> 90\%$) is the Metal-Insulator-Metal cavity. To cut-off all the modes except the TM_{00} mode the thickness of the cavity has to be chosen correctly. According to Equation (1.60) the cut-off condition is given by

$$\omega^2 \mu \epsilon < \pi/t^2. \quad (1.62)$$

This inequality can be rewritten as a condition on the cavity thickness

$$t < t_{lim} = \frac{\lambda}{2n}, \quad (1.63)$$

λ is the wavelength of the transition around which we want to work, n is the index of the active medium that is mostly composed of GaAs.

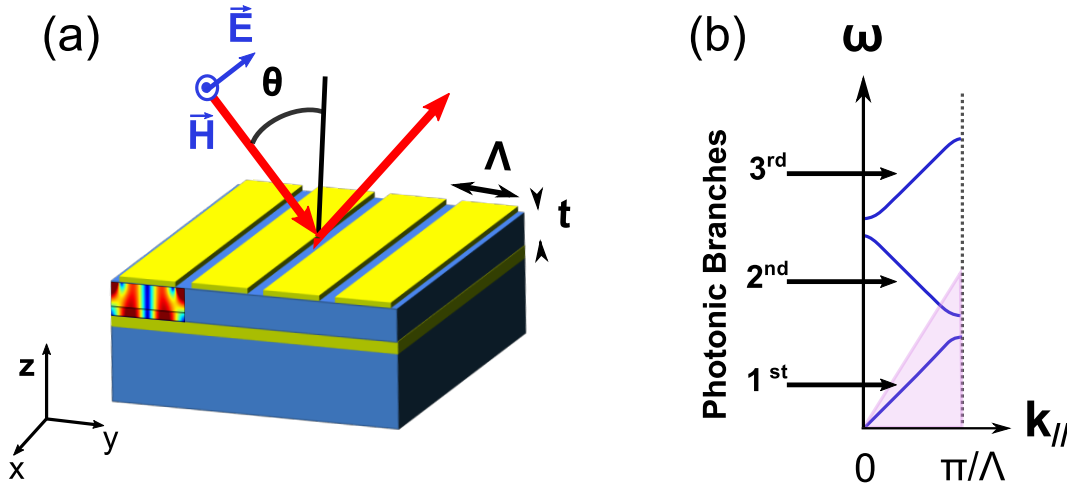


Figure 1.5: (a) The top grating introduces a periodic variation of the effective index in the active region that can be considered as a one dimensional photonic crystal. (b) The dispersion can be folded onto the Brillouin zone [40]. The effective index variation between the regions with and without metal opens a photonic band gap at the edge of the Brillouin zone. The purple area represents modes below the light cone.

However, coupling light into a M-I-M cavity is difficult because the coupling area is smaller than the diffraction limit of the THz light. To overcome this difficulty and have better control over polariton's properties, we periodically opened the top metal. The top grating enables surface coupling and generates dispersive modes that we can tune experimentally with the angle of incidence (Figure 1.5). Figure 1.5 shows that the electric field energy is confined below the metal ridges [41].

In this project, we want to couple the intersubband transition with the third photonic branch for three reasons. First, the branch is above the light cone. Second, simulations show a flat dispersion at $k_{//} = 0$ for both upper and lower polaritons, which could lead to a polariton accumulation in this experimentally accessible region. Third, if the cavity is sufficiently thin, there are no higher order TM or TE modes crossing the third photonic branch.

The M-I-M cavity is versatile and by tuning the thickness and the grating period of the cavity the 3rd photonic branch we can couple it with ISB transitions from the Mid-IR (Part

Implementation of dispersive M-I-M cavities	ISB Transition (THz)	Doping (cm^{-2})	Thickness (μm)		Grating period Λ (μm)
			QW active region	Buffer layer	
Part 1: Observation of polariton-polariton scattering in the THz domain	2.5	$\sim 10^{11}$	3	8	40
Part 3: QW infrared photodetectors in strong coupling with a dispersive M-I-M cavity	30	$\sim 10^{12}$	1	0	4

Table 1.1: Cavity geometries studied in this manuscript. Part 1 is designed for the THz and Part 3 is designed for the Mid-IR.

3 of this thesis) to the THz (Part 1 of this thesis). Table 1.1 presents the classical cavity parameters used in this manuscript.

Rigorous Coupled Wave Analysis Simulations

To solve a multi-layer system with a 1D or 2D transverse structure, a semi-analytical model is frequently used: Rigorous Coupled Wave Analysis (RCWA). This method decomposes a multi-layer system in elementary regions that can be periodic in the transverse direction (x-y) but have to be homogeneous in the longitudinal direction (z). In this section, we will first describe the general procedure of RCWA codes and then see the application in the specific case of a M-I-M cavity in strong coupling.

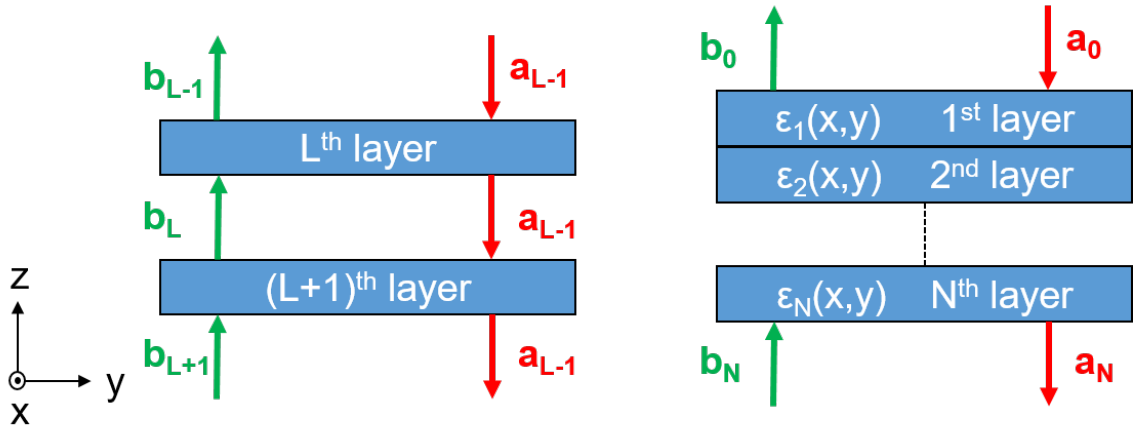


Figure 1.6: Simulation area and scattering matrix approach for a general patterned multilayer structure

In each layer, the dielectric function ($\epsilon_l(x, y)$) can be calculated knowing the geometry (thickness of the layer, periodicity in x and/or y) and materials (refractive indexes). However, the electromagnetic fields have z component, and as a first approach, the problem cannot be treated only in 2D. To solve the Maxwell's equations the fields, the dielectric function and the permeability are expanded in the Fourier space according to all the combinations

of x-y harmonics ($k_x(m) = k_{x,inc} - \frac{2\pi m}{\Lambda_x}$ and $k_y(n) = k_{y,inc} - \frac{2\pi n}{\Lambda_y}$ with $m, n \in \mathbb{N}$) [42]. The Maxwell's equation can then be rewritten in a matrix form leading to the matrix wave equation of the layer:

$$\frac{d^2}{d\tilde{z}^2} \begin{pmatrix} \mathbf{e}_x \\ \mathbf{e}_y \end{pmatrix} - \mathbf{\Omega}^2 \begin{pmatrix} \mathbf{e}_x \\ \mathbf{e}_y \end{pmatrix} = 0, \quad \text{with} \quad \mathbf{e}_x = \begin{pmatrix} E_x(1, 1) \\ E_x(1, 2) \\ \vdots \\ E_x(M, N) \end{pmatrix}, \quad \mathbf{e}_y = \begin{pmatrix} E_y(1, 1) \\ E_y(1, 2) \\ \vdots \\ E_y(M, N) \end{pmatrix} \quad (1.64)$$

where $\mathbf{\Omega} \in \mathbb{C}^{2*M*N}$ is a matrix derived from the Maxwell's equations containing all the information about the geometry and the materials of the layer, and $E_{x/y}(i, j, \tilde{z})$ are the electric field components after Fourier expansion. The analytic solutions of Equation (1.64) are under the form

$$\begin{pmatrix} \mathbf{e}_x(\tilde{z}) \\ \mathbf{e}_y(\tilde{z}) \end{pmatrix} = \exp(\mathbf{\Omega}\tilde{z})\mathbf{e}^+(0) + \exp(\mathbf{\Omega}\tilde{z})\mathbf{e}^-(0), \quad (1.65)$$

where $\mathbf{e}^+(0)$ and $\mathbf{e}^-(0)$ are the initial values for the differential equation. The superscripts + and - indicate the wave propagating respectively forward and backward in the z-direction. From this result, the remaining components of the electromagnetic fields can be calculated in the layer.

Once the band diagram ($E_{x/y}(i, j)$, $\forall i, j$) in each layer has been constructed, the layers are connected using boundary conditions at each interface. In particular, the transverse component of the wavevector is constant all over the multi-layer structure. The common way to match the electromagnetic field from one layer to another is to use the scattering matrix method (Figure 1.6). In this convention the forward and backward propagating amplitudes of waves are respectively noted \mathbf{b}_l and \mathbf{a}_l respectively [43, 44]. These forward and backward waves are related from one layer to a successive one by the scattering matrix \mathbf{S} :

$$\begin{pmatrix} \mathbf{a}_L \\ \mathbf{b}_{L+1} \end{pmatrix} = \mathbf{S}(L+1, L) \begin{pmatrix} \mathbf{a}_{L+1} \\ \mathbf{b}_L \end{pmatrix} = \begin{pmatrix} S_{11} & S_{12} \\ S_{21} & S_{22} \end{pmatrix} \begin{pmatrix} \mathbf{a}_{L+1} \\ \mathbf{b}_L \end{pmatrix} \quad (1.66)$$

Finally, the scattering matrices are determined to describe the propagation over the entire stack. The reflected \mathbf{b}_0 and transmitted \mathbf{a}_N signals of an incident plane wave (\mathbf{a}_0) are calculated from the scattering matrix of the whole structure \mathbf{S} . In terms of scattering matrix, these two coefficients are directly written:

$$\mathbf{b}_0 = S_{21}(0, N)\mathbf{a}_0, \quad \mathbf{a}_N = S_{11}(0, N)\mathbf{a}_0 \quad (1.67)$$

Practically, the M-I-M cavities used in this thesis are composed of four layers (Figure 1.7): the top gold grating with a period $\Lambda \approx \lambda/2n$, a filling factor between 70% and 85%, a thickness 250 nm; a buffer of GaAs, and an active region of composed by multiple quantum wells for a total thickness $t = t_{buffer} + t_{MQWs} \approx \lambda/10$; and a bottom gold contact thickness 400 nm. The substrate is not taken into account in the simulations because the electromagnetic field does not go through the bottom metal. Table 1.1 presents some estimation of t and Λ for the THz and the Mid-IR domains.

These materials have been widely studied in the previous chapter, except the active region for which we use the Zaluzny-Nalewajko model for the z component of the dielectric tensor [36]:

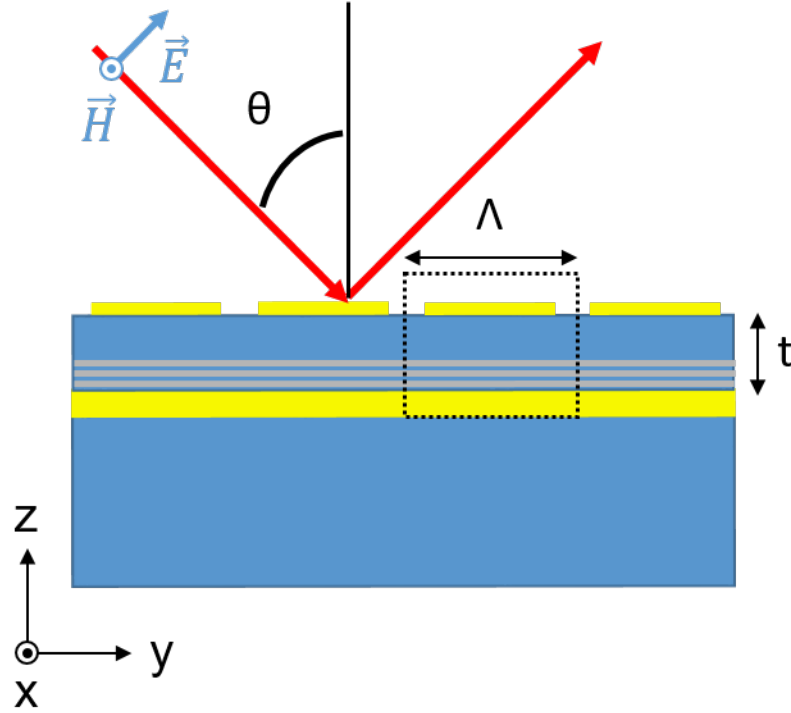


Figure 1.7: Lateral cross-section of M-I-M cavity. The dashed box corresponds to the unit cell of simulation. For this study the unit cell is generally composed by four layer a top metal grating with period Γ , a buffer GaAs layer, a multiple quantum wells region and a bottom metal layer. t is the total thickness of the cavity between the two metal layers.

$$\epsilon_z(\omega) = \epsilon_\infty \left[1 - f_0 \frac{\epsilon_\infty^2}{\epsilon_w^2} \frac{\omega_p^2}{\tilde{\omega}_{12}^2 - \omega^2 - j\omega\Gamma_{12}} \right]^{-1} \quad (1.68)$$

where $\tilde{\omega}_{12}$ is the transition frequency including depolarization shift, ω_p the plasma frequency, Γ_{12} is the FWHM of the ISB transition, ϵ_w is the dielectric constant in the well material and f_0 is the oscillator strength approximated to one for this two-level system. The plasma frequency is expressed as follows:

$$\omega_p = \sqrt{\frac{n_{2D}e^2}{\epsilon_\infty m^*(L_b + L_w)}} \quad (1.69)$$

where L_b and L_w are respectively, the barrier and well thicknesses and n_{2D} stands for the dopants sheet density.

The simulation is run on one 2D unit cell (dashed box) containing all the information about the structure. The grating is periodical in only one direction (y), and the system can thus be solved only in two dimensions y - z which highly simplifies the puzzle and permits the use of fast Fourier-transforms [45]. The band diagram can then be displayed in the angle the energy-angle or in the energy- k -vector space.

1.4 Intersubband Polaritons

When a quantum well is included in a cavity, it is possible to reach the so-called strong coupling regime. In this regime, the eigenstates are mixed states between an electronic excitation and a cavity photon. These states called *intersubband polaritons*, present new properties that can be used for emitters as well as for detectors from the mid- to the far-infrared.

The *strong coupling* between quantum well intersubband transitions and a cavity mode was proposed in 1997 [3] and was observed in 2003 using total internal reflection [2] (Figure 1.8, (a) and single plasmon [6] waveguides. Figure 1.8 (b) shows the transmission spectra in a multi-pass waveguide at different angles. At an angle of 60° the anticrossing appears, which is the signature of the strong coupling.

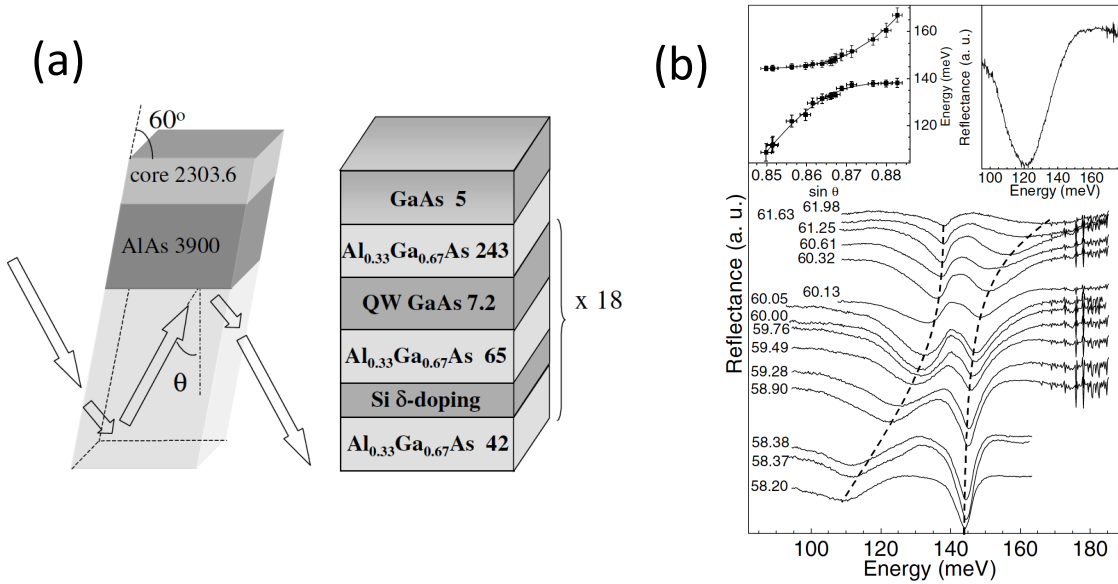


Figure 1.8: (a) Total internal reflection waveguide and multiple quantum well structure composed by 18 QWs, (b) angle resolved transmission (main panel), dipersion of the peaks minima corresponding to the polariton energies (top left inset) and the TE cavity mode reflectance (top right inset) Ref.[2].

1.4.1 Two-Level Model: Jaynes-Cummings Hamiltonian

As first model, we consider only one electron at $k = 0$, coupled with one photonic mode (Figure 1.9). We neglect the losses in the cavity. As written previously only TM modes are coupled with light. The historical semi-classical model to describe a two-level system in a cavity is Jaynes-Cummings model [46]. Initially introduced for atomic physics, this model can be applied to our two-level system [32]. The fundamental state is written $|\psi_{1,k}\rangle$ and the excited state $|\psi_{2,k}\rangle$. The respective energies of the two states are E_1 and E_2 . The electronic Hamiltonian is then

$$H_{mat} = E_1|\psi_{1,k}\rangle\langle\psi_{1,k}| + E_2|\psi_{2,k}\rangle\langle\psi_{2,k}| \quad (1.70)$$

The photon energy in the cavity can be written $\hbar\omega_c$, the photonic part of the Hamiltonian is then

$$H_{photon} = \hbar\omega_c(a^\dagger a + 1/2) \quad (1.71)$$

where a^\dagger (a) is the creation (annihilation) operator.

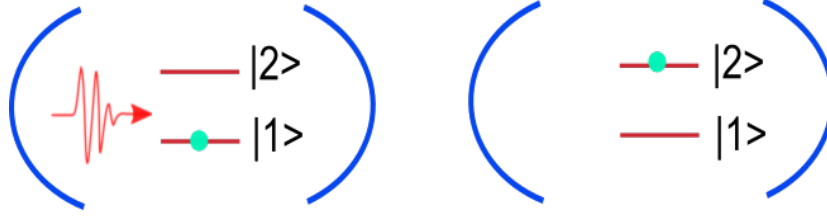


Figure 1.9: Schematics of a single electron interacting in strong coupling with a single photon.

The interaction hamiltonian is written $H_{int} = -\mathbf{d} \cdot \mathbf{E}$ in the dipolar gauge [47] where $\mathbf{d} = -e\mathbf{r}$ is the dipole electric operator. \mathbf{E} is the electric field supposed to be homogeneous inside the cavity. $\mathbf{E} = i\sqrt{\frac{\hbar\omega_c}{2\epsilon_0\epsilon_\infty V}}(a - a^\dagger)\hat{\epsilon}$ which is true for the TM_{00} mode of a metal insulator metal cavity. V is the effective volume of the cavity mode. Considering $\hat{\epsilon}$ in the direction of \vec{z} , we have

$$H_{int} = -i\hbar\Omega(|\psi_{1,\mathbf{k}}\rangle\langle\psi_{1,\mathbf{k}}| + |\psi_{1,\mathbf{k}}\rangle\langle\psi_{1,\mathbf{k}}|)(a - a^\dagger) \quad (1.72)$$

where $\Omega = \sqrt{\frac{e^2 f_{12}}{4\epsilon_0\epsilon_s m^* V}}$. By neglecting the anti-resonant terms we can simplify this equation

$$H_{int} = -i\hbar\Omega(|\psi_{1,\mathbf{k}}\rangle\langle\psi_{1,\mathbf{k}}|a + |\psi_{1,\mathbf{k}}\rangle\langle\psi_{1,\mathbf{k}}|a^\dagger) \quad (1.73)$$

We can assess the complete hamiltonian restricted to the subspace formed with the base vectors $\{|\psi_{1,\mathbf{k}}\rangle, |\psi_{2,\mathbf{k}}\rangle\} = \{|\psi_{1,\mathbf{k}}\rangle \otimes |1\rangle, |\psi_{2,\mathbf{k}}\rangle \otimes |0\rangle\}$ where $|n\rangle$ is the state with n photon in the cavity.

$$H_{JC} = H_{mat} + H_{photon} + H_{int} = \begin{vmatrix} \hbar\omega_c & i\hbar\Omega \\ -i\hbar\Omega & E_{12} \end{vmatrix}.$$

This Hamiltonian represents two resonators of energies $E_c = \hbar\omega_c$ and E_{12} coupled via the coupling constant $\hbar\Omega$. The eigenstates are named "intersubband polaritons". In the case of an intersubband transition coupled with a cavity mode, they are a linear superposition of the eigenvectors. In other terms, a combination of an electronic excitation with a cavity photon. The high energy state is noted $|UP\rangle$ ("Upper Polariton") and the lower state is noted $|LP\rangle$. They can be written

$$\begin{cases} |UP\rangle = \alpha_{UP}|\psi_{1,\mathbf{k}}, 1\rangle + \beta_{UP}|\psi_{2,\mathbf{k}}, 0\rangle \\ |LP\rangle = \alpha_{LP}|\psi_{1,\mathbf{k}}, 1\rangle + \beta_{LP}|\psi_{2,\mathbf{k}}, 0\rangle \end{cases} \quad (1.74)$$

The coefficients $\alpha_{UP/LP}$ and $\beta_{UP/LP}$ give respectively the light and matter contribution in the state of the system. They correspond to Hopfield coefficients [48] of intersubband polaritons. They can be written as a function of the detuning $\Delta E = E_c - E_{12}$

$$\begin{cases} \alpha_{UP}^2 = \beta_{LP}^2 = \frac{\Delta E + \sqrt{\Delta E^2 + (2\hbar\Omega)^2}}{2\sqrt{\Delta E^2 + (2\hbar\Omega)^2}} \\ \alpha_{LP}^2 = \beta_{UP}^2 = \frac{(2\hbar\Omega)^2}{2\sqrt{\Delta E^2 + (2\hbar\Omega)^2}(\Delta E + \sqrt{\Delta E^2 + (2\hbar\Omega)^2})} \end{cases} \quad (1.75)$$

The eigenvalues are then

$$E_{UP/LP} = \frac{1}{2}(E_{12} + E_c \pm \sqrt{\Delta E^2 + (2\hbar\Omega)^2}) \quad (1.76)$$

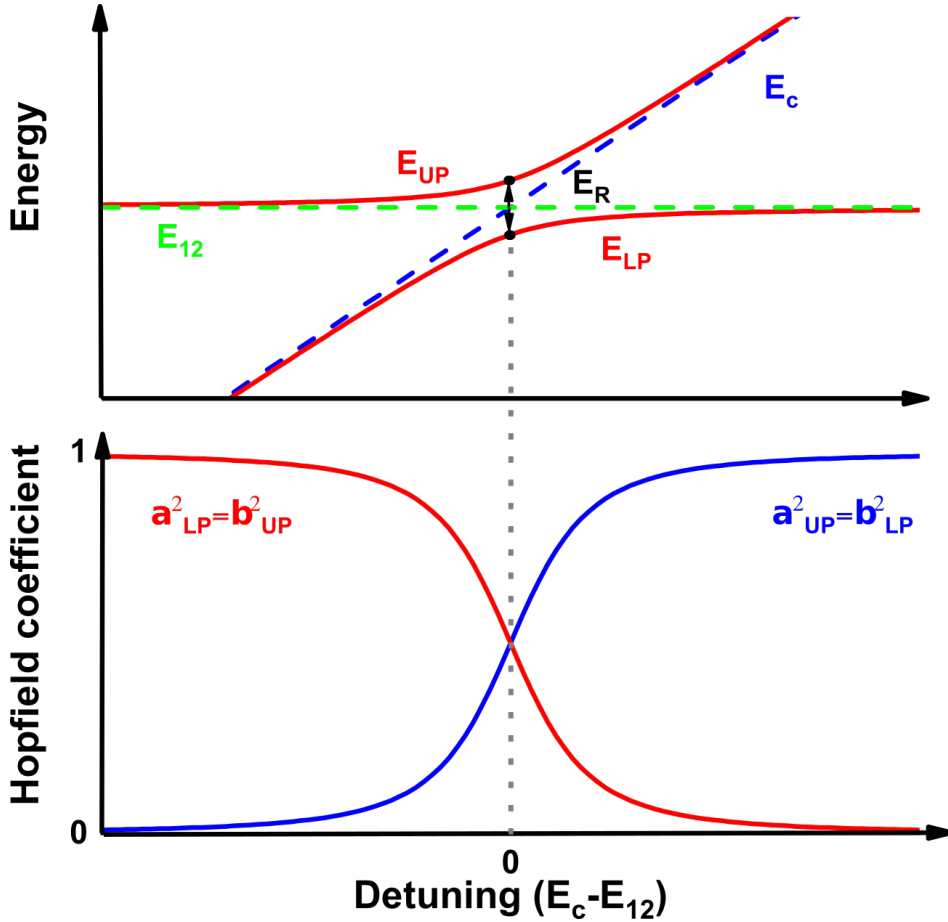


Figure 1.10: Top: Schematics of the polariton branches (red curves) energy dispersion as a function of the energy difference between the cavity mode and the intersubband transition calculated from Equation (1.76). The dashed blue line corresponds to the cavity mode and the dashed green line corresponds to the intersubband transition. The black dots represent the energies of the two polaritons when the cavity mode and the intersubband transition are resonant separated by $E_R = 2\hbar\Omega$. Bottom: Hopfield coefficients of the system; 0 corresponds to a polariton that is fully matter and 1 fully light.

The anti-crossing appears at the resonance. The asymptotes are two branches corresponding to the energy modes of the cavity and the ISB transition. When $E_c \gg E_{12}$

$$\begin{cases} E_{UP} \approx E_c \\ E_{LP} \approx E_{12} \\ \alpha_{UP}^2 = \beta_{LP}^2 \approx 1 \\ \alpha_{LP}^2 = \beta_{UP}^2 \approx 0 \end{cases}$$

Reciprocally, when $E_c \ll E_{12}$

$$\begin{cases} E_{UP} \approx E_{12} \\ E_{LP} \approx E_c \\ \alpha_{UP}^2 = \beta_{LP}^2 \approx 0 \\ \alpha_{LP}^2 = \beta_{UP}^2 \approx 1 \end{cases}$$

On the contrary at resonance $E_{UP/LP} = E_{12} \pm \hbar\Omega$ and $\alpha_{UP}^2 = \alpha_{LP}^2 = \beta_{UP}^2 = \beta_{LP}^2 = 1/2$. This configuration corresponds to the maximum of interaction between the two states and to the minimum of the energy difference between the two states: $2\hbar\Omega$ (minimum Rabi-splitting).

1.4.2 2D Electron Gas: Dark States and Bright States

Experimentally the Fermi level is positioned between the states E_1 and E_2 . The system is thus characterized by the electron density N_S (2D electron gaz) on the first subband and their coupling with the states on the second subband with the same \vec{k} . The total number of electrons is then $N = N_S S$, with S the surface of the sample. The dipolar coupling between the ISB transitions is neglected (Figure 1.11).

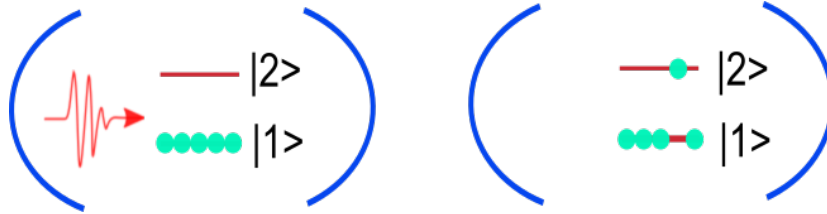


Figure 1.11: Schematics of a 2-level system interacting in strong coupling with a single cavity photon. This interaction can be simplified by considering the interaction between the photon and only one electronic state called bright state.

To describe the strong coupling regime, we need to consider the light-matter interaction between several electrons, participating to the ISB excitation, and one photonic state. The base of the considered space is composed by N+1 vectors: one cavity photon $|\phi_1, 1\rangle$, and each electron $|\phi_{2,\mathbf{k}}, 0\rangle$ of wavevector \mathbf{k}

$$H = \begin{bmatrix} \hbar\omega_c & i\hbar\Omega & i\hbar\Omega & \dots & i\hbar\Omega \\ -i\hbar\Omega & E_{12} & 0 & \dots & 0 \\ -i\hbar\Omega & 0 & E_{12} & \ddots & 0 \\ \vdots & \vdots & \ddots & \ddots & \vdots \\ -i\hbar\Omega & 0 & \dots & 0 & E_{12} \end{bmatrix}. \quad (1.77)$$

By changing the base, considering one state $|b\rangle = \frac{1}{\sqrt{N}}(\sum_{\mathbf{k}} |\phi_{2,\mathbf{k}}, 0\rangle)$ and the N-1 states deduced by orthogonal construction $|n_i\rangle$, the hamiltonian can be rewritten as follows:

$$H = \begin{bmatrix} \hbar\omega_c & i\sqrt{N}\hbar\Omega & 0 & \dots & 0 \\ -i\sqrt{N}\hbar\Omega & E_{12} & 0 & \dots & 0 \\ 0 & 0 & E_{12} & \ddots & \vdots \\ \vdots & \vdots & \ddots & \ddots & 0 \\ 0 & 0 & \dots & 0 & E_{12} \end{bmatrix}. \quad (1.78)$$

This base reveals only one electric bright mode ($|b\rangle$) coupled to the cavity mode via the constant $\hbar\Omega' = \sqrt{N}\hbar\Omega$ and $N - 1$ dark states. From the coupling with the cavity mode the two polaritonic states emerge, similarly to the previous paragraph. Because $\hbar\Omega$ is proportional to V and N proportional to S , the coupling constant is independent of the surface of the sample. Consequently, $\hbar\Omega' = \hbar\sqrt{\frac{N_S e^2 f_{12}}{4\epsilon_0 \epsilon_r m^* L_{cav}}}$. The same way, when N_{QW} are identically coupled to the cavity mode, the coupling constant is multiplied by $\sqrt{N_{QW}}$. The coupling constant that we will use in the following is

$$\hbar\Omega_R = \hbar\sqrt{\frac{N_S N_{QW} e^2 f_{12}}{4\epsilon_0 \epsilon_r m^* L_{cav}}}. \quad (1.79)$$

This energy difference is called *Rabi energy* in analogy to the strong coupling regime of atoms [49]. One of the major assets of ISB polaritons is that the Rabi-splitting is easily tunable (from weak to deep strong coupling [9]) with the doping of the quantum wells.

The *dark states* - discussed theoretically in Ref. [50]- appeared to be a major issue of the observation of polaritons under electrical injection [4, 5, 51]. In this section, we saw that only one electronic *bright state* interacts with the electromagnetic field whereas the $N-1$ electronic *dark states* do not. Besides the dark states contribute to electrical transport. Consequently, the observation of bright states is highly affected by the non-radiative scattering mechanisms of the *dark states*.

1.4.3 Coupled Mode Theory

Until now, we neglected the broadening of the energy levels directly related to the dissipation inside the system. In this last section we consider the dynamic of a photonic mode (ω_c, γ_c) coupled with a material resonance (ω_{12}, γ_{12}). This model will be particularly interesting for the study of photocurrent generation from a photodetector in strong coupling (Part 3).

The situation we are going to study is sketched in Figure 1.12. It consists of one scattering channel, one photonic resonator, and one matter resonator (intersubband plasmon). The photonic resonator we have in mind is a metal-insulator-metal photonic crystal slab resonator. This naturally coupled to the free space plane waves, which constitute the scattering channel. The matter resonator, i.e., the two-level system, is represented by a charged oscillator, and is directly coupled to the photonic resonator via the coupling constant Ω .

The dynamics of the system is described by the equations [53]:

$$\begin{cases} \frac{da}{dt} = (i\omega_c + \gamma_c)a + i\Omega b + ks^+ \\ \frac{db}{dt} = (i\omega_{12} + \gamma_{12})b + i\Omega a \\ s^- = cs^+ + ad \end{cases} \quad (1.80)$$

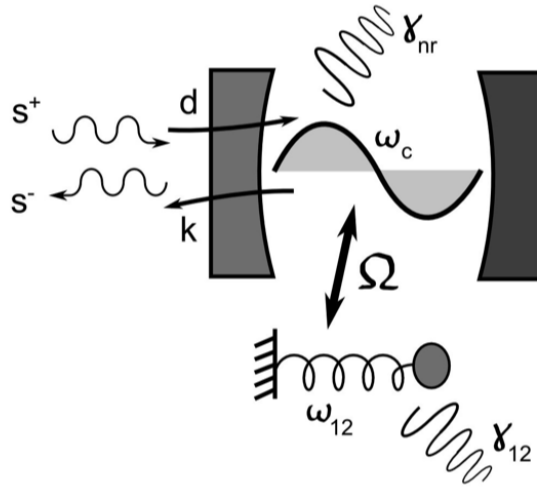


Figure 1.12: Scheme of the one-port photonic cavity. The photonic mode is coupled to the scattering channels via the coupling constants d and k connected to the radiative decay rate γ_r [52].

where s^\pm , a and b is a set of complex, time-dependent coordinates, respectively describing the input/output channels, the photonic resonance, and the matter resonance. They are defined such that

- $|s^\pm|^2$ is the energy flux per unit time ingoing (outgoing) into (out of) the system
- $|a|^2$ is the total electromagnetic energy stored in the cavity
- $|b|^2$ is the total energy stored in the matter resonator

The photonic resonator is driven from the input scattering channel through the complex amplitude k , and radiates into the output channel through d . The non-resonant scattering amplitude is given by c .

The damping rate γ_c corresponds to the total losses of the bare cavity, which we will separate in the sum of two contributions: $\gamma_c = \gamma_r + \gamma_{nr}$. The first is the main radiative mechanism, i.e., the cavity leaks into the scattering channel. The second is the sum of all the other mechanisms, either non-radiative (like absorption by free carriers or metallic components), or radiative (like the scattering into channels different from the main one: roughness scattering, diffraction losses ...). What matters is that these mechanisms must be non-resonant, i.e., they depend very slowly on the energy scale given by the overall width of the cavity mode.

We consider the situation where the ingoing scattering channel is populated by a harmonically time-dependent amplitude $s^+(\omega) = s_0^+ e^{i\omega t}$, in the steady-state, the system has a response at the same pulsation ω . In particular, the outgoing channel will be populated by an amplitude $s^-(\omega) = s_0^- e^{i\omega t}$ given by the relation

$$s_0^- = s_0^+ \left[e^{i\phi} + e^{i\phi} \frac{i(\omega - \omega_{12} + \gamma_{12})}{(\omega - \omega_+)(\omega - \omega_-)} 2\gamma_r \right] \quad (1.81)$$

The phase ϕ is calculated using the energy conservation of the system and contains the relation between: c , d , κ and γ_r . The reflection amplitude is then defined as

$$r(\omega) = \frac{s_0^-}{s_0^+} = e^{i\phi} \frac{(\omega - \bar{\omega}_+)(\omega - \bar{\omega}_-)}{(\omega - \omega_+)(\omega - \omega_-)} \quad (1.82)$$

In Equation (1.82) ϕ appears as the phase shift between the incident beam and the reflected beam. Under the simplifying hypothesis that the cavity is tuned at the two-level system resonance frequency, i.e. $\omega_{12} = \omega_c = \omega_0$, the above expression has two zeroes and two poles occurring at

$$\begin{cases} \bar{\omega}_{\pm} = \omega_0 + \frac{1}{2} \left[i(-\gamma_r + \gamma_{nr} + \gamma_{12}) \pm \sqrt{4\Omega^2 - (\gamma_r - \gamma_{nr} + \gamma_{12})^2} \right] \\ \omega_{\pm} = \omega_0 + \frac{1}{2} \left[i(\gamma_r + \gamma_{nr} + \gamma_{12}) \pm \sqrt{4\Omega^2 - (\gamma_r + \gamma_{nr} - \gamma_{12})^2} \right] \end{cases} \quad (1.83)$$

The zeros ($\bar{\omega}_{\pm}$) of Equation (1.82) represent the impedance matching conditions and in the photonics community is referred to as *critical-coupling* [53, 54]. The zeros are studied in mode details in Ref.[52] (weak and strong critical coupling).

The poles (ω_{\pm}) of Equation (1.82) are referred to as strong coupling condition. The complex poles are interpreted as damped eigenfrequencies of the free-decaying modes of the global system. Two main regimes can be recognized, depending on the sign of the quantity under the square root:

- weak coupling when $2\Omega \ll |\gamma_r + \gamma_{nr} - \gamma_{12}|$. The energy degeneracy is not lifted, only the imaginary part is affected. This phenomenon is related to the spontaneous emission modified by the coupling with the cavity mode, named Purcell effect [55].
- strong coupling when $2\Omega \gg |\gamma_r + \gamma_{nr} - \gamma_{12}|$. The degeneracy is lifted and the minimum energy difference between the two branches is named "Rabi splitting"
 $2\Omega_R = \sqrt{4\Omega^2 - (\gamma_r + \gamma_{nr} - \gamma_{12})^2} = \sqrt{4\Omega^2 - (\gamma_c - \gamma_{12})^2}$.

1.5 Conclusion

In this theoretical introduction, we presented the essential formalisms to understand the strong coupling between a metallic cavity and intersubband electronic density excitations. The detailed study of the strong coupling between a photon and a 2D electron gas revealed the existence of *dark states* that do not couple with the electromagnetic radiation. Previous works, based on electrical injection [56, 51], have shown that the *dark states* can hamper the observation of the polaritons in this configuration.

On the contrary, the bright states can be observed in reflectivity (Part 1) or in photo-current (Part 3).

After fixing the type of excitation we will work with and the conditions of the experiment, the last important choice is the geometry of the cavity. Up to now the frequently used cavities for the observation of ISB polaritons were: total internal reflection [2], single-plasmon [6], and patch cavities [41]. Nevertheless, dispersive metal-insulator-metal cavities (with a periodical opening of the top metal) are promising because they offer high confinement of the EM field within the active region. The engineering of the top metal grating and the distance between the two metallic planes offers various geometries and gives more degrees of freedom to observe the ISB polaritons.

The engineering of Mid-IR dispersive M-I-M cavities has led to the first observation of scattering mechanisms between ISB-polaritons and LO-phonons [14]. The distance between the upper and lower polariton has been engineered - via the geometry the M-I-M cavity and the QW doping - to equalize the LO-phonon (~ 36 meV for the GaAs, ~ 33.6 meV for InP).

Part 1 of this Thesis presents the implementation of dispersive M-I-M cavities in the THz domain for applications to THz-polaritons. Some scattering mechanisms of the ISB polaritons have been proposed Ref.[21] but not observed yet. By using THz quantum cascade lasers (QCLs) as a (powerful) source, we propose to observe polariton-polariton scattering mechanisms.

Part 2 presents some technical solutions to shorten the pulses of THz-QCLs implemented in TDS systems. My contribution to this topic, in the context of the H2020 Ultra-QCL project, has been to fabricate several QC laser samples with monolithically integrated Gires-Tournois interferometers.

In Part 3, I developed for the first time dispersive M-I-M cavities in strong coupling with bound-to-quasi-bound QWIP's detectors. The *bright states* are then excited with a Mid-IR thermal source (globar). Depending on the distance between the *bright states* and the continuum, a photocurrent could be generated. The originality of this study is to use the dispersive M-I-M cavity to observe the photocurrent generation over a large set of wavevectors (different polariton states). This study targets two majors purposes: first to disentangle the frequency of detection from the thermal energy activation using the strong coupling regime, second to explore the generation photo-current from ISB polaritons (fundamental purposes).

Part I

THz Polaritonic Dispersive Cavities, a Tool for THz Emitters

*"C'est qu'en vérité le chemin importe peu,
la volonté d'arriver suffit à tout."*
Le mythe de Sisyphe, Albert Camus.

Dispersive THz Cavities for the Strong Coupling Regime

THz radiation typically refers to the frequency range from 100 GHz to 30 THz . It is at the border between electronics and photonics. THz sources can rely on radiation of accelerated electrons (electronics) or on the transition between two relatively close (~ 10 meV) energy levels (photonics). Different Electronic and Photonic THz sources are presented in Figure 2.1, (a). It appears on this graph that the output power of photonic, as well as electronic, emitters decreases drastically in the THz range. The lack of powerful, compact, coherent, and room temperature operating emitters in the THz is a significant issue for applications.

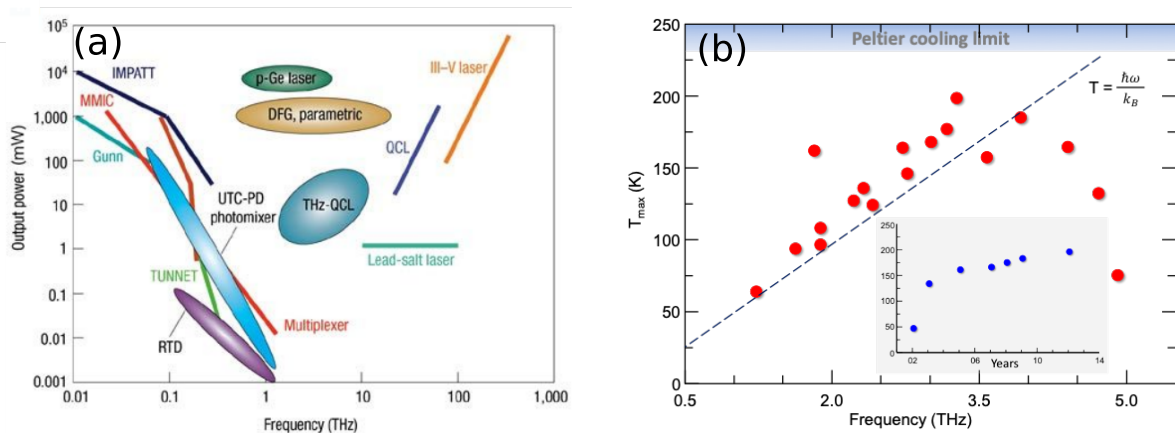


Figure 2.1: (a) Different light sources close to the THz range operating above liquid nitrogen temperature (taken from [16]). This graph shows the THz gap between electronic and photonic devices. (b) THz-QCLs maximum operating temperature as a function of the emission frequency [57].

The Quantum Cascade Laser appeared as one of the most promising sources to overcome the THz emitters limitations. Nevertheless, the operating temperature of THz-QCL (presented Figure 2.1, (b)) strongly depends on the emission frequency, and until now, no THz-QCL has operated above the Peltier cooling temperature. This experimental observation shows that the phonon activation hampered the population inversion mechanism. Currently, THz-QCL technology still depends on cryogenic cooling that is a major drawback for applications.

In the first part of this manuscript, we explore the feasibility of a new type of THz emitters operating in the strong coupling regime between light and matter. In strong coupling, the new eigenstates of the system are called polaritons. If the polariton density is below a critical density, the polaritons can be considered as bosons, and they are theoretically eligible to final-state stimulation [58]. The final state stimulation occurs when a spontaneous scattering takes place between two polaritonic states: one reservoir and one final-state. Interestingly, the final-state stimulation process is less sensitive to the temperature than the population inversion mechanism. Observing and mastering the final-state stimulation mechanism is a crucial step toward the development of a polaritonic THz source.

In this context, our objective is to provide a proof of concept of the final-state stimulation with ISB polaritons. To reach this goal, we need to identify two polaritonic states to play the role of reservoir and final-state. To allow a scattering mechanism between these two states, we adjust the position of the reservoir relatively to the final-state by introducing some degrees of freedom to the system: for the matter part, we tune the coupling strength by changing the doping inside square quantum wells; for the light part, we access a broad range of polaritonic states by using dispersive M-I-M cavities.

In this chapter, we present briefly the concept of final-state stimulation. We will then describe the fabrication process of polaritonic samples for the THz spectral range and present the measurements of these samples with a set-up that I specifically designed for this experiment.

2.1 Key Concept: Final-State Stimulation

The final-state stimulation, based on phonon-polariton or polariton-polariton scattering, is the mechanism behind Bose-Einstein condensates of exciton-polaritons [59]. The long term vision of this work is to demonstrate that final-state stimulation is also achievable with ISB-polaritons.

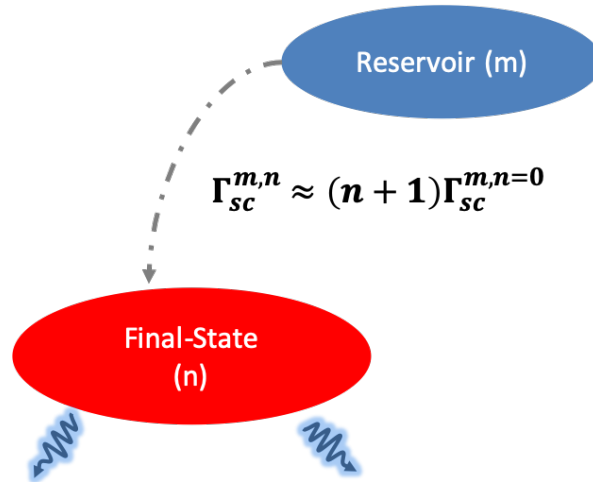


Figure 2.2: A scheme of the final state stimulation system.

The formalism of final-state stimulation for THz-ISB polaritons has been developed in Ref.[58]. A sketch of the final-state stimulation process is presented in Figure 2.2. Polaritons can scatter (spontaneous process) from a reservoir to a final state. We note m the polariton

density in the reservoir and n the polariton density in the final state. Polaritons in the reservoir are created by a pump (generally a laser). The decay rate between the reservoir and the final state increases linearly with the polaritonic density on the final state. Thus the final state stimulated rate can be expressed as:

$$\Gamma_{sc}^{m,n} \approx (n + 1)\Gamma_{sc}^{m,n=0}, \quad (2.1)$$

where $\Gamma_{sc}^{m,n}$ is the decay rate from the reservoir toward the final-state, and $\Gamma_{sc}^{m,n=0}$ is the spontaneous scattering rate.

According to equation (2.1), when the occupancy on the final state increases, the stimulated scattering rate toward the final-state increases as well. The threshold is reached when $1/\Gamma_{sc}^{m,n}$ becomes shorter than the lifetime of the final state. In this configuration, the polaritons are accumulated on the final state, and they emit coherent light with output power [60]

$$P_{out} = \frac{\hbar\omega n}{\tau_{rad}}S. \quad (2.2)$$

Where ω is the photon energy, τ_{rad} is the radiative lifetime of the final state, and S is the device surface.

The main topic of the first part of this manuscript is to define which scattering mechanism to use with THz polaritons. The scattering mechanisms must respect energy and momentum conservation. In the Mid-IR phonon-polariton scattering has been demonstrated recently in Ref.[14]. In the THz domain, phonon-polariton scattering is not useful because the energy conservation can not be respected ($E_{phonon} \gg \hbar\Omega_{Rabi}$, see section 2.6). An alternative mechanism is the polariton-polariton scattering already observed with excitonic polaritons and proposed theoretically in Ref.[21].

2.2 Active Region Design

Our approach to explore polariton scattering mechanisms combines two technologies: time-domain-spectroscopy and THz Quantum Cascade Lasers. The choice of the resonant frequency of the intersubband transition is essential to use these two technologies simultaneously.

On one hand the TDS system of the LPA is limited at high frequencies by the electro-optic crystal. On the other hand, the optical gain of broadband THz QCLs starts to drop below 3 THz (Figure 2.1). The compromise between these two technologies was found between 2.5 THz and 3 THz. In this range of frequencies, the GaAs/AlGaAs is known as the best material for quantum wells (as for THz-QCLs).

2.2.1 Schrödinger-Poisson Simulations

The simulation in Figure 2.3 shows the energy levels in one finite quantum well made of $GaAs/Al_{15}Ga_{85}As$. The thickness of the well is chosen at 36 nm. AlGaAs represents the barriers that are 20 nm thick on each side of the well. The Al proportion (here 15%) fixes the conduction band discontinuity.

Two active regions have been grown with two different n-doping sheet density : $1 * 10^{11} \text{ cm}^{-2}$ for the sample L1362 and $2 * 10^{11} \text{ cm}^{-2}$ for the sample L1412. The doping is incorporated 5 nm before the quantum well due to the carriers segregation.

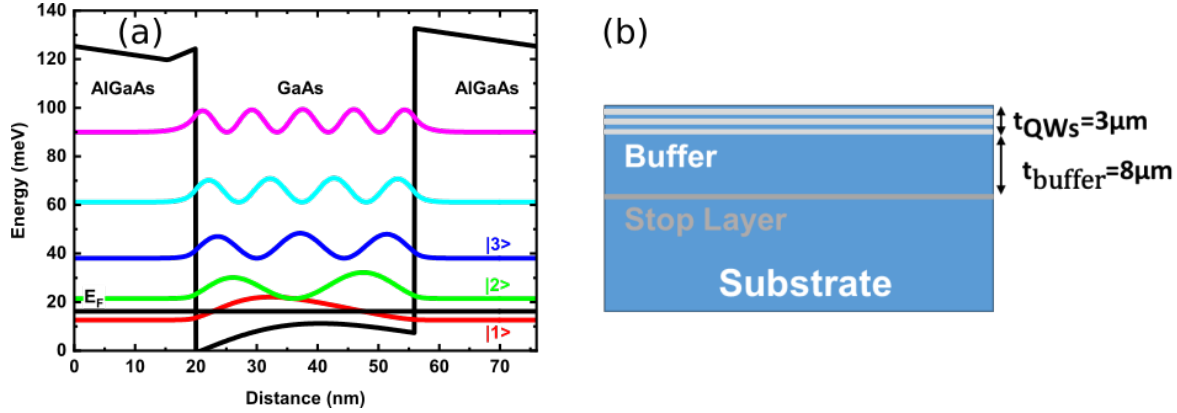


Figure 2.3: (a) Schrodinger-Poisson simulation of a structure with a 36 nm wide QW, a concentration of 15% of alumina in the barriers and a doping sheet density of $1 * 10^{11} \text{ cm}^{-2}$. The dark flat line between the first two states ($|1\rangle$ and $|2\rangle$) represents the Fermi level (E_F) inside the quantum well. (b) Lateral cross-section of the active region with 3 μm quantum wells, 8 μm of buffer layer separated from the substrate by a stop layer ($\text{Al}_{60}\text{Ga}_{40}\text{As}$).

The simulation yields a transition between the fundamental state and the first excited state at $E_{12} = 2.14 \text{ THz}$ with an oscillator strength of $f_{12} = 0.91$. The depolarization shift is taken into account by using this equation:

$$\tilde{E}_{12} = \sqrt{E_{12}^2 + E_p^2}, \quad (2.3)$$

where $E_p = \hbar\omega_p$ is the plasma energy due to the presence of the electronic plasma.

The plasma pulsations have been calculated for the two active regions using Eq.1.30 ($\frac{\omega_p(L1362)}{2\pi} = 1.3 \text{ THz}$ and $\frac{\omega_p(L1412)}{2\pi} = 1.8 \text{ THz}$). According to the expression above, the two active regions have different absorption peak frequencies for the transition 1-2: L1362 is expected to absorb at 2.5 THz and L1412 at 2.8 THz.

The growth of the QWs, done at the University of Leeds, has also to take into account the final geometry of the cavity (see Section 2.4). The thickness of the cavity is determined by the stop layer on which the epitaxy is grown. The ideal thickness to operate in the dispersive regime is $\sim \lambda/10$. The cavity cannot be filled with QWs only, as the Rabi-splitting would be too large. Thus, a buffer layer is grown on the first 8 μm before the 53 QWs (3 μm). A scheme of the sample is presented in Figure 2.3, (b). The total thickness of the active region is 11 μm . The number of this sample is L1362.

2.2.2 Multi-pass measurements

The multipass measurement is essential to evaluate the absorption peak (E_{12} , FWHM) of the active region at liquid Helium temperature. According to the absorption peak of the active region, the geometry of the cavity (period of the grating) will then be chosen.

Starting from a narrow sample piece ($8 * 3 \text{ mm}^2$), we metalize the top surface, then we polish the two facets at 45° to couple the light from the *Global* into the active region (Figure

2.4). The transmitted signal is collected on a *QMC* Bolometer and treated by a Fourier Transform Infrared Spectrometer (FTIR). The transmission is obtained with the following formula:

$$T = \frac{\frac{I_{TM,sample}}{I_{TE,sample}}}{\frac{I_{TM,chamber}}{I_{TE,chamber}}}, \quad (2.4)$$

where I_{TM} and I_{TE} are the transmitted intensities of respectively the TM and TE polarized EM waves through the sample or the empty chamber (used as a reference).

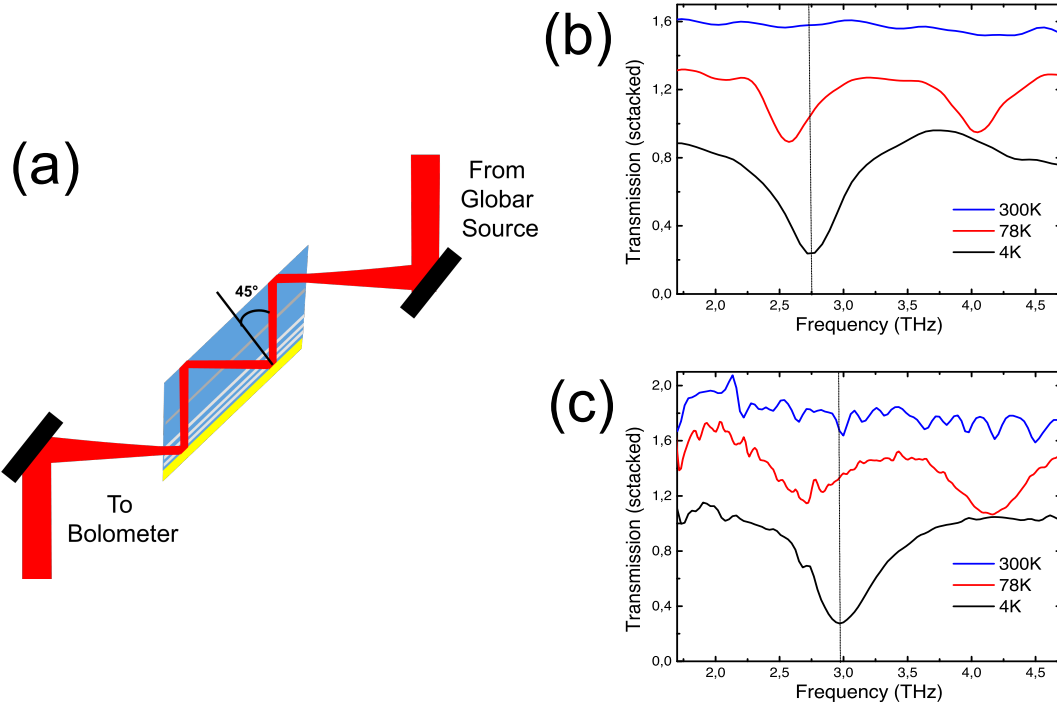


Figure 2.4: (a) Scheme of multipass measurement. The signal is collected on an external *QMC* Bolometer. (b-c) Multipass measurement of the samples L1362 and L1412 at different temperatures.

Figure 2.4, (b) and (c) shows respectively the transmissions of sample L1362 and L1412 for different temperatures. At 300 K , all the excited states are populated and the ISB is not visible. By decreasing the temperature, the electronic population decrease in the excited states. At 150 K , two absorption peaks appear: at 2.5 THz and 4 THz for the sample L1362 and at 2.6 THz and 4.2 THz for the sample L1412. These two peaks are related to the transition $2 - 1$ and $3 - 2$ (according to Fermi's golden rule there is no transition $1 - 3$, *c.f.* Chapter 1). By lowering the temperature, all the electrons are stored on the ground level. At 4 K , only the $2 - 1$ transition is observed at $\nu_0 = 2.7\text{ THz}$ with a linewidth $\gamma_{12} = 0.34\text{ THz}$ for the sample L1362 and $\nu_0 = 2.96\text{ THz}$ with a linewidth $\gamma_{12} = 0.6\text{ THz}$ for the sample L1412.

The additional blue shift of $\approx 0.2\text{ THz}$, seen on both samples, compared to the theory is probably due to an underestimation of the depolarization shift at 4 K . So far, we can not conclude on the effect of this blue shift on the compatibility of these samples with the LPA TDS system. The positions of the polaritonic branches of each sample have to be assessed to address this issue.

2.3 Design of the Cavity: RCWA Simulations

In this section, we present the cavity design for the sample L1362. The same concepts have been used to design the cavity of the sample L1412.

The thickness of the cavity is fixed in advance by the stop layer positioned during the growth of the sample (Section 2.3). For a transition at $2.7 THz$, we expect to operate below the cut-off to avoid any additional coupling with high order TE or TM modes. Thus we designed the cavity thickness to have a cut-off at $4 THz$ ($\lambda_{cut-off} = 75 \mu m$). This condition imposed a cavity thickness of $t = \lambda_{cut-off}/2n = 11 \mu m$ (Section 1.3.3). A thinner cavity would increase the overlap with the MQWs ($t_{MQWs} = 3 \mu m$) risking to reach the ultra-strong coupling regime Ref.[10] that is not in the perspectives of this work.

Knowing the experimental characteristics of the active region transition (multi-pass measurements), we finalize the design of the cavity (period and filling factor). In the perspective of pump-probe measurements, the first approach is to design the cavity such as the anti-crossing occurs at 35° . The idea is to pump close to the anti-crossing ($35-45^\circ$) and to probe at $k_{//} = 0$ where we expect to have the highest variation of reflectivity due to the scattering mechanisms (more details in Section 2.5).

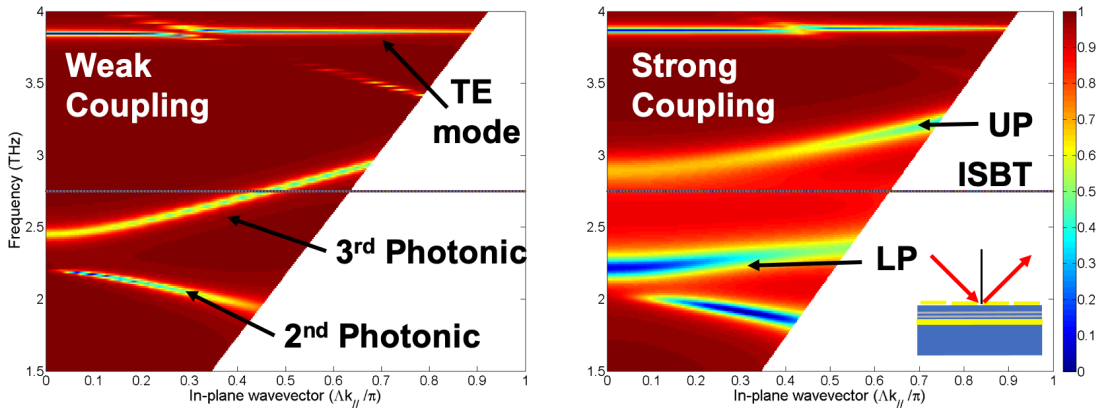


Figure 2.5: RCWA dispersions -from 1° to 60° - of a bare cavity composed by $11 \mu m$ thick GaAs buffer (left) and a cavity in strong coupling with $3 \mu m$ thick active region (53 QWs), ISB transition at $2.7 THz$, with a FWHM of 13% and a doping $1 * 10^{11} cm^{-2}$ and $8 \mu m$ GaAs (right). In both simulations the grating has a period of $40 \mu m$ and a filling factor of 80%.

Figure 2.5 shows an example of numerically calculated dispersion for a cavity with (right) and without (left) QWs. The grating period is close to one third of the wavelength in vacuum $\Lambda = 40 \mu m \approx \lambda/n$ and a filling factor 80% (classical value for M-I-M ISB polaritons Ref.[61, 14]). The rest of the parameters are taken from the nominal values of the growth sheet (Appendice B.1). The dispersion is plotted for $k \in [0; \pi/\Lambda]$ because the band diagram is symmetrical. The dispersion of the bare cavity (Figure 2.5, left) shows the second (2^{nd}) and third (3^{rd}) photonic branches of the cavity and the first TE mode at $3.9 THz$. When an intersubband (ISB) transition at $2.7 THz$ with a FWHM of 12.5% is incorporated inside the cavity ($3 \mu m$ MQWs and $8 \mu m$ GaAs) the 3^{rd} photonic branch splits into two polaritonic states lower polariton (LP) and upper polariton (UP) (Figure 2.5, right).

2.4 Fabrication & Mounting

In this section, we will detail the process of fabrication of a M-I-M structure. Most of the techniques presented here will also be used for other M-I-M structures in the Mid-Infrared as well as for THz QCLs.

The fabrication of THz photonic cavities requires optical lithography as the smaller object of the process is the slit of the cavity that typical width is 5-8 μm .

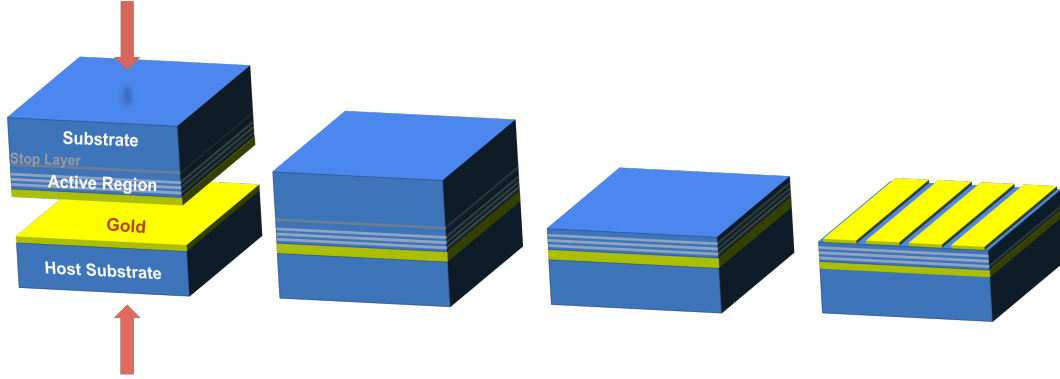


Figure 2.6: Schematics of the THz M-I-M cavity fabrication process. From left to right: wafer bonding, substrate etching until the stop layer and top metal deposition of the grating.

In the perspective of optical pumping the polaritonic states we designed the cavities to have the anti-crossing at 35° and to have a good balance between the absorption and the broadening of the polariton branches. For this purpose, two masks have been designed for this project. The first mask was constituted by $2 * 2 \text{ mm}^2$ gratings with various grating periods. Preliminary spectral measurements at 13° gave information about the most relevant period for the strong coupling. Once we identified the appropriate period, we designed the second mask with one larger grating: $4 * 4 \text{ mm}^2$ and different filling factors.

2.4.1 Cleanroom Processing

The following section presents the principal steps of fabrication of THz Metal-Insulator-Metal cavities that I performed in the C2N-Orsay cleanroom.

Wafer Bonding & Substrate Removal

The wafer bonding integrates a metallic layer (future bottom contact) below the active region. A sticking layer of Titanium (10 nm) and then a gold layer (200 nm) are deposited on both the active region and a bulk wafer host substrate. The two wafers are then bonded together (Figure 2.6, left) by their metallic surfaces in the wafer bonder (bonding parameters 45 min/320°C/4.5 MPascal). Here the bottom contact has no electrical functionality, and it is used only for thermal and optical properties.

The substrate (typically 500 μm thick) on which the active region has been grown is then removed using first a manual polishing followed by a selective chemical etching (citric acid). The active region is protected from the etching by an $\text{Al}_{60}\text{Ga}_{40}\text{As}$ stop layer, presented in dark grey on the Figure 2.6. Note that the stop layer is positioned during the epitaxy and fixes the thickness of the cavity. The stop layer is finally removed with hydro-fluoridric acid.

Optical Lithography, Top Metal Deposition & Lift-off

Once the active region is uncovered the patterning of the top surface can be realized. The first step consists in coating the active region with a reversible photo-resist (AZ5214). This resist is $1.4 \mu\text{m}$ thick and has a resolution of $1 \mu\text{m}$, which corresponds to our specifications.

The lithography is performed with the mask aligner MJB4 (*Suss MicroTec*). The Mercury (Hg) lamp emits at 365 nm has a power density of $\sim 10 \text{ mW/cm}^2$. The first exposure consists of removing the extra volume of the resist that generally accumulates on the edges of the sample (edge removal). The pattern is then transferred on the resist, with first short exposure. The unprotected regions of the resist are chemically transformed in acid radicals. These radicals are then cross-linked (stable state insensitive to the developer) with a bake at 120°C . A final flood exposure transforms the rest of the resist in radicals that are removed by the developer leaving only slits of resist onto the active region.

Once the mask is transferred on the sample, the residual resist is removed with a short oxygen plasma. The surface of the sample is then deoxidized with hydrochloric acid ($\text{HCl:H}_2\text{O}$) for better adhesion between the metal and the sample surface.

The sample and the reference (bulk GaAs wafer that has the same height as the host substrate) are deposited in the e-beam evaporator. The metals are contained inside carbon or tungsten crucibles that are heated with an electric beam until the sublimation of the metal. The sample and the reference are then covered by the same amount of metal measured with a piezo-electric balance (quartz). In this process, we use a Ti/Au deposition: 10 nm of Ti to adhere on the sample surface and 150 nm of Au to ensure the confinement of the light inside the cavity.

Typically, the thickness of the metal should not exceed one-fourth of the resist thickness. This is the case in this process, and after a few minutes in acetone, the resist is removed, opening the top metal with periodical slits.

2.4.2 Mounting

Before leaving the cleanroom the back side of the sample is metalized with Ti/Au to ensure good adhesion to the copper block that is crucial for measurements at liquid Helium temperatures. The sample and the reference are then cut in identical squares of $4 \text{ mm} \pm 50 \mu\text{m}$.

After processing the sample and the reference are then soldered with indium on a copper block (Figure 2.7, (a)). The direction of the grating is chosen to have inside the FTIR the electric field that is perpendicular to the slits.

Moreover, to avoid spurious reflections, the sample is surrounded with sandpaper (in red Figure 2.7, (b)) of grit comparable with the wavelength range of interest ($\approx 100 \mu\text{m}$).

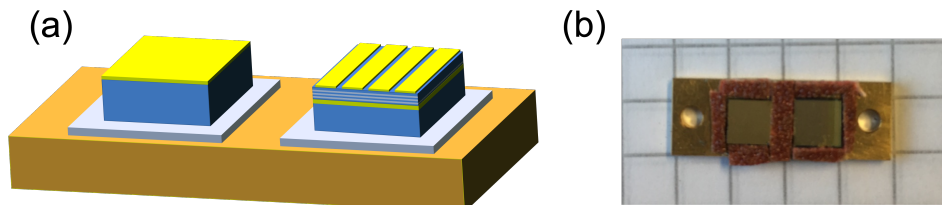


Figure 2.7: (a) Schematics of the mounted sample and its reference. The grey zone below the sample represents the indium solder. (b) The picture of the sample shows the sandpaper (red) positioned around the samples acting as a THz absorber.

2.5 Set-up for Measuring the Polaritonic Dispersion at Low-T

The dispersion of THz polaritonic cavities has already been measured in the past Ref.[62] for a set of angles. However, to know precisely what are the proper incidence angles for pumping and probing the polaritonic system, we must measure dispersion in the THz range over a large set of angles. This issue led to the development of a dedicated cryostat system.

2.5.1 Fourier Transform Interferometer and Beam Condenser

All spectroscopic measurements presented in this section are obtained with a FTIR spectrometer Bruker *Vertex 70*. The instrument is sketched in Figure 2.8. The FTIR spectrometer core is reminiscent of a Michelson interferometer: an IR beam from an internal source is split in two by a beam-splitter; one beam is back-reflected from a fixed mirror while the other one is reflected from a mobile mirror either continuously oscillating (*rapid scan modulation*) or translating in discrete positions (*step scan modulation*). The beams are then recombined at the beam splitter. The beam arrives collimated in the sample compartment and is focused onto the sample (at 13°) with a *beam condenser*.

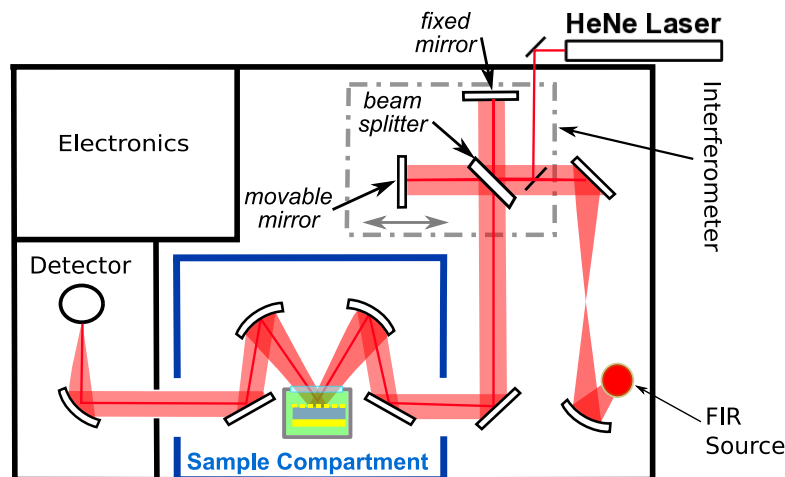


Figure 2.8: Schematics (top view) of the purged Bruker *Vertex 70* FTIR spectrometer with a *beam condenser* accessory. The interferometer is highlighted within a grey dashed line. The sample is inside a small volume cryostat head with a ZnSe window (vacuum region in green) and positioned on the focal point of the *beam condenser*. A He-NE laser beam is used for interferometer auto alignment.

The reflected light from the sample is then collected on an internal detector. For each spectral component, the collected signal intensity will have a beating-like modulation depending on the optical path difference between the two beams. Fourier analysis allows one to recover information on the intensity of each spectral component from the collected signal (interferogram). The frequency spectrum is recovered by a Fourier transformation of the interferogram [63]. For THz measurements, the internal source employed is either a Globar (a heated SiC rod emitting black-body radiation) or a mercury-vapor lamp. The beam-splitter is a $6\text{-}\mu\text{m}$ -thick Mylar film and the internal detector is a pyroelectric DTGS crystal. For

low-noise measurements, a He-cooled Si bolometer is used as an external detector in the following.

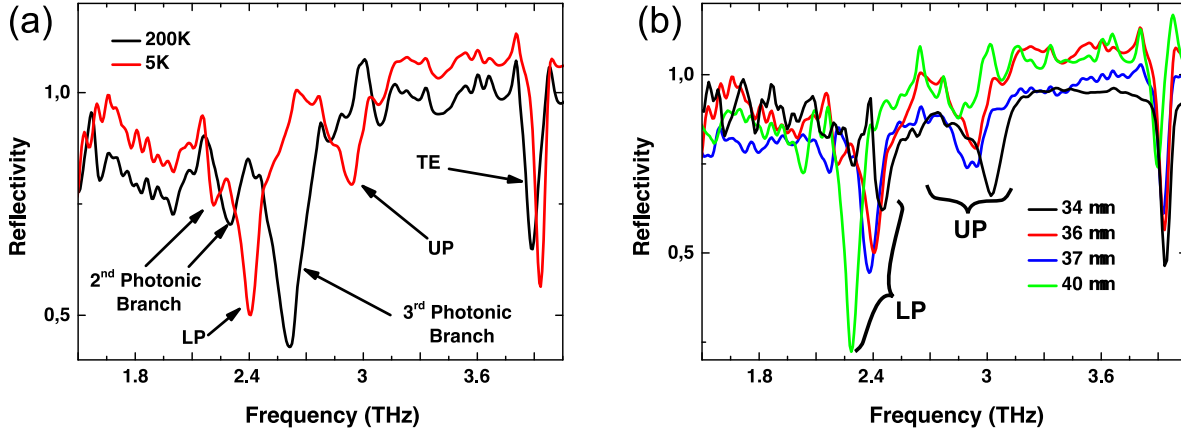


Figure 2.9: Reflectivity measurement with the beam condenser at 13° (a) Sample L1362 with grating of 36 μm period and 80% filling factor at a temperature of 200 K and 5 K (b) Samples L1362 with grating periods: 34, 36, 37, 40 μm and filling factor 80% at 5K and 13° incident angle. UP and LP mean respectively Upper and Lower Polariton.

Passive metal-metal resonators can be fully characterized by reflection spectroscopy as the metallic ground plane prevents transmission of radiation. Resonator modes appear as dips in the reflectivity (R) spectrum and the sample absorptivity spectrum (A) can be recovered as $A=1-R$. Experimentally the relative reflectance spectra shown above are obtained taking the ratio of the reflected intensity from the sample to the reflected intensity from a reference gold mirror of the same size [64]:

$$R_{relative} = \frac{I_{sample}}{I_{ref}} \quad (2.5)$$

The incidence angle of the beam condenser is fixed at 13°. To check if the cavity was operating in strong coupling with the active region (L1362), we measured the absorption of the device with the beam condenser at different temperatures. Figure 2.9 (a) shows that at 200 K only the cavity modes exist, while the polaritonic states appear at 5K. To measure the dispersion with the beam condenser, the period of the grating is changed. Figure 2.9 (b) shows the sample dispersion for different grating periods (34, 36, 37 and 40 μm). These two graphs confirm that the device is operating in strong coupling.

The next step is to measure the full dispersion of one sample. To do so, we need to adapt the sample compartment of the FTIR.

2.5.2 Variable Angle Inset

In order to measure $R(\theta) = \frac{I_{sample}(\theta)}{I_{ref}(\theta)}$ a variable angle reflection unit (Bruker A513/Q) can be inserted into the FTIR chamber. The schematics of this unit is sketched in Figure 2.10. Two spherical mirrors M and M' can be rotated in the incidence plane of the setup ySz allowing one to explore incidence angles ranging from 13° to 83° .

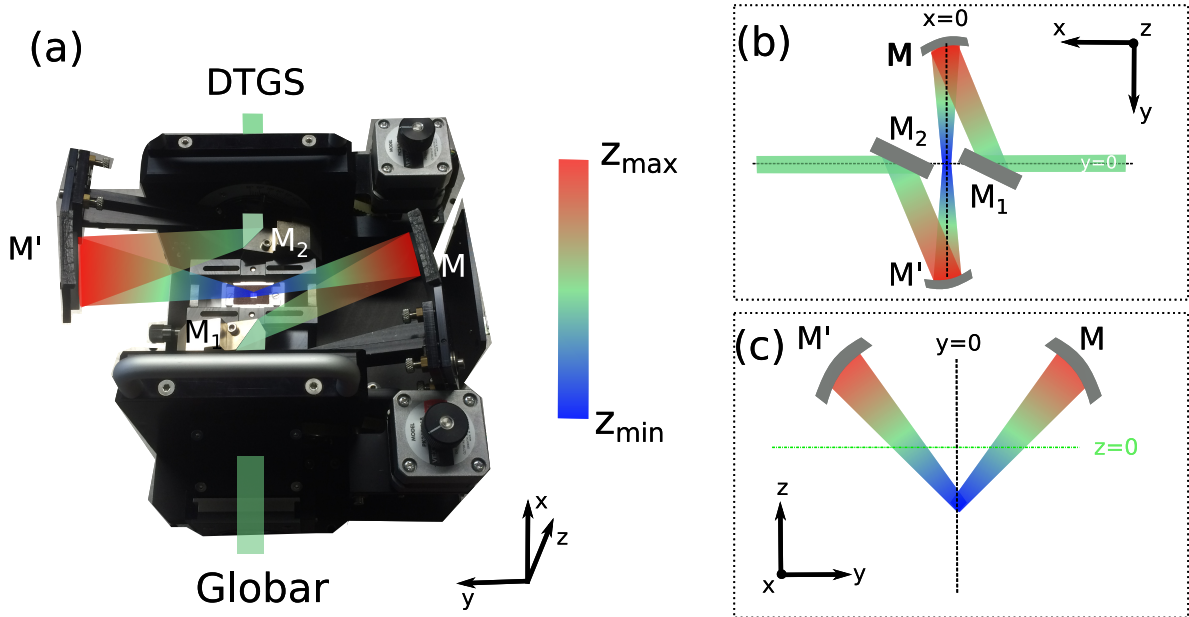


Figure 2.10: (a) Picture and (b-c) schematics of the reflectivity unit. The rotative mirrors are labeled M and M' .

The THz radiation enters the chamber propagating from right to left (Figure 2.11). A plane mirror M_1 deflects the incoming radiation towards M . Light is then focused at point S where the sample is placed on a micro-translation stage enabling signal maximization. The reflected light is collected from M' and again deflected towards the detector by an identical mirror system M_2 . To select the impinging polarization of THz radiation, a polarizer can be placed on the rotating arm before the mirror M_1 .

As THz ISB polaritons are not observable at room temperature, the sample needs to be cooled at liquid Helium temperature. The geometry of the two mirrors accessory does not host the head of a cryostat, and an alternative solution had to be found.

We decided to transform the compartment chamber of the FTIR into a cryostat (Figure 2.11). First, we had to ensure that this compartment is hermetic. The purging lines were blocked, and two TP windows (transparent blue in Figure 2.11) were mounted to pump independently the sample compartment and the FTIR. Specific pieces completely hermetic (thick metallic alloy) have been fabricated in the C2N workshop: one to insert the cold finger of a standard cryostat inside the chamber and a second to see the sample from the top of the chamber.

To avoid water condensation on the sample at 10 K during the few hours required to align the sample and the reference and measure the dispersion, we needed to reach a vacuum of at least 10^{-5} mbar in the sample compartment. To meet these specifications we integrated three pumping systems: the FTIR was pumped under a primary vacuum; the sample compartment was first pumped with a turbo pump (grey), then we added a liquid nitrogen trap (cyan); and

finally the cold finger (brown) cooled down to 10 K plays the role of a second cryogenic pump.

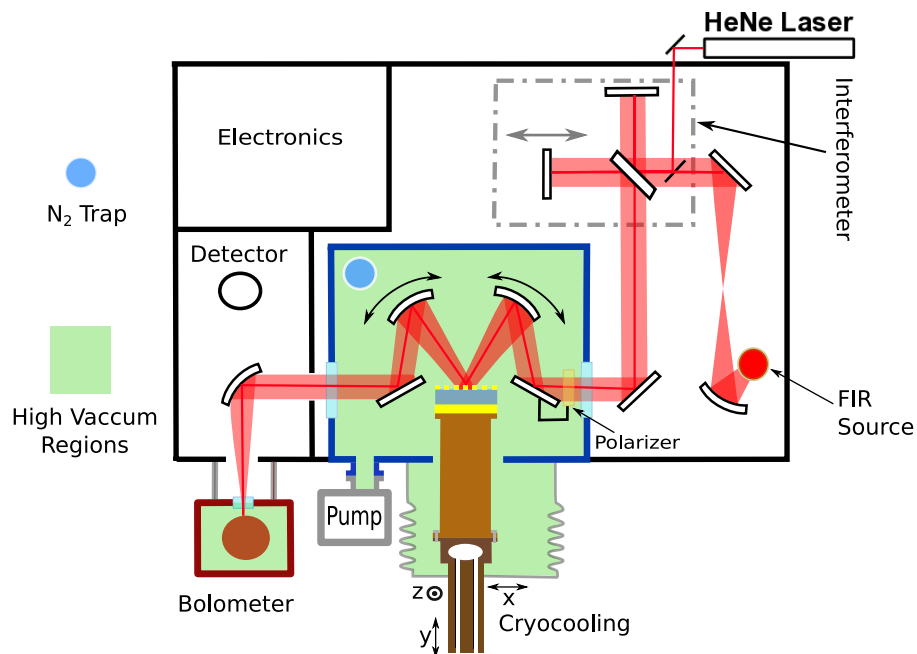


Figure 2.11: Schematics of the low-temperature dispersion measurement set-up. The chamber compartment of a standard FTIR is transformed into a cryostat under high vacuum (green area). Two motorized mirrors are rotating around the focal point of the unit and collect the reflectivity of the sample for a large set of angles.

The optical performances of the set up are comparable with the *beam condenser* set-up. In both cases, most of the absorption comes from the *TPX* windows (30% absorption each) of the cryostat. The polarizer is interlocked in the arm of the first mirror and rotates with the system. Therefore the same polarization is kept for all the incident angles. The beam is focused on the sample by the parabolic rotative mirror. The spot on the focal point has a diameter of ≈ 2 mm that is why the samples size have been chosen $4 * 4$ mm².

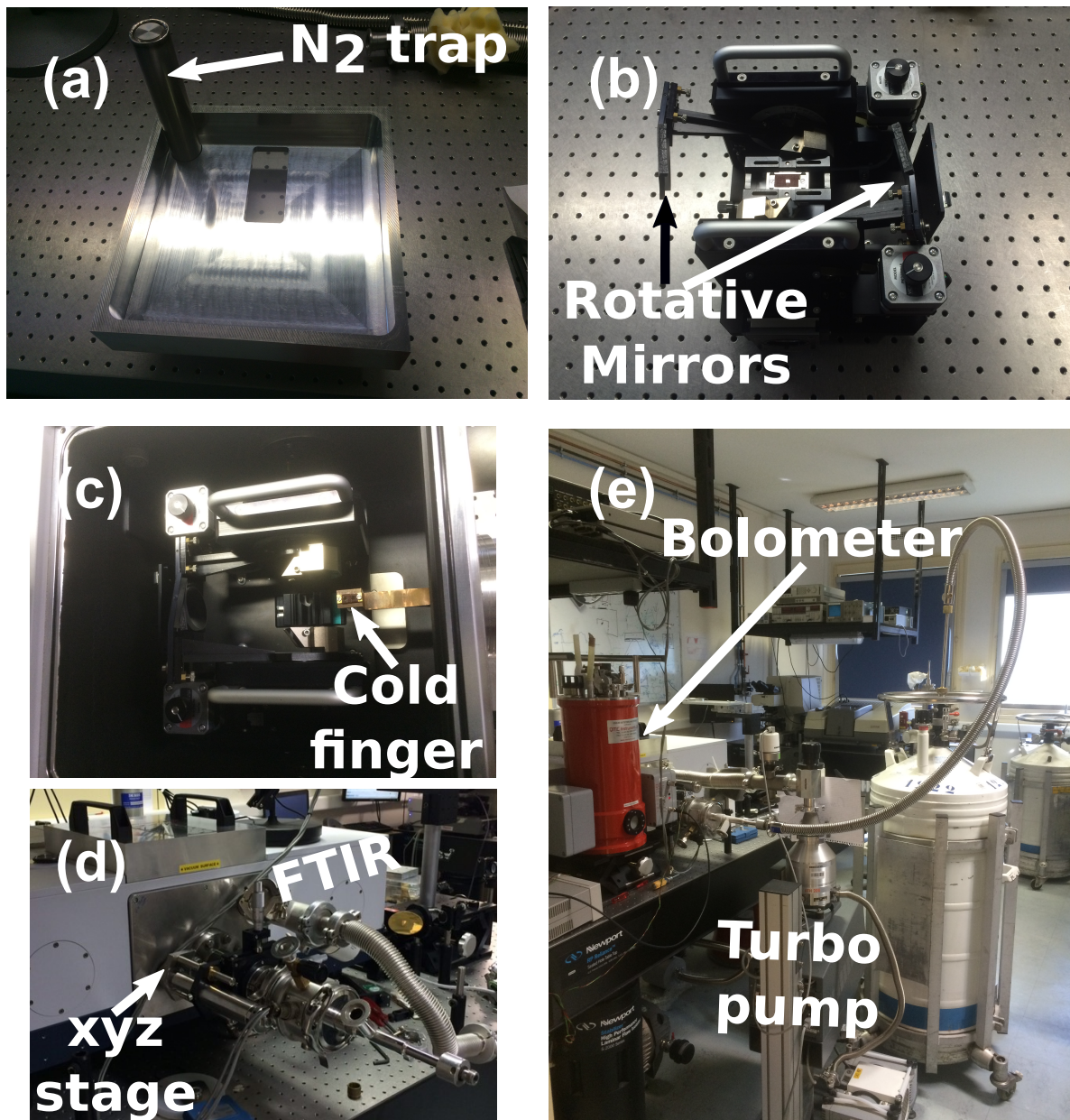


Figure 2.12: Pictures of the experimental set up: (a) the coffer with a nitrogen trap and a window to align the sample, (b) the rotative mirrors stage, (c) the customized cold finger close to the focal point of the two mirrors movable mirrors system, (d) Cryostat horizontal positioned into the sample compartment with the actuators to position the sample and (e) the full set-up during the measurement at liquid Helium temperature. The red cylinder is the *QMC* bolometer.

2.5.3 Dispersion Measurements

After the fabrication and optimization of the sample compartment of the FTIR, the dispersion has been measured for 4 samples.

Influence of the QW Doping

Figure 2.13 shows the highly resolved (5° angular steps) THz dispersions at room temperature and at 10K of two samples: L1362 (a-b) with a grating period of $40 \mu m$ and 80% filling factor (FF); and L1412 (d-e) with a grating period of $34 \mu m$.

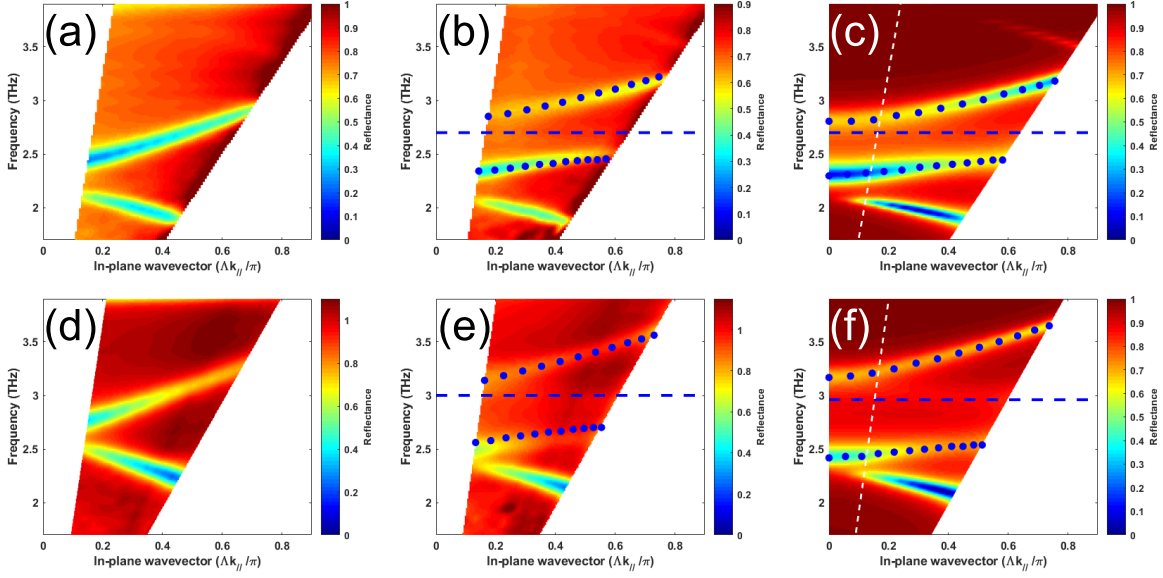


Figure 2.13: Dispersions obtained with highly resolved (5° angular steps and a spectral resolution of 2 cm^{-1}) presented in the k-space. (a) and (b) are the dispersions of sample L1362 with $40 \mu m$ grating period and 80% filling factor respectively at room temperature and at 10K. (d) and (e) are the dispersions of sample L1412 with $34 \mu m$ grating period and 80% filling factor, respectively at room temperature and at 10K. (c) and (f) are respectively the RCWA simulations of sample L1362 and L1412. The horizontal blue dashed lines represent the ISB transition and the white dashed line correspond to the angle limit of the experimental set-up. The blue dots represent the minima of reflectivity of the polaritonic branches for each sample.

The bare cavity dispersions (left panels, (a) and (d)) are given by the measurement of the cavity at room temperature, when the thermal effects hide the intersubband transition ($k_B T > \hbar \omega_{12}$). The TE mode here around 3.9 THz depends on the thickness of the cavity and the index of refraction of the active region. The second and third photonic branches depend on the period and the filling factor of the grating.

At low temperature (middle panels, (b) and (e)), the ISB transition is active, and the strong coupling with the third photonic branch occurs. The reflectivity baselines vary between 80% and 110% (instead of 100%) due to the non-ideal conditions on the device surface (coming from the optical lithography and the lift-off) that possibly scatter the light partially.

For each sample, RCWA simulations have been performed (Fig. 2.13, (c) for L1362 and (f) for L1412). The simulation parameters have been set using the multipass measurement for

the ISB transition (Section 2.1.2) and SEM images to estimate the grating period and filling factor. The thickness of the bulk GaAs and the doping have been slightly changed from the nominal values: $t_{bulk} = 7.6 \mu m$ for both samples; $d_{QW} = 6 \times 10^{10} cm^{-2}$ for L1362 and $d_{QW} = 1.2 \times 10^{11} cm^{-2}$ for L1412.

The comparison between experiment and simulations show an excellent reflectivity agreement on the full range of measurements for both active regions. As predicted by the simulations, the upper polariton of sample L1412 overcomes the limit of detection of the TDS system for $\frac{\Delta k_{//}}{\pi} > 0.6$. In addition, the polariton absorption peaks of sample L1412 are smaller than the ones of sample L1362 (see Table 2.1). For these two reasons, the sample L1412 is not compatible with the TDS system of the LPA.

At this step, the highly resolved reflectivity dispersion set-up enabled us to discriminate between different samples and verify the compatibility between the polaritonic samples and the TDS system. In the following, we will only consider the sample L1362.

Influence of the Grating Filling Factor

For each sample, two grating filing factors have been processed. Figure 2.14 presents two experimental dispersions of the sample L1362 with the same grating period of $40 \mu m$ and different filling factors: 70% (a) and 80% (b).

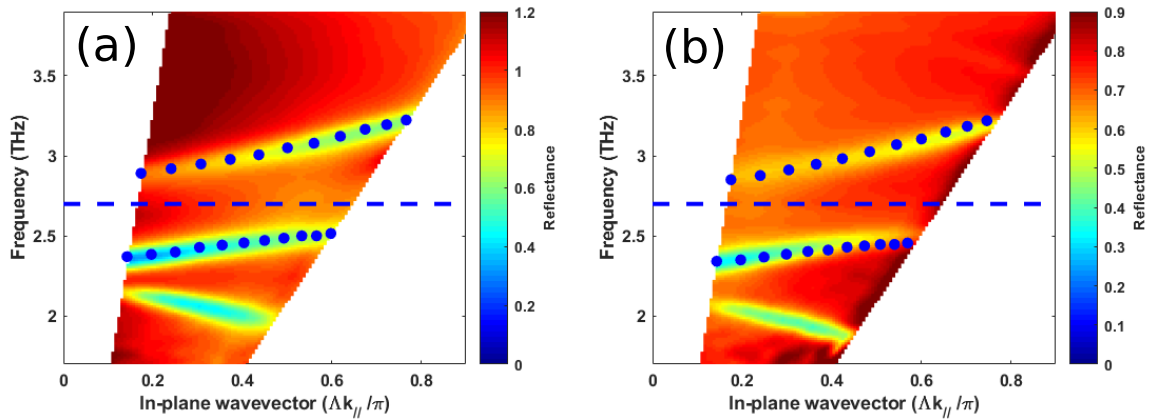


Figure 2.14: Dispersion at 10K of two different samples:(a) L1362, grating with $40 \mu m$ period and 70% filling factor, (b) L1362, grating with $40 \mu m$ period and 80% filling factor. The horizontal blue dashed lines represent the ISB transition. The blue dots represent the minimum of reflectivity of the polaritonic branches for each sample.

The positions of the polaritonic branches are the same for both samples and the main differences are the absorption peaks that are deeper for the sample with the lower filling factor (a). Finally, both samples are compatible with the TDS system.

Comparison between Experiment and Simulations

In the last part of this section, a more accurate comparison between the experiment and the simulations for the sample L1362 with a filling factor of 80% is presented.

Figure 2.15 (a) shows reflectivity measurement (red) and RCWA simulations (black) at 35° . The photonic branch confirmed the grating period, the upper and lower polaritons

were used to adjust the doping of the material ($d_{QW} = 6 \times 10^{10} \text{ cm}^{-2}$ for L1362) and the first TE mode was used to evaluate the cavity thickness. The overestimated absorption of the simulated photonic branch is due to the imperfections of the grating and the metal. Nevertheless, the Q - factors of the polaritonic branches show a much better agreement with the simulations.

After the adjustment of the doping and the thickness, the simulations have been performed for all the angles accessed experimentally. Figure 2.15 (b) compares the polariton peaks of absorption in the k -space for angle from 13° to 65° . The agreement is good over the full range of angles measured in reflectivity. In the following section, we will use the good agreement between experiment and simulations to extend the simulations in the region close to $k_{//} = 0$ that is difficult to access experimentally.

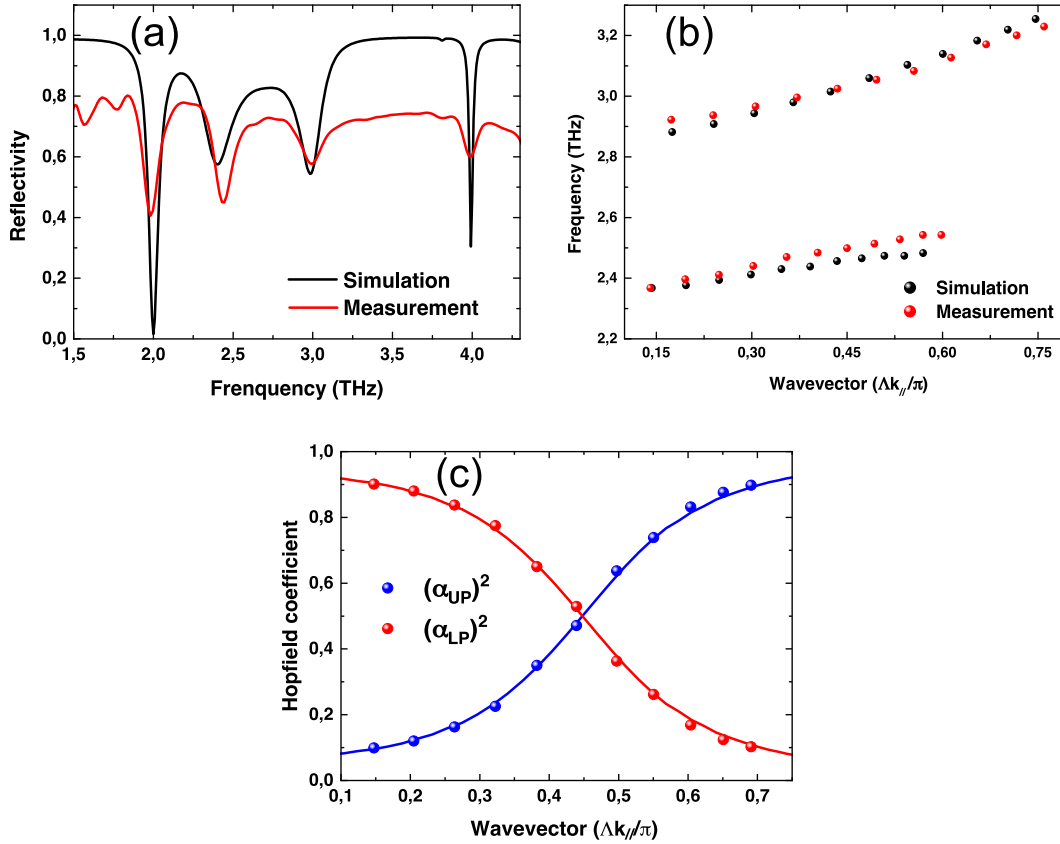


Figure 2.15: Comparison between experiments and RCWA simulations for the sample L1362. The grating period is $40 \mu\text{m}$ and the filling factor is 80%. (a) Spectra under an incidence angle of 35° . (b) Dispersion of the polariton peaks. The simulations (black dots) were performed with a doping of $6 \times 10^{10} \text{ cm}^{-2}$. (c) The Hopfield coefficients of the LP and UP as a function of the in-plane wave vector.

With THz dispersive cavities, it is possible to access the position of the 3^{rd} photonic branch with the measurement at room temperature (Figure 2.13, (a)). By knowing the ISB transition (multipass measurement), it is then possible to calculate the Hopfield coefficients. The matter part of the Hopfield coefficients ($\alpha_{UP/LP}$) has been calculated according to Equation 1.75. They confirm a Rabi-splitting at $k_{//} = 0.45 * \frac{\pi}{\Lambda}$ which represents an angle of 35° . At $k_{//} = 0.1$ the lower polariton is mostly "light" and the upper polariton mostly "matter". The portion of light/matter influences the polariton properties and will be taken into account

for the pump-and-probe experiment design.

Table 2.1 sums up the four dispersion at room temperature and at 10 K that have been performed during my Ph.D. The two samples L1362 (Figure 2.14 (a,b)) have relatively high absorption levels (down to 60% at the polaritonic resonance). The Q-factors are relatively balanced between the lower and upper polaritons ($Q \in [13,20]$). The absorption decreases when the filling factor increases. Since the UP frequency stays below the limit of detection of the TDS system when using a GaP crystal ($3.3\text{ THz} < 3.5\text{ THz}$) these two samples are the best candidates for pump and probe experiments.

Sample	Nominal Doping per Well (cm^{-2})	ISBT (THz)	Q-factors				Rabi Splitting (THz)
			ISBT @4K	Photonic @RT	LP @10K	UP @10K	
L1362, FF=80%, $\Lambda = 40\ \mu\text{m}$,	1×10^{11}	2.73	8	14.48	19.93	17.83	0.52
L1362, FF=70%, $\Lambda = 40\ \mu\text{m}$	1×10^{11}	2.73	8	12.16	15.87	13.12	0.52
L1412, FF 80%, $\Lambda = 34\ \mu\text{m}$	2×10^{11}	2.96	5	12.57	6.98	18.38	0.61
L1412, FF 70%, $\Lambda = 34\ \mu\text{m}$	2×10^{11}	2.96	5	13.05	6.57	14.93	0.62

Table 2.1: Comparison of the Q-factors of the different polaritonic branches of samples L1362 and L1412 at the incidence angle of 35° . FF is the grating filling factor. Λ is the grating period.

The samples L1412 (Figure 2.13 c,d) exhibit reduced absorption levels at the LP and UP frequencies. The larger depolarization shift and Rabi-splitting push the upper branch of the polariton beyond the TDS limit of the LPA system for angles larger 45° . Even if the TDS system can be modified to operate at higher frequencies, the misbalance between the Q-factors of the upper and lower polaritons ($Q_{UP} \sim 6.5$ vs $Q_{LP} \sim 18$) poses a critical problem in the pump-and-probe measurement.

To conclude, the THz dispersion set-up has been a crucial tool to select the samples potentially compatible with the TDS system. It showed that the RCWA simulations are predictive for a large set of angles. According to the good agreement between experiment and simulations, it was possible to extend the simulations close to the normal incidence ($k_{//} \sim 0$) that is an interesting region to observe polariton-polariton scattering.

2.6 Perspectives: Polaritonic LEDs Based on Polariton-Polariton Scattering

In the Mid-Infrared spectral range, a polariton can scatter from the upper (\vec{k}_{UP}, E_{UP}) to the lower branch (\vec{k}_{LP}, E_{LP}) by emitting ($E_{LO,phon}^{GaAs} \approx 36 \text{ meV}, \vec{k}_{LO,phon}$) [60]. This mechanism proposed in 2009 [58] and demonstrated in 2018 [14] respects the energy and momentum conservation:

$$\begin{cases} \vec{k}_{UP} = \vec{k}_{LP} + \vec{k}_{LO,phon} \\ E_{UP} = E_{LP} + E_{LO,phon} \end{cases} \quad (2.6)$$

In the THz domain the LO-phonon energy is much larger than the Rabi-splitting ($E_{LO,phon}^{GaAs} \approx 36 \text{ meV} > E_{Rabi,THz} \approx 3 \text{ meV}$). Consequently, no scattering mechanism is possible between a THz-polariton and an optical phonon.

The *polariton-polariton* scattering is an alternative mechanism observed with exciton-polaritons [65, 66] that could also exist in the intersubband polariton domain. The theoretical framework proposing intersubband polariton-polariton scattering has been described in only one publication Ref.[67], and has not yet been explored experimentally.

Considering the simulations around $k_{||} = 0$ plotted in Figure 2.16, polariton-polariton scattering could appear on both the upper and lower branches. This mechanism is described as follows:

$$\begin{cases} \vec{k}_{init}^{(1)} + \vec{k}_{init}^{(2)} = \vec{k}_{final}^{(1)} + \vec{k}_{final}^{(2)} \\ E_{init}^{(1)} + E_{init}^{(2)} = E_{final}^{(1)} + E_{final}^{(2)} \end{cases} \quad (2.7)$$

Initially the first ($\vec{k}_{init}^{(1)}, E_{init}^{(1)}$) and the second ($\vec{k}_{init}^{(2)}, E_{init}^{(2)}$) are in the same state ($\vec{k}_{init}^{(1)} = \vec{k}_{init}^{(2)}$ and $E_{init}^{(1)} = E_{init}^{(2)}$). The first polariton would then transfer part of its energy and momentum to the second polariton. Both polaritons would stay on the same polaritonic branch. The conservations of energy and momentum limits the number of states on which this mechanism could occur.

Experimentally, light is injected in the system at a specific angle (named *magic angle*) and a specific frequency. By injecting photons at the *magic angle* with the correct energy, the polariton-polariton scattering mechanism can be enabled. Because the two branches (LP and UP) have an energy minimum at $k_{||} = 0$, a THz-polariton accumulation is possible. Note that the two magic angles -drawn on both upper and lower branches- proposed on Figure 2.16 are not unique in our system, thanks to the elevated broadening of the polariton states.

Observing polariton-polariton scattering requires a controlled light injection to induce polariton-polariton scattering without bleaching the ISB transition. Time-domain spectroscopy associated with THz quantum cascade lasers appears as a suitable experimental set up to observe polariton-polariton scattering mechanisms, for two reasons:

- The reflections of the THz-QCL signal do not affect the measurement because the QCL has a different phase than the fs pulse.
- The phase resolved measurement gives access to the observation of both amplitude and phase.

The road-map for the observation of THz ISB polariton-polariton scattering is the following: first observe the scattering mechanism independently from the decay time of the

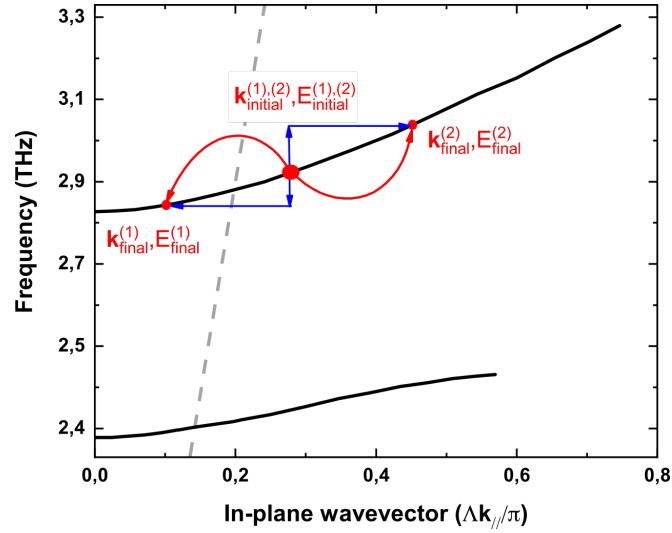


Figure 2.16: Simulation of the dispersion of the sample L1362, with a grating period $\Lambda = 39 \mu m$, a filling factor of 70%. The possible "magic angles" positions on both LP ($\theta = 16^\circ$) and UP ($\theta = 20^\circ$) are indicated. The dashed grey line represents the limit between experiment and simulations.

polaritons; then evaluate the polariton-polariton scattering decay time ($\gamma_{p-p,scat}$).

The first experiment consists in pumping with a time scale longer than the decay time of the polariton ($\delta t_{pump,on} \approx \mu s \gg \tau_{p-p,scat} = \frac{1}{\gamma_{p-p,scat}}$). In this configuration the polaritons are excited "continuously" by the pump and a steady state can be established. The comparison between the polariton absorption peaks with and without the pump would give information about the possible scattering mechanisms.

Once the scattering mechanisms have been identified, the pumping time will be decreased, down to a few ps (see developments done in Chapter 4). When the pumping time will approach the scattering time ($\delta t_{pump,on} \sim \tau_{p-p,scat}$), the dynamics of the system would change (an example with Mid-IR polaritons is given in Ref [8]). If these changes are observable experimentally it will be possible to estimate the polariton-polariton scattering lifetime.

2.7 Conclusions

In this chapter, we have presented a new set-up to measure polaritonic dispersions at low temperature. This set up has been applied to measure a highly resolved THz polariton dispersion at 10 K.

Four samples from two different heterostructures have been measured. Depolarization shifts larger than the simulations were observed on both samples. The highly doped structure (L1412) had the stronger depolarization shift of $\approx 0.5 THz$. As a result, the ISB transition is incompatible with the TDS measurement system.

Consequently, only the samples *L1362* will be studied in TDS in the follow-up.

The TDS system is the best tool to observe the polariton-polariton scattering because the measurement of the probe is not affected by the scattered light from the pump. Besides the TDS system is suitable to decrease the pumping time down to the ps [27].

Chapter 3 presents preliminary results on the measure of the THz-ISB polaritons with a pumping time that is much longer than the decay time of the polaritons.

Initial Pump-Probe Experiment of THz Polaritonic Structures

Fundamental features of intersubband polaritons, such as scattering mechanisms or condensation phenomena, require powerful and precise instruments to be measured. The time-domain spectroscopy (TDS) coupled with quantum cascade lasers (QCLs) appears as a promising approach offering a narrow pump (QCL), a broadband THz probe and various measurement configurations (transmission, reflectivity, pump-probe).

I collaborated with the team of S.Dhillon at *Pierre Aigrain Laboratory* (ENS/LPA Paris) for the measurement of the THz polaritonic structures that I implemented in Chapter 2, in the context of the Ultra-QCL FET European project. The TDS measurements have been performed in his team at ENS.

3.1 Principle of the Pump and Probe Measurement

The scheme of a pump and probe measurement is similar to a classical optical parametric oscillator (OPO) experiment.

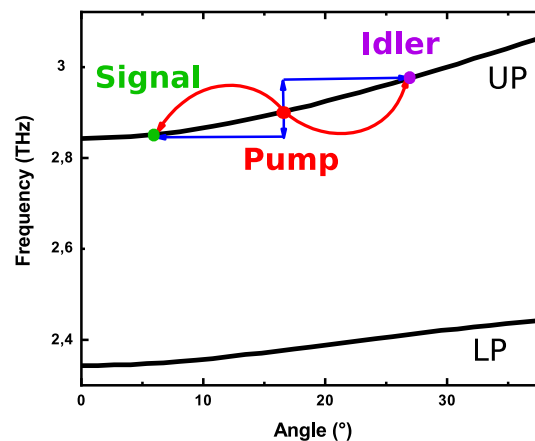


Figure 3.1: Schematic of the optical parametric oscillator (OPO) experiment based on the polariton dispersion of the sample L1362. The upper polariton is pumped with a THz-QCL and the signal is measured with the probe of the TDS system, close to normal incidence.

Figure 3.1 presents the absorption minima of the polaritonic branches of sample L1362 for different angles. One interesting configuration to observe polariton-polariton scattering (according to Section 2.6) is to pump at 2.9 ± 0.1 THz with an incidence angle at $17 \pm 3^\circ$. The narrowband pump (THz-QCL) is used to create polaritons into a reservoir. The signal is measured with a broadband probe around 2.85 THz and close to the normal incidence (note that the probe already creates a density of polariton on the final state, which in principle facilitates to reach the threshold). The goal of this measurement is to observe the influence of the pump intensity on the absorption (or emission) of the final-state. Beside, the direct detection of the idler beam (typically at larger angles and frequencies than the pump and the signal beams) would be a strong evidence that optical amplification is indeed taking place in the system.

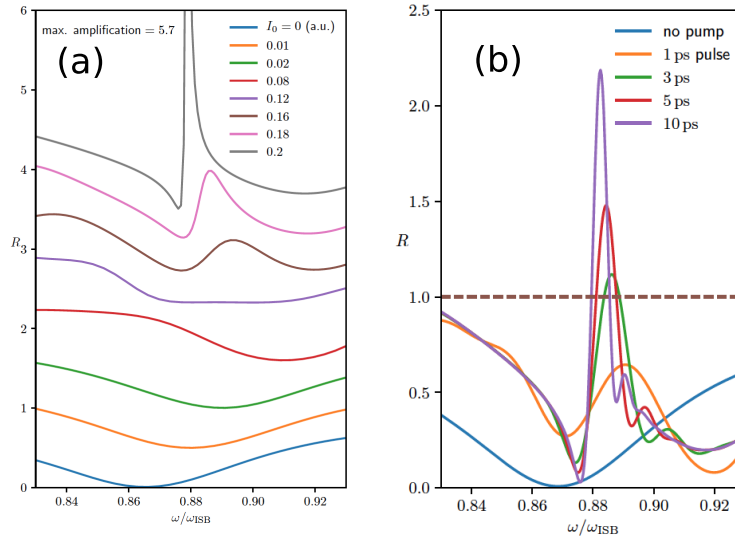


Figure 3.2: (a) Numerically simulated emission spectra with continuous wave pump of growing intensity. (b) Numerically simulated emission spectra with a pulsed pump of increasing duration. The peak intensity is kept at $I_0 = 0.2$ (from Ref.[68]).

The Gross-Pitaevskii model in Ref. [68] gives a theoretical vision of the expected signal at $k=0$ (for the lower polariton), and typical numerical results are presented in the Figure 3.2. Due to the assumptions done in these simulations (see Ref.[68] for more details), the pump intensities are not given in terms of physical pump intensity but in arbitrary units (a.u.).

Under these conditions, when the pump is quasi-continuous wave (Figure 3.2, (a)), pulses longer than 150 ps a shift of the absorption is expected at low pump intensity ($I_0 < 0.08$). Above threshold (a pump intensity of $I_0 = 0.2$), an emission (reflectivity superior to 1) is observed with an amplitude maximum at 5.7. The continuous wave regime will be explored in this chapter to explore the existence of the polariton-polariton scattering process.

A second configuration employs a pulsed pump (pulses shorter than 10 ps). In this case, the pump has to be synchronized with the probe. Figure 3.2, (b) shows the expected signal for different pump pulse widths. The pulse regime can provide information on the decay rate of the polariton-polariton scattering. In Part 2, of this manuscript, we fabricated THz-QCL with Gires-Tournois cavities to generate pulsed shorter than 5 ps.

3.2 Main Components of a Time-Domain Spectroscopy System

THz-TDS is a technique that allows us to coherently detect the time-resolved electric field of THz pulses emitted by synchronized THz sources with a fs laser. It typically includes 3 parts: 1) A femtosecond optical/near-infrared laser, 2) THz generation system and 3) THz detection system. Commonly used generation system in THz-TDS are photoconductive antennas and the detection system is typically based on electro-optic sampling.

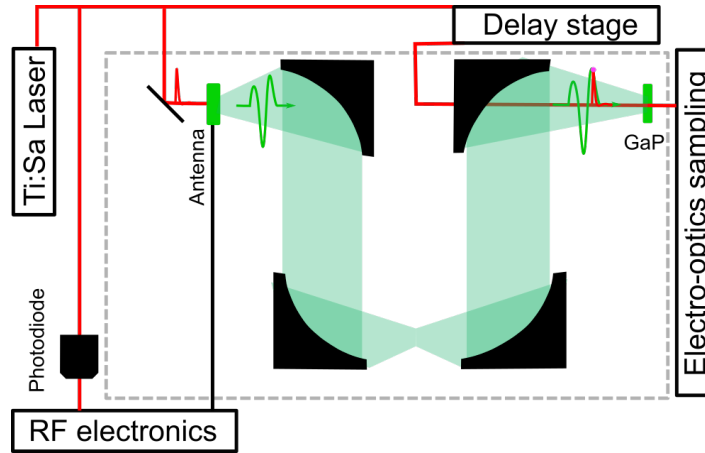


Figure 3.3: Schematics of a TDS measurement system in transmission configuration with an antenna source.

Using a TDS system, we can directly measure the absorption of the polaritonic samples in amplitude and phase. The TDS system can also operate in the pump-and-probe configuration when a first impulsion excites the sample and a second impulsion measures the sample. We use a THz-QCL as a pump to generate polaritons in the reservoir state and observe absorption variations due to the presence of the pump.

3.2.1 THz Pulsed Broadband Source: Photo-conductive Antenna

Various optoelectronic sources exist for TDS: two-color filamentation by ionization of the air with a focused laser beam (Kerr effect [69]), frequency mixing in nonlinear crystals [70] and antenna excitation with a femtosecond laser [71]. The LPA's TDS uses an antenna excited with a near-infrared Ti:Sa fs laser ($\lambda \sim 800 \text{ nm}$).

A photoconductive antenna is a device that can generate broadband THz pulses covering the frequency range from 0.1–4 THz [71]. It consists of two metal electrodes deposited on a GaAs semi-insulating substrate, as illustrated in Figure 3.4 in its simplest form. When a femtosecond infrared laser pulse, typically from a Ti:sapphire laser, with photon energy larger than the band-gap of the material, excites the GaAs substrate between the positive and negative contacts, electrons in valence band will be excited to the conduction band and become free carriers. With the antenna biased, a transient photocurrent I_{PC} will be generated between the electrodes.

The THz radiation of a photoconductive antenna can be obtained by applying the Hertzian dipole antenna model. The time-dependent emission expression in free space is [73]:

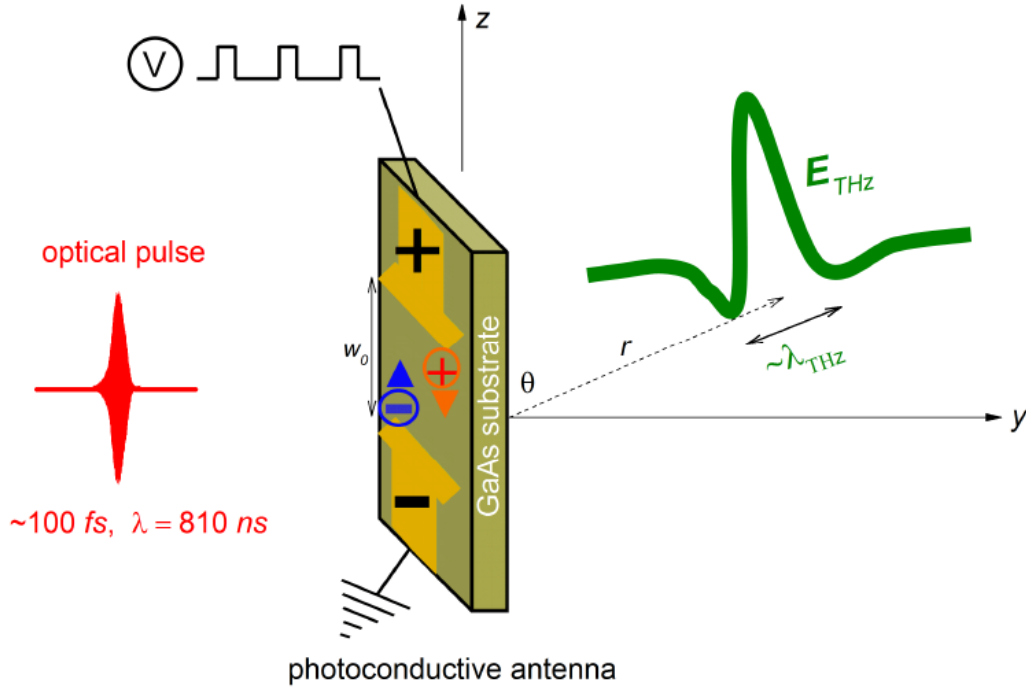


Figure 3.4: Schematic diagram of a photoconductive antenna for THz pulse generation under femtosecond optical pulse excitation [72].

$$\vec{E}_{THz} = \frac{\mu_0 w_0 \sin(\theta)}{4\pi r} \frac{d}{dt_r} [I_{PC}(t_r)] \hat{\theta} \propto \frac{dI_{PC}(t)}{dt} \quad (3.1)$$

where μ_0 is vacuum permeability, w_0 is the gap distance between the negative and positive electrodes, r and θ are, respectively, the distance and angle of photoconductive antenna radiation, $t_r = t - r/c$.

If an ultrafast, for example ~ 100 fs, a laser pulse is employed to create the transient photocurrent, the generated electric fields will also last a few hundred femtoseconds, which corresponds precisely to the THz frequency range.

3.2.2 THz Pulse Sampling

The sampling of the THz pulse is performed exploiting the *Pockels effect* in a crystal (ZnTe, GaP). It is an electro-optic (EO) sampling [74]. The measurement principle relies on the additional birefringence induced in a EO crystal by the THz field. In the appropriate geometry, this additional birefringence turns the polarization of the infrared beam crossing the crystal. The measurement of the polarization rotation determines the amplitude of the electric field.

Figure 3.5 presents the schematics of an electro-optic sampling system for THz electric field detection. On one hand, we suppose that only a vertically polarized infrared fs pulse represented in red - that previously excited the THz antenna - arrives on the ZnTe crystal. If no THz wave (green) passes through the EO crystal, there is no induced birefringence and the polarization of the fs pulse remains vertical. When the fs wave passes through the quarter-wave plate after the ZnTe crystal, the vertical polarization will become circular. The vertical and horizontal components of the optical pulse are then separated by a Wollaston prism and

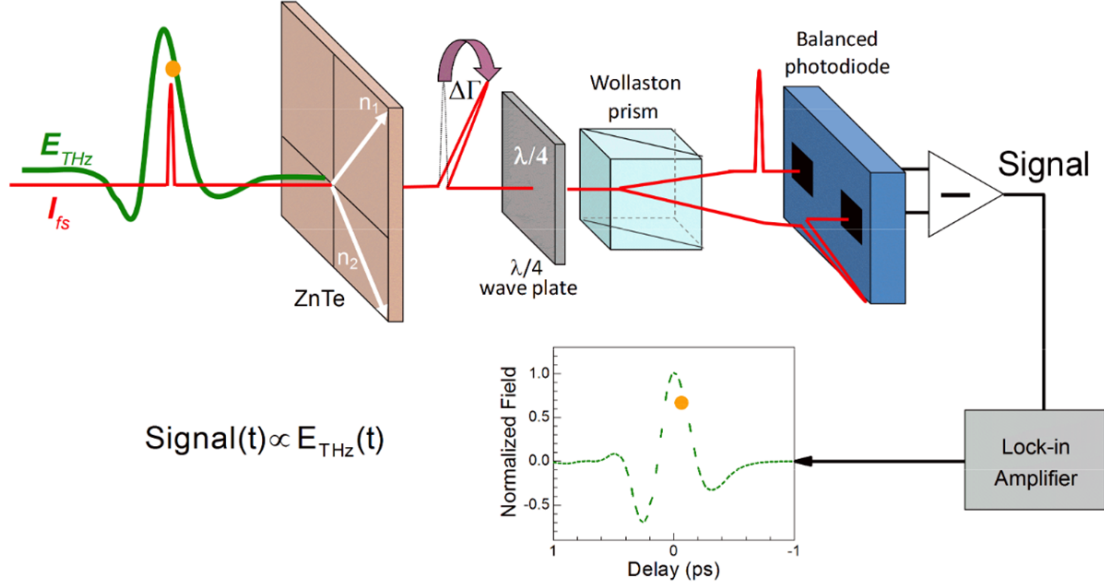


Figure 3.5: Schematics diagram of an electro-optic sampling system for THz electric field detection. ZnTe: nonlinear crystal for Pockels effect. Wollaston prism: separates horizontally and vertically polarized components of fs optical pulses after quarter-wave-plate. Balance photodiode: detect respectively the horizontal and vertical components of fs optical pulses and their difference is determined and sent to a Lock-in amplifier for coherent detection [72].

are sent onto a balanced photodiode detector. This situation corresponds to the reference and is used to calibrate the photodiode. On the other hand, when a THz pulse travels together with the fs pulse, the refractive indexes n_1 and n_2 in directions \vec{n}_1 and \vec{n}_2 of the crystal (indicated in Figure 3.5) are modified owing to the Pockels effect (induced birefringence). Passing through the nonlinear EO crystal of thickness L , the phase retardation between the vertically and horizontally linearly polarized components of the beam is [73]

$$\Delta\phi = (n_1 - n_2)\frac{\omega L}{c} = \frac{\omega L}{c}n_0^2r_{eo}E_{THz}. \quad (3.2)$$

Where n_0 is the refractive index at the optical frequency and r_{eo} is the EO coefficient. Therefore, the fs optical pulse will become elliptically polarized after the quarter-wave plate. The horizontal I_x and vertical I_y components of the signal can then be written

$$\begin{cases} I_x = \frac{I_0}{2}(1 - \sin(\Delta\phi) \approx \frac{I_0}{2}(1 - \Delta\phi)) \\ I_y = \frac{I_0}{2}(1 + \sin(\Delta\phi) \approx \frac{I_0}{2}(1 + \Delta\phi)). \end{cases} \quad (3.3)$$

Where I_0 is the intensity of the incident fs pulse. After separation of the electric components on the Wollaston prism the final detected signal on the balanced photodiode is

$$I_s = I_y - I_x = I_0\Delta\phi = \frac{I_0\omega L}{c}n_0^2r_{eo}E_{THz} \propto E_{THz}. \quad (3.4)$$

Equation 3.4 shows that the intensity imbalance measured on the photodiode is proportional to the THz electric field corresponding to the point that is in temporal superposition

with the fs optical pulse (orange point Figure 3.5). Consequently, the amplitude of the THz electric field can be sampled at this point by reading the photodiode output signal. By controlling the arrival time between the THz pulse and the fs pulse -using a mechanical delay-line- it is possible to reconstruct the THz electric field (both amplitude and phase). A lock-in amplifier is used to detect the signal from the balanced photodiodes with, as a reference, the modulation frequency of the photoconductive antenna use to generate the THz beam.

3.2.3 Choice of the Crystal to Study Polaritons at 3 THz

With an upper polariton frequency between $2.7 THz$ and $3 THz$ the choice of the crystal appeared to be critical. Figure 3.6 shows that the $ZnTe$ strongly absorbs the signal between $2.5 THz$ and $3.5 THz$, exactly in the region of the polaritonic branches of the sample L1362. Consequently, a GaP crystal has been chosen, which has a narrower operation range, but more signal in the investigated window $2.5-3.5 THz$.

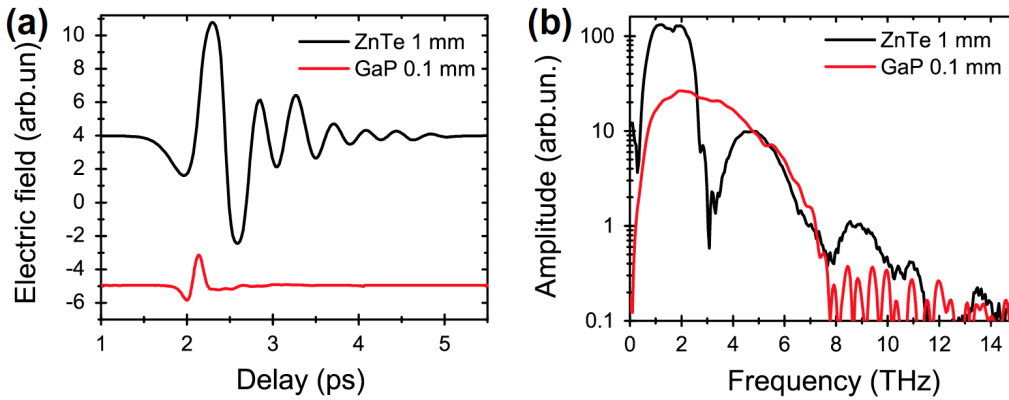


Figure 3.6: Influence of the crystal, $ZnTe$ or GaP , on the recorded electric field (a) and corresponding spectra (b) [69].

Nevertheless, the $ZnTe$ is still used for alignment procedures because it has almost one decade more of signal amplitude in the range of $0.5-2 THz$, where the TDS system is optimized.

3.3 Reflectivity Measurements

Before exploring the polariton dynamics, the first step is to measure the polariton reflectivity with the TDS system. Figure 3.7 shows a TDS system for reflection measurement. The antenna pulse is collimated with a first parabolic mirror and focused with a second mirror onto the sample at 45° . After reflection onto the polariton cavity, the pulse coming from the antenna is deformed owing to the absorptions of the polaritons. The out-coming pulse is then analyzed by electro-optics sampling using a GaP crystal. The spectrum of the sample is obtained by the Fourier transform of the signal in time and normalized by the spectrum of a reference gold plate.

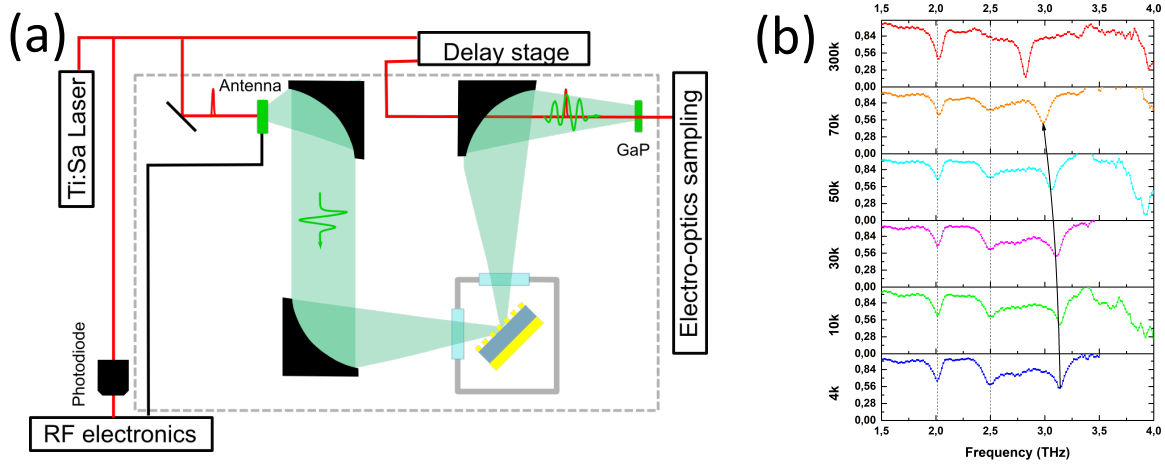


Figure 3.7: (a) Schematics of the a TDS system with a GaP crystal in reflectivity configuration at an angle of incidence of the probe at 45° , (b) Normalized reflectivity spectra at 45° for the sample L1362, with a filling factor of 80% and a grating period of $40\mu m$ for different temperatures

Figure 3.7 shows the measured reflectivity of polaritonic sample L1362 at different temperatures. The results are similar to the measurements with the FTIR. At room temperature, only the cavity modes are visible. Below $70 K$ the intersubband transition starts to absorb, and the splitting of the photonic branch appears. The lower the temperature, the stronger the absorption, and the larger the Rabi-splitting. The LP at $2.5 THz$ and the UP at $3.1 THz$ are visible at 45° and stay below the set-up detection limit of $3.5 THz$.

The next step is to pump the UP with a QCL emitting at a frequency of $3.1 THz$. The first campaign of measurements has been launched with both pump and probe impinging on the sample at 45° . The TDS is particularly adapted to this experiment because - after averaging- the electro-optic sampling is only sensitive to the probe signal and not to the QC laser reflections (that are de-phased from the fs laser). This configuration with both pump and probe impinging at 45° will not permit to observe polariton-polariton scattering. However, it will provide information about the impact of the pumping with a THz-QCL onto the polaritonic branches.

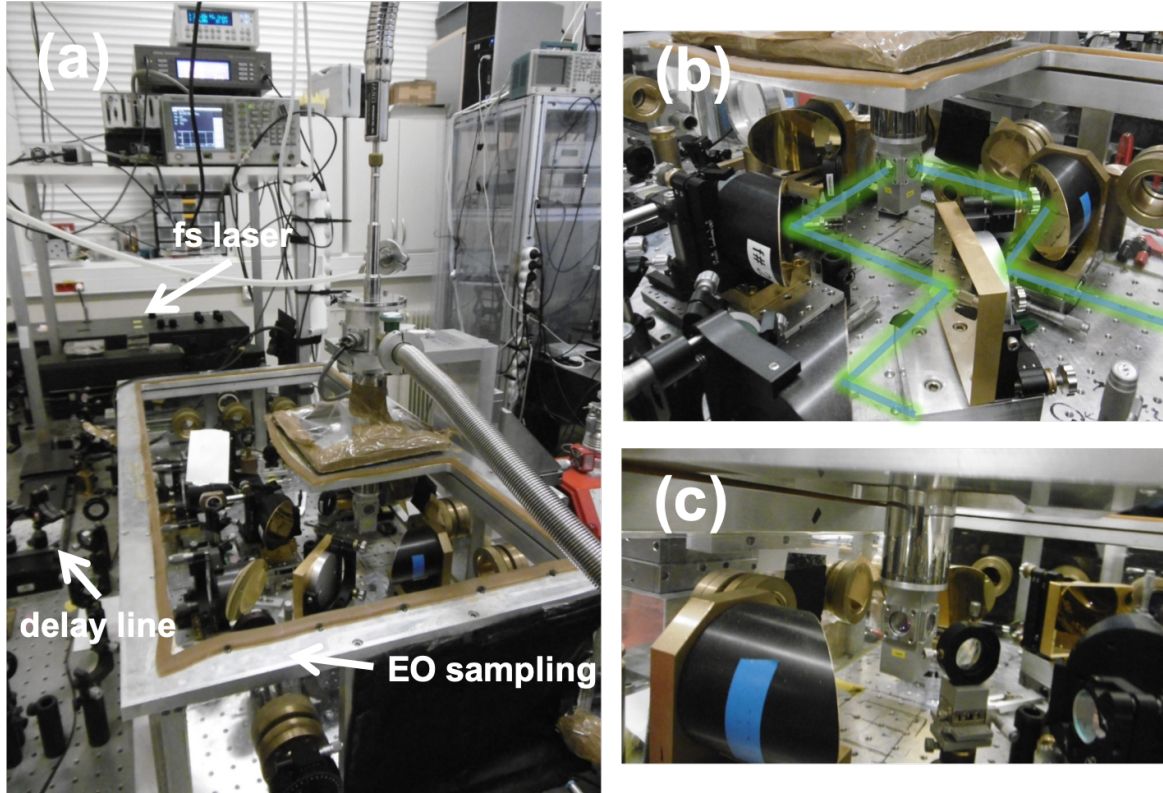


Figure 3.8: Images of the experimental set-up, at LPA, in reflectivity configuration. (a) A large view of the full set-up with the fs laser, the delay line and the EO sampling. (b-c) Zoom on the cryostat head inside which is the polariton sample. In green, the THz beams coming from the antenna and probing the polariton sample.

3.4 Initial Pump and Probe Measurements

In this section, we motivate the choice of the pump and present the performances of the QCL that will be used for optical pumping of the polaritonic sample. After optimization of both the laser and the antenna signals, the pump-probe measurement has been performed at an incidence angle of 45° on the polariton's cavity.

3.4.1 Saturation of the ISB Polariton

The polaritonic states can be studied until the saturation of the two-level system (bleaching). The saturation flux of the system is given by the equation [75]:

$$\Phi_{sat} = \frac{\hbar c \epsilon_0 n_{op} \Gamma_1 \Gamma_2}{2\omega D_{12}^2} \quad (3.5)$$

where Γ_1 is the inelastic relaxation rate, Γ_2 dephasing rate, n_{op} the optical index and c speed of light in vacuum.

$\Phi_{sat, MIR}$ has been experimentally evaluated in the Mid-Infrared domain Ref.[76] around $0.5\text{-}1\text{MW}/\text{cm}^2$. According to Equation 3.5 and considering the dipolar matrix element D_{12} as roughly proportional to the wavelength, we estimated the saturation of a THz polaritonic

system at $\Phi_{sat,THz} \approx \Phi_{sat,MIR} * 10^{-1} \approx 50 - 100 \text{ kW/cm}^2$.

The best source to reach such a power density is the Quantum Cascade Laser. THz-QC lasers emit up to 1W peak power per facet [17, 24]. After focusing the light on a 100 μm diameter spot and considering the losses in the windows of the cryostats (one for the laser and one for the sample) the final power density impinging on the sample can be of $\sim 1 \text{ kW/cm}^2$. With such a laser, we expect to operate below the saturation with sufficient power to highlight scattering mechanisms in the system.

3.4.2 Source Description

One of the main parameters to increase the output power of a THz-QC laser is the thickness of the active region, which is limited by the epitaxy running time. A remarkable work recently proposed to waferbond two symmetric active regions together [24]; the resulting peak output power was 470 mW per facet. More recently, the epitaxy running time has been increased, and it has been possible to grow 24 μm -thick active regions [17] delivering an output peak power larger than to 1 W.

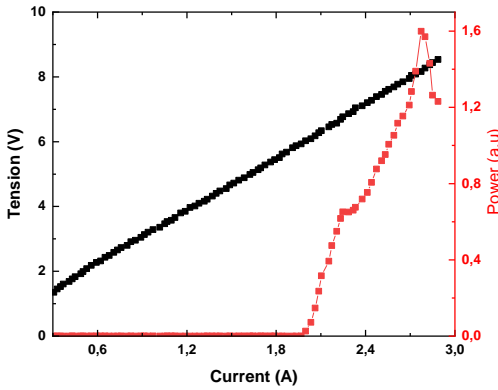


Figure 3.9: Laser L1498MC Light-Voltage versus Current (L-I-V) at 4 K with a repetition rate of 40 kHz and a duty cycle of 2% . The geometry of the cavity is 21- μm -thick, 375- μm -wide and 1.5 mm long.

The laser chosen to pump our THz polariton system is based on a bound-to-continuum transition with a one-well injector embedded in a surface-plasmon waveguide. These active regions have a laser threshold current density of 400 A/cm^2 at 10 K [17]. Considering a maximum output current of the power supply at 5 A, an appropriate geometry of the cavity to maximize the output peak power of the laser is 375 μm wide and 1.5 mm long (for a thickness of the active region 21 μm). With such a geometry the threshold current is reached around 2 A, and the maximum output power is estimated to 300 mW [17]. Figure 3.9 shows the L-I-V of sample L1498MC used for the optical pumping experiment.

The optical gain of laser L1498 covers a range of frequencies between 2.9 THz and 3.2 THz and the spectrum is not strongly dependent on the bias (Figure 3.10, (a)). Such an optical gain corresponds to the target frequencies: 3.2 THz for pumping at 45° and 3 THz for pumping at 15°. The output peak power reaches a maximum of 340 mW at 3.5 A applied current and a duty cycle of 10% and a repetition rate of 40 kHz (Figure 3.10, (b)).

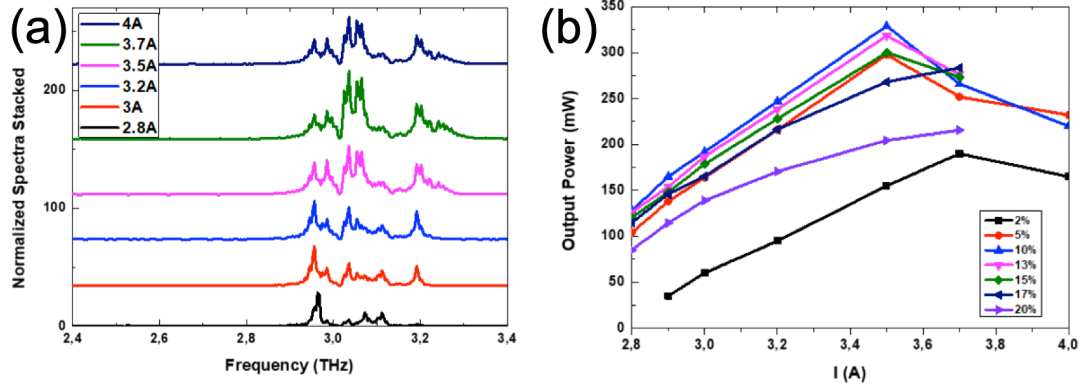


Figure 3.10: Laser L1498MC driven at 40 kHz : (a) Spectra for different driving current. (b) Output power as a function of the driving current for different duty cycles.

The repetition rate of the laser L1498MC can be synchronized with the fs laser and thus with the antenna using a fast photodiode to trigger the power supply. Nevertheless, the phase of the QC laser changes each time it is turned on and is different from the phase of the fs laser. Consequently, -after averaging- the pump signal is not measured on the electro-optics sampling line.

3.4.3 Pump and Probe Measurements at 45°

The laser signal is collimated using a parabolic mirror and then superposed with the optical path of the antenna pulse using a beam-splitter (Figure 3.11). The probe is then collected and sent on the EO sampling for analysis.

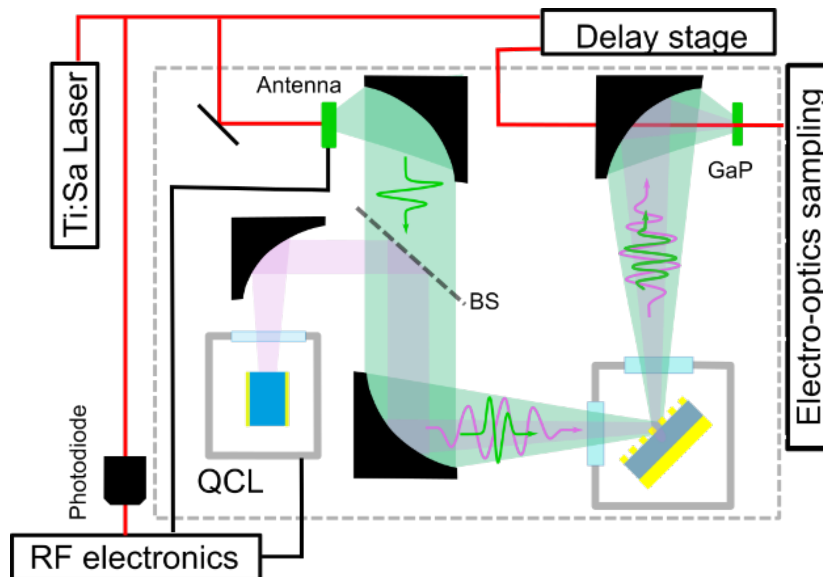


Figure 3.11: Schematics of the TDS with a GaP crystal in pump-probe configuration. The laser signal is integrated to the optical path of the antenna impulsions using a beam splitter (BS).

During the first measurement campaign, the pump and the probe were not synchronized. The QCL was operating 40 kHz repetition rate, with 2% duty cycle while the antenna at a rate of 7 kHz with 50% duty cycle. In this configuration, the polariton is excited only 2% of the probing time (Figure 3.12, a).

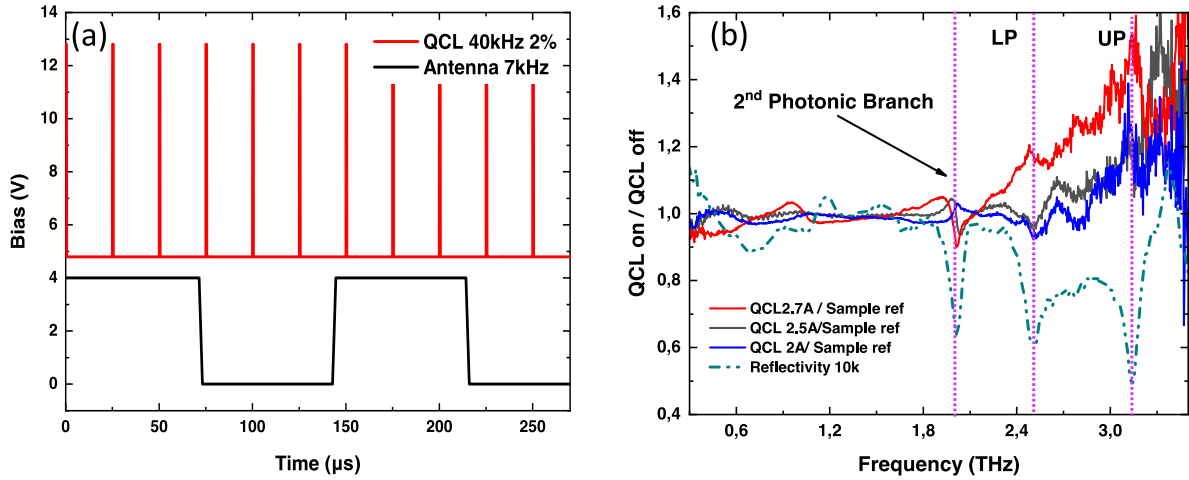


Figure 3.12: (a) Electrical injection of the antenna at 7 kHz , 50% duty cycle and the QCL at 40 kHz , 2% duty cycle. (b) Green dashed: reflectivity measurement at 45° and 10 K . The blue, grey and red curves correspond to the ratio of the reflectivities on the polariton sample with and without laser pump for different laser driving currents (i.e. output power).

The ratio between the reflectivity measurement with and without the QCL pump, as a function of the power for different pump power, ($R_{QCL, on}(\omega)/R_{QCL, off}(\omega)$) is shown in Figure 3.12, (b).

Below 2 THz , the baseline is almost equal to one with slight variations. Some significant oscillations appear around the purely photonic cavity mode at 2 THz . After stabilization of the baseline between the photonic branch and the LP a second oscillation occurs and between the two polaritonic branches the ratio starts to form from the baseline up to 1.6 . This phenomenon is amplified when the laser output power increases.

These preliminary results suggest an influence of the pump on the absorption peaks and particularly the polariton peaks. A second campaign aimed to probe the sample only when the pump is on. To do so the laser and the antenna have been synchronized together using the femto second laser and a fast photodiode. The laser was still driven at 40 kHz , but the duty cycle was increased to 10% . The emission time window of the antenna is chosen slightly narrower than the laser pulse to be sure that the polariton is excited during the probing time (Figure 3.13). As seen in Figure 3.11 the laser pulse arrives slightly before the antenna pulse.

The spectra under different laser excitations are shown in Figure 3.14 (a). They show that at this power density impinging on the sample, we are still far from polariton saturation.

Figure 3.14, (b) shows the ratio between the spectra with and without laser pumping. Below the photonic branch, the ratio is close to one, as already observed in the previous measurement.

A first peak appears on the 2^{nd} photonic branch at 2 THz . The curve returns to unity between 2.1 THz , and 2.4 THz where there is no absorption. The oscillation comes back for the LP (2.6 THz) and UP (3.1 THz).

The results with the QCL and antenna synchronized are different than the ones with no

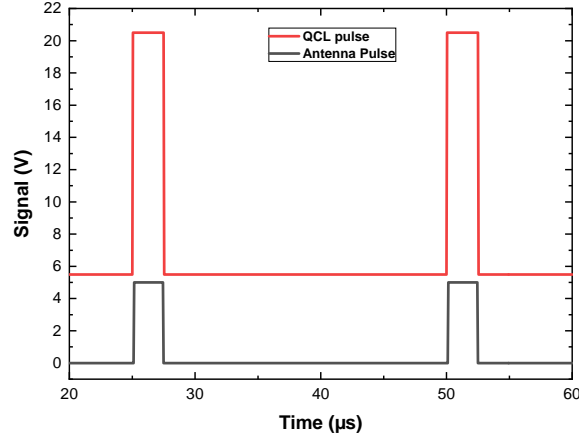


Figure 3.13: Laser and antenna driving voltages as a function of time. The laser and the QCL are now synchronized and driven at a frequency of 40 kHz with a duty cycle of 10%.

synchronization (Figure 3.12). Despite a higher duty cycle of the laser pump, the absorption variation is smaller in this second configuration, with a maximum ratio at 1.27 for the UP. At frequencies higher than the UP the ratio drops sharply.

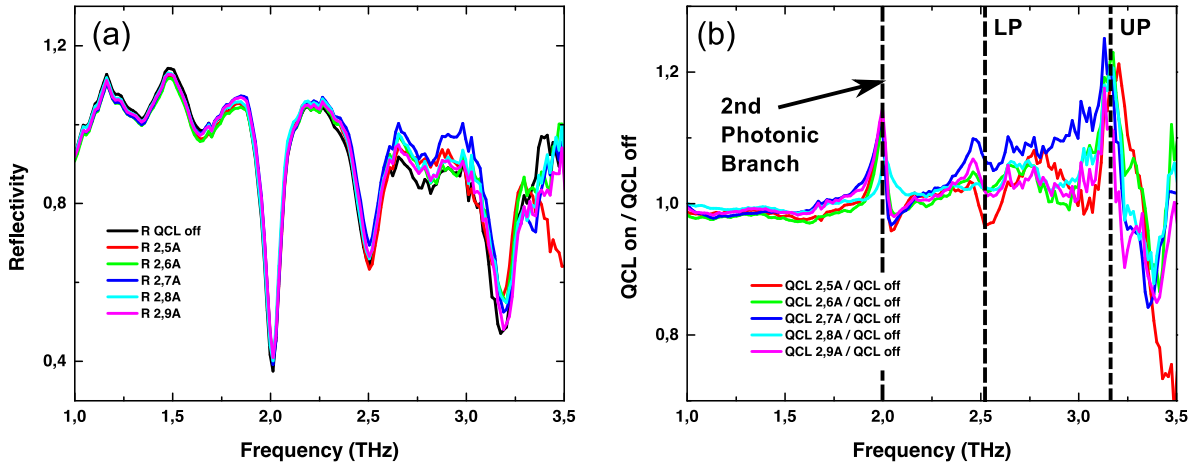


Figure 3.14: (a) TDS measurement in frequency domain for different output power of the laser L1498MC. (b) The ratio of the spectra with and without laser pumping.

This first observations in TDS shows that the system and particularly the polaritonic absorptions are sensitive to the optical pump and that we are far from bleaching the transition. However, these preliminary results are not conclusive, and further characterizations need to be performed in the future.

3.5 Conclusion and Perspectives

In this chapter, we introduced the TDS system and analyzed the THz polaritons in reflectivity, and pump-probe at 45° , the incidence angle of both pump and probe. One polaritonic cavity has been studied in reflectivity with and without pumping by a THz-QCL with emission frequency resonant with the UP state. In reflectivity the photonic, as well as the polaritonic branches, are visible and no bleaching of the polaritons is observed. The pumping has a different effect on each branch. No interpretation can be drawn so far, and further observations need to be performed.

The main perspective is to modify the TDS set-up to probe the sample at a different angle than the pump. Particularly, an interesting configuration is to probe at 0° . We expect to have a polariton accumulation at $k_{\parallel} = 0$ and consequently a maximum of spectral variation at this angle. The laser could impinge on the cavity under various angles from 45° (as conceptually presented in Figure 3.15) to 12° .

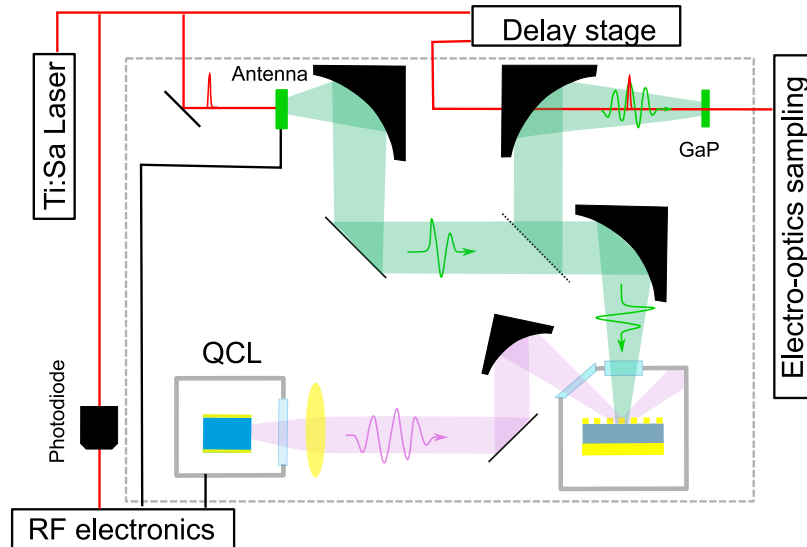


Figure 3.15: Schematics of a possible TDS configuration to pump with a THz-QCL at 45° and probe at 0° .

As shown in Figure 3.15 the incident angle of the laser on the cavity can be tuned, offering new degrees of freedom to explore polariton-polariton scattering phenomena.

Part II

Development of Short Pulse THz Lasers

"I asked questions; I wanted to know why.",
Katherine Johnson

THz Quantum Cascade Laser Integration in Time-Domain Spectroscopy

In parallel to the activity on polaritons, I have been involved via the H2020 project *Ultra-QCL* in the development of new techniques to implement THz Quantum Cascade Lasers (THz-QCL) that can operate in the mode-locking regime. The final goal of the project is to increase the output peak power and shorten the pulses emitted by these lasers.

To reach this goal, one approach is to broaden the spectral gain of the QC laser while keeping a good dispersion compensation. In this perspective, my main involvement was to develop an ICP etching recipe to fabricate the Gires-Tournois Interferometers (GTI) that have a challenging high aspect ratio geometry.

In this chapter, we first briefly describe mode-locked lasers to motivate the study of short pulse lasers. Then we present the development I performed to obtain selective, anisotropic and reliable ICP etching recipes. After this development, I fabricated THz-QC lasers equipped with monolithic GTIs, and the characterizations were completed at LPA/ENS.

4.1 Detecting the QCL Emission with EO Detection: Seeding

Intuitively the fs laser and the QCL could be electrically synchronized by using a fast photodiode to trigger the THz-QCL. The delay due to the electrical circuit would be constant and could be compensated. However, when the QCL is electrically pumped its phase is random as the laser action is initiated by spontaneous emission. Consequently, the phase of the QCL changes at each repetition and cannot be synchronized with the fs laser. On the electro-optical detection, the electric field would then be averaged to zero.

To overcome this problem, the solution consists of seeding the QCL with the phase-resolved THz pulse generated by the photoconductive antenna that is excited by the fs laser [77]. In this way, the phase of the THz-QCL emission can be controlled and synchronized with the fs laser via the antenna.

In more detail, the QCL is held below threshold by a square electrical signal with a frequency of 20 kHz and a duty cycle of 10%. When the seed pulse is coupled into the QCL cavity, the laser is brought above threshold by a short electrical pulse of 6 ns , triggered by the fs laser.

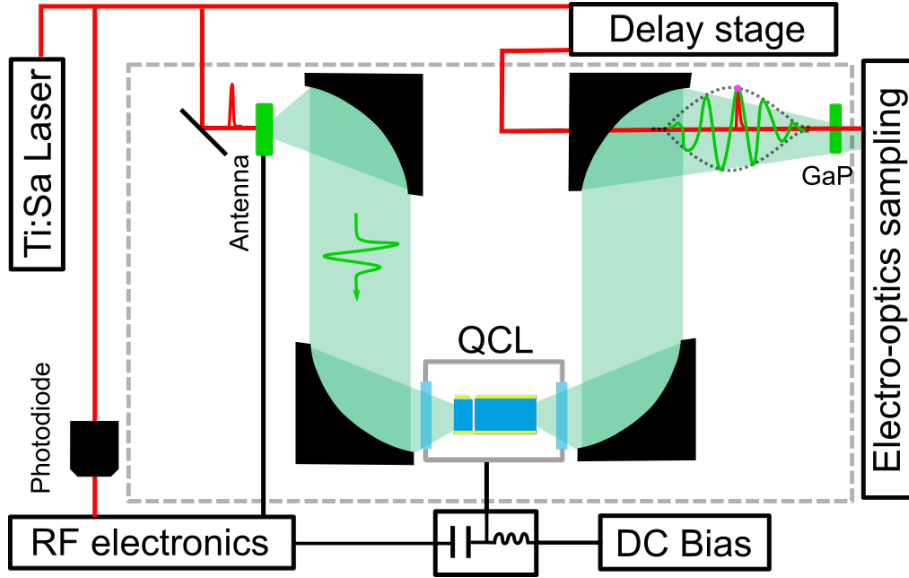


Figure 4.1: Schematics of a THz QCL seeded by a THz pulse generated by the antenna.

This technique works for THz-QC lasers, and have a temporal resolution of 10 fs to access the ultrafast dynamics of QCLs.

The seeding is, therefore, a valuable tool, and it is then employed in all the following TDS measurements using QCLs.

4.2 Optimization of the Laser Gain and Cavity

In this section, we briefly describe the THz-QCL cavity, the mode locking and the implementation of the GTI cavity based on the first generation of GTI-QCLs that had been implemented before my arrival. These concepts are still valid for the second generation of GTI-QCLs that I developed.

4.2.1 Fabry-Pérot Cavity in a Metal-Metal Waveguide

The metal-metal waveguide is commonly used for THz-QCLs because the light is highly confined in the cavity, and the losses in the metal are not critical. In the perspective of mode-locking, this cavity also facilitates the GHz modulation.

The standard M-I-M cavity with two facets is a Fabry-Pérot resonator. Two mirrors typically compose a Fabry-Pérot cavity. Each mirror has its own reflectivity (r_1 and r_2) and transmission coefficient (t_1 and t_2). In Figure 4.3, the active region is represented in blue and the mirrors in grey. First, we consider that the active region is not dispersive (the index n_0 is the same for all the wavelengths). The different electric fields: incident E_i , internal E_c and transmitted E_t can be related together using the reflection and transmission coefficients.

After one round trip, the internal field must be equal to itself:

$$E_c = r_1 r_2 E_c e^{-i2kL} + t_1 E_i. \quad (4.1)$$

From this equation, we can write the internal and transmitted fields as a function of the incident electric field:

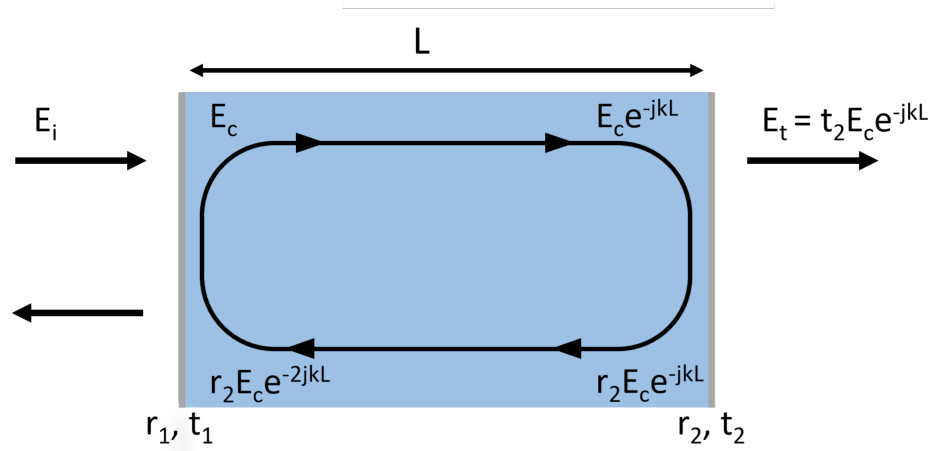


Figure 4.2: Schematic of a Fabry-Pérot resonator with the different electric fields propagating through the structure

$$\begin{cases} E_c = \frac{t_1 E_i}{1 - r_1 r_2 e^{-j2kL}} \\ E_t = t_2 E_c e^{-jkL} = \frac{t_2 t_1 E_i e^{-jkL}}{1 - r_1 r_2 e^{-j2kL}}. \end{cases} \quad (4.2)$$

In the case of symmetric mirrors, we can write the transmission coefficient as the square root of the transmission power coefficient (T) $|t_1| = |t_2| = \sqrt{T}$ and the reflection coefficient of the mirrors as a function of the reflection power coefficient (R) $r_1 = r_2 = \sqrt{R} e^{2j\phi_R}$. ϕ_R is the phase shift induced by the mirror.

The transmitted intensity can then be written as an Airy Function:

$$\frac{I_t}{I_i} = \left| \frac{E_t}{E_i} \right|^2 = \frac{T^2}{1 - R^2} \frac{1}{1 + \mathcal{F} \sin^2(\phi/2)}, \quad \phi = -2kL + 2\phi_R, \quad (4.3)$$

$\mathcal{F} = \frac{4R}{(1-R)^2}$ is the *finesse* of the cavity and it increases with the mirror reflectivity. Figure 4.3 shows that the maxima of transmission in a Fabry-Pérot occur when $\phi = 2m\pi = |2kL|$ with m an integer ($\phi_R = \pi$ for a reflection from low to high index). Therefore there is a discrete number of modes that can be transmitted inside a Fabry-Pérot cavity defined by the length of the cavity:

$$\omega_m = \frac{\pi c_0}{n_0 L} m, \quad m \in \mathbb{N}. \quad (4.4)$$

It is on these modes that the light will be amplified. The free spectral range (FSR) of a free running laser is then constant

$$\Delta\omega = \omega_{m+1} - \omega_m = \frac{\pi c_0}{n_0 L}. \quad (4.5)$$

In Figure 4.3 (a) the plain lines present the equally spaced modes inside a Fabry-Pérot cavity with uniform amplitude distribution. In Figure 4.3 (b) the amplitude is shaped by a Gaussian function centered around ω_0 representing schematically the gain of a THz-QCL. As a first approach, we consider a laser in which each mode (m) has its own phase (ϕ_m). The total electric field amplitude of all the modes around the central mode in the cavity can be written [78]:

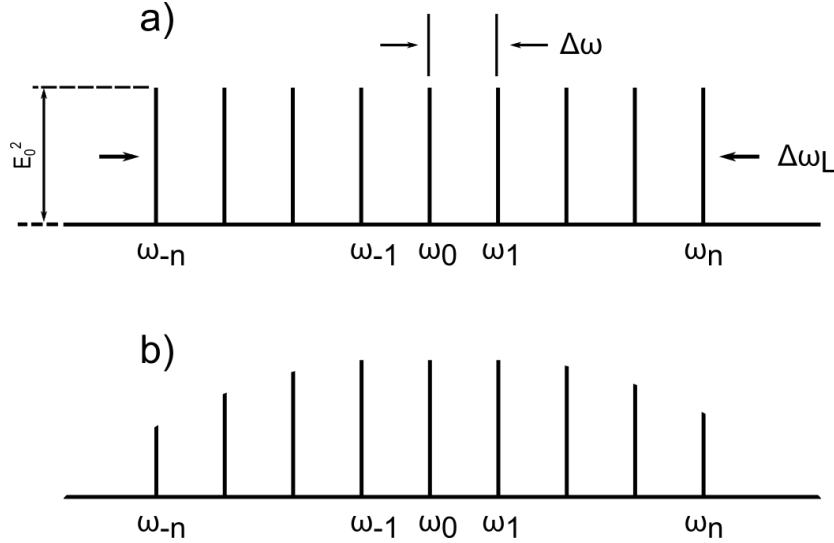


Figure 4.3: Schematic mode amplitude (represented by vertical lines) versus frequency for a mode-locked laser. (a) Uniform amplitude distribution, and (b) Gaussian amplitude distribution.

$$E(t) = \sum_{m=-n}^n E_l(t) = \sum_{l=-n}^n E_0 \exp(j((\omega_0 + m * \Delta\omega)t + \phi_m)) = \exp(j\omega_0 t) A(t), \quad (4.6)$$

where

$$A(t) = \sum_{m=-n}^n E_0 \exp(j((m\Delta\omega)t + \phi_m)). \quad (4.7)$$

If we can lock the phase of all these modes in order to have $\phi_{-n} = \phi_{-n+1} = \dots = \phi_n = \phi$, the time reference can be changed to a new time reference t' such that $\Delta\omega t' = \Delta\omega t + \phi$. In terms of the new variable t' , the Equation 4.7 can be transformed into:

$$A(t') = \sum_{m=-n}^n E_0 \exp(jm\Delta\omega t'). \quad (4.8)$$

In this last equation, we recognize a geometric progression with a ratio $\exp(j\Delta\omega t')$ between the consecutive terms. This progression is then summed to obtain [78]

$$A(t) = E_0 \frac{\sin((2n+1)\Delta\omega t')}{\sin(\Delta\omega t')}. \quad (4.9)$$

Figure 4.4 shows the quantity $A^2(t')/E_0^2$, $A(t')$ being proportional to the beam intensity, versus time t' for $2n+1=7$ oscillating modes. The phase-locking yields constructive interference, producing a train of evenly spaced light pulses. The pulse maxima occur when the denominator of Equation 4.9 vanishes. The first maximum is at $t'=0$. The value of the numerator (Equation 4.9) also vanishes at $t'=0$. Making the approximation that $\sin(\alpha) \approx \alpha$ for small values of α , the value of the squared amplitude at $t'=0$ is $A^2(t') = (2n+1)^2 E_0^2$. The

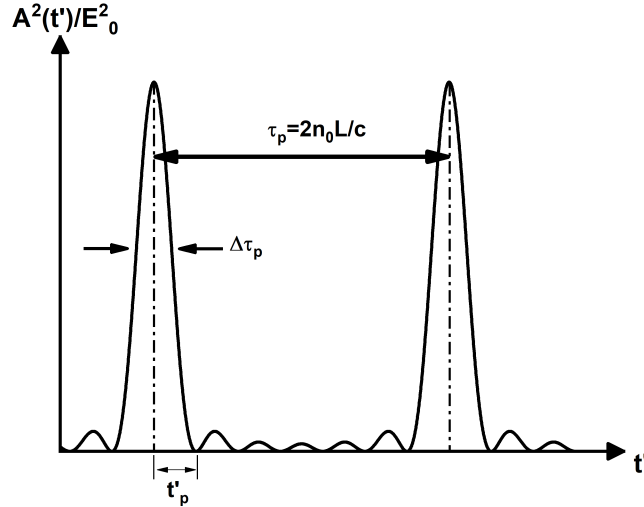


Figure 4.4: Time behavior of the square amplitude of the electric field for the case of seven laser modes with equal, locked phases and equal amplitudes, E_0 .

next pulse occurs when the denominator in Equation 4.9 vanishes again, and this happens at time t' such as $\Delta\omega t'/2 = \pi$. Two successive pulses are therefore separated by a time

$$\tau_p = \frac{2\pi}{\Delta\omega} = 2n_0L/c_0. \quad (4.10)$$

The first zero of Equation 4.9 occurs instead when the numerator vanishes again. This happens at time t'_p such that $(2n+1)\Delta\omega t'_p/2 = \pi$. Since the width $\Delta\tau_p$ (FWHM) of $A^2(t')$, is approximately equal to t'_p , we have

$$\Delta\tau_p \approx \frac{2\pi}{(2n+1)\Delta\omega} = \frac{2\pi}{\Delta\omega_L}, \quad (4.11)$$

where $\Delta\omega_L$ is the total laser bandwidth (Figure 4.3, a).

This example is idealistic and in reality the gain of the laser is bell shaped (Figure 4.3, (b)), but the results on the shape of the pulse are comparable to the one with the uniform amplitude distribution (see Figure 4.5, (c)). In general, when the mode-locking condition holds, the field amplitude is given by the Fourier transform of the magnitude of the spectral amplitude. In such a case, the pulsewidth $\Delta\tau_p$ is related to the width of the laser spectrum $\Delta\omega_L$ by the relation $\Delta\tau_p = 2\pi\beta/\Delta\omega_L$, where β is a numerical factor (of the order of the unity) that depends on the particular shape of the spectral intensity distribution.

From the analytic developments, it emerges that the pulse width $\Delta\tau_p$ could be reduced by increasing the optical gain width (broadband active region).

In the next section, we describe the development of broadband QCL active regions coupled with a monolithic Gires-Tournois cavity that compensates the dispersion of the active region.

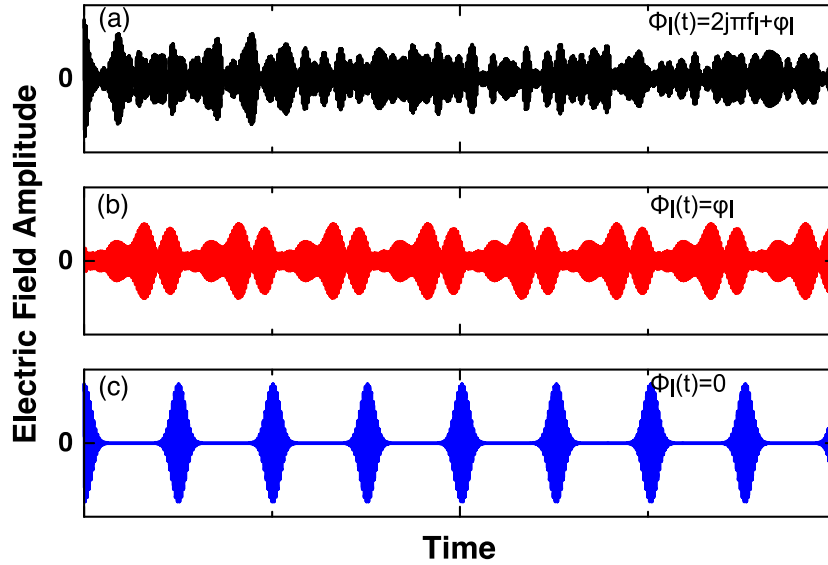


Figure 4.5: Simulation of the real part of the electric field amplitude versus time for 100 lasing modes modulated by a Gaussian gain. (a) *free running* laser, (b) hybrid modelocking that compensate completely the active region dispersion and (c) hybrid mode-locking with seeding.

4.2.2 Dispersion Compensation: Gires-Tournois Interferometer (GTI)

The quantity $GDD = \left(\frac{d^2\phi}{d\omega^2} \right)_{\omega_1}$ is referred to as the *Group Delay Dispersion* at the frequency ω_1 . Its magnitude gives the pulse broadening per unit of bandwidth of the pulse. An associated quantity defined as *Group Velocity Dispersion* $GVD = \left(\frac{d(1/v_g)}{d\omega} \right)_{\omega_1} = GDD/L$ with v_g the group velocity and L the length of the cavity.

The goal of the following development is to reduce the GDD of a QCL active region embedded inside a M-I-M waveguide to generate short THz pulses.

The GDD (GVD) depends on three main components: the semiconductor material, the waveguide, and the dispersion associated with the intersubband optical gain. In 2016, the GVD of a broadband active region (composed of three different QC structures centered at 2.3, 2.6 and 2.9 THz) M-I-M THz-QCL has been measured with TDS in Ref. [79]. The experimental results are presented in Figure 4.6, (a). The experimental GVD was compared with GVD models for the active region material, the intersubband gain, and the waveguide. This study conclude was that the main contribution to the GVD is the intersubband gain ($GVD \approx 2.5 \times 10^5 \text{ fs}^2/\text{mm}$). Thus the GVD of this M-I-M THz-QCL can be approximately modeled by the combination of optically active intersubband transitions, each one considered as a Drude-Lorentz dispersive medium. At that time, the challenge for the THz-QCL community was then to find a way to compensate the dispersion of the biased active region.

The same year, judicious processing of a Mid-IR QCL-comb waveguide succeeded to compensate the dispersion of the biased active region (Figure 4.6, (b)). In particular, the Gires-Tournois interferometer, obtained with a high reflection coating (300nm Al_2O_3 and 150 nm of gold) of the facet, appeared to have a dispersion profile that can compensate the dispersion of the biased active region [80].

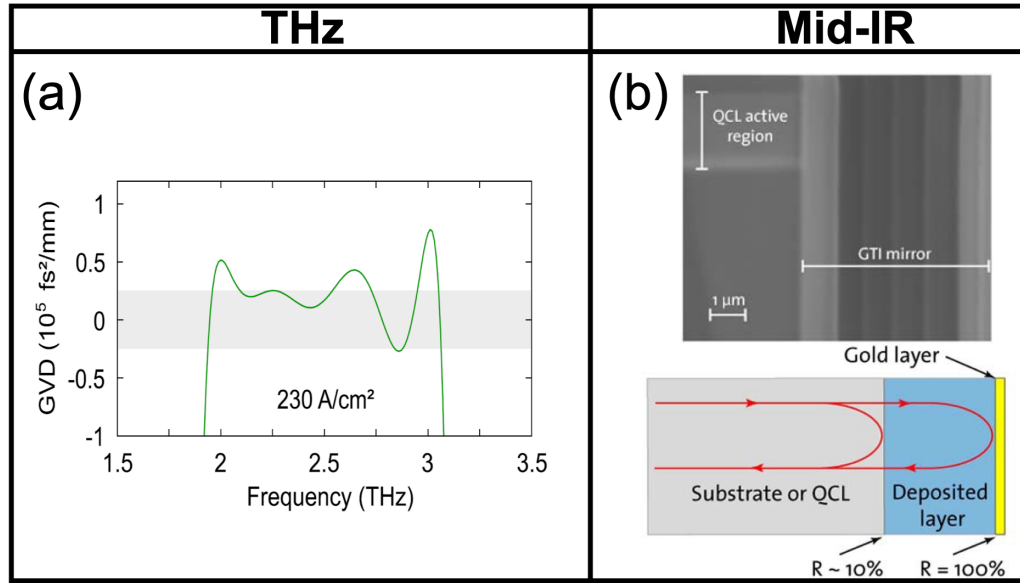


Figure 4.6: (a) Experimentally determined group velocity dispersion (GVD) of a THz-QCL active region operating at a currents of 230 A/cm^2 . The 2.48mm long and 75 mm wide laser section was driven in quasi-DC mode (10 kHz, 10 ms pulse) and lossy side-absorbers at the edges of the metal-metal waveguide were used to eliminate all higher order lateral modes [79]. (b) Schematics and SEM picture of a cross section parallel to the laser ridge of the QCL-comb and the GTI mirror composed by 300 nm Al_2O_3 and 150 nm of gold [80].

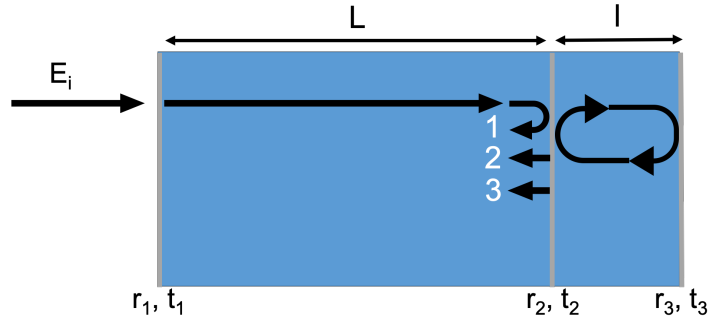


Figure 4.7: Schematics of a GTI coupled with a QCL to compensate the dispersion with the goal of obtaining ultrashort THz pulses.

A Gires-Tournois cavity is composed of two mirrors, as presented in Figure 4.7. The front mirror r_2 is partially reflective and the back mirror r_3 is highly reflective. The Group-Delay Dispersion of a Gires-Tournois interferometer can be written as follows [26]:

$$GDD_{GTI} = -\frac{2\tau^2(1-r_2)\sqrt{r_2}\sin(\omega\tau)}{(1+r_2-2\sqrt{r_2}\cos(\omega\tau))^2}, \quad (4.12)$$

where $\tau = 2nl/c$ denotes the round trip time of the GTI where n is the refractive index, c the speed of light in vacuum and l the length of the GTI. Equation (4.12) shows that once the cavity material (n) and geometry (r_2 and r_3) are settled the GDD_{GTI} can be tuned with only the length (l) of the GTI cavity.

In the case of a M-I-M THz-QCL, a monolithic approach has been proposed to compensate the active region dispersion with a GTI cavity in Ref.[26] (Figure 4.8). The front mirror was obtained by opening a thin slit ($1.5 \mu\text{m}$ wide) parallel to the facet of the M-I-M THz-QCL, and at the distance $l \sim 30 \mu\text{m}$ from it. The mirrors reflectivity in this configuration can be calculated with *Meep* software (by J.Jukam at the University of Bochum). The simulations show that the front mirror reflectivity is $r_2 = 0.61$ and it is different from the back mirror reflectivity $r_3 = 0.83$.

The GDD of the biased active region was obtained by applying the Kramers-Kronig relation on the shape of the active region gain (LO-phonon depopulation scheme) with central frequency at 3.1 THz . The so-called Gain GDD - presented in green in Figure 4.9 (a)- is positive between 2.3 THz and 2.45 THz and negative between 2.45 THz and 2.7 THz . The Gain GDD has dispersion peaks of about $\pm 0.5 \text{ ps}^2$ that is much larger than the GaAs GDD that is an almost null ($\sim 0.18 \text{ ps}^2$) and flat (grey line). Consequently, the modes strongly dephase with each other while propagating in the cavity. This dephasing leads to enlarging the THz pulses.

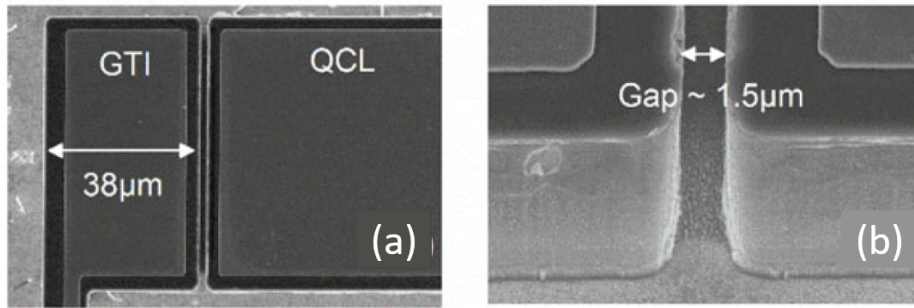


Figure 4.8: SEM images of the first generation of THz-QCLs with monolithic GTI: (a) top view of the GTI cavity, (b) side view of the GTI slit [26].

To overcome this difficulty, it is possible to simulate the $GDD_{GTI}(l)$ for different lengths of the GTI cavity (with only GaAs inside the waveguide) and compare it with the GDD of the active region. Figure 4.9 (b) shows the adaptation of the GTI to the laser, with the GDD presented in green [26]. For a GTI length of $38 \mu\text{m}$ the GDD_{GTI} stays negative but increases strongly between 2.3 THz and 2.7 THz . On the other hand for the length $58 \mu\text{m}$ the GDD_{GTI} changes sign at 2.5 THz . The Gires-Tournois cavity, therefore, appears to have a dispersion that compensates the gain GDD. After implementing the GTI on the active region, the total GDD (Figure 4.9, (b), red and blue curves) is sharply reduced and flattened particularly in the range from 2.4 THz to 2.65 THz .

Finally, the monolithic implementation of the GTI combined with active mode-locking can significantly reduce the THz pulse length compared to a standard Fabry-Pérot cavity laser. The first generation of hybrid mode-locked lasers led to the compression of the pulse down to 4 ps [26]. In this chapter, I will present the results of the second generation devices that I implemented using broader gain.

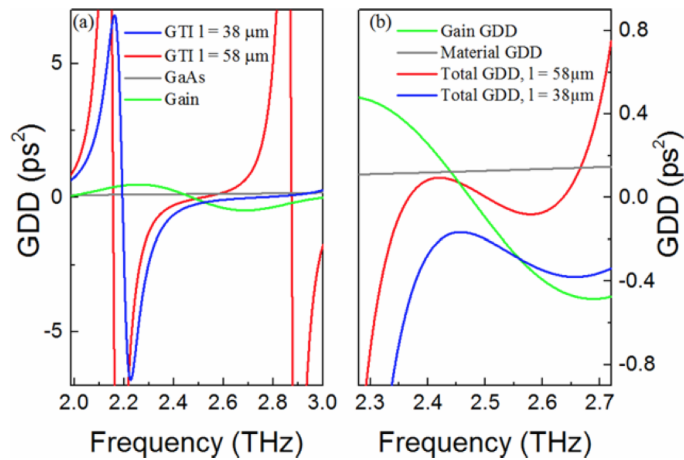


Figure 4.9: Group Delay Dispersion simulation of the gain material and GTI biased on a QC-heterostructure. (a) The individual GDD contributions of the GTI, bulk GaAs (grey), and QCL gain (green curve). The GTI GDD is shown for a $58 \mu\text{m}$ (red) and $38 \mu\text{m}$ (blue) cavity length. (b) The total GDD-GTI, material and gain for a $58 \mu\text{m}$ (red) and $38 \mu\text{m}$ (blue) GTIs. The contribution of the gain and material GDD is also shown for comparison (green and grey curves) [26]. Note the different y-axis scale in panels (a) and (b).

4.3 ICP Etching: Recipe Development

The critical step in the process of the monolithic GTI cavities is the etching of the QCL active region. The target geometry is presented in Figure 4.10, the thickness (t) of the active region is between $15 \mu\text{m}$ and $20 \mu\text{m}$ and the opening of the Gires-Tournois slits (s) should not exceed $s = 2 - 3 \mu\text{m}$. Such a geometry with an aspect ratio $t/s \approx 5 - 10$, at the limits of the photo-resist specifications. Only a dry etch can fulfill such an-isotropic etching.

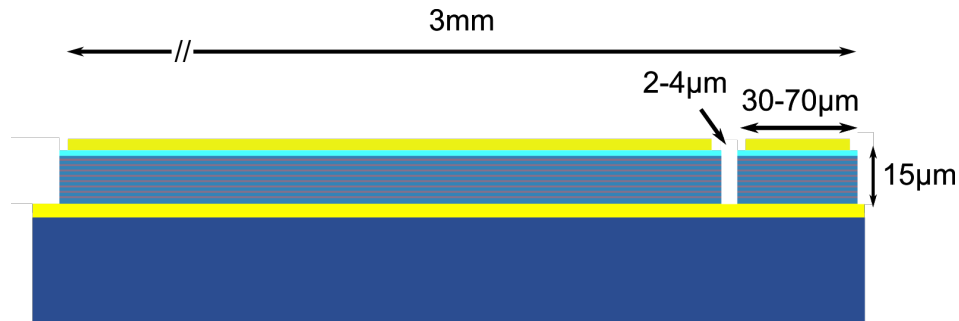


Figure 4.10: Cross-section of the final GTI cavity. The laser cavity is 3 mm long, $57 \mu\text{m}$ wide and $15 \mu\text{m}$ thick, the GTI is $30\text{-}70 \mu\text{m}$ long and the slit between the laser cavity and the GTI is only $2\text{-}3 \mu\text{m}$ wide.

When I started my Ph.D., the Inductively Coupled Plasma (ICP) etching recipe had drifted from the last etching of the GTI cavity (First generation of GTI [26]), and an important micromasking was typically observed (Figure 4.11). Despite relatively vertical and smooth sidewalls, the micromasking could strongly deteriorate the laser performances for the various cavity geometries we were studying in our group (3^{rd} order Distributed-Feed-Back lasers [81])

and micro-lasers [82]). For GTI cavities, the presence of micro-pillars into the slit strongly affects the dispersion of the cavity.

My major contribution to this project was to develop a new ICP recipe to solve this difficulty. During this development, we considered not only GTI cavities, but more generally the etching of GaAs/AlGaAs heterostructures to obtain a versatile and reliable etching recipe for the different projects of the group.

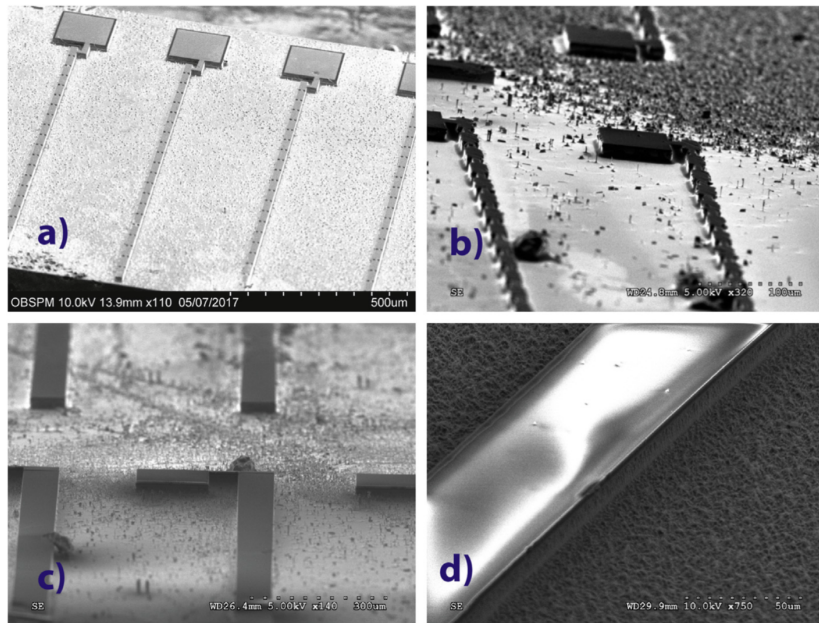


Figure 4.11: SEM images of features etched into a GaAs wafer with micromasking effects apparent on the surface. The magnification of the images are: (a) $\times 110$, (b) $\times 320$, (c) $\times 140$ and (d) $\times 750$

The aforementioned applications demand anisotropic etch profiles, as well as smooth sidewalls and bottom surfaces and high etch rates and selectivity. Conventional reactive ion etching (RIE) is often used for the selective etch process of III-V compounds [83]. However, RIE processes rely on only one RF chuck (called platen or bias power), making it difficult to achieve good etch uniformity on large wafers. Moreover, elevated RF platen bias is typically necessary to achieve vertical sidewalls. This also leads to high etch rates, but the physical impact of the ions on the III-V compounds and the mask is increased too. The former one can cause damage to the device [84, 85, 86]. The latter one reduces the mask selectivity. One solution is to use an ICP-Deep Reactive Ion Etching (ICP-DRIE) reactor where two power inputs are employed for the plasma. One is the platen power, similar to a RIE reactor. The other is the ICP source power. The latter one plays the crucial role of ionizing and generating the plasma. This technology provides almost independent control of ion density and energy, respectively. With optimized ICP conditions, typically a low RF chuck power and a high ICP source power, minimum damage or damage-free etch with high etch rate can be obtained with III-V materials [87, 88].

Several approaches to increase the etch selectivity have been developed. The use of gases promoting the formation of polymer films on the surfaces was shown to favor the selectivity. In this section, we show that a $\text{BCl}_3/\text{Cl}_2/\text{N}_2/\text{Ar}$ plasma chemistry can produce highly

anisotropic etching of GaAs/AlGaAs heterostructures in combination with photoresist-based masks. Each ICP-DRIE etching parameter affects the rate, anisotropy, surface roughness, and sidewall morphology. All of them must be carefully controlled for reliable device manufacturing. I paid special attention to the problem of plasma-induced structural damages such as the micromasking and the sidewall roughness. My objective was to optimize III-V compounds etching using a ICP-DRIE etcher for my application. In the end, I have identified plasma conditions that provide not only adequate surface chemistry but vertical and smooth sidewalls as well.

4.3.1 Experiment

The experiments were performed in a STS (Surface Technology Systems) reactor, equipped with a 900 W, 13.56 MHz RF coil generator. The gases employed in this study were BCl₃, Cl₂, Ar, N₂ and O₂. During all the experiments, the temperature of the electrode was fixed at 25°C. A 5-min-long oxygen clean procedure was performed between each run to remove any polymer from the reactor sidewalls, minimize contamination, and preserve process repeatability.

Recipe	Pa (mTorr)	Gas Flow rate (sccm)			Results	
		BCl ₃ /Cl ₂	Ar	N ₂	Etch rate ($\mu\text{m}/\text{min}$)	Selectivity
1	10	4	0	0	3.64	6.67
2	10	2	0	0	3.6	6.5
3	10	2.5	0	0	2.38	4.3
4	10	4	5	0	2.38	4.43
9	10	6	5	2	3.84	5.95
10	10	6	5	2.5	4	7.22
11	10	6	5	3	4	6.2
16	5	20	5	3	1.14	2.5
17	10	20	5	3	1.8	4
18	20	20	5	3	2.36	5.2
20	30	20	5	3	3.7	12.33
21	30	20	5	5	5.56	16
24	20	20	10	3	2.8	8.9
25	20	20	20	3	3	8
26	20	20	30	3	2.5	7.28
27	20	20	50	3	2.23	6.42

Table 4.1: Typical results from the different etch processes I studied, with coil power : platen power ratio fixed to 8:1. The green lines correspond to recipes that reduce the micromasking (Section 4.3.2), the coral lines correspond to recipes with a etch rate $>3.6 \mu\text{m}/\text{min}$ (Section 4.3.3) and the blue (dark blue and cyan) lines correspond to recipes that passivate the sidewalls keeping an-isotropic etching over long etching times (Section 4.3.4). In dark blue (R17) the selected recipe for the GTI-processing presented in this thesis.

The samples were loaded into the reactor by mounting them on an alumina carrier wafer with silicone grease to ensure good thermal contact. As part of the optimization of the etching parameters, a mask design with different kinds of test structures (trenches and cavities)

for measuring the process outcome was employed. In this investigation, a surface inspection of the etch result was the best way to check the etch characteristics. All test samples were $1\text{ cm} \times 1\text{ cm}$ pieces of bulk GaAs or $\text{GaAs}/\text{Al}_{0.15}\text{Ga}_{0.85}\text{As}$ THz quantum cascade lasers [89]. We studied several different etch processes, and their general characteristics were compared. Typical parameters from these processes are summarized in Table 4.1, with an etching time set at 5 min for all the samples. Photoresist (AZ9260, $6\text{ }\mu\text{m}$ -thick), was patterned with test geometries on GaAs wafers, or on GaAs / $\text{Al}_{0.15}\text{Ga}_{0.85}\text{As}$ THz quantum cascade heterostructures [89], and used as the mask material. The mask erosion was estimated by measuring its thickness pre- and post-etching. The mask selectivity was estimated by calculating the ratio of the semiconductor etch rate to the photoresist etch rate. The samples were etched and studied using an optical microscope and a Scanning Electron Microscope (SEM). The latter one provides error on the measurement due to the pixel size of the image. The error bars on the depth and angle measurement, or on the etch rate and selectivity are plotted in all the figures.

4.3.2 Reduction of Micromasking: Chemical Etching with Cl_2

Micro-masking occurs when material liberated during the etching is redeposited elsewhere on the sample and creates an undesirable additional etch (Figure 4.12). It is most frequently encountered when a metal mask is used because of the physical sputtering of small metal particles, that are not volatile (as seen in Figure 4.11, (a)). A photoresist mask may also induce polymer deposition on the etched sidewalls due to a reaction with the plasma and result in roughly etched surfaces due to micro-masking (as shown in Figure 4.11 (b), (c) and (d)). As a consequence, the micromasking phenomena can significantly reduce the etch rate. Figure 4.13 shows SEM images of the samples after an etch with a Cl_2 -based chemistry. The samples present very smooth bottom surfaces.

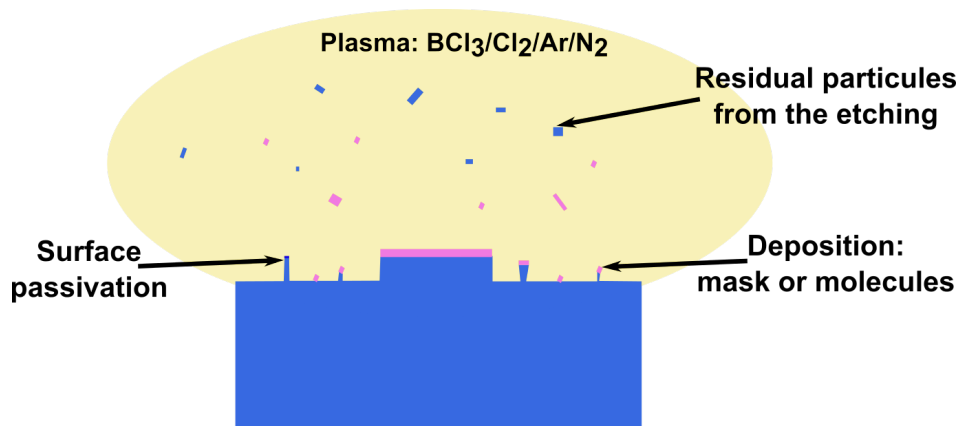


Figure 4.12: Main phenomena causing micro-masking: deposition of resist mask or Boron-containing molecules appearing during the etching and passivation of the sample surface observed while increasing the N_2 flow.

However, an undercut is also observed and the sidewalls are rough. As predicted for Cl_2 -rich environments, GaAs and AlGaAs were chemically etched causing severe undercut as observed in Figure 4.13, when using the recipes R1-R3. In BCl_3 -rich environments instead,

when using the recipe R4, GaAs and AlGaAs are in general slightly passivated and the undercut effect is reduced [90, 91, 92]. Note: BCl_3 may cause a problem because Boron-containing molecules can be deposited onto the wafer surface. By adding Ar in the BCl_3/Cl_2 mixture, it is possible to sputter these non-volatile products away. With the Ar in the BCl_3/Cl_2 mixture, we obtained less under etching (see Table 4.1: R4, R24, R25, R26, and R27). The effects of the gas mixture on the etch characteristics of GaAs show that by increasing the Cl_2 flow rate, the etched surface becomes very smooth, but the etch profile is isotropic and the sidewalls are very rough. In the next section, the effect of plasma process parameters on the etch rate and the photoresist mask is studied.

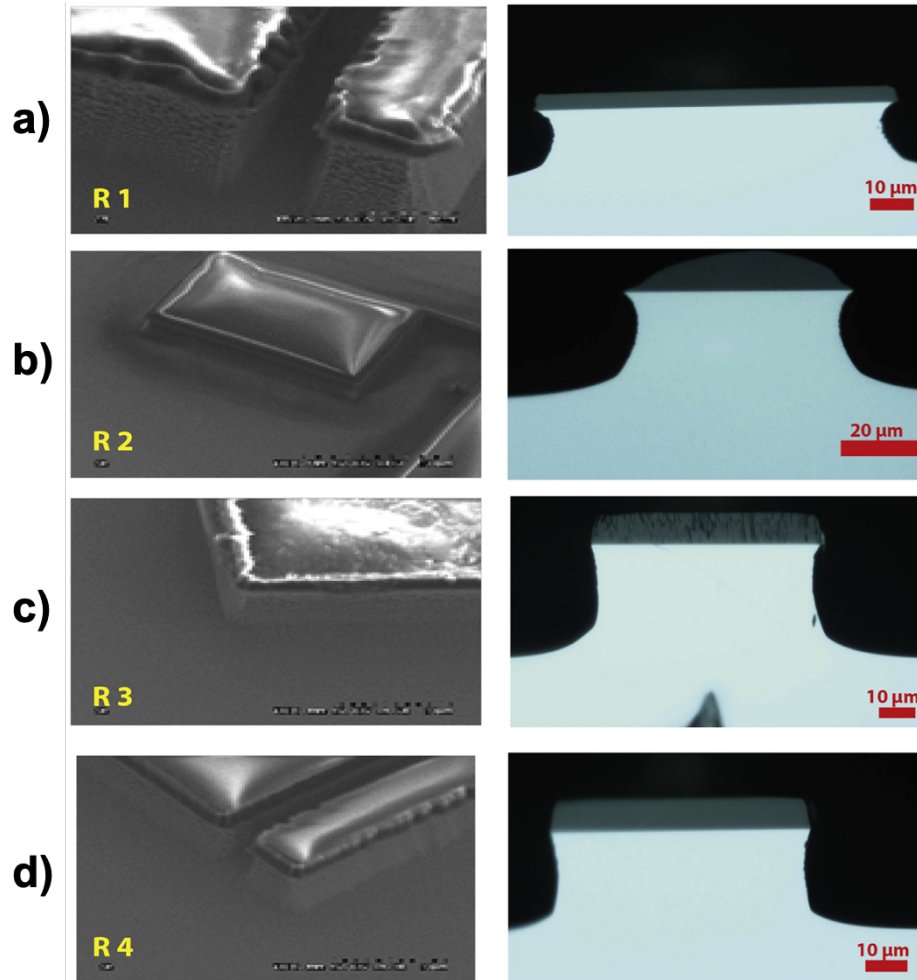


Figure 4.13: SEM micrographs and corresponding optical photographs of features etched into GaAs with a BCl_3/Cl_2 chemistry. (b-d) exhibit a smooth floor, but (a) exhibit rough sidewalls. The recipes used are R_1 for panel (a), R_2 for panel (b), R_3 for panel (c) and R_4 for panel (d)

4.3.3 Obtaining a High Etch Rate: Ar & N_2

To etch thick QCL active regions ($15 - 20\mu\text{m}$) we need to develop a recipe with high selectivity to preserve the most the photoresist. For deep etching, high etch rates are generally preferred and present good selectivity. Our objective is to develop a recipe with an increased

etch rate by facilitating the availability of chloride ions as a result of the reaction between BCl_3 and Cl_2 . The addition of Ar or N_2 to the BCl_3/Cl_2 mixture modifies the chlorine ions density, thereby affecting the etch rates too. In essence, adding Ar or N_2 can result in a different degree of dissociation of Cl_2 . As shown in Table 4.2, the dissociation enthalpies of the used gases are different: a balance in terms of injected gas flow ratio, and the power used is required.

Parameters	BCl_3	Cl_2	N_2	Ar
Dissociation enthalpy (kcal mol^{-1})	110	58	226	363

Table 4.2: Dissociation enthalpy of BCl_3 , Cl_2 , N_2 and Ar.

We investigated the introduction of N_2 to the $\text{BCl}_3/\text{Cl}_2/\text{Ar}$ mixture. It is important to note that adding only a very small amount of N_2 (2 or 5 *sccm*) already resulted in a sizeable increase of the GaAs etching rate, as shown in Table 4.1. From these results, it is also observed that the etch rate increases rapidly with increasing Cl_2 flow rate in the ratio BCl_3/Cl_2 due to the increase in the supply of reactive Cl^+ species at the sample surface. On the other hand, at a fixed Cl_2 flow, the etch rate increases with the BCl_3 flow is not as dramatic. This stems from the higher dissociation energy of BCl_3 molecules that leads to a smaller number of available Cl radicals for the reaction.

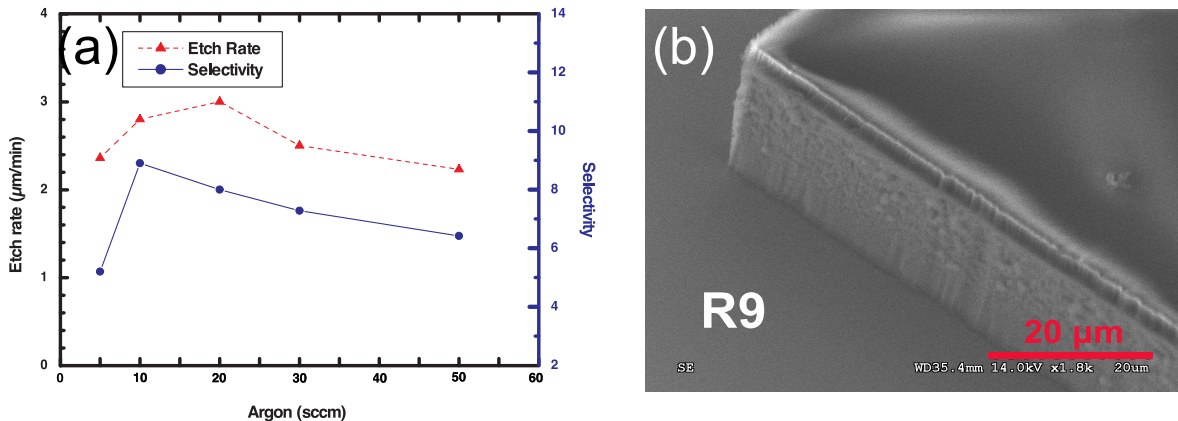


Figure 4.14: (a) GaAs etch rate and selectivity variation with argon. The gas mixture is BCl_3/Cl_2 : 20 and N_2 :3 *sccm* at 20 *mTorr*, (see Table 4.1). (b) SEM picture of the sidewall roughness after etching with recipe R9.

The optimum conditions for obtaining a higher etch rate were obtained at a high concentration of N_2 gas in the $\text{BCl}_3/\text{Cl}_2/\text{Ar}$ mixture at 10 *mTorr* (see Table 4.1 : R9, R10 and R11) and at even higher operating pressures of 20-30 *mTorr* (see Table 4.1: R20 and R21).

To be able to control the anisotropy of the process, the Ar concentration was adjusted by varying the relative flow rates. Despite the addition of Ar in the gas mixture BCl_3/Cl_2 : 20, (see Table 4.1 : R4), some under etching with rough sidewalls was always observed and the slope was still found to be around 90° . On the other hand, by adding Ar in the gas mixture BCl_3/Cl_2 : 20 with N_2 : 3 *sccm* (see Table 4.1), increasing the Ar gas flow from 5 to 50 *sccm* leads to an increase then a decrease of the etch rates as shown in Figure 4.14, (a). This trend

in etch rate is attributed to a change from a chemically dominated reaction to a physically dominated one. This is further confirmed by the decreased selectivity with an increase in the Ar flow, due to the increased physical character of the etching.

In these first two subsections, we estimated the impact of each chemical specie (BCl_3 , Cl_2 , Ar and N_2) on the etching (etch rate, selectivity, and anisotropy). To etch thick GaAs/AlGaAs active regions the optimal chemistry is: a ratio $\text{BCl}_3/\text{Cl}_2 = 20$, a flow rate of N_2 at 3 *sccm* and a flow rate of Ar at 5 *sccm*. However, some roughnesses and ripples are still observed on the sidewalls (Figure 4.14, (b)) of the etched samples. These defects, due to the sidewall passivation rupture, are few hundreds nanometers deep. They could be neglected in a standard M-I-M process, but in the case of GTI process, these defects could hamper the opening of GTI-slit ($2 - 3\mu\text{m}$). To overcome this last issue, the last parameter to tune is the pressure.

4.3.4 Obtaining Vertical and Smooth Sidewalls: Resist Profile and Pressure Control

The final steps of this dry etching recipe development are specific to the high aspect ratio of monolithic-GTI cavities. It consists of the optimization of the photo-resist profile (vertical edges and resolution) and the adjustment of the pressure to find a compromise between high etch rate and sidewalls passivation.

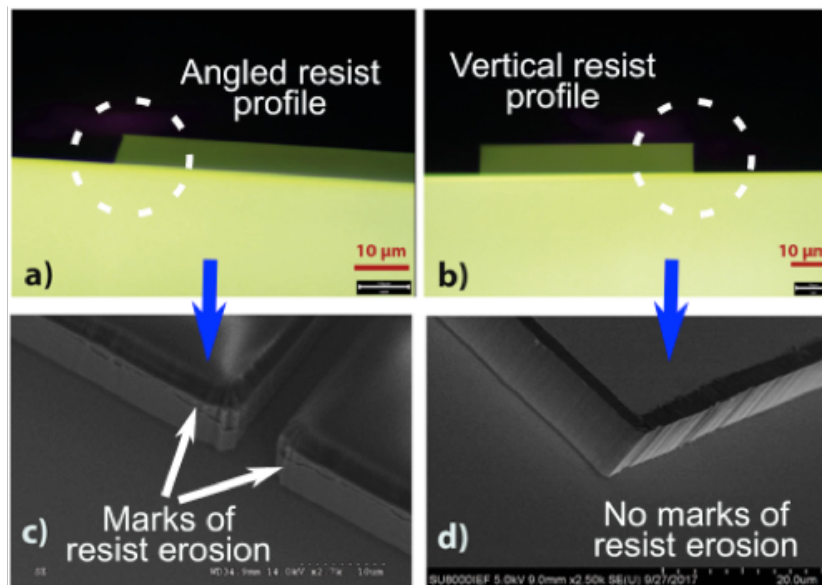


Figure 4.15: (a,b): The AZ9260 photoresist profiles: the overcut profile (a) and the optimized vertical profile (b) (c,d): SEM images after etching -with recipe R17- a GaAs wafer using a resist mask with overcut profile (c) and vertical profile (d).

The major disadvantages of using a thick photoresist are poor resolution and difficulty in obtaining straight wall profiles. The profile is critical since an etch of a $15\mu\text{m}$ -thick active region engenders a reduction (consumption) of $\sim 3\mu\text{m}$ (50%) of the resist thickness. In these conditions, the mask erosion by the plasma ions mainly impacts the rounded or sloped edges of the photoresist mask. These results in an angled photoresist profile and - in case of deep etching - this angle is transferred to the etched pattern by the gradual erosion of the

photoresist at the mask edges (Figure 4.15, (a-c)). Consequently, the positive-tone photoresists were optimized to obtain a high resolution with excellent vertical profiles. Straight wall profiles achieve the best pattern fidelity (Figure 4.15, b-d)).

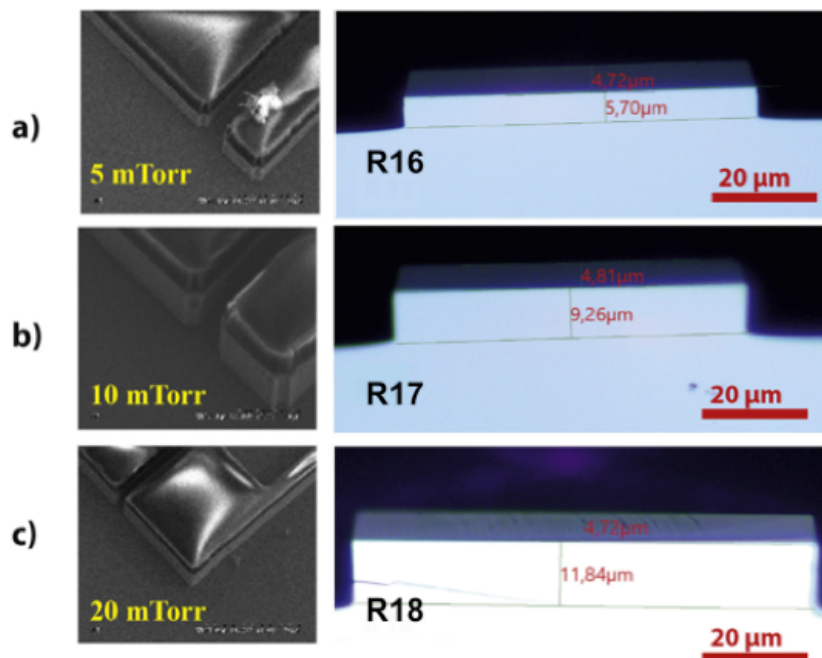


Figure 4.16: SEM micrographs and corresponding optical photograph of features etched into GaAs with $\text{BCl}_3/\text{Cl}_2/\text{Ar}/\text{N}_2$. Typically found when using recipes R16; R17 and R18.

After the optimization of the resist profile, the etching recipe has been modified to improve the passivation while keeping high etch rate and selectivity. The chemistry of the recipe and the coil and platen powers were fixed according to the previous sections. The last parameter to tune is the pressure. Figure 4.16 shows the etch profiles as a function of operating pressure (Recipes R16-R18). Vertical profiles are obtained for pressures as high as 20 mTorr . The advantage of operating at higher pressure is to improve the selectivity with the photoresist mask. Nevertheless, the higher the pressure, the less smooth the sidewall surface is. Finally, the intermediate pressure 10 mTorr has been chosen as a compromise between a relatively high etch rate and the smoothness of the side walls.

4.3.5 Conclusion of the Etching Development

During this development campaign, we adapted the etching recipe to the new condition of the ICP machine and chamber. We followed three steps schematized in Figure 4.17:

- 1 Reduction of the micromasking with a more chemical etching (increase of Cl_2).
- 2 Increase of the etching rate and the passivation with additional species (Ar and N_2) to reduce the curvature of the sidewalls.
- 3 Control of the resist profile and tuning of the pressure, to accentuate the anisotropy and make the sidewalls smoother.

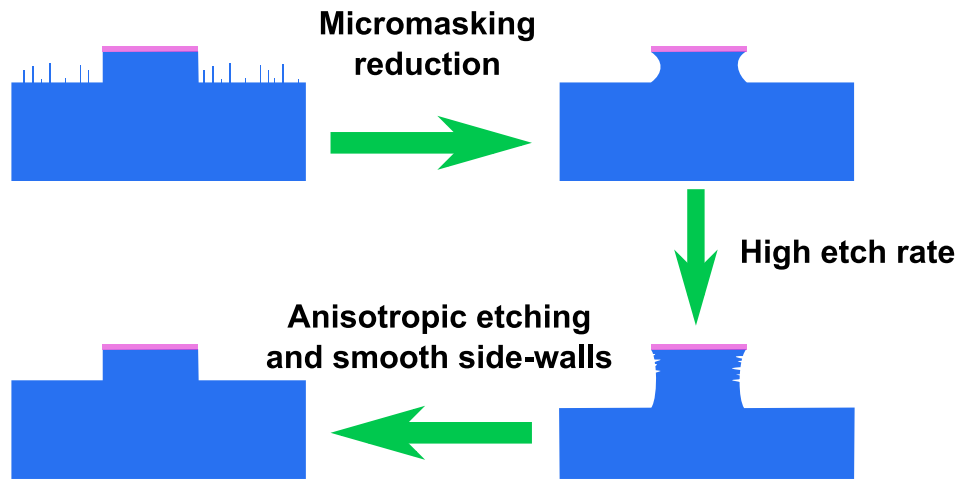


Figure 4.17: Schematics of the different steps followed during the ICP recipe development.

Eventually, I developed an optimized recipe (R17). It yields anisotropic etching with a moderate etch rate and very smooth surfaces. Compared to etching with only BCl_3/Cl_2 or $\text{BCl}_3/\text{Cl}_2/\text{Ar}$, a mixture of $\text{BCl}_3/\text{Cl}_2/\text{Ar}/\text{N}_2$ seems optimal. This is due to a balance of the physical and chemical etching mechanisms.

As we saw that there is no significant difference between etching GaAs and GaAs/AlGaAs heterostructures, recipe R17 has been successfully implemented for the etching of broadband active regions with Gires-Tournois interferometer as well as all the other devices for the group.

In addition, the recipe R17 with the resist AZ9260 suits the etching of very thick QC active regions, that are necessary to obtain spectrally (broadband) optical gains [93, 24, 17]. Figure 4.18 shows that for large apertures (distance between two ridges) recipe R17 can etch down to $21 \mu\text{m}$ without consuming all the resist.

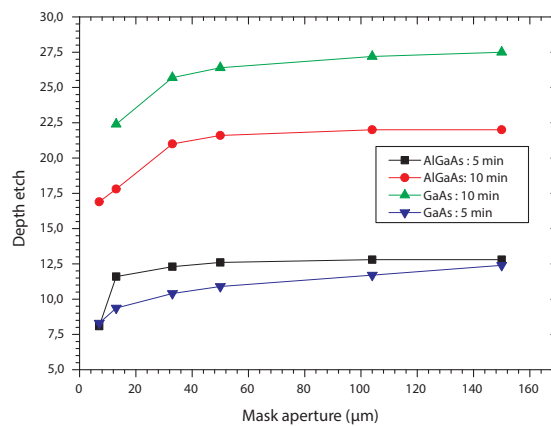


Figure 4.18: Etch depth of GaAs and of a GaAs/AlGaAs heterostructure, as a function of the mask aperture size for two different etching times (recipe R17). Etch depths of $>21 \mu\text{m}$ can be achieved.

4.4 Second Generation of GTI-THz-QCLs Used in this Work

Previous works on QCL integration in TDS showed that shorter pulses were obtained with metal-metal waveguides (compared to single plasmon ones) featuring a GTI cavity at one end of the waveguide [72]. The second generation, I fabricated, reuses the GTI implementation on metal-metal structures, using broader gain active regions to increase the spectral width of the laser spectrum and reduce the pulse duration. Table 4.3 presents the structures of the first and second generations active regions.

Sample	Type of active region	Layer structure (nm)	Al Barrier (%)	Periods number	AR thickness (μm)	Ref
L1194	phonon-resonant	4.85 /10.24/ 2.77 /9.37/ 4.62 /18.4	13	200	10	[93]
L1410	L1194: phonon-resonant	4.85 /10.24/ 2.77 /9.37/ 4.62 /18.4	13.3	120	11.8	[93]
	L1074: phonon-resonant	4.39 /8.97/ 2.63 /9.79/ 4.6 /17.66	15	120		
L1369	LO-phonon-assisted interminiband transitions	3 /9.5/ 3 /11.8/ 2 / 12.9/ 1 /16.2/ 0.5 / 10.1/ 4 /14.5/ 3 / 17/ 3 /7.1/ 3 /8.6	15	115	15	[94]

Table 4.3: Description of the heterostructures used for the second generation of GTIs. In the layer structure, bold is for the AlGaAs barriers.

4.4.1 The THz QCL Active Regions used in this Work

The first generation (Ref. [26]) of GTI THz QC lasers was engineered to operate at 2.5 THz to be compatible with a TDS system. This generation used a LO phonon depopulation scheme based on the design of Ref.[93]. In this manuscript, the heterostructure is labeled L1194, and a typical spectrum is presented in the Figure 4.20, (a) (red curve).

The second generation targets a broader gain to have larger optical gain bandwidth and eventually shorter pluses. Two types of heterostructures have been grown: stacked heterostructures based on phonon-resonant designs (Table 4.3, 1194 and 1410) and a broadband structure based on nine QWs forming a cascade of alternating photon and longitudinal optical (LO) phonon-assisted transitions between quasi-minibands (L1369, Table 4.3). The conduction band diagrams related to typical LO-phonon resonant and hybrid designs are presented in the Figure 4.19.

Four heterostructures have been pre-tested at Leeds University in standard M-I-M cavity. Figure 4.20 shows the optical gains of the active region L1194 (2.25-2.6 THz) and L1074 (2.4-2.8 THz) that have been combined to form the active region L1410. Figure 4.22 exhibits the impact of the side absorbers on the optical gain of the active region L1369.

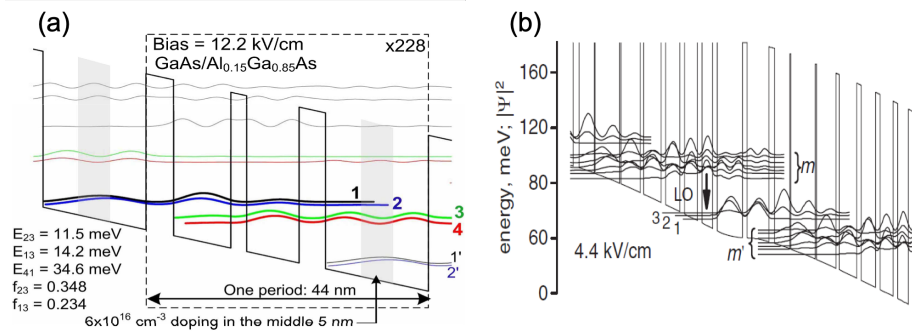


Figure 4.19: Conduction band diagrams and squared moduli of the wavefunctions of two quantum cascade structures: (a) resonant phonon based three QWs at the design electric field of 12.2 kV/cm [93]; (b) LO-assisted interminiband transition designs at 4.4 kV/cm , where m and m' denote quasi-minibands of different cascades [94].

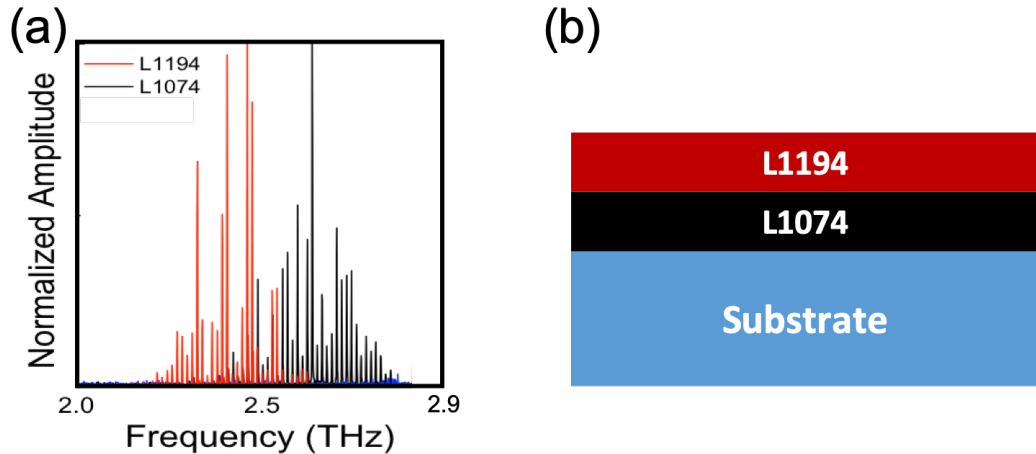


Figure 4.20: Two different QC designs (L1074 and L1194) have been combined to produce the active region of L1410. (a) Typical laser spectra for each design. (b) Schematics structure of sample L1410.

4.4.2 Side Absorbers Permit to Broaden the Laser Spectra

A technique employed for broadband THz QCLs in M-I-M cavity to offset the mode competition is to add highly doped layers [95, 96, 97] on top of the active region to increase the cavity losses of higher order modes. These so-called "side absorbers" increase the losses of the modes whose field overlaps most with the ridge sides (Figure 4.21, (b)). The TM_{00} mode has much of its electric field confined below the top metal, hence it is less affected than the higher order transverse modes by the presence of the side absorbers.

The side absorbers that can be added on the side of the ridge are typically obtained by Ni deposition [98]. Alternatively, a part of the top n-doped layer of the active region can be left in place during processing instead of being chemically removed.

The effect of the broadening of the spectrum has been observed on sample L1369, as shown in Figure 4.22. Consequently, for the processes of the second generation of GTIs the n^+ -doped on top of the active region [97] (after wafer-bonding) has been only partially removed with $H_2SO_4 : H_2O_2 : H_2O$ to leave $200 - 300 \text{ nm}$ of the n-doped layer in place.

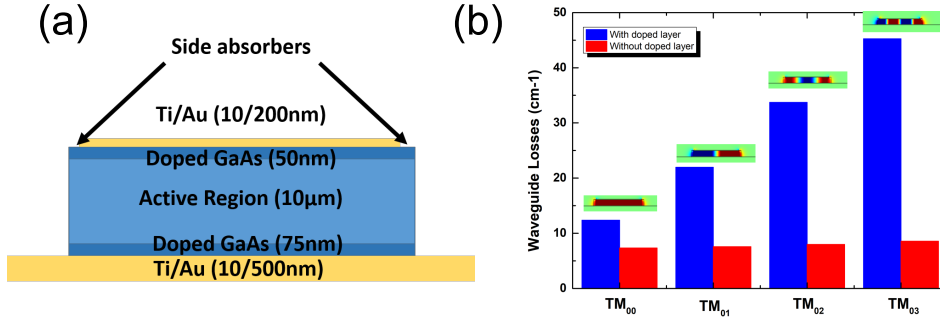


Figure 4.21: (a) Lateral cross-section of a Metal-Insulator-Metal cavity with n-doped side absorbers. (b) 2D *finite element* simulation of the waveguide losses for different transverse magnetic modes in a 10 μm thick metal-metal cavity, 100 μm wide and 4 μm wide side absorbers. The dielectric function of the active region and the doped layer are respectively $\epsilon_{GaAs}=13$ and $\epsilon_{n+-doped} = 7 + i25$. The electric field distribution of the simulated modes is displayed on the same graph. The electric field component orthogonal to the metallic layers is plotted.

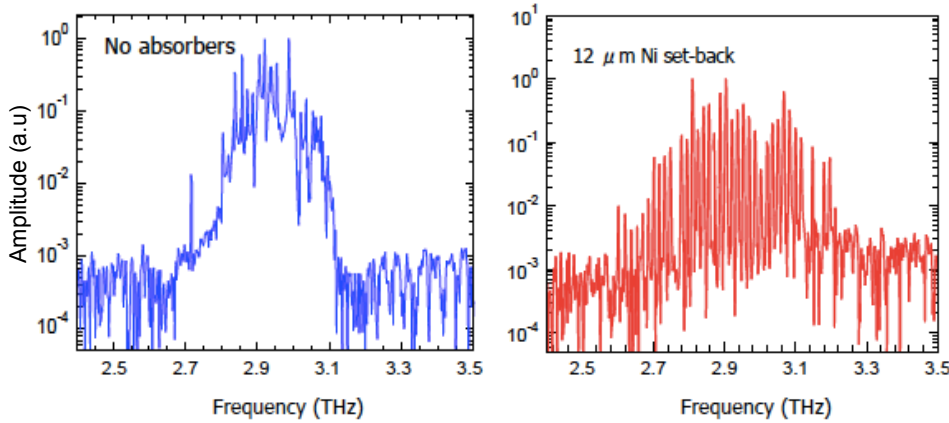


Figure 4.22: Broadband laser L1369 (grown at Leeds University), with (right) and without (left) 12 μm wide 5 nm thick Ni side absorbers, as measured at CNR/PISA SNS. The side absorbers have a dramatic impact on the spectral laser width.

4.4.3 Fabrication

Each active region has been first tested in a standard metal-metal waveguide geometry (in CNR Pisa) to estimate the gain of the active region, estimate the GDD by using the *Kramers-Kronig* relation and fix the length of the GTI using Finite Elements Simulations (LPA). For each active region (Table 4.4) I designed a specific mask with several GTI lengths around the target GTI length.

The length of the cavity defines the round trip time and the GHz beating between the modes $f_{beat} = \frac{c}{2 \cdot n_{AR} \cdot L}$. With a $L = 3mm$ length, the beat note of the cavity is at $\approx 13 GHz$.

The first step for fabricating a metal-metal cavity active region consists in wafer bonding the active region onto a host GaAs substrate (Figure 4.23, (a)). To do so, the host substrate and the active region are both covered with 10 nm Ti for adhesion and 250 nm Au for the

bonding.

Sample	Gain Width	GTI width	Measured laser pulse width	Remarks
L1194	2.4-2.7 THz	38 μm and 58 μm	4 ps	First Generation of GTI lasers [26]
L1410	2.6-3.2 THz			In-homogeneous threshold
L1369	2.9-3.1 THz and 3.5-3.6 THz	35.5-38.5 μm and 50-53 μm	5 ps	Best result without GTI

Table 4.4: Lasers processed during this PhD. Ridges are typically 56 μm wide and 3 mm long.

The substrate (typically 500 μm thick) on which the active region has been grown is then removed using first a manual polishing followed by a selective chemical etching (citric acid/ H_2O / H_2O_2 3/3/1). The active region is protected from the etching by the *stop layer* highly concentrated in aluminum ($\text{Al}_{60}\text{Ga}_{40}\text{As}$, Figure 4.23, (a-b)). Note that the stop layer is positioned during the epitaxy and fixes the thickness of the cavity, which is - in the case of GTI-lasers - between 15 and 18 μm . The stop layer is finally removed with hydrofluoric acid for 2 min.

The 700 nm n^+ -doped ($2 \times 10^{18} \text{ cm}^{-3}$) GaAs top contact that is now above the active region is used as *side absorber* [96]. Only 300 nm of this layer are removed using a chemical etching ($\text{H}_2\text{SO}_4 : \text{H}_2\text{O}_2 : \text{H}_2\text{O}$ [99]) and checking the depth of this etch with a profilometer.

Once the active region is uncovered, the patterning of the top surface can be realized. The first step consists in coating the active region with image-reversal photoresist (AZ5214, described in Chapter 2). The lithography is performed with the mask aligner MJB4. The ridge pattern with the slit of the GTI on one side is transferred on the resist via optical lithography (Figure 4.23, (c)). Once the mask is transferred on the sample, the residual resist is removed with a short O_2 plasma. The surface of the sample is then deoxidized for better adhesion between the metal and the sample surface.

Recipe	Pressure (mTorr)	Coil (W)	Platen (W)	BCl_3 (sccm)	Cl_2 (sccm)	Ar (sccm)	N_2 (sccm)
GaAs-Au	20	800	200	40	1	0	0
MGaAs	5	500	50	50	0	0	8
New recipe (R17)	10	800	100	50	2.5	5	3

Table 4.5: ICP-Etch recipes commonly used in our group.

The top metal - composed of 10 nm of Ti to adhere on the sample surface and 250 nm of Au - is then deposited with an e-beam evaporator. The resist is removed by acetone leaving only the top metal that is used as the top electrode (Figure 4.23, (d)).

The ridges are covered with AZ9260 resist (presented in the previous section) except on the slit area. The sample is then etched in the ICP reactor during ~ 7 minutes (Figure 4.23, (d)). After this step, all the active region that was not under the resist is totally removed and

access is possible to the bottom contact for wire-bonding. The resist on the top of the ridge is then removed with acetone and O₂ Plasma.

Finally, the back-side of the host substrate is manually polished and coated with Ti/Au (10/150 nm) for mounting purposes on a copper block.

Figure 4.24 shows the SEM images of the typical devices at different magnification scales. The device images (a), (c) and (d) were obtained with the recipe R17 and the image (b) with the recipe MGaAs (Table 4.5). A clear reduction of the micro-masking has been possible with the new recipe R17 that I developed.

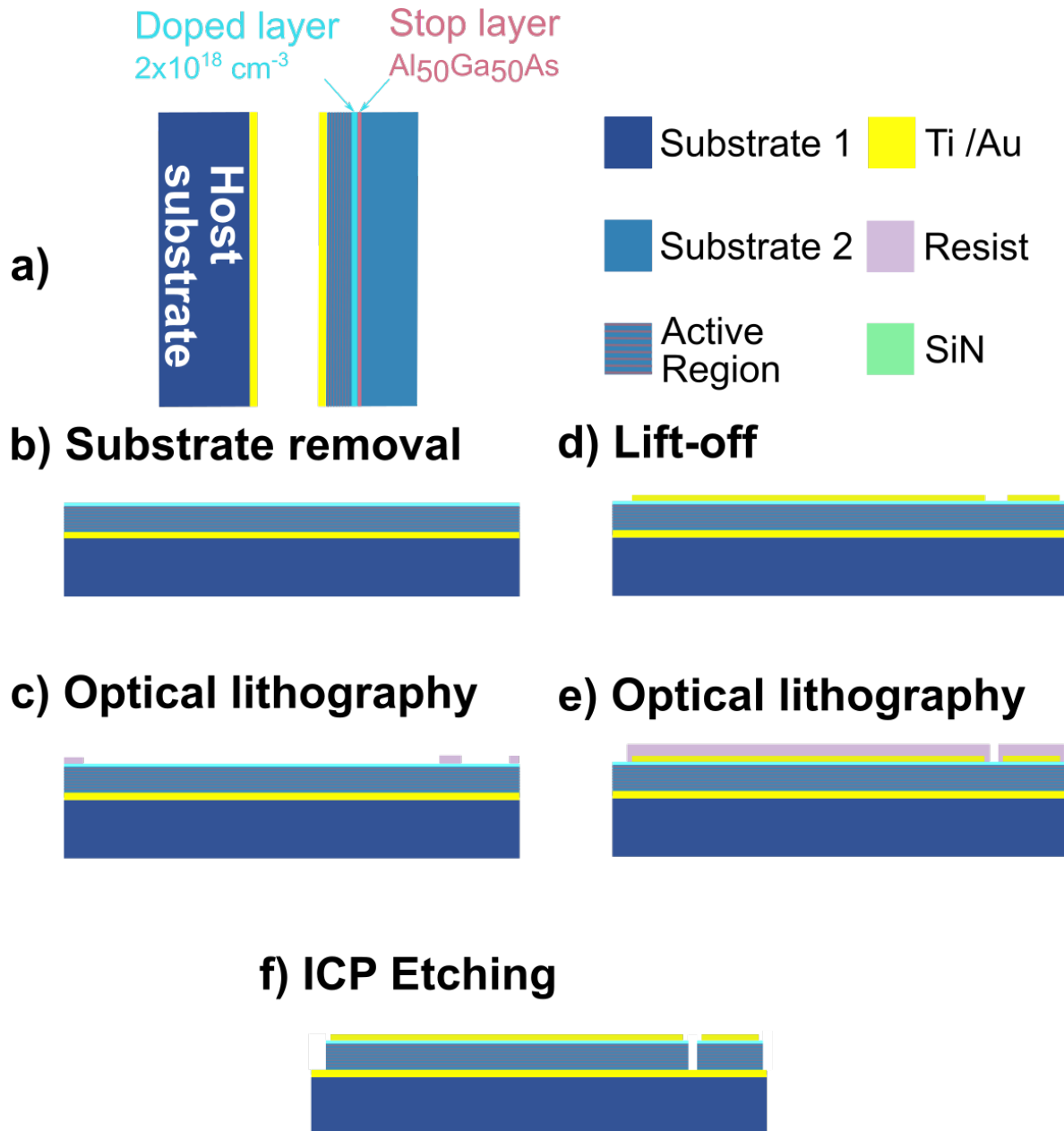


Figure 4.23: Schematics of the GTI cleanroom processing.

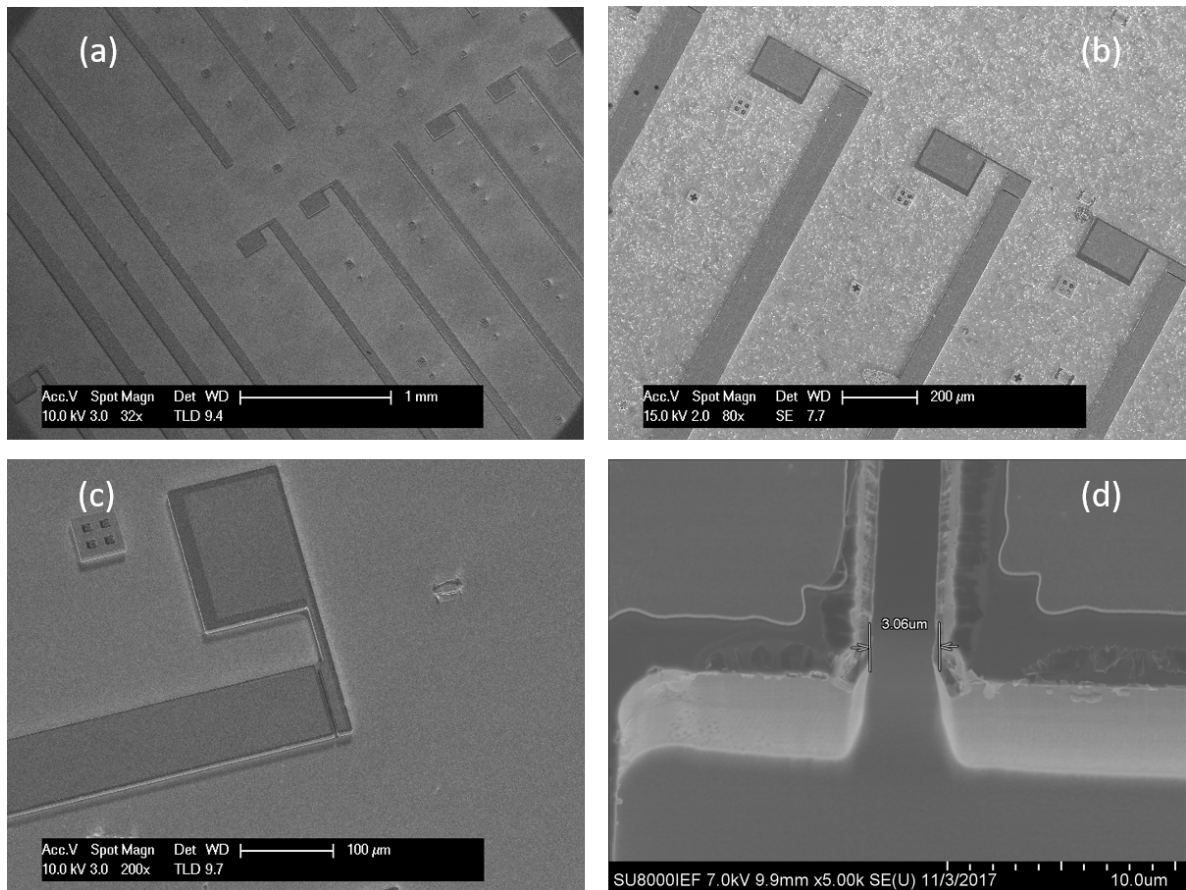


Figure 4.24: SEM images with different magnifications of GTI cavities after processing: a) global view of the sample, b) shows different positions of the slits (length of the GTI), c) shows the GTI region of one sample and d) shows the slit opening of $3 \mu m$. a), c) and d) were etched with the recipe R17 and b) with the recipe MGaAs see Table 4.5.

4.4.4 Sample Mounting

After processing, the samples are cleaved on the opposite side of the GTI cavity. Samples are then mounted with indium on a specific copper block. The copper block central length of 3 mm equals the sample length (particularly useful to avoid reflections during the seeding). Two types of pads can be implemented on the copper block (Figure 4.25): a normal connection pad for standard characterizations and a high-speed SMP connector with an integrated coplanar transmission line for compatibility with RF applications. This second connector can operate up to ~ 26 GHz.

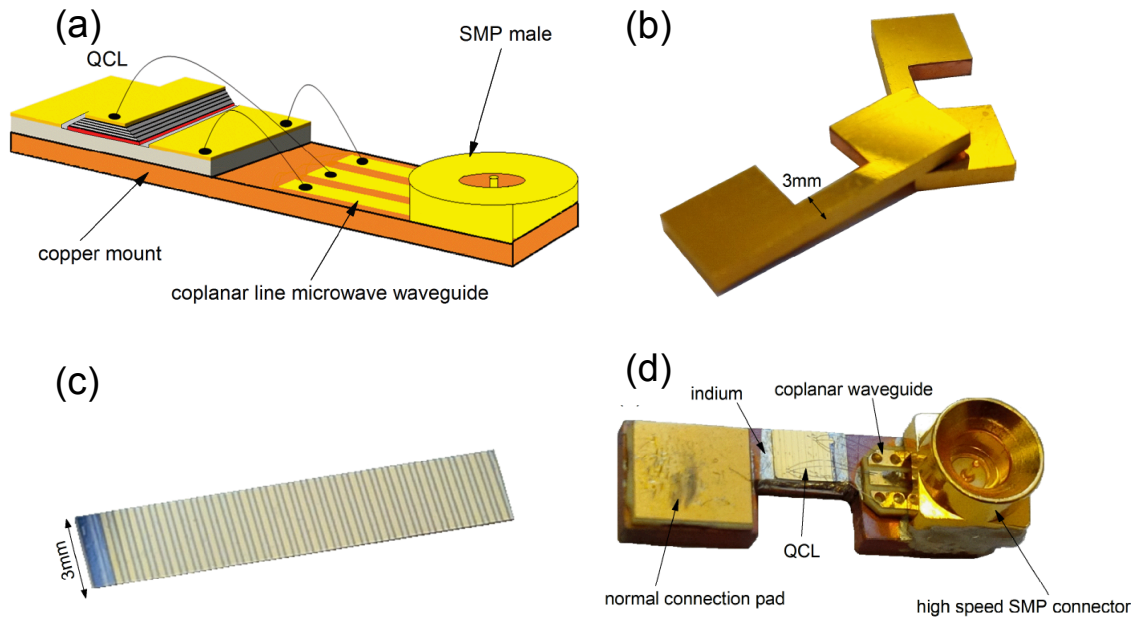


Figure 4.25: (a) Diagram of a QCL mounted on a copper mount with a microwave waveguide and a SMP connector (b) Gilded mounting block for THz QCLs. (c) Picture of a processed sample after cleaving. (d) THz QCLs mounted on a copper block with high-speed coplanar transmission line waveguide and integrated SMP connector [72].

The electrical connection between the QCL and the connectors is realized through microwave bonding. In the case of the SMP connector the ridge is connected to the central line of the co-planar waveguide.

4.4.5 Characterization of GTI QCLs (ENS/LPA)

In this section, we present the characterizations of the broadband QCLs, I fabricated, performed at LPA (L1410 and L1369). Table 4.4 summarizes the most relevant results obtained with these devices.

L1410

The sample L1410 lases over a broadband frequency range but not simultaneously because the threshold currents of the two different parts of the active region are different.

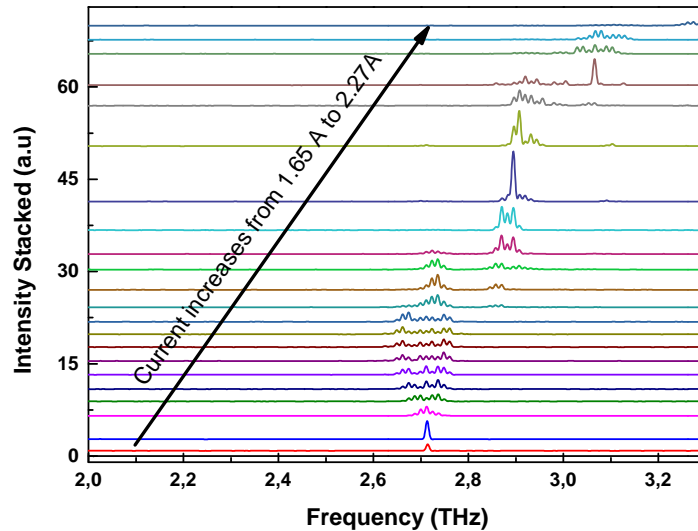


Figure 4.26: Spectra of sample L1410 for different currents.

No further characterizations have been performed for this sample and the heterostructure has not been regrown.

L1369

The active regions L1369 emits a regular and continuous "comb" in the range of $2.7 THz$ to $3.1 THz$ ($400 GHz$). These two heterostructures have suitable properties to be studied on a TDS set-up.

For sample L1369, the best results in mode-locking were surprisingly obtained with the reference sample. One single pulse of the reference sample (without GTI) is shown in Figure 4.27, (b) with a pulse width of $4.5 ps$ at a round trip time of $70 ps$. The dispersion of this active region was flatter than expected. Figure 4.27, (d) shows on the same graph the broader spectrum obtained from a GTI-THz QCL (see Figure 4.27, (c) and the GTI compensation profile calculated for the same laser. The laser spectra have three distinguishable regions centered respectively at $2.85 THz$, $3.15 THz$ and $3.5 THz$. The shape of the GTI dispersion (Figure 4.27, (d) red) is not designed for such a spectral gain and does not reduce the total dispersion of the laser. Consequently, the pulse is larger ($6 ps$) than the reference.

The GTI cavities have clearly a strong effect on the spectra. The sample with a GTI of $34.5 \mu m$ is particularly interesting because it shows a potential $900 GHz$ wide spectrum

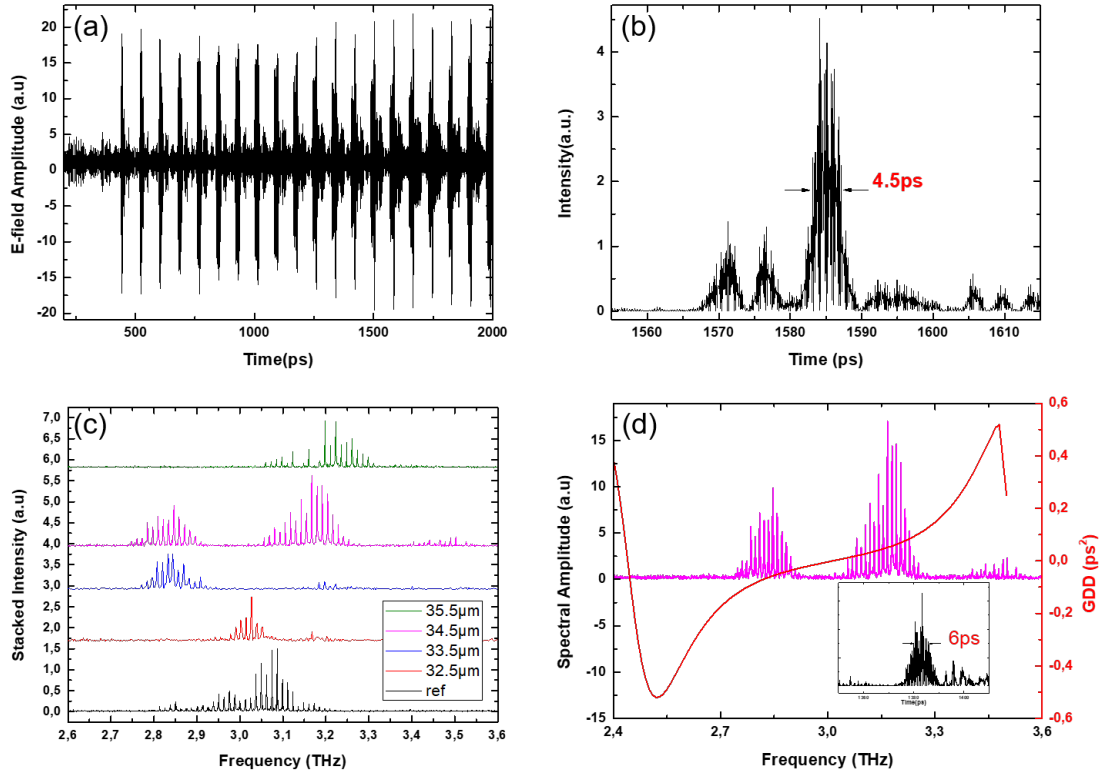


Figure 4.27: (a) and (b) pulses of the reference sample of L1369, (c) Spectra of the different GTI geometries compared to the reference sample, (d) Spectrum of the $34.5 \mu\text{m}$ long GTI cavity (purple) and the calculated (LPA) GTI dispersion profile. The inset shows a pulse of 6 ps obtained with this laser.

(pink curve in Figure 4.27, (c)). However, a phenomenon of spatial hole burning can be observed [100] that possibly hinders the generation of very short pulses.

4.5 Conclusions

In this chapter, we have presented the development of THz-QC lasers equipped with monolithic GTIs for the emission of short THz pulses. To further reduce the pulse width generated by the laser, a spectrally broad emission spectrum is of crucial importance.

To widen the spectral gain, two types of active regions have been grown: two phonon-resonant active regions with different central frequencies were grown successively on the same wafer, and LO-phonon assisted interminiband transition active regions.

The phonon-resonant active regions stack (L1410) had an inhomogeneous threshold over the two subregions. Consequently, the subregions were lasing at different injected currents, limiting the broadening of the spectral gain.

On the contrary, the LO-phonon assisted interminiband transition active regions (L1369) do not have subregions and have a homogeneous threshold intrinsically. The optical gain of these active regions was broad (500 GHz) and could be fully exploited using side absorbers (up to 900 GHz).

The dispersion of the LO-phonon assisted interminiband transition active regions is different from the phonon resonant active regions of the first GTI generation (L1194 [26]). The dispersion compensation - performed with Gires-Tournois Interferometers (GTI)- was thus adapted to this new laser active region.

The critical step of the fabrication of GTI-laser cavities is the high aspect ratio between the slit opening of the GTI (2-3 μm) and the thickness of the active region (15-20 μm). For this reason, I developed an anisotropic, selective and reproducible ICP etch recipe Ref. [28] to etch GaAs/AlGaAs heterostructures.

Three different active regions (presented Table 4.4) have been processed with this recipe. The shortest pulse recorded for the second generation was 5 ps (L1369), slightly longer than the first generation (4 ps). Nevertheless, these devices are still characterized by our colleges at the LPA and suggest a potential improvement of the performances of the broadband GTI-QC lasers.

Part III

Mid-Infrared Polaritonic Detectors

"La communication ne se fait pas de l'un à l'autre mais ensemble contre le bruit.",
Michel Serres

Quantum Wells Infrared Detectors: Introductory Theory

In the second part of this thesis, we explore the strong coupling from the detection point of view. Among various type of quantum detectors, we decided as the first approach to work with quantum well infrared detectors (QWIP). The advantage of these structures is that the quantum engineering of the energy levels is simple, which is an asset for the design of the structures as well as the interpretation of the results. The following chapter presents this type of detector and introduces the fundamental concepts related to these devices.

5.1 Brief Introduction to Quantum Well Infrared Detectors

In this section, we introduce the general concepts related to QWIPs as T_{Blip} , Dark Current, Photo-current, Noise Equivalent Power, Detectivity, and Responsivity. These concepts are useful to understand the QWIP development, the different limitations of this type of detectors, and to interpret the experimental results of our study.

5.1.1 Black Body radiation

To fully understand the process of infrared detection, we also need to know some basic properties of the source. The Bose-Einstein function describes the energy distribution of a photon field at a frequency ν with the temperature T

$$f_B(\nu) = \frac{1}{\exp(h\nu/k_B T) - 1}. \quad (5.1)$$

This equation applied to the electromagnetic mode in a cavity yields *Planck's radiation law*. The *irradiance* \mathcal{I}_ν is the power of a blackbody source irradiated over the full solid angle divided by the area of the same source. It is written

$$d\mathcal{I}_\nu = \frac{2\pi h}{c^2} \frac{\nu^3 d\nu}{\exp(h\nu/k_B T) - 1}. \quad (5.2)$$

Figure 5.1 shows the irradiance at different temperatures.

Nevertheless, only a portion of the light radiated from the source reaches the detector. A general concept to evaluate the impinging power onto the detector is the *radiance* (radiation

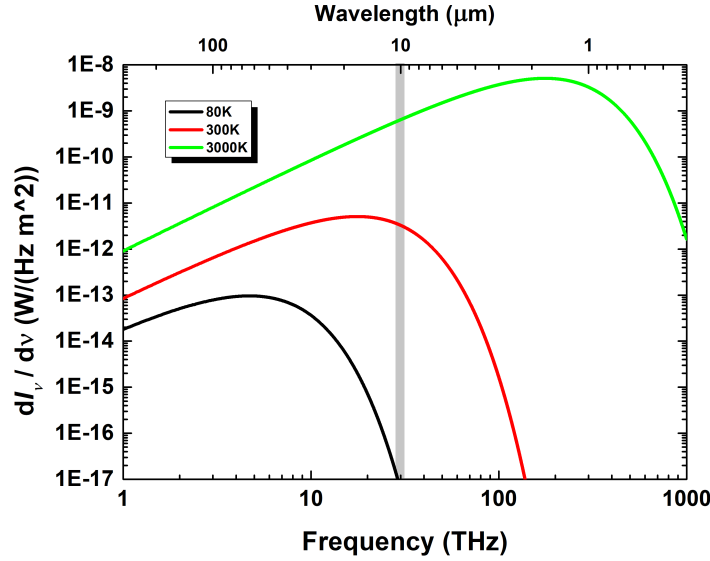


Figure 5.1: Energy distribution of the black body radiation vs. photon frequency for an emissivity equal to 1. The grey area corresponds to the detection spectral window of our detectors.

power per unit area and steradian). Consider a greybody that has an anisotropic radiation described by the *emissivity* $\mathcal{E}(\nu, \Omega)$. The *emissivity* of the surface of a material is its effectiveness in emitting energy as thermal radiation. The ratio varies between 1 (perfect black body) and 0. The *radiance* can be expressed in spherical coordinates as [101]

$$\delta\mathcal{H}_{\nu,\Omega} = \mathcal{E}(\nu, \Omega) \frac{2h}{c^2} \frac{\nu^3 d\nu \cos(\theta) d\Omega}{\exp(h\nu/k_B T) - 1}. \quad (5.3)$$

Where $d\Omega = \sin(\theta)d\theta d\phi$, with θ the polar angle and ϕ the azimuthal angle. In the following we consider an ideal blackbody source, i.e $\mathcal{E}(\nu, \Omega) \approx 1$.

To estimate the optical power impinging on a detector (without focusing), we need to integrate the radiance over the surface of the source with the spherical coordinates centered on the detector. Considering the surface A of the detector sufficiently small we assume that all the points of the detector see the source under the same solid angle and directly multiply the radiance by the area A . The power P per frequency interval radiated from the blackbody onto the detector can be expressed as a function of the radiance $\mathcal{H}_{\nu,\Omega}$

$$dP_\nu = A \int_{\theta,\phi} \delta\mathcal{H}_{\nu,\Omega} = A \frac{2h}{c^2} \frac{\nu^3 d\nu}{\exp(h\nu/k_B T) - 1} \quad (5.4)$$

This formula is useful to calculate the responsivity and the detectivity of a detector.

5.1.2 Material and Electrical Transport Properties

QWIP detectors cover a large range of frequencies from the NIR to the THz. For this project, we targeted a wavelength $\lambda \sim 10 \mu\text{m}$ (more details in subsection Operating Temperature). The dimensions of the grating resonator operating at $\sim 10 \mu\text{m}$ are few microns of the grating period and $\sim 1 \mu\text{m}$ thick cavity. These dimensions are achievable in the C2N cleanroom using wafer bonding and e-beam lithography.

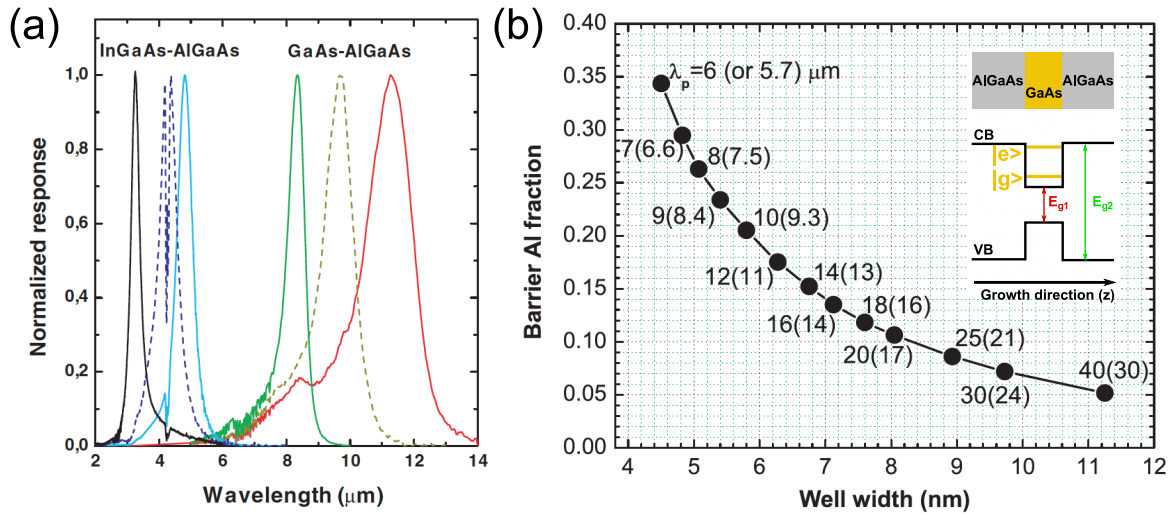


Figure 5.2: (a) Spectral response curves of six QWIPs covering the two atmospheric transmission windows of 3-5 and 8-12 μm wavelength. (b) Calculated parameters of barrier Al fraction in a GaAs/AlGaAs heterostructure and well width for a given peak detection wavelength (λ_p). The values in parentheses give λ_p including many-body effects for a doping density of $5 \times 10^{11} cm^{-2}$ [101]. The inset represents the valance (VB) and the conduction (CB) bands of a bound to quasi-bound GaAs/AlGaAs quantum well. The ground ($|g\rangle$) and excited ($|e\rangle$) states are represented in yellow.

In the second atmospheric window, GaAs/AlGaAs is an ideal material system (Figure 5.2, (a)). The design rules for optimized QWIP structures are shown in Figure 5.2, (b)). Our structures target an operating wavelength of $\sim 10 \mu m$ which is obtained for a quantum well thickness close to 6 nm and an Alumina fraction around 20%.

Bound-to-Quasi-Bound Design

In a QW the continuum is defined by the ensemble of the wave functions that are not null at an infinite distance from the quantum well. In this energy region, the electrons are free to flow, especially when a bias is applied. The continuum is a continuity of energy levels.

A singular disposition of the energy levels inside a QW is when the first excited state $|e\rangle$ is quasi-bound. This means that the energy of the excited state is very close to the barrier energy, and therefore, to the continuum.

To generate photocurrent carriers are needed. Thus an electronic doping is inserted inside each quantum well by doping with silicon apporportion of the QW (typically 4nm) to a density of $4 \times 10^{18} cm^{-3}$.

Under bias, the electrons from the fundamental state $|g\rangle$ can generate a current if they are excited by a photon at the energy $\Delta E_c = E_e - E_g$. When the electron is in the excited state it tunnels into the continuum to the electrodes.

Note that in a QWIP it is possible to generate a photocurrent from the absorption of light at inter-band transition energy ($E_{g2} \approx E_{valence} - E_{conduction}$). Experimentally, we can always detect the red laser of the FTIR and we used this to pre-align the sample.

Dark-Current

In this section, we make the assumption that the barrier width between two wells is large enough (>20 nm) to avoid any tunneling phenomena between two wells. Under these conditions the main contribution to the dark-current is the thermal activation of the carriers into the continuum. This configuration has first been modeled by J-Kane et al. using the *3D carrier drift model* [102]. This model, that relies on the Arrhenius law, is based on 3 assumptions: (a) the interwell tunneling is negligible, (b) the electron density remains the same in each QW and (c) mainly one bound state is confined in the QW.

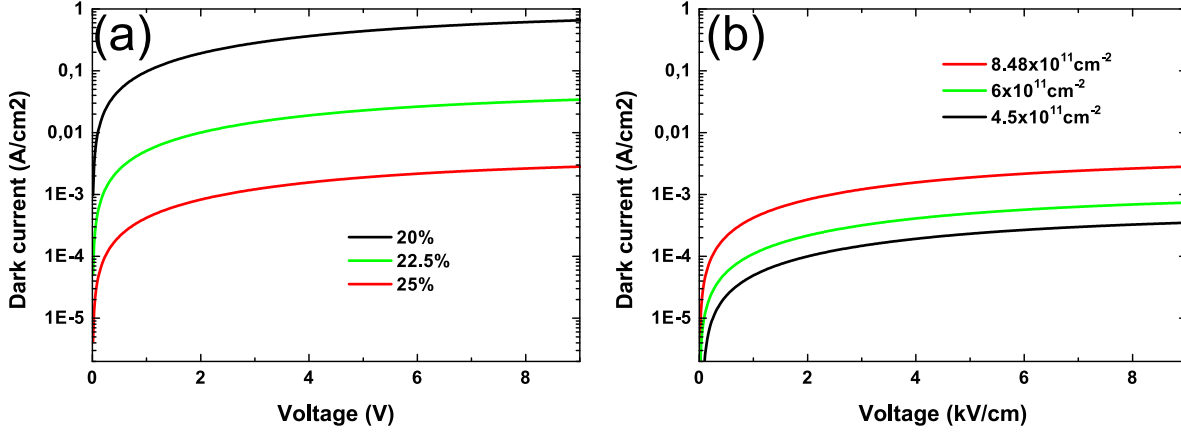


Figure 5.3: Dark current simulated using the *drift model*. The thermal activation energy is estimated with a Schroedinger-Poisson model applied on a 6.5 nm wide well with 20 nm barriers, the doping is in the center of the well. (a) the doping is fixed at $8.48 \times 10^{11} \text{ cm}^{-2}$ and the barrier height is modified by changing the Al fraction (20%, 22.5% and 25%). (b) The barrier height is fixed at 25% and the doping (Fermi level) varies (4.5 , 6 and $8.48 \times 10^{11} \text{ cm}^{-2}$).

Following these assumptions, the thermionic current is given by [102]

$$j_{th,Kane} = eN_{3D}v(F), \quad (5.5)$$

where $v(F)$ is the drift velocity when an electric field F is applied to the quantum well (in our case $\sim 5 \text{ kV cm}^{-1}$). The N_{3D} density is calculated by treating the barriers as a bulk semiconductor. Superlattice band structure effects are neglected, which is justified because the barriers are much thicker than the wells and the resulting superlattice miniband gaps are less than the thermal energy $k_B T$ at device operating temperatures. The quantum well confinement in the QW is taken into account in the evaluation of the Fermi energy E_f . Assuming a complete ionization, the 2D doping density equals the electron density within a given well $N_D = \frac{m}{\pi \hbar^2} E_f$. It is then possible to write

$$N_{3D} = 2 \left(\frac{m_b k_B T}{2\pi \hbar^2} \right)^{3/2} \exp\left(-\frac{E_{act}}{k_B T}\right), \quad (5.6)$$

where m_b is the barrier effective mass and E_{act} the thermal activation energy which equals the energy difference between the top of the barrier (dependent of the Al fraction) and the top of the Fermi sea in the well (dependent on the doping). Quantitatively the thermal energy activation can be written $E_{act} = V_b - E_F - E_{ex}$ where V_b is the barrier potential, eFL_{well} represents the voltage drop across the well (assuming that the ground state E_g is independent of F) and E_{ex} is the exchange energy that we took equal to -13.5 meV for our simulations[103].

The drift velocity takes the usual form:

$$v(F) = \frac{\mu F}{[1 + (\mu F/v_{sat})^2]^{1/2}}, \quad (5.7)$$

where μ is the low field mobility and v_{sat} is the saturating velocity. The final expression of the thermionic current is then

$$j_{th,Kane} = 2ev(F) \left(\frac{m^* k_B T}{2\pi \hbar^2} \right)^{3/2} e^{-\frac{V_B - E_F - E_{ex}}{k_B T}}. \quad (5.8)$$

The 3D carrier drift model shows that the dark current depends on the doping, the fraction of Al in the barrier height, the applied field and the temperature. Figure 5.3 presents the relative variation of the dark current for fixed doping with different barriers (a) and a fixed barrier with different dopings. We observe that the barrier height has a major impact on the dark current because it fixes the regime of operation of the QWIP: bound-to-continuum, bound-to-quasi-bound or bound-to-bound. Once the regime of the QWIP (Al fraction) is chosen the doping can be tuned for the desired application. This model is particularly adapted to devices that operate at a relatively high temperature (78K), at low temperature the *sequential tunneling* starts to be predominant [103].

Photo-Current

Photoconductivity in solids has been widely studied [104, 105]. The device operation of a photoconductive QWIP is similar to extrinsic semiconductor detectors [106]. The major distinction between QWIPs and conventional intrinsic or extrinsic photoconductors is the discreteness. The incident photons are absorbed in discrete quantum wells that are much narrower than the inactive barrier regions.

The photoconductive gain is defined as the number of electrons flowing through the external circuit for each photon absorbed. Figure 5.4 (top panel) shows the dark current paths, while the bottom panel indicates the direct photoemission and the extra current injection from the contact to balance the loss of electrons from the well. The dark current paths remain the same under illumination. The total collected photocurrent is the sum of the direct photoexcited and the extra injection contributions.

Considering the same assumptions as subsection *Dark Current*, the emission current of direct excitation of electrons into the continuum for one QW can be written [101]

$$i_{photo}^{(1)} = e\Phi\eta^{(1)} \frac{\tau_{relax}}{\tau_{relax} + \tau_{esc}} \equiv e\Phi\eta \frac{p_e}{N}, \quad (5.9)$$

where Φ is the incident flux of photons, the superscript (1) indicates quantities for one well, τ_{esc} is the time to escape the QW, τ_{relax} is the intersubband relaxation time, $\eta \equiv N\eta^{(1)}$ the total absorption quantum efficiency, N is the number of wells, and the escape probability for an excited electron from the well is given by

$$p_e \equiv \frac{\tau_{relax}}{\tau_{relax} + \tau_{esc}}. \quad (5.10)$$

Considering Figure 5.4 from an eulerian point of view the number of photoemitted electrons from the QW ($i_{photo}^{(1)}$) must be balanced by the extra trapped electrons $i_{photo}^{(1)}/p_c$. Where p_c , the probability to capture an electron is defined by

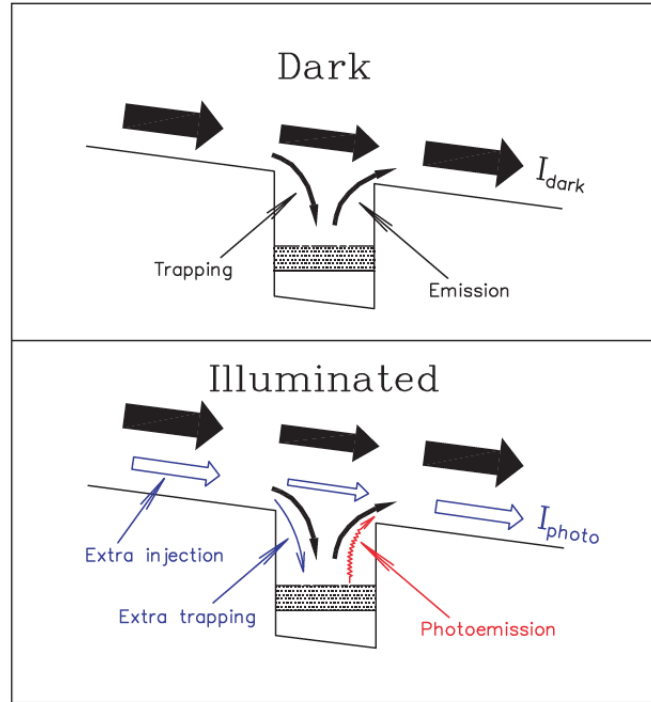


Figure 5.4: Photoconductive gain mechanism in QWIPs [101].

$$p_c \equiv \frac{\tau_{trans}}{\tau_{trans} + \tau_c}, \quad (5.11)$$

τ_{trans} is the transit time for an electron across the QW and τ_c is the capture time for an excited electron back to the well. To ensure the conservation of electrons the observed photocurrent equals the injection current.

Note that $\tau_{trans} \approx L_p/v$ where L_p is the quantum well period, and v is the velocity drift. For typical parameters of $v = 10^7$ cm/s and $L_p = 30$ -50 nm, τ_{trans} is estimated to be in the range of 0.3-0.6 ps

$$I_{photo} = \frac{i_{photo}^{(1)}}{p_c} = e\Phi\eta \frac{p_e}{Np_c} \equiv e\Phi\eta g_{photo}. \quad (5.12)$$

The photoconductive gain of the QWIP is then $g_{photo} = p_e/Np_c$.

5.1.3 Detector Performance

After presenting the main two mechanisms behind the current generation in a QWIP (thermal and optical), we present the parameters that are experimentally used to assess the performances of a QWIP.

Operating Temperature

The appropriate figure of merit to gauge the temperature performance of a QWIP is the BLIP condition (Background Limited Infrared Photodetection). The BLIP condition is defined when the photocurrent stemming from the background is as large as the dark current. We say

that the detector operates under BLIP condition when the detector temperature is below the T_{blip} . Thus the T_{blip} decreases when the dark current increases.

As we saw in Equation 5.5 the dark current is directly related to the activation energy $J_{dark} \propto \exp(-E_{act}/k_bT)$. In first approximation the activation energy depends mainly on the intersubband energy transition ($E_{act} \approx E_{12} = h\nu$). For a given temperature (T) we can deduce that when the frequency decreases, the activation energy decreases too, and the dark current increases exponentially. To compensate the increase of the dark current at low frequencies, the temperature has to be decreased to meet the Blip condition. We can, therefore, infer that the T_{blip} decreases with the wavelength, as shown in Figure 5.5.

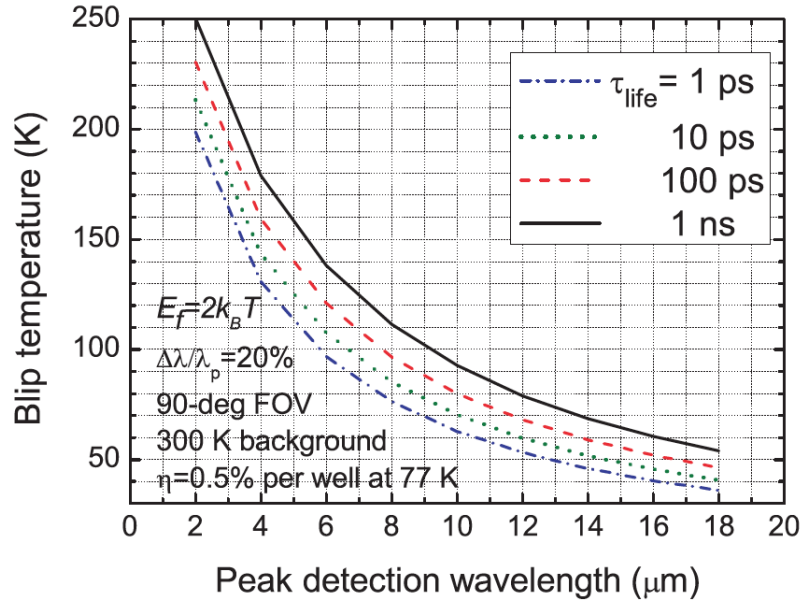


Figure 5.5: Calculated background-limited infrared performance (blip) temperature vs. peak detection wavelength and different carrier lifetimes (τ_{life}) [101].

Responsivity

The responsivity represents the ratio between the number of excited electrons contributing to the photocurrent and the number of incident photons on the detector. Considering an incident beam of photons with frequency ν and power P_S . The number of incident photons is defined by $\Phi = P_S/h\nu$. According to Equation 5.12 the responsivity is:

$$\mathcal{R} = \frac{I_{photo}}{P_S} = \frac{e}{h\nu} \eta g_{photo}. \quad (5.13)$$

Under the assumption that $\eta \propto N$ the responsivity is independent of the number of wells. Note that the absorption also depends on the overlap between the quantum wells and the electromagnetic field. In our case with M-I-M cavities the overlap is close to one, but for cavities like single plasmon ones a lower overlap has to be taken into consideration.

Taking into account the formula of the dark current Equation (5.8), the total current can be written

$$I = \mathcal{R}P_S + \mathcal{R}P_B + I_{Dark}, \quad (5.14)$$

where P_B represents the incoming power of all the background objects on the environment (adjacent signal sources, stray light, optics) of the detector

Depending on the relative magnitude of $\mathcal{R}P_S$, $\mathcal{R}P_B$, I_{Dark} the detector is defined signal-noise limited, background-limited or dark-current-limited.

Noise Equivalent Power, Detectivity

A continuous signal (electrical, optical, thermal) is carried by quanta (electron, photons, phonons). It is the discrete character of carriers associated with the random nature of transport that generates signal variations. This mechanism gives the theoretical limit of the signal to noise ratio. In the case of the electrical current, it has been described for the first time by W.Schottky in thermo-ionic diodes in 1918 [107].

In an "ideal" photoconductor the carrier generation and recombination (g-r) are associated with a Poisson distribution. In the case of an integration time (τ_{int}) much larger than the signal pulses associated with individual detected photons ($\tau_p \ll \tau_{int}$), the generation-recombination noise is

$$i_{n,gr}^2 = 4eg\bar{I}\Delta f, \quad (5.15)$$

where \bar{I} is the mean value of the intensity, $\Delta f = 1/2\tau_{int}$ is the frequency bandwidth and g is the noise or photoconductive gain [108].

For detectors the minimum power for which the ratio signal over noise ratio equals one is called the *Noise Equivalent Power* (NEP). As we saw in Equation (5.14) the noise depends on the operating conditions of the detector, and the NEP as well. Above T_{blip} the dominant noise is the dark current and the detector is *Dark-current limited* ($g = g_{noise} = \frac{1}{N_{pc}}$). When instead the detector operates under blip condition, two cases are possible: the QWIP is limited by the background photons (*Background limited*, $g = g_{photo}$) or by the oscillations of the photocurrent itself (*Signal-noise limited*, $g = g_{photo}$). The NEP can be calculated in each case as presented in Table 5.1.

Signal-noise limited	Background limited	Dark-current limited
$\frac{2h\nu}{\eta\tau_{int}}$	$\sqrt{\frac{2h\nu P_B}{\eta\tau_{int}}}$	$\frac{h\nu}{\eta} \sqrt{\frac{2G_{th}V}{\tau_{int}}}$

Table 5.1: NEP for the three different types of noise. G_{th} is the thermal generation rate, and V the volume of the detector and τ_{int} is the integration time [101].

In the following chapter, we will see that our devices are principally limited by a high dark current related to the doping of the wells.

The *detectivity* D is defined as the inverse of the NEP (\mathcal{R}/i_n). In order to specify the performance of a detector, the *specific detectivity* is normalized with respect to the detector area (A) and bandwidth (Δf): $D^* = \sqrt{A\Delta f}D$. This leads to the general expression

$$D^* = \frac{R\sqrt{A\Delta f}}{i_n}. \quad (5.16)$$

5.2 Selected Developments of Mid-IR Detectors from the Literature

In this introduction, we present a few selected works related to QWIP detectors operating between 9 and 11 μm (Figure 5.6). We first detail two devices in weak coupling and then two in strong coupling. These works represent interesting points of comparison to our devices. The theoretical concepts are discussed in the second section of the chapter.

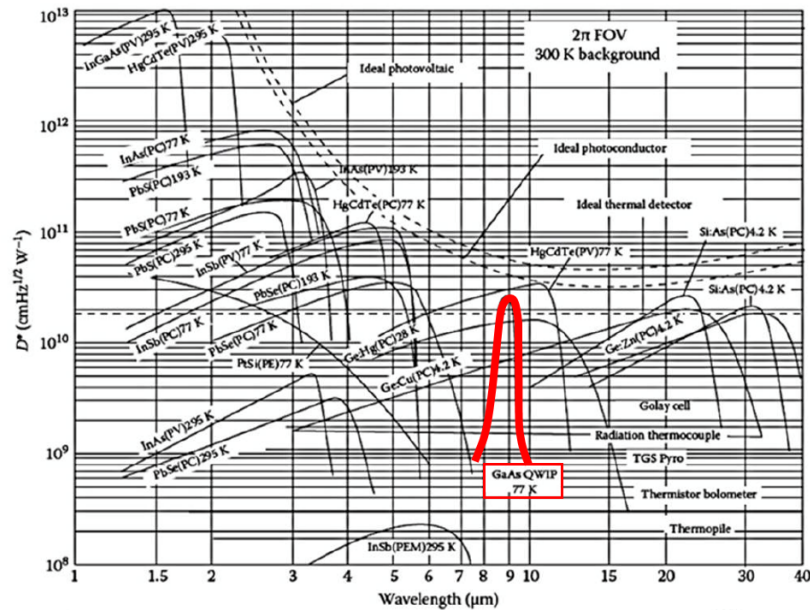


Figure 5.6: Specific detectivity (D^*) and spectral range coverage of various commercially available IR detectors[109].

5.2.1 QWIP Developments and Recent Improvements

The most common photodetectors in the Mid-Infrared spectral range are based on Mercury Cadmium Telluride (MCT, HgCdTe). Nevertheless, these detectors using interband transitions are relatively slow with an output bandwidth at 3dB in the order of $\sim 100 \text{ MHz}$ [110]. Alternative technologies based on intersubband transitions have been developed at the end of the 20th century, thanks to progress in GaAs and InP epitaxy.

Mastering the epitaxy offers a high control on the bound states inside the quantum well, and led to the development of the QWIP. The first demonstration of a Quantum Well Photodetector used a superlattice of GaAs/AlGaAs detecting at 10 μm [111]. The waveguide (inset of Figure 5.7) was a single plasmon structure structured as Mesa, and the light was coupled to the cavity via the substrate polished at 45° . A responsivity of 0.52 A/W was measured. Since then, QWIPs started to be an active research topic: the dark current has been reduced, and the temperature performances increased. Thus QWIPs have been implemented in several imaging applications [112], the detection speed has reached several GHz [113, 18] and the operating temperature [114].

Nevertheless, most of QWIP devices need cryogenic cooling, which limits the possible applications. To overcome this limitation, different solutions have been experimented to im-

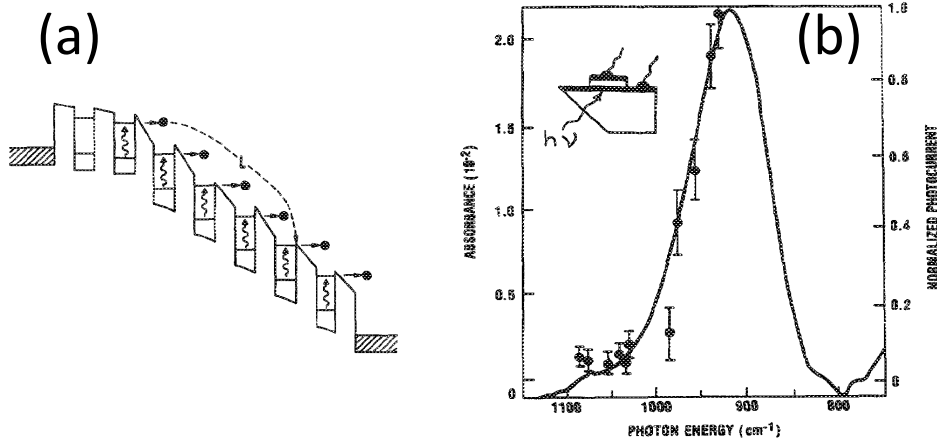


Figure 5.7: (a) Original concept of QWIP using a superlattice of QWs. (b) First measurement of a QWIP using a mesa geometry (inset) [111].

prove the temperature performances.

The design of the waveguide is critical for the QWIP performances because it defines the volume of the detector (dark current) and its efficiency in capturing photons (that influences the responsivity). Over the last decade, M-I-M cavities appeared as an efficient and versatile solution to confine light into a small volume. In particular patch cavities are defined by a strip width $s = \lambda/2n_{eff}$, where λ is the detection wavelength and n_{eff} the effective index of the active region, and a thickness t much smaller than the wavelength λ .

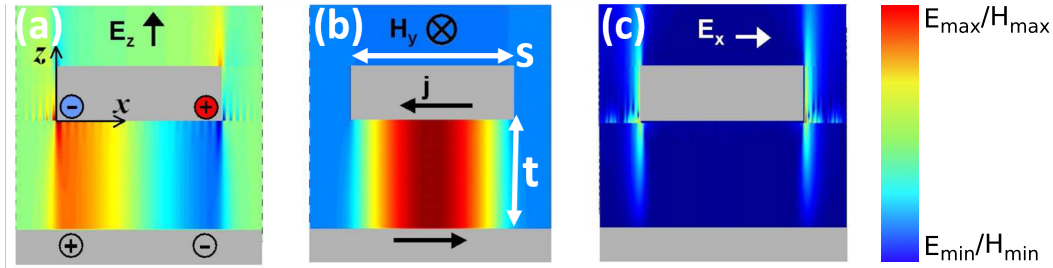


Figure 5.8: Plot of the three components (a) E_z , (b) H_y and (c) E_x of the electromagnetic field for the first resonance of a patch cavity. The thickness of the cavity is t and the stripwidth is $s = \lambda/2n$. The maximal values are in red and minimal in blue. The induced charges and currents are also presented [41].

When an electromagnetic wave impinges on the patch cavity it creates a sheet charge density (σ) and a surface current (\vec{j})

$$\sigma = \vec{E} \cdot \vec{z}, \quad \vec{j} = \vec{H} \times \vec{z}. \quad (5.17)$$

The surface current and charges induced by the mode are indicated in Figure 5.8, (a). The induced charges and currents in the lower metallic plane are the reverse images of the ones induced on the stripes. In this configuration, a purely vertical (z -direction) electric field is generated between the two metals. This TM mode can then couple with the active region.

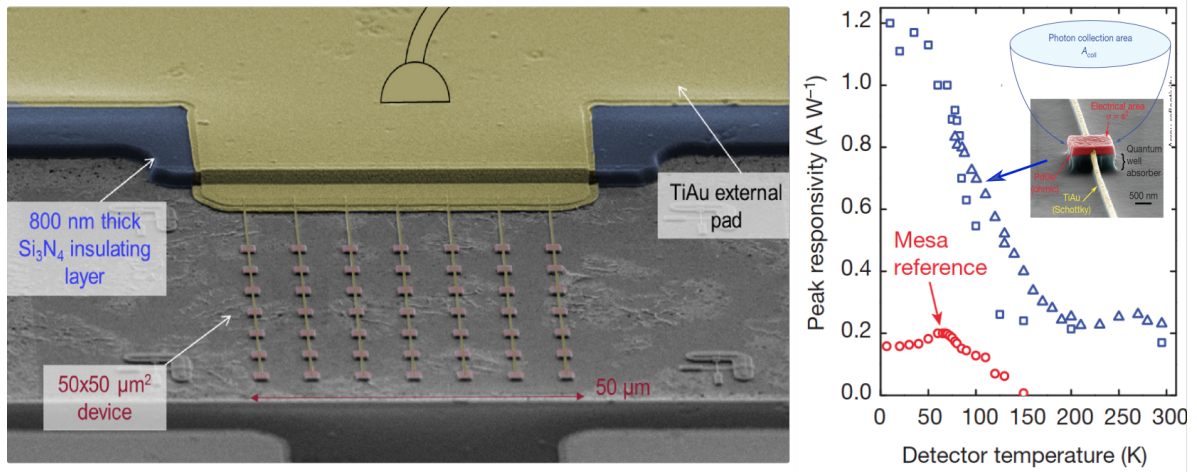


Figure 5.9: From the reference [114] (left) SEM picture of the patch-cavity QWIP. (right) Comparison between the responsivity of the patch-cavity QWIP compared to a Mesa.

A remarkable approach combining patch cavities (with patch size of $s = 1.30 \mu\text{m}$), separated by a distance of $3.30 \mu\text{m}$ and a QWIP active region with 4 QWs (for a total thickness $\sim 300 \text{ nm}$) resonant around $9 \mu\text{m}$ showed detection at room temperature (Figure 5.9, left) [114]. The main idea of this work was to shrink the volume of the detector (composed of 49 patch cavities covering a surface of $50 \times 50 \mu\text{m}^2$) to reduce the dark current while keeping the same light capture efficiency. Even without a major improvement of the $T_{Blip}^{Mesa} = 73\text{K}$ vs. $T_{Blip}^{Cavity} = 80\text{K}$, these detectors had 14 times more detectivity at room temperature than the Mesa devices (Figure 5.9, right).

Inspired by these previous and recent results, we explore in the follow up of this thesis a new strategy to improve the T_{Blip} that takes advantage of the strong coupling regime.

5.2.2 Infra-Red Detectors Operating in Strong Coupling

Simultaneously to the development of QWIPs, strong coupling in the Mid-IR has been widely studied. Influenced by the tremendous results in excitonic polaritons [59], the intersubband community has first tried to develop polaritonic emitters electrically pumped using a quantum cascade heterostructure embedded in a cavity. First, the spontaneous emission quantum cascade structures (QC-LEDs) were strongly coupled to a single plasmon cavity [4]. By applying a bias on these structures, the polaritonic electroluminescence was measured. The polaritons were distinguishable on the dispersion and in agreement with the simulations. This work associated with a theoretical framework [58] was meant to pave the way to the realization of an electrically pumped laser.

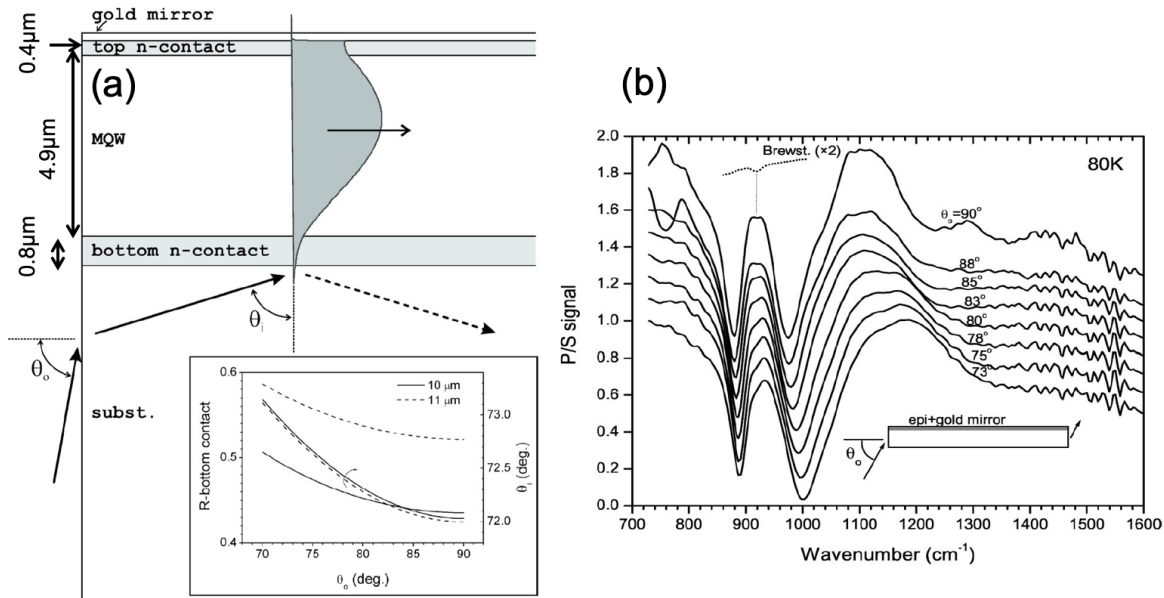


Figure 5.10: (a) Schematics of the prism-like coupling technique. The inset plot shows the reflectivity of the P-polarized light of the $0.8 \mu\text{m } n^+$ bottom layer for two wavelengths. (b) Normalized ratios between P and S-polarized transmissions through the waveguide sample for different angles of incidence [6].

A few studies tried to develop electrically injected polaritonic emitters [4, 41, 5, 51]. These approaches have been tried with different cavities as patch modes [41] or M-I-M dispersive cavities [51]. However, these developments did not achieve their final goal because most of the injected energy is dissipated into the dark states and not into the polariton states.

An alternative way to take advantage of the strong coupling properties is to explore them in detection. Effectively only the *bright* states are interacting with the electromagnetic field. So by injecting light and collecting the induced photocurrent we circumvent the *dark states* and the properties of the bright states can directly be observed. Even though this approach appears appealing, only few works have been done on intersubband detectors in strong coupling and on the electron-polariton tunneling process. The following paragraphs will present two experimental studies that have observed the strong coupling in detection.

A pioneering work was performed by E. Dupont and H.C. Liu in 2003 [6] who aimed to use strong coupling to yield a QWIP with a very low doping sheet density $2 \times 10^{10} \text{ cm}^{-2}$

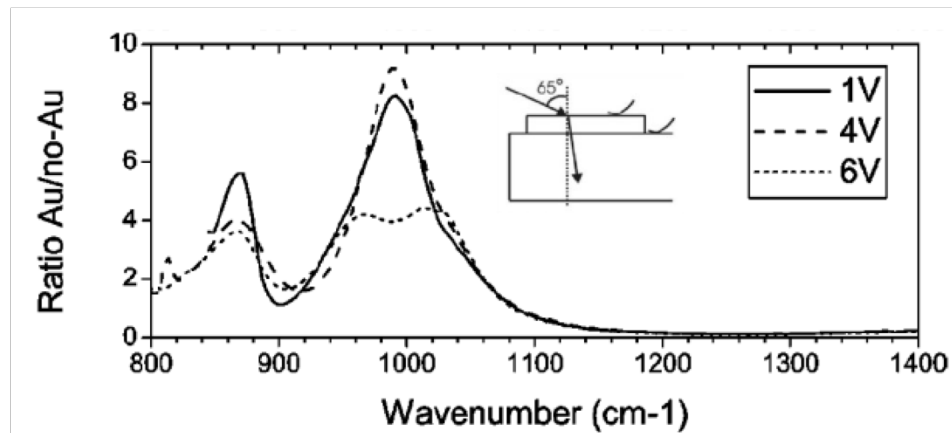


Figure 5.11: Ratio of responsivity between a device with a top GaAs/Au interface and devices with a dielectric GaAs/air interface [6]. The Rabi splitting is significantly modified with the bias. The inset shows the incident beam arriving at 65° on the structure and the two electrical contacts[6].

(20 times lower than the standard QWIPs). The dark current would then be reduced and the absorption increased [101] leading to a potential high-temperature operation. Experimentally, 140 Quantum-Wells were embedded in a single plasmon waveguide with a highly doped bottom n-contact to confine the electric field on the area of the MQWs Figure 5.10. To reach the strong coupling regime, the p-polarization (TM) has to be coupled within the waveguide. Thus the light is injected to arrive on the bottom n-contact close to Brewster's angle [115] ($\theta_i \approx 70^\circ$). Thus the incident beam on the facet of the waveguide (θ_0) should be between 70° and 90° . Note the coupling with single plasmon waveguide does not grant a large set of configurations to investigate the strong coupling regime.

By using this technique, the dispersion in transmission (Figure 5.10) was collected via different angles of incidence.

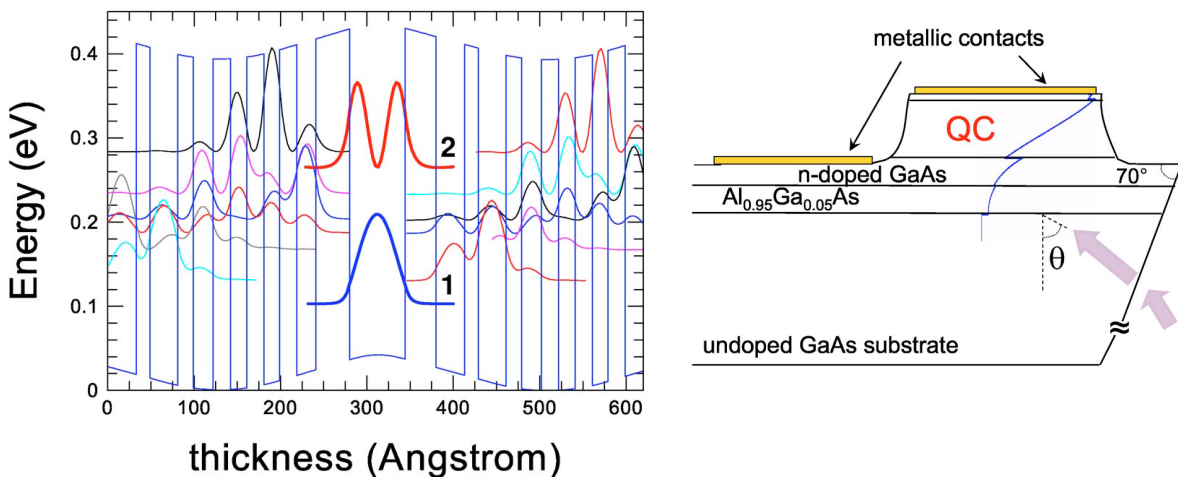


Figure 5.12: Left) QC structure with two bound states originally designed for electroluminescence [7]. Right) Schematics of the light injection onto the single plasmon cavity. The facet is polished at 70° and the beam is intersect the bottom contact with an angle θ .

Electrically, two samples were tested: one - in weak coupling - with a GaAs/Air interface

and a narrow electrode and a second - in strong coupling - with a gold mirror covering the top of the mesa. The light was impinging on the device from the top surface at an angle 65° with respect to the normal of this surface. The ratio between the spectra (Figure 5.11) of the two devices (single plasmon in strong coupling divided by air-confinement in weak coupling) performed at 80° shows two peaks at 860 cm^{-1} and 990 cm^{-1} corresponding to the polariton peaks in reflectivity (respectively 890 cm^{-1} and 990 cm^{-1}). The applied bias (from 1 to 6 V) can significantly modify the Rabi splitting.

More recently, in relation with developments on QC-LEDs [4], strong coupling has been observed with a quantum cascade (QC) structure (Figure 5.12, Left) in a single plasmon waveguide (Figure 5.12, Right) [7]. The active region operates similarly to a quantum cascade detector (QCD) even though the QC structure was initially designed for LED emission. The states ($|1\rangle$ and $|2\rangle$) are bound. On both sides of the larger QW, the electrons can flow through the thin barriers of the structure via tunneling effect.

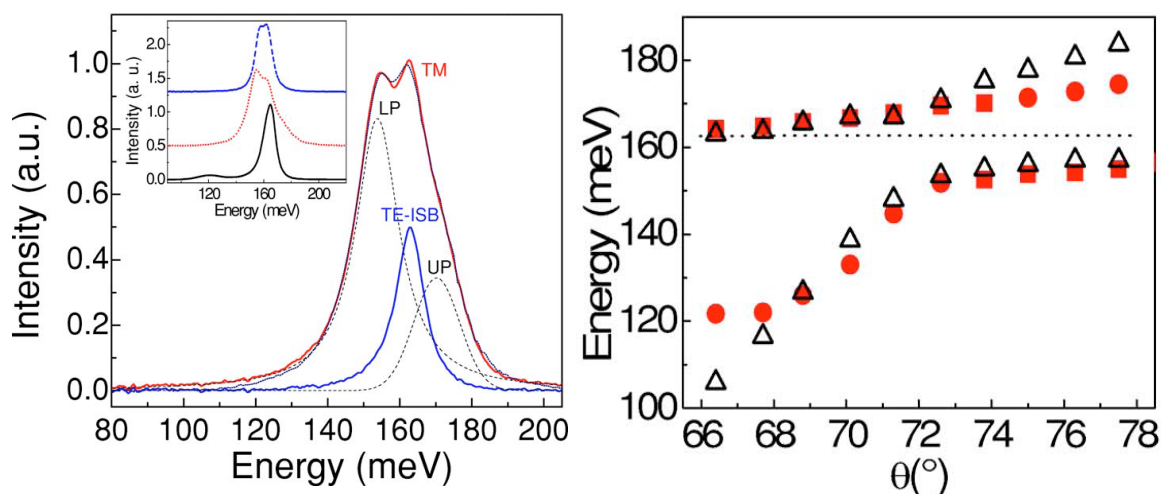


Figure 5.13: Left) Normalized photo-voltage spectra for $\theta = 75^\circ$ at 78 K . The solid lines represent the TM- and TE-polarized light respectively in red and blue. The two dashed lines labeled LP and UP, are the Lorentzian and Gaussian functions respectively, used in the fitting procedure explained in the text. The result of the three curve fit is shown by the blue-dotted line. Inset: photovoltage spectra with different incident angles: 67.7° in black, 76.3° in red and 81.2° in blue. Right) Energy position for the different photovoltage peak power as a function of the incident angle of the radiation (squares for Lorentzian function and circles for Gaussian functions) compared with the results of the transfer matrix calculation (open triangles). The dashed line is the energy of the bare ISB transition [7].

Figure 5.13, Left) shows the spectrum in photo-voltage of this QC detector for an angle of $\theta = 75^\circ$ and at 78 K . The weak coupling configuration is represented by the TE-measurement. Although the ISB transition only couples to TM mode, the spurious TE signal is possibly produced by photons that have undergone a scattering event and therefore have lost their original phase. The signal analysis shows that this signal was composed by three peaks: the lower polariton (LP, dashed line), a middle peak (TE-ISB) and the upper polariton (UP, dashed line). The TE-ISB has been adjusted in height by a factor 5 compared to the original spectrum. Note that the FWHM is significantly increased from weak (6 meV) to strong (30 meV) coupling. Note that such a broadening has recently been observed with organic

photodiodes [116].

The dispersion has been measured by injecting light at different angles θ from 57.8° to 83.6° . The inset of Figure 5.13, Left) shows the normalized spectra for $\theta = 67.7^\circ$, 76.3° and 81.2° . After peak analysis, the extracted polariton dispersion is presented Figure 5.13, Right). The shape of the dispersion confirms that the device operates in strong coupling. However, the simulation is not completely fitting the experimental results, particularly when the polaritonic branches are distant from the ISB transition. At 66° the simulation positioned the lower polariton at 105 meV when the measured photocurrent is at 120 meV. At 78° the simulation positioned the upper polariton at 180 meV when it is at 170 meV. This overestimation of the energy difference between the ISB transition and the polaritonic branch far from the anti-crossing might be related to phenomena that are not considered in the simulations.

These two works suggest that detectors are appropriate devices to observe the bright states of a ISB polariton system. These detectors in strong coupling represent a platform to explore the properties of ISB polaritons, in particular, the scattering mechanisms between the bright states.

In terms of performance, a broadening of a QCD detection range has been observed, but no significant improvement of the performances (T_{blip} , detectivity, responsivity) have been noticed.

5.3 Motivations to Study QWIPs in Strong Coupling

Increasing the T_{blip} of a detector is a major issue. To do so we need, at a given wavelength and operating temperature, to significantly reduce the dark current. The design of the cavity is an important parameter, but it appears from the previous description of the QWIP that the main limitation is the dark current direct link to the activation energy. What would be the impact of the strong coupling on the thermal activation? Is it possible to disentangle the thermal activation energy from the energy of the absorbed photons?

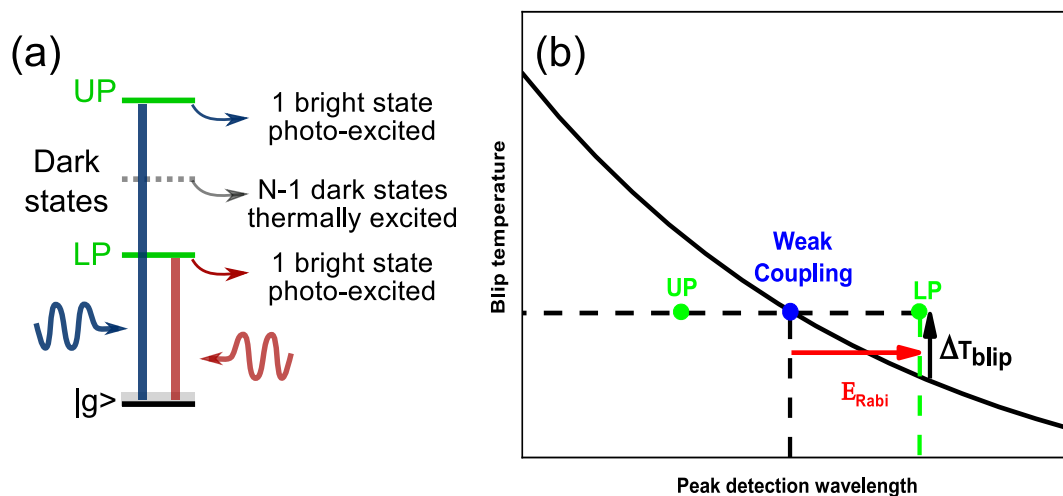


Figure 5.14: (a) Schematics of the dark and bright states relative energy levels of a SC-QWIP. The $N-1$ dark states contribute to the dark current and the two bright states contribute to the photocurrent. (b) T_{blip} as a function of the peak detection wavelength. In strong coupling the lower polariton detects at lower wavelength with the same T_{blip} .

Part 3 of this thesis has been initially motivated by this vision: can operation in strong coupling affect the T_{Blip} ? We have at first step explored if a QWIP in strong coupling (SC-QWIP) can detect photons at energies different than a QWIP with the same active region but that operates in weak coupling.

Schematics 5.15, a) shows the relative energies of the different accessible states. Considering N electrons on the ground state and 1 photon in the cavity, we obtain in strong coupling two bright states (LP and UP) and $N-1$ dark states. The $N-1$ dark states are thermally activated at an energy level close to the activation energy (E_{act}). The major contribution to the dark current in strong coupling are the dark states. The bright states couple with electromagnetic waves and contribute to the photo-current. By introducing the Rabi energy $E_{Rabi} = \hbar\Omega_{Rabi}$, we can write

$$\begin{cases} E_{WC} = E_e - E_g \approx V_b - E_g = E_{act} \\ E_{SC,LP} \approx E_e - E_g - \hbar\Omega_R < V_b - E_g = E_{act} \end{cases} \quad (5.18)$$

Where E_{WC} is the detection energy in weak coupling, $E_{SC,LP}$ is the energy of the lower polariton, E_e and E_g the energy levels of the excited and ground states and V_b the barrier potential.

As an example, we consider an ISB transition at $\lambda = 8\mu m$. According to Figure 5.15 the activation energy fixes the blip condition at $T_{blip}(\lambda = 8\mu m) = 85K$ ($\tau_{life} = 10$ ps carrier lifetime). A cavity in weak coupling does not impact the value of the transition energy nor the activation energy and cannot reach blip conditions above $85K$.

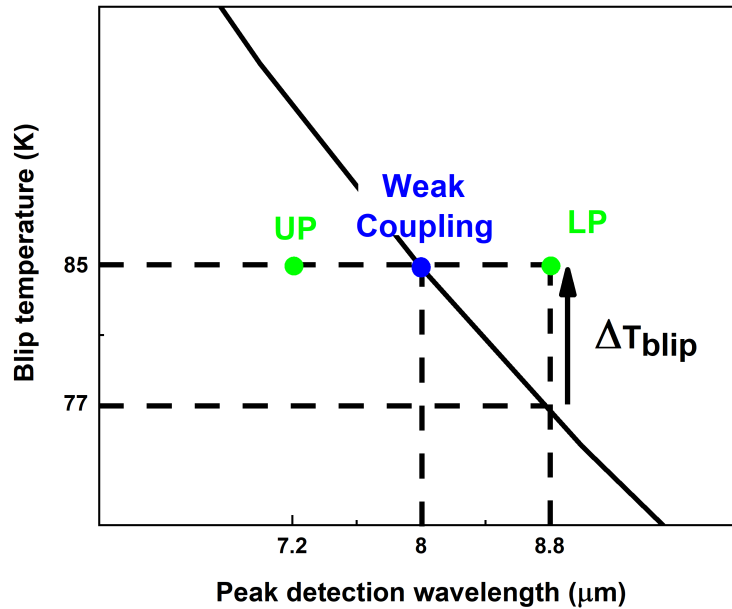


Figure 5.15: Extracted data from the Figure 5.5 with a carrier lifetime $\tau_{life} = 10ps$.

In strong coupling, two polaritonic states are generated on each side of the transition. By considering a Rabi splitting ($2\hbar\Omega_R$) at 20% of the transition, we obtain a lower polariton at $\lambda = 8.8 \mu m$. In this range of wavelength ($8.8 \mu m$) the T_{blip} of a QWIP in weak coupling

would not exceed 77K ($T_{blip}(\lambda = 8.8 \mu m) = 77K$) whereas the QWIP in strong coupling could in principle be operated under blip condition until 85 K.

For our study we decided to operate at $\lambda = 10 \mu m$ where the T_{blip} is low and the slope $dT_{blip}/d\lambda$ is high. In addition, QWIPs in strong coupling with a dispersive cavity are an ideal platform to explore the fundamental properties of ISB polaritons.

A second motivation to study SC-QWIPs is to get information on the microscopic mechanisms underlying the tunnel-coupling process of a polariton (collective state) into an electronic (single particle) state. Recent developments based on the electrical injection of polaritonic devices (LEDs and lasers [4, 5, 60]) could not efficiently excite the bright states because most of the electrons tunnel into the dark states. We studied a detector because dark states do not play an important role as incoming photons only excite bright polariton states. This is a strong motivation for developing SC-QWIPs and SC-QCDs, as they appear as an ideal system to elucidate elusive problems in intersubband polaritonics.

5.4 Conclusion

In this chapter, we presented some fundamental concepts related to detectors. We illustrated them with two types of detectors in weak coupling.

The photo-detection appears to be an efficient technique to study the ISB polaritons. Because the electromagnetic field interacts only with the bright states, there is no implication of the dark states in this process.

In addition, the strong coupling could be an elegant solution to disentangle the detection energy window of a QWIP from the thermal activation energy. The literature reports two works in which intersubband detectors operate in strong coupling[6, 7]. In both cases, a single plasmon cavity was used. The ISB polaritons have been observed and in the QCD, case the dispersion measured in photovoltage. The comparison of the dispersion measurement with the simulations was not completely satisfying, suggesting that some unknown processes might be at stake. In terms of performance, these two prospective studies did not report significant improvements compared to the same structure in weak coupling.

Inspired by these previous results, our approach introduces a M-I-M cavity with more degrees of freedom to couple with the ISB transition and to access experimentally more angles, particularly close to $k_{//} = 0$. The first step would be to integrate this cavity with a QWIP active region for two reasons: (i) to confirm the generation of photocurrent from the polaritonic states, (ii) to exploit the strong coupling regime to disentangle the detection energy from the activation energy.

Quantum Well Infrared Detectors in Strong Coupling

In this last chapter, we propose a metal-insulator-metal cavity design to explore the dispersion of a quantum well infrared photodetector operating in strong coupling (SC-QWIP). The issues at stake are twofold: in term of device performances, the strong coupling is used to disentangle the detection wavelength ($E_{\text{detection}}$) from the thermal activation energy ($E_{\text{activation}}$). In terms of polaritonics, we expect to gain insight on the alignment between *dressed* (polaritons) and single particle (electrons) states.

As a first step, the active regions are characterized in weak coupling: multipass and single plasmon mesa devices. Secondly, the losses in the M-I-M cavity are discussed to evaluate their impact on the detector properties.

Finally, the new generation of SC-QWIP is studied electrically and in angle-resolved photoresponse. These results have been published in Ref.[15].

6.1 Active Region

Three structures have been grown by molecular beam epitaxy (Table 6.1, epitaxy by G.Biasiol) on a SI-GaAs substrate with a 400 nm stop-layer. They consist of 31 repetitions of 6.5 nm-thick GaAs QWs separated by 20 nm-thick $Al_xGa_{1-x}As$ barriers where x is the Alumina fraction (x=20/25%). The QWs are nominally doped in the center to $n_{2D} = 4.24/8.48 \times 10^{11} \text{ cm}^{-2}$, and the structure is sandwiched by 100 nm-thick n^+ -GaAs contact layers (see the growth sheets in Appendice B.2).

Figure 6.1 shows the wavefunctions inside the quantum well for two different barrier energy levels after solving the Schroedinger-Poisson equation. The distance between the excited state ($|e\rangle$) and the top of the barrier is significantly different in these two cases. In the case of low barriers (Figure 6.1, (a) the excited state is 3 meV below the barrier whereas in the case of the higher barrier (Figure 6.1, (b) this distance is 22 meV. Consequently, we expect to observe differences on the dark current and responsivity between these two structures. In this manuscript, we will consider these two QWs as bound-to-quasi-bound.

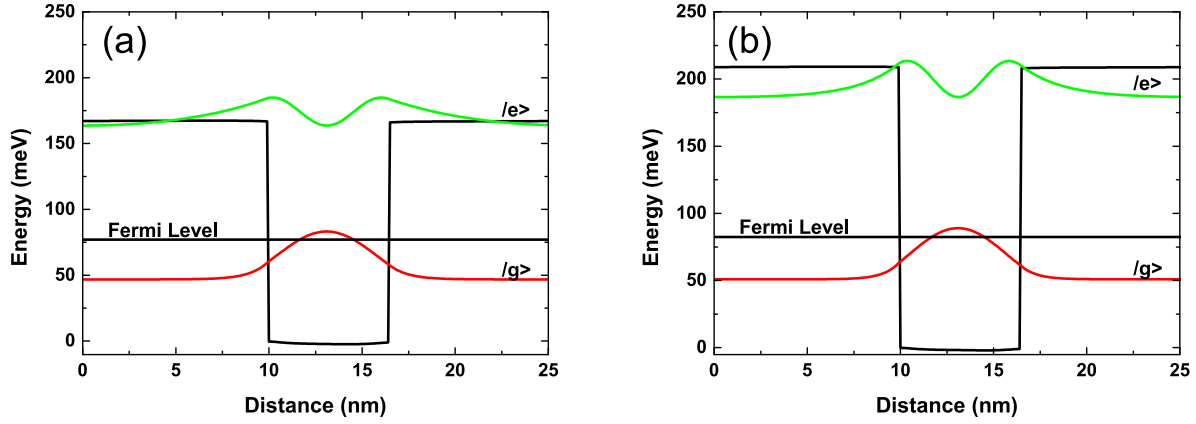


Figure 6.1: Schrodinger-Poisson simulation of the energy levels inside the structures: (a) HM4059 with 20 % Al fraction in the barriers, (b) HM4065 with 25 % Al fraction in the barriers. The Fermi energy is calculated for a doping of $8.48 \times 10^{11} \text{ cm}^{-2}$.

6.1.1 Multipass Measurements

The initial characterization is the multipass waveguide transmission. A thin portion of the wafer is cleaved, the top surface is coated with gold and the two facets of the waveguide are polished at 45° . The light injected through the polished facets propagates with several reflections inside the wave-guide (5 to 10 passes through the active region). The signal that has crossed many times the active region is then collected on the detector of the FTIR.

Figure 6.2 presents the spectra of the samples HM4058, HM4059, and HM4065. The transmission spectra of the low barrier sample HM4059 (Figure 6.4 (b)) shows an ISB transition at 939 cm^{-1} with a FWHM of 10.4% at room temperature. The transition is blue shifted at low temperature up to 968 cm^{-1} , and the FWHM decreases to 8.1%.

At room temperature, the ISB transition of sample HM4065 is at 1091 cm^{-1} with a FWHM of 9.1%. At 78 K the transition is blue shifted to 1098 cm^{-1} , and the FWHM is narrower 7.3%. The blue shift at 78 K stems from a combination of (i) increase of the conduction band offset and (ii) increase of the electronic carrier density in the ground state.

The absorption of the sample HM4058 has been measured only at room temperature. The transmission spectra is presented in Figure 6.2, (c), the ISB transition is at 968 cm^{-1} and the FWHM is 12.8%.

All multipass measurements are resumed in Table 6.1.

Sample name	Doping 10^{11} cm^{-2}	Barrier Al %	ISBT cm^{-1} @300K	FWHM @RT (%)	ISBT cm^{-1} @78K	FWHM @78K (%)
HM4058	4.24	20	921	12.8		
HM4059	8.48	20	939	10.4	968	8.1
HM4065	8.48	25	1060	9.1	1098	7.3

Table 6.1: Inventory of the three different heterostructures received for the project and their ISB Transitions measured in multipass waveguide configuration.

In the perspective of this project, we investigated the samples with the higher doping (HM4059 and HM4065) essentially. These samples will have a larger Rabi splitting ($\Omega_R \propto$

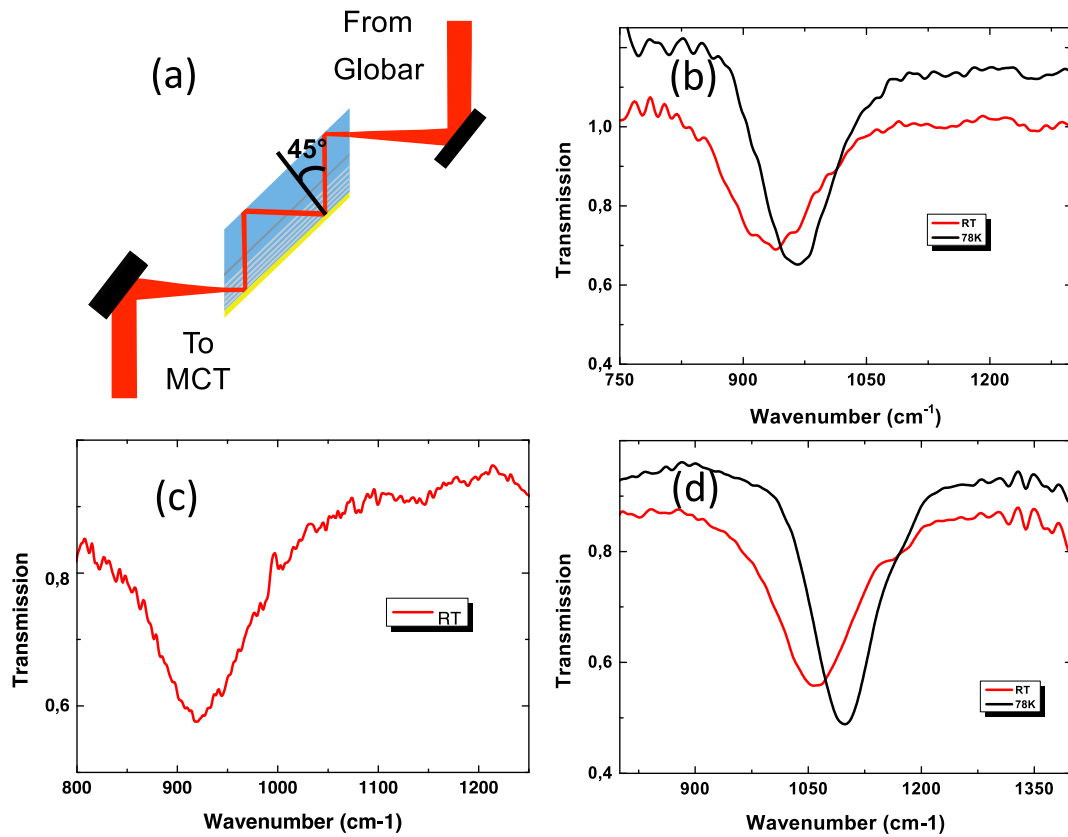


Figure 6.2: (a) Schematics of the multipass measurement collecting the light on a MCT detector. (b) HM4059 (c) HM4058 and (d) HM4065 multipass absorptions performed inside a purged Bruker FTIR

$\sqrt{N_{3D}}$). The sample HM4058 gives information about the responsivity of the detector in weak coupling instead.

6.2 QWIP in Weak Coupling: Mesa Resonator

In this second section, I present the fabrication of the reference devices operating in weak coupling. I processed these samples in the cleanroom of C2N-Orsay and I characterized them.

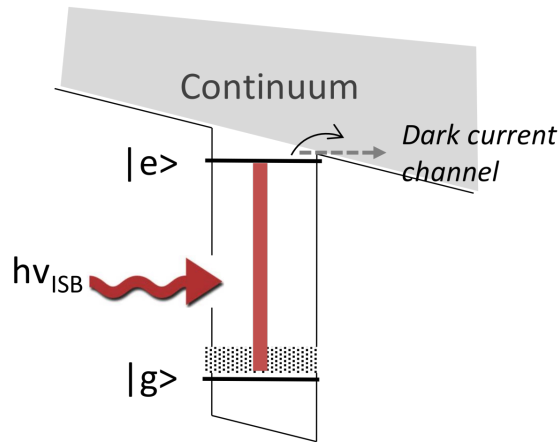


Figure 6.3: Schematics of a biased QWIP operating in weak coupling. The position of the excited level $|e\rangle$ sets the detection wavelength and the dark current.

6.2.1 Mesa: Design & Fabrication

The sample is patterned in square mesas of 1 mm or 300 μm sides. A positive tone photoresist (S1818) is used as a mask for GaAs/AlGaAs wet etch with a sulfuric acid solution. The etch depth is carefully controlled during the process with a mechanical profilometer to stop into the bottom n^+ -GaAs slab, allowing the subsequent bottom contact definition. Ni/Ge/Au/Ni/Au bottom metallization surrounding the mesas is defined via negative tone photoresist and lift-off. The evaporated layers are then annealed at 420°C for 1 min in a rapid thermal annealing (RTA) oven to create a diffused ohmic metal-semiconductor contact.

Similarly, Pd/Ge is evaporated on the mesas top surface and annealed at 360°C for 5 min. Pd/Ge contact is preferred here due to its short diffusion depth (a few tens of nm) in contrast with Ni/Ge/Au/Ni/Au which diffuses farther in the semiconductor and could then damage the active region. A second top contact evaporation (Ti/Au) is performed to facilitate the application of wire bonds. Finally, the sample is back-polished and a back Ti/Au contact is evaporated to guarantee a good mechanical and thermal contact with the copper block used to mount the sample in the cryostat.

Before mounting the sample, the facet is polished at 45° to inject light from the substrate into the mesa. The mechanical polishing leads to a quasi-mirror surface to avoid light diffusion at the surface.

Finally, the sample is mounted with indium on a copper block. The polished facet is manually positioned at the edge of the copper block. Moreover, the contacted Mesa are chosen close to the facet to maximize light capture before reflection inside the sample.

a) MBE growth



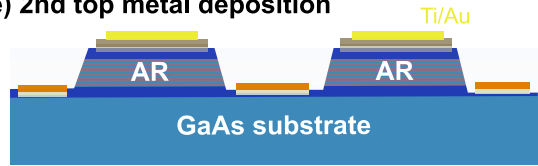
d) 1st top metal deposition + annealing



b) Mesa wet etch



e) 2nd top metal deposition



c) Bottom contact deposition + annealing



f) Back side polishing and metalization



Figure 6.4: Schematics of the mesa processing.

6.2.2 Measurements

In the following, I will present mostly the results of the two heterostructures with higher doping HM4059 and HM4065. Although they have drawbacks concerning their dark current, they should exhibit a larger Rabi-splitting when operated in SC due to their high doping.

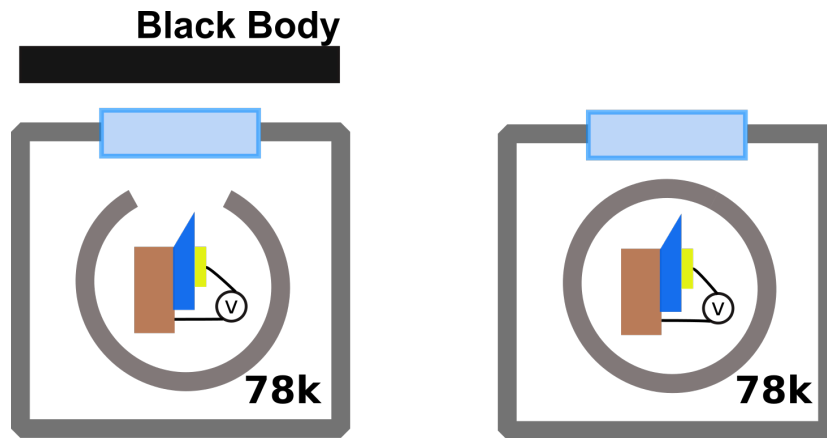


Figure 6.5: Schematics of the photo- (left) and dark- (right) current measurements.

Dark Current

The measured dark currents are presented in Figure 6.6. Specific instrumentation source meter as *Keithley 2636* is required to measure the IVs at room temperature and at 78K. The IVs of the Mesa were acquired from $-1V$ to $1V$ (Figure 6.6). At low temperature, the dark current decreases by three orders of magnitude compared to the room temperature measurement.

The photo-current generated by a black body at room temperature (placed at 10 cm from the detector with a field of view of 24° , Figure 6.5) is not displayed because it was too weak

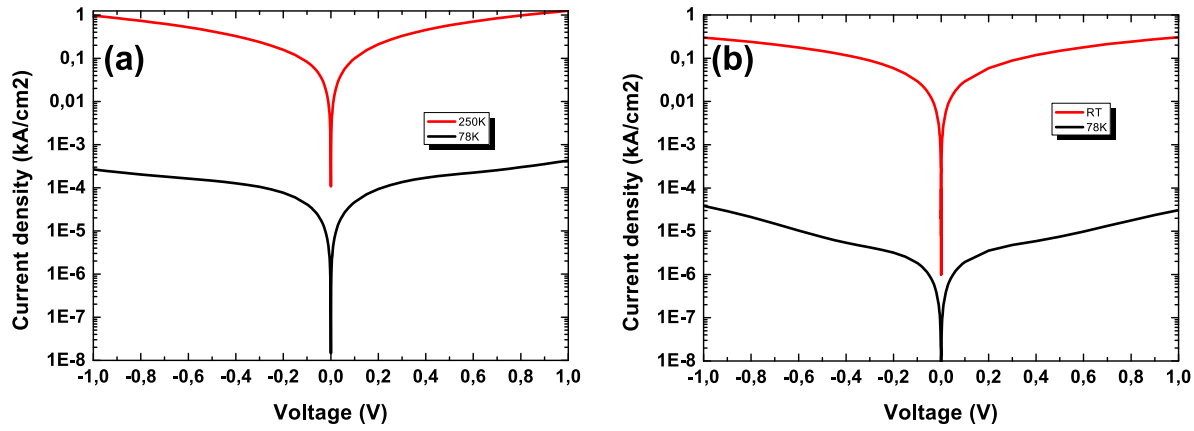


Figure 6.6: Absolute value of the dark current density measured for two mesa samples: (a) HM4059 75 μm diameter; (b) HM4065 200 μm diameter.

compared to the dark current and the total current is superposed to the dark current curve. To overcome this difficulty a warmer calibrated blackbody could be used, but we did not have this type of instrument in our lab. Nevertheless, this high dark current did not appear critical to measure the spectra of a *Globar* source and to explore the properties of strong coupling.

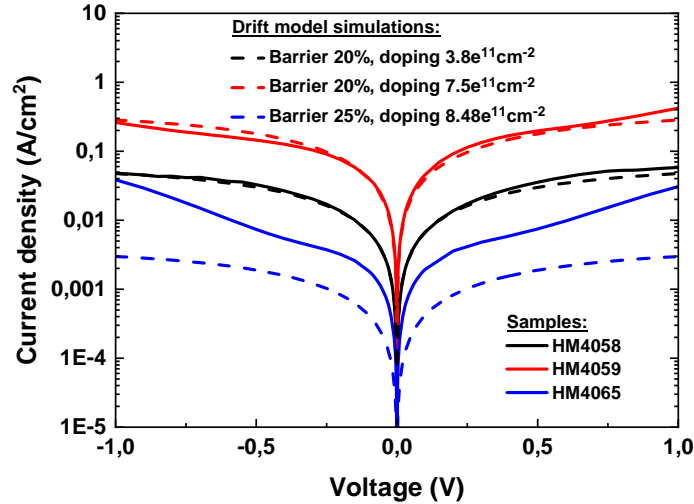


Figure 6.7: Comparison of the dark current at 78K (plain lines) of three different heterostructures in mesa configuration. The dashed lines are simulated dark currents with the 3D carrier drift model. The activation energy -considered independent of the voltage- has been calculated with a Shroedinger-Poisson model. The energy exchange was equal to -13.6 meV.

We observe that the dark current density of HM4065 is smaller than the one of HM4059 (almost a decade) at 78K whereas it is similar at room temperature. Because these two samples have the same doping the only parameter that explains this difference is the alumina fraction. As we saw in the previous chapter the high alumina fraction raises the barrier potential. Consequently, the excited state of HM4059 is closer to the continuum than the sample HM4065. Thus HM4059 behaves more as a bound-to-quasi-bound QWIP whereas HM4065 behaves as a bound-to-bound QWIP. In the bound-to-bound structure, the activation

energy to reach the continuum is higher which reduces the dark current. In the following we will see that the dark current has a major impact on the SC-QWIP performances.

The comparisons between dark current densities at 78K of the three heterostructures and the 3D drift model simulations are presented Figure 6.7. For the samples with low barriers (HM4058 in black and HM4059 in red) the simulations fit with the measured dark current density. The increase of the dark current with the doping is also respected. The increase of the barrier potential increases directly the activation energy and sharply reduces the dark current (dashed blue lines). However, the experimental dark current of the HM4065 is one order of magnitude higher than the simulation predictions.

This disagreement suggests that the heterostructure HM4065 has a source of dark current that is not taken into account in the 3D shift model. An additional mechanism could be the sequential resonant tunneling [117]. In the context of this work, we did not try to apply a second model to this phenomenon.

The peculiarity of the sample HM4065 is also visible on the optical spectra. Nevertheless, the structure HM4065 still has the lowest dark current of the three heterostructures and has been chosen to operate in strong coupling.

Optical spectra

Once mounted in the cryostat, the sample is cooled down to 78 K. The output signal of the FTIR is sent into the device through the facet. To align the sample on the focal point of the ZnSe lens (2 inches diameter, 2 inches focal) a chopper modulates the incident beam at a frequency of 11 Hz (below the cut-off of the amplifier) and the electrical signal is measured after amplification with a lock-in amplifier. After optimizing the position of the sample, and the amplification, the signal of few millivolts on the Lock-In is directly measurable in rapid scan on the FTIR.

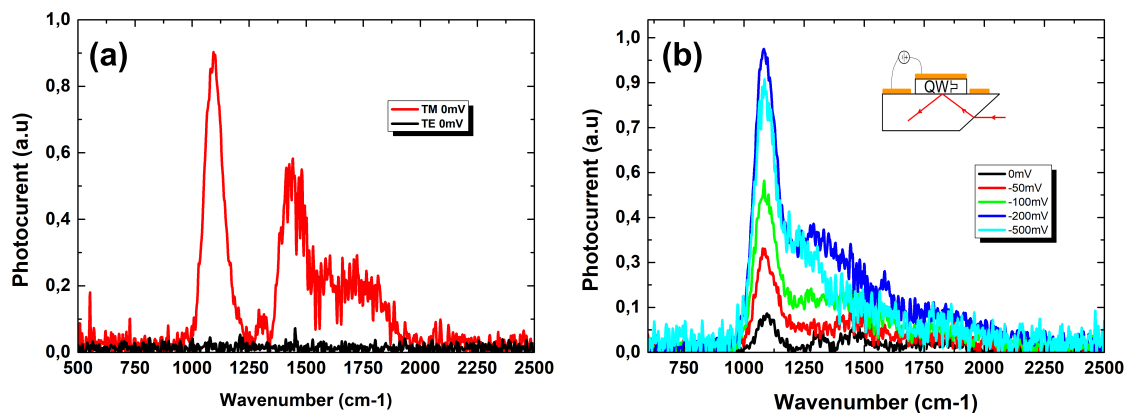


Figure 6.8: HM4065 Mesa photocurrent: (a) at no bias for different light polarizations (TE and TM), (b) for different biases without polarizer.

Figure 6.8 shows spectra of the sample HM4065 light polarization (a) and at different biases (b). As expected, the active region interacts only with TM-polarized radiation. The main peak of photocurrent is related to the bound-to-quasi-bound transition. The effect of the bias on the spectra intensity is important (Figure 6.8, (b)). At zero bias it is already possible to measure a signal due to the internal field generated by the in-homogeneity of the

doping layers or the contact. When a bias is applied on the structure the potential is leaned (Figure 6.3) and the barrier between the continuum and the excited state of the bound-to-quasi-continuum QW (HM4065) decreases. The photo-excited electrons can then access the continuum and participate in the photocurrent. For the sample HM4065 the maximum of the signal is obtained for a negative bias of -0.2 V. At higher biases, the dark current is increased without a significant increase of the photocurrent. A signal decrease (as seen at 0.5 V) is observed as the amplification of the low-noise amplifier must be reduced to avoid saturation.

At higher frequencies, we observe that the samples behave differently from standard QWIPs that have only one peak of photocurrent. In fact a broad photoresponse signal (1300 cm^{-1} and 1500 cm^{-1} at 0 V) is observed that is not predicted by the theory. This high frequency signal could stem from the transition towards the continuum. However, it is difficult to infer the exact cause of this peculiar behavior from electrical and optical characterizations. This phenomenon is not crippling for the observation of the polaritons via the photocurrent, but has to be taken into account in the discussion.

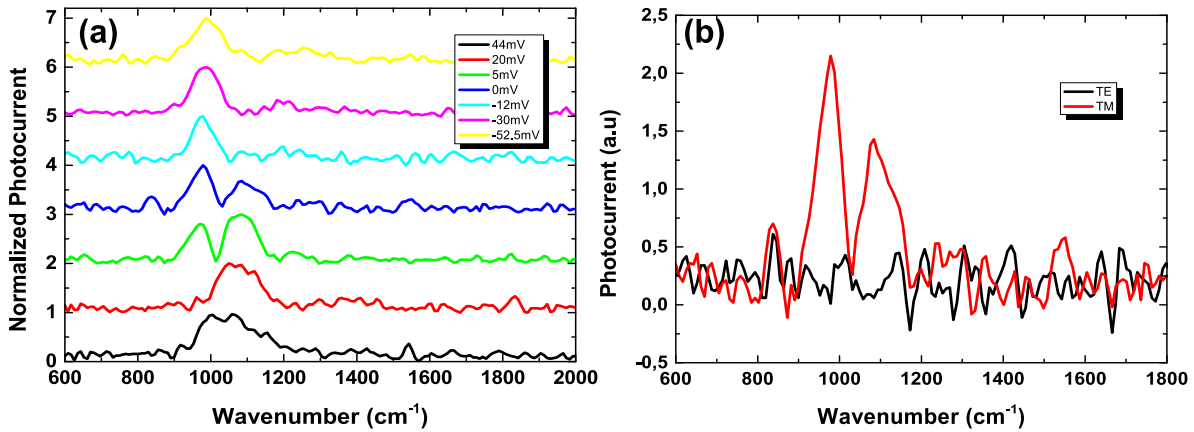


Figure 6.9: Photocurrent of the Mesa HM4059 100 μm diameter: (a) at no bias for different light polarizations, (b) for different biases without polarizer.

Figure 6.9 shows the spectra for different biases for the sample HM4059. The detection window of this second heterostructure is narrower than the mesa HM4065, and there is no signal above 1025 cm^{-1} . At zero bias the photocurrent has two peaks around 1025 cm^{-1} (Figure 6.9, (a)), the low-frequency peak is increased when a negative bias is applied, whereas the high frequency peak is increased when a positive bias is applied.

Despite a narrower spectral window, this sample has a drawback which is the signal to noise ratio that is two times smaller than sample HM4065 at 0 V. This is possibly due to the height of the barriers that is lower for HM4059 and leads to an elevated dark current. For this reason, we cannot operate at high biases (100 mV) without saturating the amplifier.

Responsivity

The dark current and photocurrent (blackbody source at 300 K describes in detail in the supplementary of [18]) have been measured for HM4058, HM4059 and HM4065 at 78 K (and even at liquid Helium temperature for HM4059 and HM4065). The photocurrent has been clearly observed only for the sample HM4058 (Figure 6.10, (a)).

To calculate the power impinging on the detector, we first calculate the radiance L of a blackbody at 300 K using the Planck's law over the detector spectral sensitivity window

(between 26.4 THz and 31.9 THz). In this range the radiance is $L = 19.27 \text{ W}/(\text{m}^2 \text{sr})$. Only a part of this power reaches the detector due to the surface of the detector (A_p) and the field of view of our experiment ($\theta = 48^\circ$) giving a projected solid angle $\Omega = \pi \sin^2(\theta/2) = 0.519 \text{ sr}$. The impinging power can then be estimated $\mathcal{I} \approx LA_d\Omega_d = 752 \text{ nW}$.

The responsivity is then written as the ratio of these two components

$$R = (I_{\text{BlackBody}} - I_{\text{dark}})/\mathcal{I}, \quad (6.1)$$

and calculated for each voltage. The maximum value of the responsivity is 0.4 A/W for a bias of $\pm 500 \text{ mV}$. This value is comparable with mesa performances of similar works [6, 114, 118].

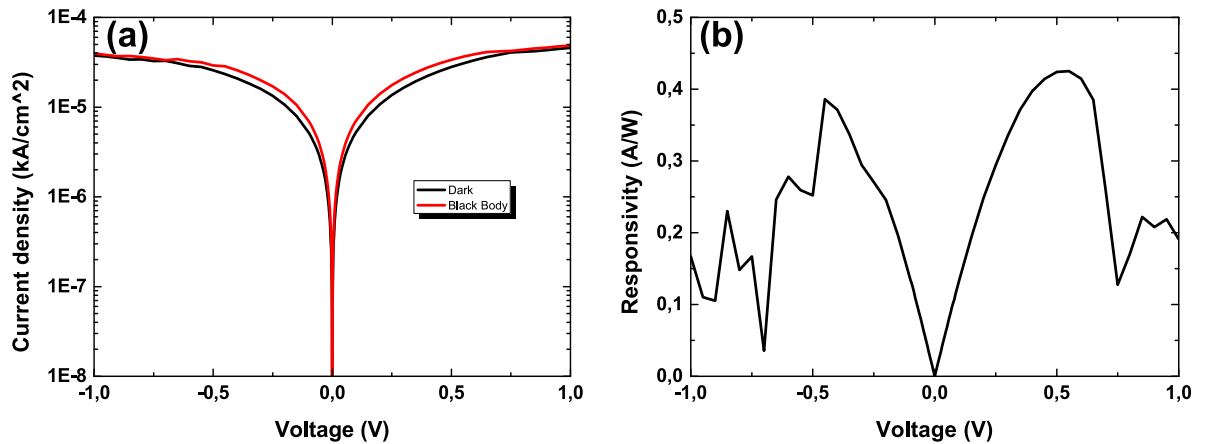


Figure 6.10: (a) HM4058 comparison between dark- and photo-current densities at 78 K in Mesa configuration. (b) Responsivity of the same sample.

However, for the two other heterostructures (HM4059-HM4065) we could not extract the photocurrent from the dark-current and thus calculate the responsivity. One main reason is probably the doping that is twice higher in these heterostructures. The doping increases significantly the dark current as we show Figure 6.7 where the dark current of HM4059 ($8.48 \times 10^{11} \text{ cm}^{-2}$) is almost one decade higher than the one of HM4058 ($4.24 \times 10^{11} \text{ cm}^{-2}$). For the same reason, a high doping can reduce the T_{flip} . On the other hand, HM4065 has the lowest dark current. We do not have a definitive explanation for the very low responsivity of this sample.

A second way to measure the responsivity would be to have a blackbody at a higher temperature (3000 K for instance). However, we did not have a calibrated source to calculate precisely the responsivity. That is why the following discussion will mainly focus on the properties of the QWIPs in strong coupling more than their performances.

6.2.3 Conclusions QWIPs Measurement in Weak Coupling

This measurement campaign on the mesa showed that all the heterostructures were detecting in the mid infrared, but that the performances of the detectors highly depend on the doping and the alumina fraction of the barriers. The compromise between a high doping and a low dark current seems to be obtained with sample HM4065 with high alumina fraction in the barrier. We will, therefore, focus on this active region in the following.

6.3 QWIP in Strong Coupling: Simulations, Design and Fabrication

After the design and the characterization of three active regions in the weak coupling, we present the design of the cavity of these active regions. First, RCWA simulations are performed to define the best geometry for the cavity. Second finite element simulations explore the impact of the metal layers on the total losses of the cavity. Third, an intermediate sample is then fabricated to confirm the simulations with a dispersion measurement in reflectivity. Finally, the SC-QWIP process is presented.

6.3.1 Simulations & Cavity Optimization

In the previous section, the characteristics of the active regions have been precisely determined. These characteristics will be implemented in the simulations to design the appropriate cavity.

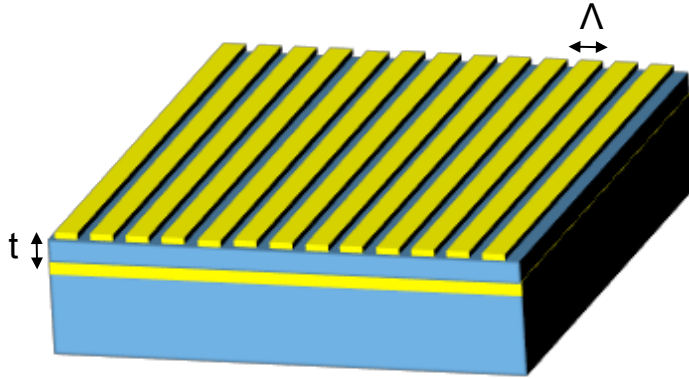


Figure 6.11: Schematics of the M-I-M in the Mid-IR. The thickness t of the cavity is equal to $1 \mu m$ and the grating period Λ varies between $3.2 \mu m$ and $4.5 \mu m$.

Rigorous Coupled Waves Analysis (RCWA)

The RCWA code - already presented in Chapter 2 - is used to select the proper range of grating periods to observe strong coupling. According to previous works in photo-luminescence (and global perspective of electrically pumped polaritonic emitters), we designed our cavities to couple the ISB transition with the 3^{rd} photonic branch. In fact, in this configuration, the lower polariton dispersion as a minimum at $k_{||} = 0$ which is convenient to access experimentally. The cavity thickness is chosen below the cut-off ($t = 1 \mu m < \lambda / (2n) \approx 1.4 \mu m$) in order to work with the TM_{00} mode only. In this preliminary work, we simulated a large set of grating periods to analyze the strong coupling in different configurations.

In Figure 6.12, two different grating periods ($3.2 \mu m$ and $3.7 \mu m$) have been simulated. Because of the 3^{rd} photonic modes redshifts when the grating period increases, the minimum splitting with the ISB transition occurs at different angles (from 65° to 0°). On these graphs in reflectivity, only the polaritonic branches have to be considered because the photonic branches are not supposed to yield a photocurrent (not coupled with the active region).

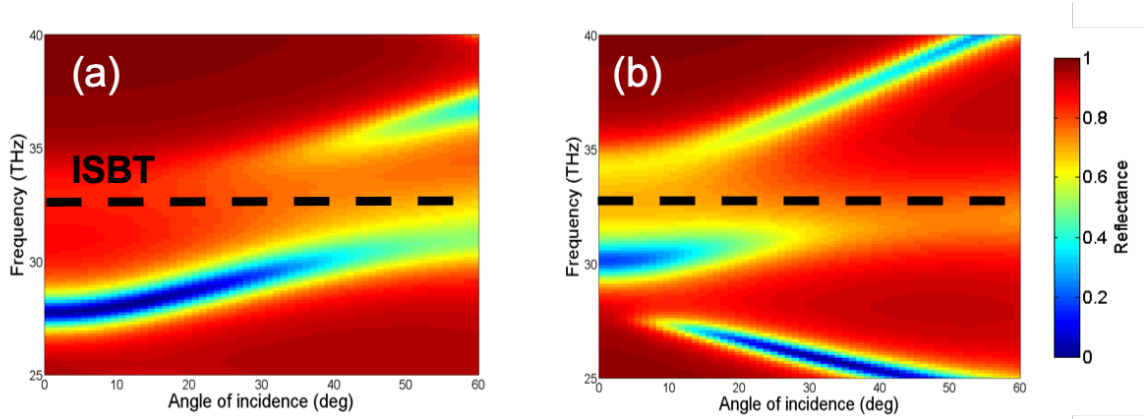


Figure 6.12: Reflectivity simulations using a RCWA code on the sample HM4065 (transition at $32 THz$, $\gamma = 13.9\%$ and doping $8.48 \times 10^{11} cm^{-2}$) for different grating periods: (a) $3.7 \mu m$, (b) $3.2 \mu m$.

From the detection point of view, the larger grating period (a) is interesting because the Rabi splitting is below 35° , which is the common field of view of a QWIP. Considering the absorption, it seems that the period $3.5 \mu m$ has a higher integrated absorption over angle and frequencies. The smaller grating period (b) has a more fundamental interest. In fact, for this sample, the LP reaches much lower frequencies (down to $25 THz$ for the $4 \mu m$ sample) with respect to the peak detectivity frequency of the QWIP when operating in the weak coupling regime ($32 THz$). One of the objectives of the following experimental work is also to observe if such a widening of the QWIP detection window towards a larger wavelength is possible.

Considering the RCWA simulations we designed cavities with the grating periods: between $3.2 \mu m$ and $4 \mu m$ for HM4065 and between $3.6 \mu m$ and $4.2 \mu m$ for HM4059. Nevertheless, these first simulations only take the absorption into account and need to be completed with additional simulations considering the interaction of the polaritons with the continuum of states above the barriers, that yield the photocurrent signal.

Finite Element Simulations

The association of QWIP and M-I-M resonators raises the issue of the role of the metal losses. In fact, the losses in the QWs provide photocurrent, whereas the losses in the metal provide only heating. Potentially the losses of the metal could compete with the absorption of the QWs and deteriorate the performance of the detector. To compare these two losses, we use finite-element simulations to calculate the electromagnetic field at each point of the detector.

The structure is simulated in 2D considering the direction parallel to the slits infinite. Two planar gold mirrors are separated by a $1 - \mu m$ -thick active region. The width of the elementary cell is fixed at $4.1 \mu m$ with periodic conditions on the edge, and the top metal is $3.3 \mu m$ wide representing a filling factor of 80% (Figure 6.13). The transition was chosen at $27.23 THz$ with a FWHM of $3.8 THz$ and the dielectric function was calculated using the Zaluzny formalism [36].

In *Frequency Domain* analysis we have simulated the structure for different angles of incidence and at different frequencies. The simulation in finite element are compatible with the RCWA simulations in terms of absorption peaks position and amplitude for photonic and polaritonic branches. When the electromagnetic wave is not resonant with the cavity it

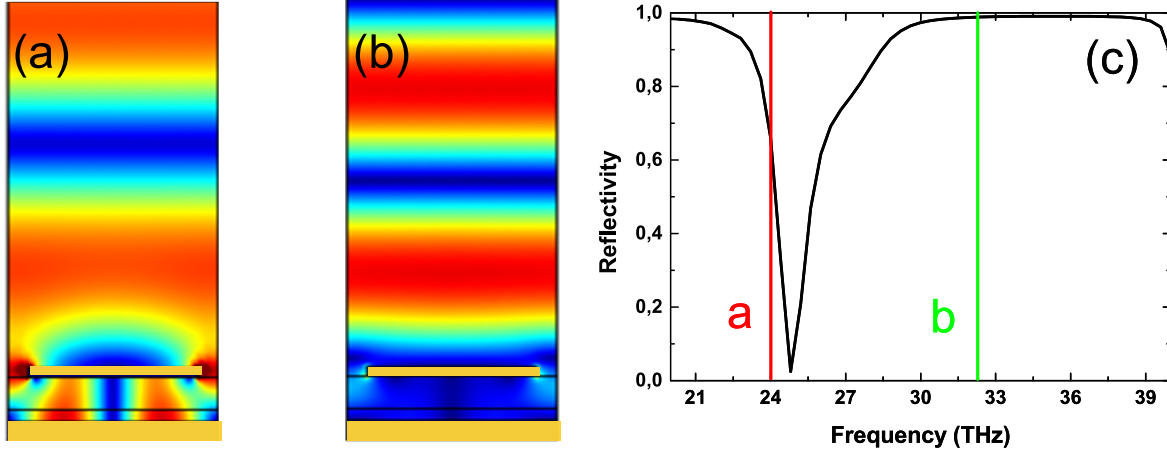


Figure 6.13: (a) and (b) FEM simulations of the norm of the electric field ($|E|^2$) for a $4.1 \mu\text{m}$ grating period, a doping of 4.24 cm^{-1} and an incident beam at 0° , in a region of low absorption at 32 THz (b) and a region of high absorption at 24 THz (a). (c) represents the spectra at 0° . The red line corresponds to the panel (a) and the green line to the panel (b).

is completely reflected by the top metal. At the resonant frequencies (Figure 6.13 (b)) the electric field penetrates in the cavity and can interact with both the active region and the metal planes.

To discriminate which area will absorb the most we calculate the resistive losses (W). The resistive losses are generally calculated by integrating the differential form of the Joule heating equation $dP/dV = \vec{j} \cdot \vec{E} = \sigma(\omega)|E|^2$ over the considered volume. Because in these simulations we are working in two dimensions we are calculating the linear resistive function (W/m) obtained with the surface integration

$$Q_r(\omega, \theta) = \iint_S \text{Im}(\epsilon(\omega)) |E(\omega, \theta)|^2 dS, \quad (6.2)$$

where the dielectric function of the active region is calculated with the Zaluzny-Nalewajko model [36], and the one of the metal is calculated with the Drude model

$$\begin{cases} \epsilon_{\text{metal}}(\omega) = 1 + \frac{j\sigma(\omega)}{\epsilon_0\omega} \\ \epsilon_{\text{AR}}(\omega) = \epsilon_\infty \left[1 - f_0 \frac{\epsilon_\infty^2}{\epsilon_\omega^2} \frac{\omega_p^2}{\omega_{12}^2 - \omega^2 - j\omega\Gamma_{12}} \right]^{-1} \end{cases} \quad (6.3)$$

From Equation (6.2) it is difficult to predict which parameter will be dominant between the surface of integration (larger for the active region) and the conductivity (much higher for the metal).

Consequently, an analytical calculation of resistive losses has to be performed for each angle and at each frequency. The color plots for different dopings of the QWs are presented in Figure 6.14 for the active region (Left) and the metal (Right).

In the empty cavity ($n_{2D} = 0 \text{ cm}^{-2}$) almost all the EM field is absorbed by the metal. The resistive losses on the 3^{rd} photonic branch are in the order of $\sim 0.4 \text{ W/m}$ versus $\sim 3 \times 10^{-3} \text{ W/m}$ inside the dielectric.

The introduction of a doping ($5 \times 10^{-10} \text{ cm}^{-2}$) inside the QWs increases the resistive losses on the 3^{rd} photonic branch by two orders of magnitude inside the active region ($\sim 0.4 \text{ W/m}$). The AR losses become comparable with the losses inside the metal. An explanation of this

result is that the surface of absorption of the EM field in the metal is limited by the skin depth ($\delta = \sqrt{\frac{2}{\sigma_0 \omega \mu_0}} = 13.8 \text{ nm}$), while the active region thickness is $1 \text{ }\mu\text{m}$. Consequently, the integration surface of the resistive losses appears dominant.

At low doping $5 \times 10^{10} \text{ cm}^{-2}$ the polaritons do not exist yet. When the losses increase ($4.24 \times 10^{11} \text{ cm}^{-2}$ and $8.48 \times 10^{11} \text{ cm}^{-2}$) the signature of the polaritons - on the 3rd photonic branch - appears on the resistive losses because the absorption of the cavity is modified. The losses in the QWs increase (on the LP $Q_{AR} \sim 0.8 \text{ W/m}$ and the radiation is rapidly absorbed by the active region. The losses in the metal decrease then significantly ($Q_{metal} \sim 0.1 \text{ W/m}$).

In summary, these preliminary simulations show that for highly doped QWs the resistive losses inside the active region are dominant, and the losses inside the metal planes can be neglected. These results were *a priori* predictable considering the patch cavity detectors in Ref.[114]. Nevertheless, the M-I-M geometry is different from the patch cavity, with different active region thicknesses and top metal patterning that could have impacted the absorption and the energy dissipation. It was then judicious to reevaluate the distribution of the resistive losses that confirms the feasibility of the introduction of M-I-M dispersive cavities for detection applications.

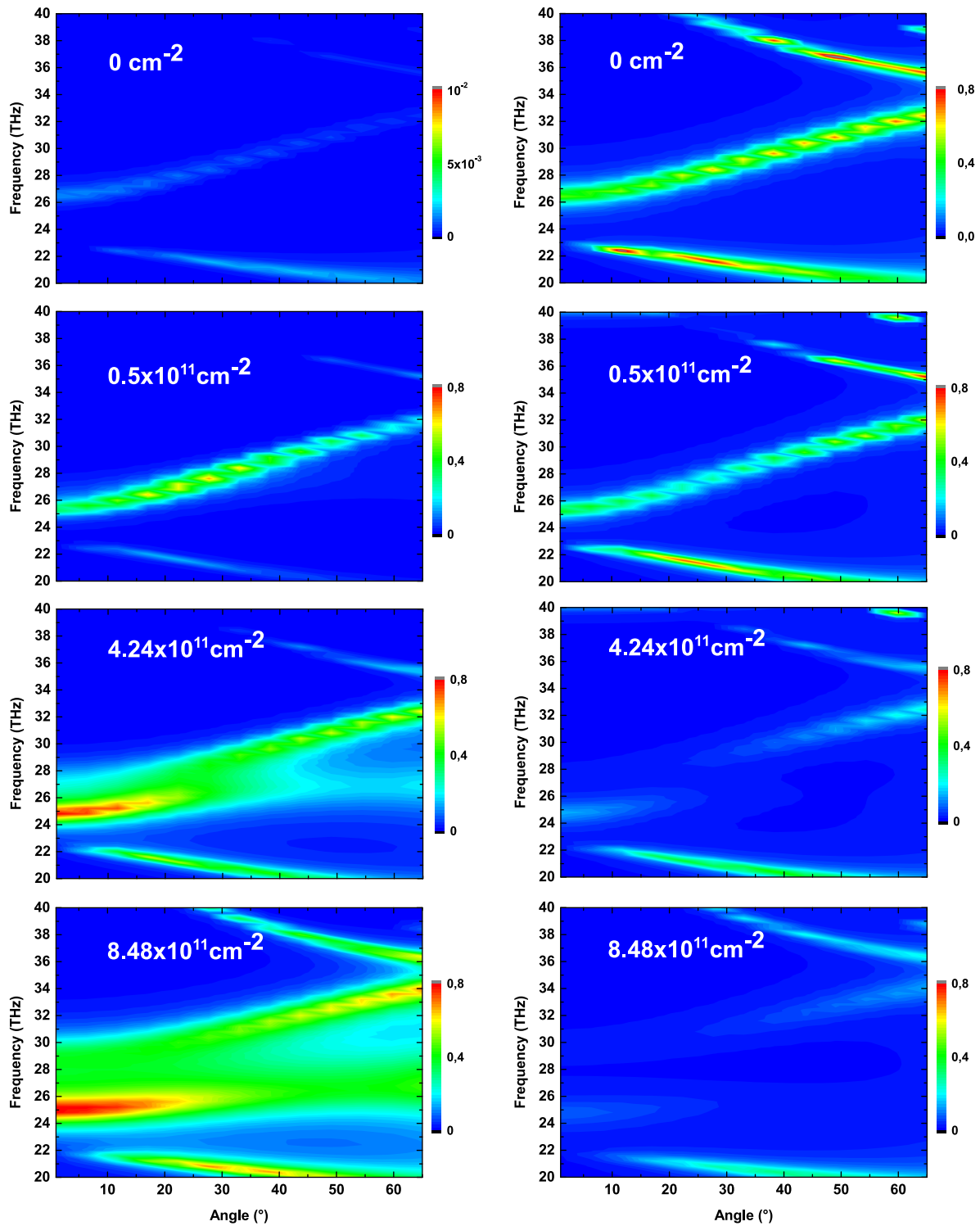


Figure 6.14: Linear resistive losses simulations in W/m (color scale) inside the active region (Left) and inside the top and bottom metals (Right) for different dopings in a grating of $4.1 \mu m$ period and a filling factor of 80%.

6.3.2 Experimental Dispersion in Reflectivity

We have first implemented a very large ($2.2 * 2.2 \text{ mm}^2$) metal-AR-grating passive dispersive resonator with sample HM4065 using the design and fabrication procedure reported in Ref.[12]. This architecture is extremely practical as the polaritonic dispersion can be easily probed with angular-resolved surface reflectivity. The result reported in Figure 6.15 shows the room-temperature photonic dispersion (energy vs incidence angle, color plot) $R(E, \theta)$ as inferred from the reflectivity measurements. The upper (UP) and lower (LP) polaritonic branches are clearly observed, evidence that the system operates in the strong light-matter coupling regime.

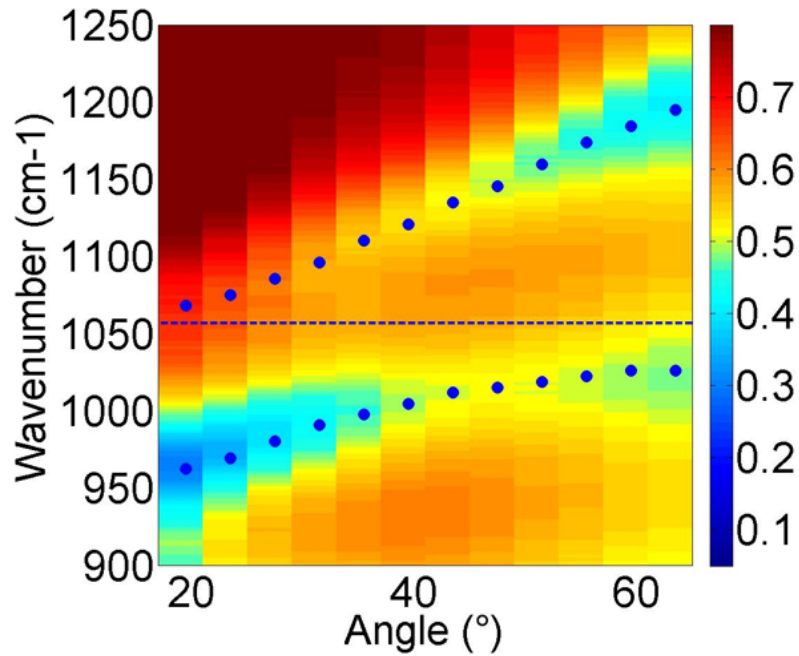


Figure 6.15: Dispersion in reflectivity of the HM4065 grating period $3.8 \mu\text{m}$, duty cycle 70% at room temperature and comparison with simulations absorption minima (blue dots) to set the experimental geometry. The blue dashed line represents the position of the ISB transition absorption.

The dots in Figure 6.15 indicate the position of the reflection minima predicted for the two polariton branches using a RCWA (rigorous coupled wave analysis) numerical simulation of the structure with the nominal parameters, except for the doping that has been set to $n_{2D} = 5.5 \times 10^{11} \text{ cm}^{-2}$, instead of $8.48 \times 10^{11} \text{ cm}^{-2}$ as per growth sheet. Once this reduced doping level is included, the agreement with the experiment is excellent, which fully confirms that RCWA simulations can be employed as an extremely predictive numerical tool in the analysis that follows.

6.3.3 SC-QWIP: Fabrication & Design

I then processed the SC-QWIP. Figure 6.16 presents the different steps of this process.

Wafer Bonding & Substrate Removal

The first step of the process is to deposit the bottom ohmic contact on the active region [119]. The ohmicity of the contact is assured by a Pd/Ge deposition (25/75 nm) annealed at 360°C during 5 minutes [120, 121]. The resulting contact ensures the ohmicity at this interface and the adhesion of the metal. After the annealing there is a reprise of Ti/Au (10/200 nm) for the wafer bonding.

The two wafers are then bonded together (Figure 6.17, (a)) by their metallic surfaces in the wafer bonder (parameters 45 min/ 320°C/4.5 MPascal).

After the wafer bonding, the active region is in the middle of the new wafer. A polishing of the active region substrate is then required to uncover the active region again (Figure 6.16, (b)). The first hundreds of micron are mechanically polished. Then a chemical citric acid solution - citric powder/H₂O/H₂O₂ 3:3:1 warmed up at 40°C - etches the last few microns at a rate of 2 μm/min until the stop layer. This stop layer (Al₅₀Ga₅₀As) protects the active region from the chemical etching.

The last step consists in removing the stop layer using a fluoridric acid (HF) etching. The active region on top of the bottom contact is then ready to be processed (Figure 6.17, (b)).

Grating: E-beam lithography

According to the simulations, the desired grating must have a period between 3 and 5 μm with a filling factor between 70% and 90%. Thus the smallest pattern of the grating is below 500 nm and requires electron beam lithography that is limited by the diffraction of the electrons De Broglie wavelength of few nanometers. Thus by using an electron flux, it is possible to achieve the necessary resolution on a PMMA resist (Figure 6.17, c).

Once the grating is written and developed on PMMA A6 (thickness 300 nm), a titanium-gold (5-70 nm) deposition is performed on the sample. Then the sample is submerged in acetone for the lift-off (Figure 6.17, (d)).

Electrodes

Once the grating is deposited, electrodes are fabricated in order to extract the current from the system. One precaution to be taken is to force the photocurrent to flow below the grating in the region where the strong coupling takes place. To do so a layer of 300-nm SiN (Figure 6.17, (e)), deposited by PECVD at high frequency and etched with 30-minute plasma CHF₃ (Figure 6.17, (f) and (g)), is deposited below the electrode (Figure 6.17, (h) and (i)). The electrode is then deposited (Ti 10nm/Au 300 nm) on the SiN and at the edges of the grating (Figure 6.17, (i)).

Finally to reduce the dark current and access the bottom contact, the remaining bare active region is etched (Figure 6.17, j and k) using ICP recipe R17 (Chapter 4).

According to the results in weak coupling, the process has been performed on the two active regions with the higher doping: HM4059 and HM4065. Effectively these two samples present suitable properties for strong coupling. Their high doping is particularly use to obtain

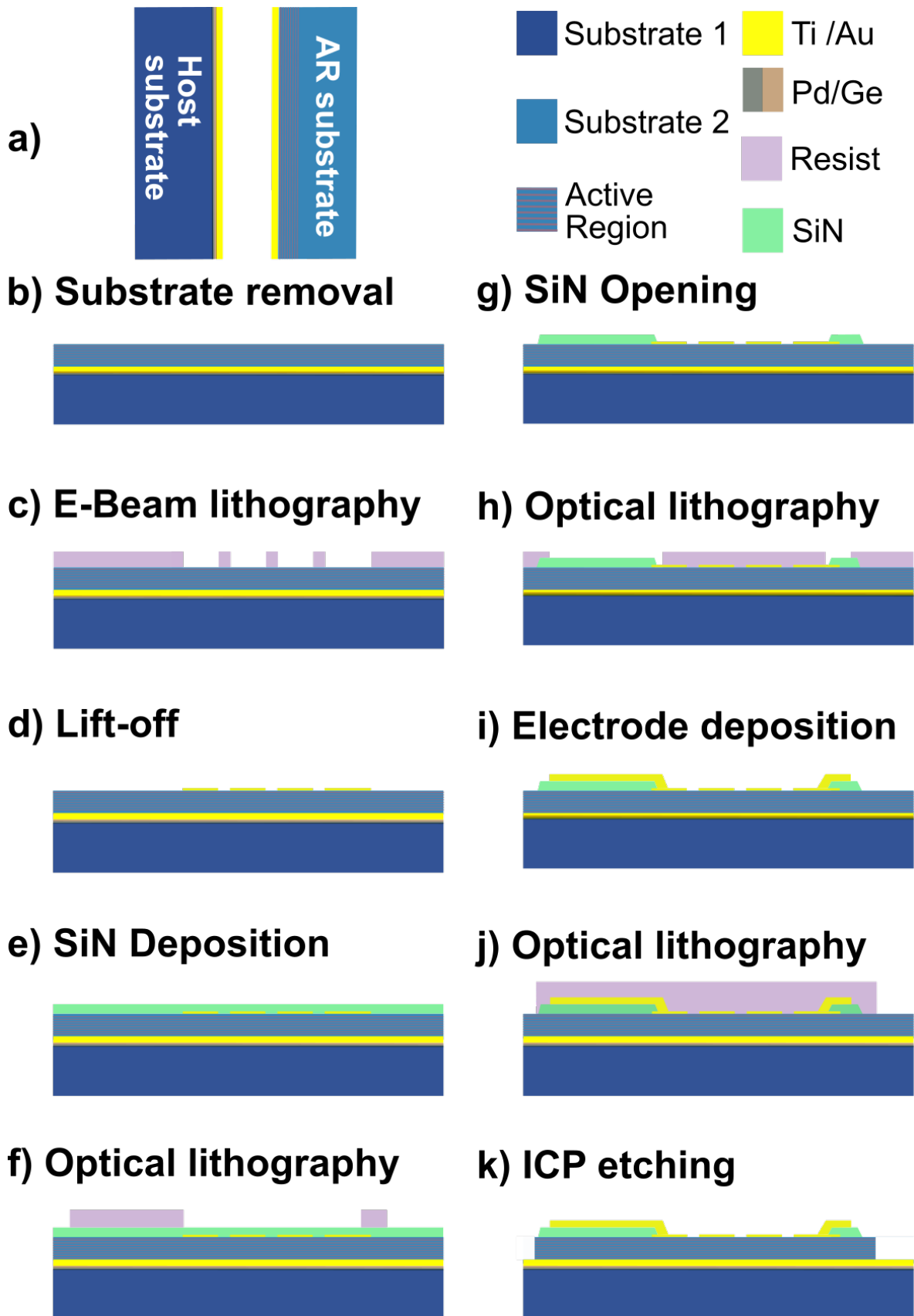


Figure 6.16: Schematics of the SC-QWIP process.

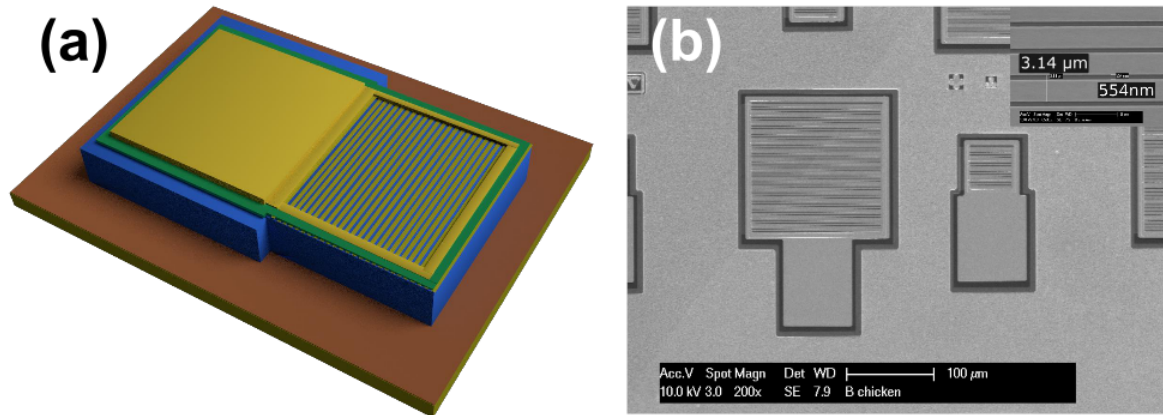


Figure 6.17: a) 3D image of the final device representing: the active region (blue), the SiN insulator (green), the gold top contact (yellow) and ohmic PdGe bottom contact (dark orange). b) SEM image of two final devices with the same grating period $\Lambda = 3.2 \mu\text{m}$ and different grating area $150 \times 150 \mu\text{m}^2$ (left) and $50 \times 50 \mu\text{m}^2$ (right).

a large Rabi splitting. The major drawback of the high doping is that it strongly increases the dark current (cf. Chapter 5). The T_{Blip} is then hampered.

However, the strong coupling in principle could compensate the impact of the doping by disentangling the detection frequency from the thermal energy activation. Theoretically it is difficult to evaluate which effect would be dominant on the T_{Blip} between the doping and the strong-coupling. To define a hierarchy between these two competing phenomena experimental characterizations are essential.

6.4 SC-QWIP Measurements

The specificity of SC-QWIP characterization is to measure the photocurrent dispersion of the devices to gain a maximum of information about the polaritonic branches. Thus the measurement is angle-resolved and requires a specific set-up.

6.4.1 Experimental Set-Up

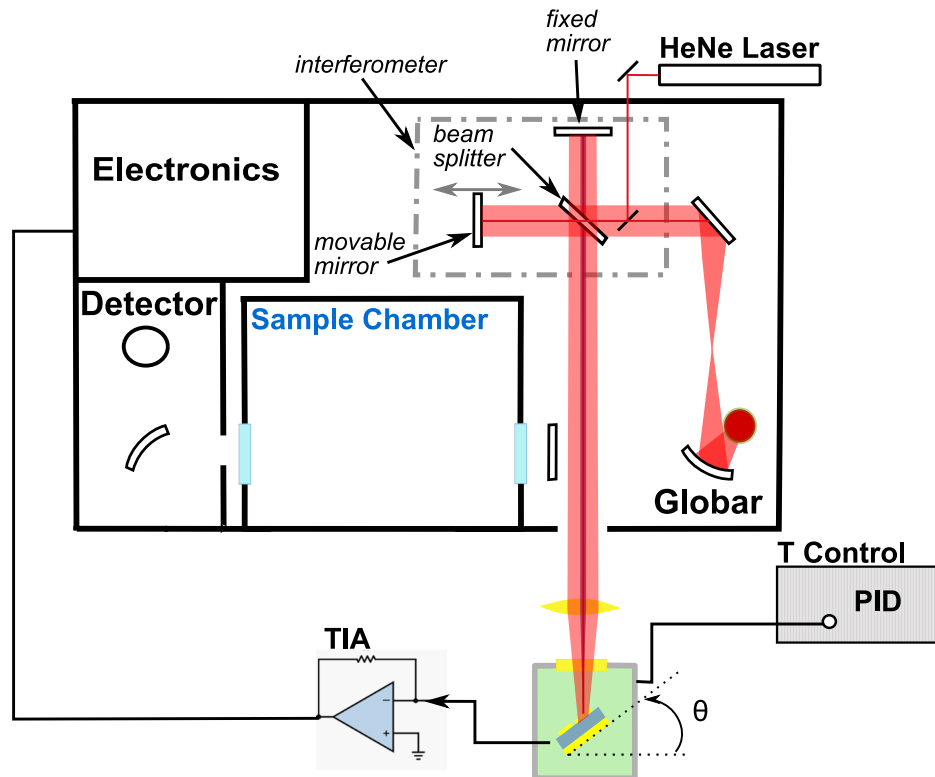


Figure 6.18: Schematics of the experimental set-up with the SC-QWIP measured as an external detector. The SC-QWIP is cooled at 78 K and can rotate inside the cryostat.

During the experiment, the FTIR and the box containing the cryostat are purged with nitrogen. The head of the cryostat is designed to position the sample close to the center of rotation of the system. In this configuration, the sample is at 4 cm from the cryostat window, and a long focal length (4 inches) is needed to align the sample with the focal point. Besides the diameter of this ZnSe lens must be large (2 inches) in order to focus the maximum of light coming from the broadband source (Globar) onto the detector.

As the photocurrent is weak (down to pA) and bias needs to be applied, we use a Low-Noise Current Preamplifier (Stanford SR570) to transform a low current signal into a measurable voltage.

The amplifier has a different calibers named sensitivity (in A/V). The sensitivity limits the modulation frequency (20 Hz at 1 nA/V). Typically the optimum operating point of the SC-QWIP was 5 nA/V and 20 Hz for zero bias.

The amplifier can also apply a bias on the SC-QWIP. Under bias, more current goes through the structure, and the caliber has to be decreased to avoid saturation. With a bias

of 500 mV , the sensitivity caliber was of the order of 500 nA/V . Note that the caliber would change significantly from one sample to another.

Once the sample is cooled we search for the signal using a lock-in amplifier (LIA). First, we modulate the signal by adding a chopper on the optical path. The output current of the detector is sent after amplification to the LIA.

Because the LIA is synchronized with the chopper, only the signal with the appropriate frequency is detected. Note that this technique enables to filter the noise from the black body radiation of the environment.

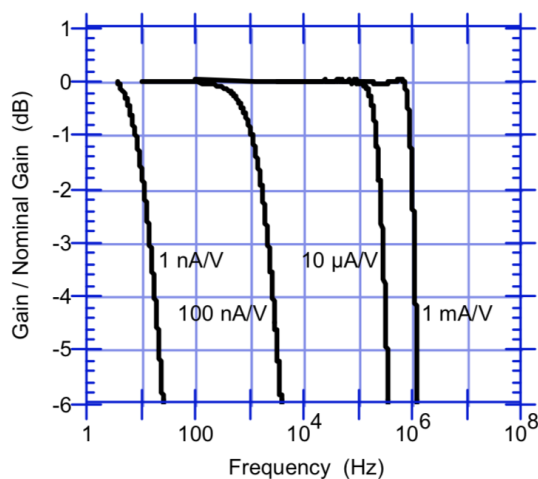


Figure 6.19: Amplifier Stanford SR570 bandwidth for several sensitivity settings in Low Noise Mode (extracted from the manual).

The LIA was principally used to align the sample, as for the best SC-QWIP sample we had typically 1 mV on the lock-in that is sufficient to measure in rapid scan mode. The measurement in step-scan was not showing better spectra than in rapid scan.

The influence of the polarizer and a Si filter to cut the red laser signal have been tested in weak and strong coupling. The heterostructure absorbs TM polarized radiation as expected, in weak and strong coupling. The Si filter was a fast indicator of the quality of a detector. In fact, all the detectors were responding to the HeNe laser of the FTIR spectrometer that we used to align the detector. Once the sample was aligned, the Si filter was introduced on the optical path filtering the HeNe laser. If a signal was remaining on the LIA after this step it meant that the detector had a response in the Mid-IR, as a Globar source was used.

6.4.2 Measurements

Electrically the SC-QWIPs behave differently from the Mesa devices. First, the IVs are asymmetric due to only one ohmic bottom contact. Compared to the mesa IVs, the dark current at room temperature is lower for the SC-QWIP and at 78 K it is the mesa dark current that is lower compared to the SC-QWIP.

Second, from 300 K and 78 K the dark current density is decreased by two orders of magnitude against four for the mesa. The sample HM4065 (Figure 6.20, (b)) appears to have a higher reduction of photocurrent compared to the sample HM4059 (Figure 6.20, (a)).

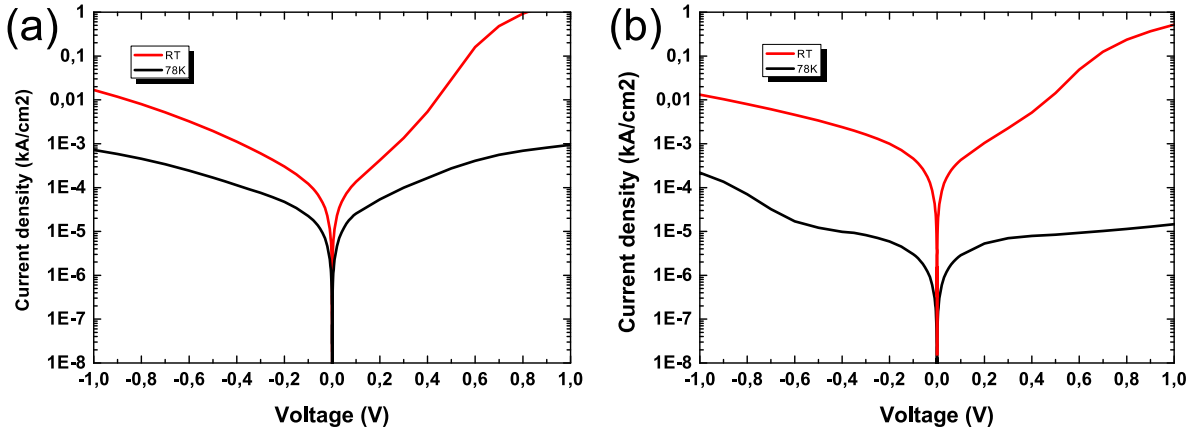


Figure 6.20: Dark current measurement at room temperature and 78K for $150 \times 150 \mu\text{m}^2$ SC-QWIP samples HM4059 (a) and HM4065 (b).

Since the information on the alignment of the polaritonic *vs* single-particle states is obtained from the comparison between absorption *vs* photocurrent spectra, it is crucial to verify that the polaritonic absorption is not affected by the presence of the electric field when the detector is operated under bias.

Figure 6.21, (a) shows reflectivity spectra at 78K for different biases performed on a $3.5 \mu\text{m}$ grating period, 80% filling factor (FF) SC-QWIP device. The overall size of the grating ($150 \times 150 \mu\text{m}^2$) is much smaller than the one of the passive devices, so reflectivity measurements have been performed with a FTIR microscope at a fixed incidence angle of 20° . To cool down the sample, we use a platform equipped with a cryogenic system (T95 Linkam system controller) and compatible with the microscope FTIR measurement. The absorption peaks of the polaritons (upper polariton 1140 cm^{-1} , lower polariton 1015 cm^{-1} and 2^{nd} photonic branch at 880 cm^{-1}) are not sensitive to the bias. The results confirm that the polaritonic absorption is unaffected by the applied bias.

Photo-current measurements have been performed on the two samples HM4059 and HM4065. The samples yield is relatively low probably, due to inhomogeneous annealing of the electrical bottom contact. Nevertheless, the sample HM4065 rapidly appeared as the sample with the better detection properties and tolerating high voltages (up to 2 V). Three grating periods ($3.2 \mu\text{m}$, $3.7 \mu\text{m}$ and $4 \mu\text{m}$) have been consistently measured with excellent reproducibility.

As for the Mesas, the SC-QWIPs can operate as photovoltaic devices, but the optimal signal is obtained for bias between 0.5 V and 1 V (respectively to the Mesa results). The common sensitivity on the Amplifier is $1 \mu\text{A}/\text{V}$. These parameters result from a compromise between the bias and the sensitivity. In fact, the bias increases the current going through the

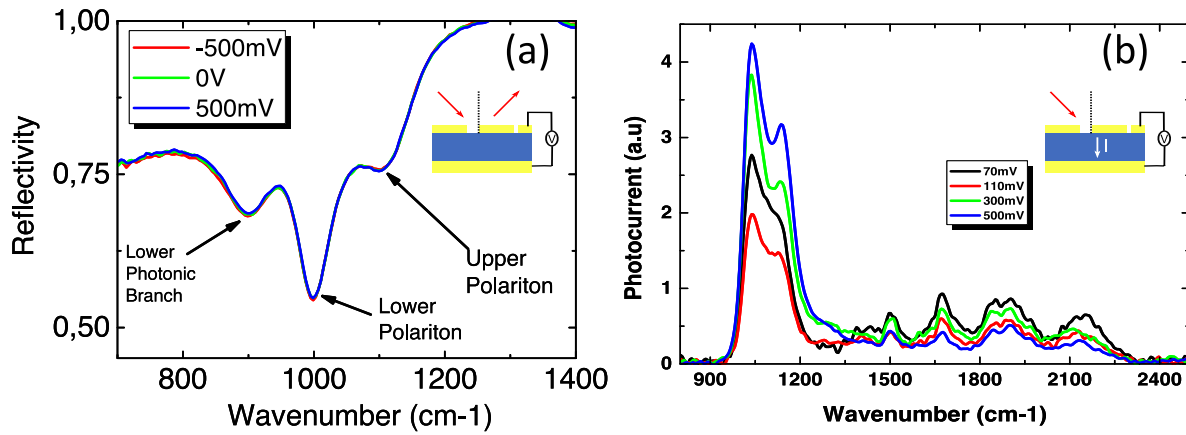


Figure 6.21: HM4065 sample with a $150 \mu\text{m}^2$ area: (a) reflectivity at 20° and 78K of a $150 \times 150 \mu\text{m}^2$, $3.5 \mu\text{m}$ grating period and 80% filling factor sample the absorption is independent of the applied bias; (b) Photocurrent measurement of a sample with $3.7 \mu\text{m}$ grating period, area $150 \times 150 \mu\text{m}^2$ and with a ff of 80% at 78 K and 30°

device. The higher the bias the higher the current until reaching the saturation level of the amplifier. The sensitivity needs then to be reduced to increase the saturation current. On these samples, at high bias ($>1 \text{ V}$) the sensitivity is too low to amplify correctly the signal and the signal is reduced.

In strong coupling the applied bias increases the signal to noise ratio below 1300 cm^{-1} (Figure 6.21, (b)). As seen on the mesa, the sample HM4065 exhibits photodetection at high frequencies (from 1500 cm^{-1} to 2300 cm^{-1}) modulated by the absorption of the grating. Particularly the 4^{th} photonic branch can be almost observed on the dispersion of the $4 \mu\text{m}$ period device (Figure 6.22).

After signal optimization, the dispersion in photocurrent has been measured for three different grating periods (Figure 6.22). Note that for the dispersion measurement, no cryo-shield was used to access a wider set of incidence angles. As expected, the 3^{rd} photonic branch is split into two polaritonic branches on both sides of the intersubband transition at 1090 cm^{-1} . RCWA simulations (white dots) fits with the upper polaritonic branch. However, the lower polariton does not correspond to the simulations. Conversely to the upper polariton that is located in the continuum (Figure 6.24), the lower polariton is buried into the QW. When the LP is heavily redshifted with respect to the bare ISB transition, the distance with the continuum is too high and no photocurrent generation is possible. On the contrary, when the LP is more matter part (Hopfield coefficient close to 0), it gets closer to the continuum and a photocurrent can be generated.

This configuration is not taken into account in the simulation and reveals a large difference between the observation of the lower polariton in reflectivity and in photocurrent. In particular, the SC-QWIP is limited in detection at a wavelength much lower than the bare ISB transition. Nevertheless, this first generation of SC-QWIP is an asset to explore the matter part of intersubband polaritons.

The dispersions on HM4059 were also measured showing the same behavior than described previously but with a lower signal to noise ratio.

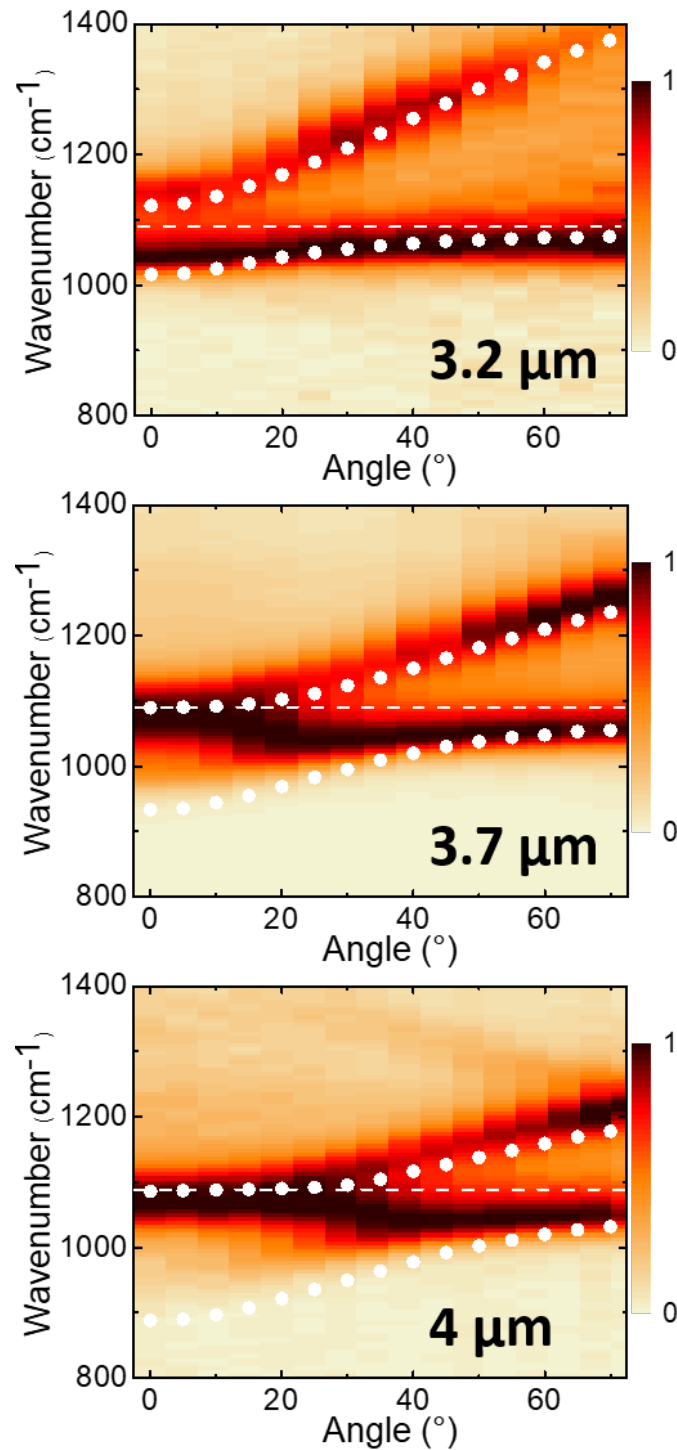


Figure 6.22: Angle-resolved spectral photocurrent for three SC-QWIPs ($150 \mu\text{m}$ side, 80% filling factor) with grating periods of $3.2 \mu\text{m}$, $3.7 \mu\text{m}$ and $4 \mu\text{m}$ (from top to bottom). The measurements are performed at 78 K , with a resolution of 12 cm^{-1} , under a bias of 500 mV for an angle span from 0° to 70° . The white dots correspond to the 2D RCWA simulation for each device, with the following identical parameters for all three samples (except for the grating): top metal thickness 200 nm ; filling factor 80%; active region thickness 940 nm ; bottom metal 400 nm ; ISB transition 32.8 THz ; doping $5.5 \times 10^{11} \text{ cm}^{-2}$.

6.4.3 Interpretation of the Experimental Results

The color plots of the photocurrent response reveal that the SC-QWIP detectors do operate in the strong light-matter coupling regime: in contrast to the single peaked response found in the weak coupling shown in Figure 6.8, two dispersive branches clearly appear, which we attribute to polaritons. While the UP branch in detection closely follows the polaritonic dispersion (white dots) extracted from the reflectivity dips or, equivalently, from absorption peaks, the LP branch displays an interesting feature: it does not extend to wavelengths much longer than the peak detection wavelength of the device operating in weak coupling.

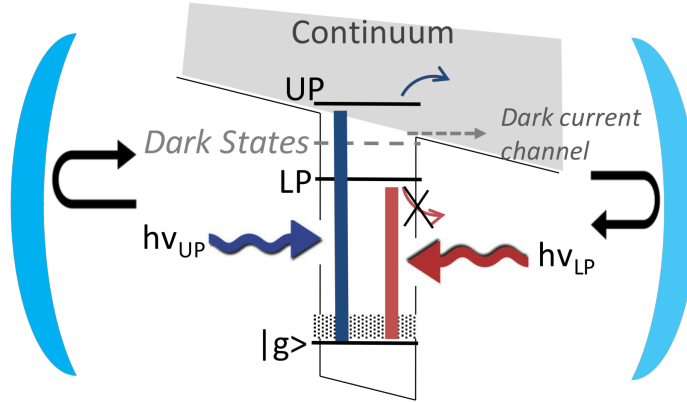


Figure 6.23: Schematics of the QWIP operating in the strong coupling, and possible polaritonic level alignment.

This finding is in agreement with the level alignment sketched in Figure 6.23. Taking the initial state with all electrons in the ground state of the well as a reference for energies, the UP positions itself at higher energy with respect to the QW edge. As a result, it overlaps with the electronic states in the quasi-continuum, so we can expect that the electronic part of the polariton promoted to the excited state has enough energy to yield a sizable photocurrent signal. On the other hand, the relatively large value of the Rabi splitting $2\Omega_{Rabi}$ pushes the energy of the LP below the bare $g \rightarrow e$ transition energy and, thus, well below the QW edge. As a result, the electronic part of the polariton does not have enough energy to escape above the QW edge and the potential barrier for moderate values of the applied electric field in the 1-5 kV/cm range prevents significant tunneling. The photocurrent is therefore strongly suppressed at small incidence angles.

While this qualitative picture is already quite clear, extracting quantitative information from the data requires a theoretical model of the photocurrent process. Here we will focus on a simple phenomenological model that is able to accurately reproduce the experimental data in terms of a single transfer function summarizing the frequency dependence of the probability rate of escape from the QW for an electron in the excited (e) state (Figure 6.24). The model is based on the temporal coupled-mode theory (see Section 1.4.3) of laterally patterned cavities in strong light-matter coupling regime developed in [61]. The escape of electrons from the QW is included in the theory as an additional, frequency-dependent decay of the ISB transition of rate $\gamma_{tunn}(\omega)$.

In its simplified formulation for spatially homogeneous cavities [61], the steady-state of the cavity photon a_k and ISB b_k fields under a monochromatic and spatially plane-wave incident electromagnetic field of amplitude E_{inc} and in-plane wavevector k at frequency ω

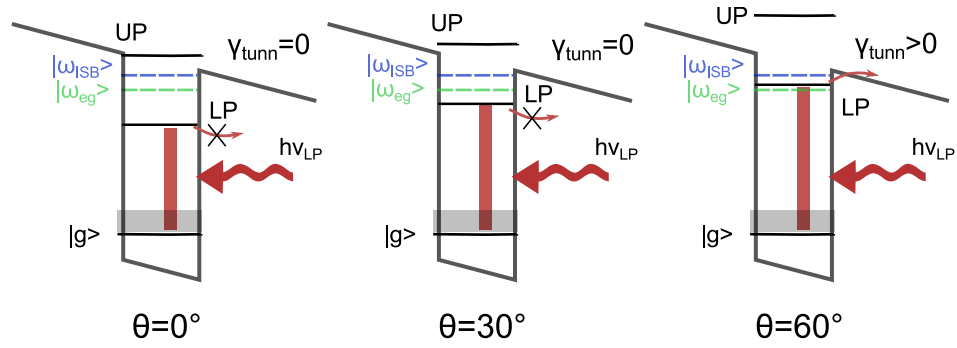


Figure 6.24: Schematics of the QW with the two polaritonic states for different angles of injection. The transition of the bare cavity is ω_{eg} whereas the ISB transition is ω_{ISB} (depolarization shift)

reads:

$$\omega a_k = \omega_k^{cav} a_k - i(\gamma_{rad} + \gamma_{nr})a_k/2 + \Omega_{Rabi}b_k + E_{inc} \quad (6.4)$$

$$\omega b_k = \omega^{ISB} b_k + \Omega_{Rabi}a_k - i(\gamma_{hom} + \gamma_{tunn}(\omega))b_k/2, \quad (6.5)$$

where ω_k^{cav} is the photon dispersion along the cavity plane, the effective frequency ω^{ISB} of the bright ISB transition coupled to the cavity mode includes the depolarization shift, Ω_{Rabi} is the Rabi frequency of the light-matter coupling, γ_{rad} , γ_{nr} and γ_{ISB} are respectively the radiative and non-radiative loss rates of the cavity photon, and the homogeneous decay rate of the ISB transition. $|a_k|^2$ and $|b_k|^2$ can be seen as the energy stored respectively in the cavity and in the material excitation. In this formalism, the reflected light field reads:

$$E_{refl} = E_{inc} - i\gamma_{rad}a_k, \quad (6.6)$$

and the photo-current intensity is, modulo a constant factor,

$$I_{pc} = \gamma_{tunn}(\omega)|b_k|^2. \quad (6.7)$$

On physical grounds, we can anticipate that a reasonable choice for $\gamma_{tunn}(\omega)$ is to have a sharp cut-off on the low-energy side slightly below the effective ISB transition frequency ω_{ISB} and a slow decay at high frequencies. As it is sketched in Figures 6.7 and 6.23, escape from the QW is rapidly suppressed when the electron energy is pushed well below the QW edge (following a Fowler-Nordheim behavior [122]), while the high-frequency decay is due to the reduced overlap between the electron wavefunction in the QW and the one of fast moving outgoing states.

An example of such a shape is shown in Figure 6.25 and the corresponding color plots of the frequency- and angle- dependent photocurrent spectra are shown in Figure 6.26 for the three values of lattice spacing used in the experiments. Once again, the white dots indicate the position of the reflectivity minima calculated using the same theory. As one can see comparing these plots with the experimental ones shown in Figure 6.22, the agreement on the position of the reflection minima and of the photocurrent maxima is excellent. Even more importantly, the disappearance of the lower photonic branch at low energies is reproduced by the theory.

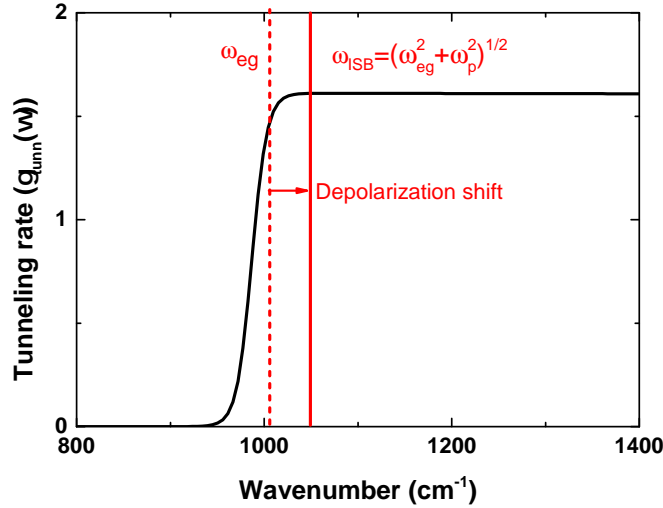


Figure 6.25: Transfer function representing tunnel-coupling from an electronic reservoir into a polaritonic system. ω_{eg} is the energy difference between $|g\rangle$ and $|e\rangle$ single particle states and $\omega_{ISB} = \sqrt{\omega_{eg}^2 + \omega_p^2}$ is the ISB transition of the doped active region (ω_p is the plasma frequency of the doped QW).

It is interesting to note that the agreement between the theory and the experiment requires that the low-energy cut-off of the tunneling rate $\gamma_{tunn}(\omega)$ be located at $\delta_{cut} \sim 50\text{cm}^{-1}$ below the ISB transition frequency ω_{ISB} , as clarified in Figure 6.25. Physically, this can be understood in terms of the depolarization shift due to Coulomb interactions in the QW, that blue-shifts the effective ISB frequency ω_{ISB} above the single particle energy difference ($\hbar\omega_{eg} = E_e - E_g$). The amount of this shift, of course, depends on the QW parameters and on the electron surface density and in the current sample, using the real doping level, we obtain $\approx 41\text{cm}^{-1}$, a value that is comparable in magnitude to δ_{cut} . Since the excited state is very close to the QW edge, this finding is consistent with a simple physical idea of tunneling being quickly suppressed as the energy drops below the QW edge.

The simple transfer function $\gamma_{tunn}(\omega)$ that we have employed permits to reproduce the polaritonic peak positions and validates the level alignment proposed in Figure 6.23.

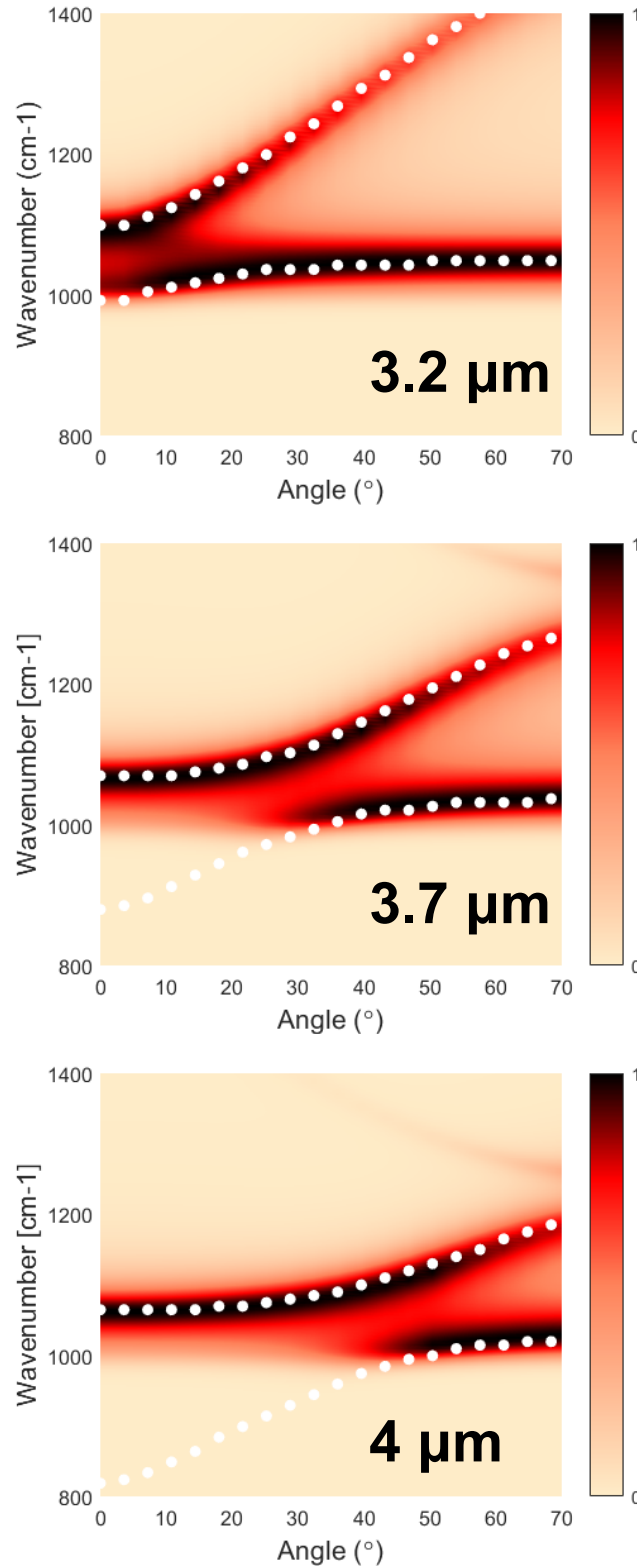


Figure 6.26: Theoretical color plots of the dependence of the photocurrent intensity on the frequency and angle of the incident light. The white dots correspond to the peaks of absorption obtained with RCWA simulations. The three panels correspond to the three devices used for the experimental plots in Fig.3. Parameters used in the calculations: $\Omega_{Rabi} = 57cm^{-1}$, $\gamma_{nr} = 32cm^{-1}$, $\gamma_{rad} = 20cm^{-1}$, $\gamma_{hom} = 65cm^{-1}$, $\omega_{ISB} = 1053cm^{-1}$. Other cavity parameters: effective refractive index $n_0 = 3.1$, Bragg frequency $\omega_{Bragg} = 24cm^{-1}$, grating periods $3.2 \mu m$, $3.7 \mu m$ and $4 \mu m$ (from top to bottom).

6.5 Conclusions & Perspectives

This last chapter had two main goals: first exploring the possibility of disentangling the detection wavelength from the activation energy in a QWIP, second to explore the fundamental properties of the bright states of the ISB polaritons with photodetection experiment. To reach these goals, I designed, fabricated, and measured QWIPs in weak and strong coupling. The M-I-M process appeared to have a significant impact on the electrical properties (Schottky barriers). Nevertheless, it was possible to extract the photocurrent and observe the Rabi splitting and therefore the strong-coupling regime on two different detectors (HM4059 and HM4065). The best results have been measured for the structure with the higher barriers (HM4065). This heterostructure appeared to have the lower dark current, offering the best signal to noise ratio.

The dispersion in photocurrent has been measured for three different samples. Although the dispersion of the upper polaritonic branch was predicted by the theory (RCWA simulations), the lower polaritonic branch had an almost flat dispersion that was in contradiction with the theory and different from the dispersion in reflectivity.

To understand the specificity of the dispersion in photocurrent, we have taken into account the generation of photocurrent from the two polaritonic states. The upper state is in the continuum and can efficiently produce a current. Conversely, the lower polaritonic state is inside the cavity, so it cannot be coupled to the continuum and generate a photocurrent.

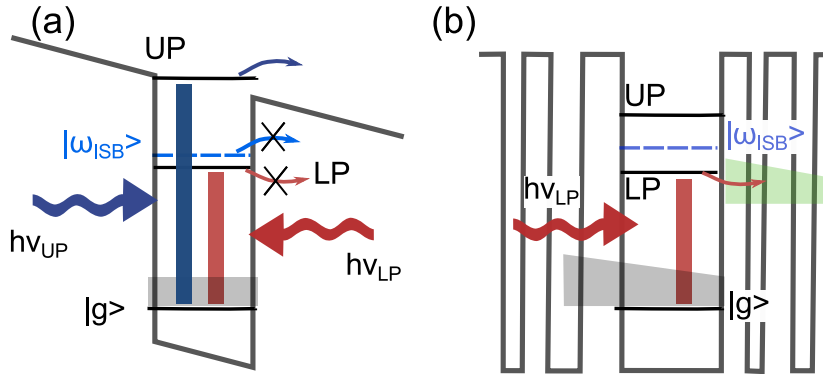


Figure 6.27: Schematics of the next generations of detectors: (a) bound-to-bound QW with only the UP in the continuum, (b) QC structure extracting the photocurrent from the lower polariton.

A transfer function representing the tunneling rate has been introduced to take into account this phenomenon. At low frequencies, this transfer function has a cut-off and a slow decay at high energy. This shape represents the electron tunneling through a barrier from the lower polariton state into the continuum. To be coherent with the experiment, the low energy cut-off is located at the energy of the bare transition. This theoretical observation is in agreement with the previous study of SC-QWIP [6] in which the lower polariton was not generating photocurrent below the energy of the bare transition.

A theoretical perspective would be to refine the transfer function to directly link it to a microscopic model of the electronic transport in a QWIP detector and also reproduce the relative intensities of the polaritonic photocurrent. This is beyond the scope of this Ph.D., but it is an immediate follow-up.

These results proved that we were not incorrect configuration to observe the impact of the

strong coupling on the thermal activation processes. In fact, to improve the performance of a SC-QWIP the design of the quantum well has to be reconsidered to correspond to the properties of the polaritons. To do so, we need to move away from the design rules of standard QWIPs. Thanks to a more precise comprehension of the generation of photocurrent from polaritonic states we envision three new detector designs:

- The first one would be based on a bound-to-bound QWIP with the excited state half a Rabi energy below the top of the barrier ($\sim 7meV$). In this case that only the upper polariton can interact with the continuum (Figure 6.27, (a)) and the dark current would be reduced.
- The second detector would be based on a quantum cascade detector (QC Ref.[7]) designed to allow extraction of the photocurrent from the lower polariton level (Figure 6.27, (b)).

Conclusions and Perspectives

After fifteen years of intersubband polariton development, some of the peculiar properties of these quasi-particles are still unexplored. A deeper understanding of the polaritons is needed to access their fundamental properties and develop their applicative potential as efficient emitters or detectors in the mid-infrared and THz.

In this manuscript, we used Metal-Insulator-Metal cavities with a top metal periodic grating as a platform to explore the physics of ISB polaritons. The advantages of M-I-M are twofold: first operating under the cut-off of the cavity enables us to isolate the TM_{00} mode (**Chapter 1**); second the dispersion of the cavity -over a broad set of in-plane wave vectors- offers a practical experimental configuration to observe the polaritons in both reflection and photo-detection.

The ISB transitions were implemented using GaAs/AlGaAs quantum wells with the appropriate widths (**Chapter 1**). Doping and barriers heights are adapted to each range of frequencies, from the Mid-IR to the THz. The M-I-M cavity has been tailored to operate in strong coupling with the ISB transition for each application.

In the THz domain (**Part 1**) common sources (QCLs) and detectors (Bolometer, QWIPs) are expensive and operate at low temperatures. In the long term, the implementation of ISB polaritons onto THz devices could be an elegant solution to improve their performances because polaritons are potentially less sensitive to temperature. Until now, experiments on THz ISB polaritons have been limited, and some of the elemental polariton's properties as lifetime or the saturation energy still need to be measured.

During this Ph.D., we developed structures that are potentially useful for the exploration of the scattering mechanisms of THz ISB polaritons. In fact, in this range of frequencies, the phonon-polariton scattering is not permitted, and we expect to observe polariton-polariton scattering. The dispersive cavity is a major asset to study these mechanisms because it provides more degrees of freedom to engineer the system.

Measuring the dispersion is crucial to access the different states of the system and determine the best configuration to explore scattering mechanisms (**Chapter 2**). For this purpose, we fabricated a new experimental set-up to measure the polariton dispersion at liquid Helium temperature (4K). This set-up required the fabrication in the C2N workshop of a specific system compatible with a commercial FTIR spectrometer. Four samples with different grating duty-cycles and ISB transitions have then been measured with this system; two samples

have been selected for the Time-Domain Spectroscopy (TDS) measurement at *LPA* (**Chapter 3**). After the observation of the polaritons in reflectivity, a pump-probe experiment was performed on these devices. The first configuration with both pump and probe impinging on the sample at the same angle (45°) has been realized showing a slight reduction of the polariton's absorption compared with the measurement without the pump. These first results are not conclusive, and a different configuration of the TDS system will have to be implemented in order to confirm these first observations. In particular pumping at 25° and collecting the signal at 0° appears to be the most promising configuration.

In parallel to the exploration of THz polaritons, I contributed to the development of techniques to shorten the pulses of THz quantum cascade lasers in a metal-insulator-metal waveguide. Assuming that all the laser modes are in-phase, constructive interferences between these modes generate optical pulses. The width of the pulses is inversely proportional to the bandwidth of the optical gain. In **Part 2** we explored a monolithic technique to compensate the dispersion of a QCL broadband active regions.

In **Chapter 4**, we reassess the concept of dispersion compensation of the monolithic Gires-Tournois Interferometers (GTI) adapted to thick broadband THz active regions [26]. Tailoring the GTI cavities appeared critical because it required a deep etching with a high aspect ratio. To overcome this difficulty, I have developed an anisotropic ICP-etching recipe together with a thick photo-resist [28]. Once the etching met the specifications, I fabricated the GTI-cavity in the C2N-Orsay cleanroom. The measurement -performed at *LPA*- of the QCLs in hybrid-mode locking (GTI and Mode-Locking) showed a slight reduction of the pulse width (3.8 ps) compared to the first generation of GTI-THz QCL [26].

The third part of this manuscript (**Part 3**) presents the implementation of M-I-M dispersive cavities on a bound-to-quasi-bound quantum well infrared photo-detector designed to detect in strong coupling. In this study, we targeted two main objectives: from the device point of view, the strong coupling can disentangle the frequency of detection from the thermal energy activation and reduce the dark current at a given frequency. From the polaritonic point of view, these devices represent an original tool to probe polariton's properties electrically.

Chapter 5 introduced the theoretical concepts related to detectors (responsivity, detectivity, signal to noise ratio, ...), black body radiation (radiance) and electrical transport in QWIPs (dark current, photo-current). We then applied these concepts to describe four detectors (two detectors in weak coupling and two detectors in strong coupling) from the literature that inspired this work.

Chapter 6 focused on quantum well infrared detectors operating at a wavelength of $10 \mu\text{m}$ in strong coupling with a M-I-M dispersive cavity. The active regions have been characterized in transmission (multi-pass) and in photo-detection (mesa). The QW parameters (barriers height and doping of the quantum wells) appeared as critical criteria that fix the dark current level following a 3D drift model. At 78 K the devices were limited by the dark current and a responsivity of 0.4 A/W was measured at 78 K and 500 mV on the best measured sample with the lower doping. These results in weak coupling limit the possibility of device performance improvement, but using them as a tool to study the polaritonic states via photocurrent measurement was still possible.

We have chosen to process only the two MQWs active regions with the higher doping to maximize the Rabi-splitting. The fabrication of SC-QWIPs was completed in the C2N-

Orsay cleanroom. Two sets of detectors with different grating periods and sizes have been implemented and characterized. Electrically the sample with the higher barriers exhibits the lower dark current. The dispersion in photocurrent for this sample has been measured for different periods. The dispersion showed a peculiar behavior of the lower polariton - compared to the measurement in reflectivity - that has never been highlighted in the literature.

We proposed a theoretical model to explain this peculiar behavior. In this model the lower polariton is energetically pushed inside the QW and can not generate a photo-current, except when it gets closer to the excited state of the transition. A transfer function with a cut-off below the excited state has been integrated to the simulations. The final simulation taking into account the tunneling effect reproduced the experimental dispersions of the three different devices explored. Further explorations on detectors (QWIPs or QCDs) in strong coupling will need to rethink the detectors design entirely to align the position of the extractors with the target polariton states (LP for QCD and UP for QWIP).

External Cavity for THz Double-Metal Waveguides

A perspective to improve the peak power of the THz-QCL pulse is to reduce the free spectral range by increasing the length of the cavity. A monolithic approach is appealing but the elevated current threshold of such a structure is a major issue. That is why we focused on THz anti-reflection coatings for M-I-M cavities that have a vast set of applications, and in particular could enable an external cavity architecture.

In a standard M-I-M THz QCL of length L , the reflectivity of the facet is $R \approx 90\%$ ($\alpha_m = -\ln(R)/2L$) [123]. A reduction of one facet reflectivity ($R_c < R$) induces a modification of the facet losses ($\alpha_c = -\ln(R_c)/2L > -\ln(R)/2L$) and increases the threshold current according to the equation [124]

$$\frac{I_{th}^c}{I_{th}} = \frac{\alpha_{wg} + \alpha_m + \alpha_c}{\alpha_{wg} + 2\alpha_m} \quad (\text{A.1})$$

where I_{th} is the threshold of the standard laser and I_{th}^c is the threshold of the same laser with a coated facet. If the coated facet losses are comparable to the waveguide losses ($\alpha_{wg} \sim 15 \text{ cm}^{-1}$) the increase of the threshold current would be noticeable.

An illustrative example is to consider a 1 mm long laser with one coated facet ($R_c = 4\%$) and one cleaved facet. The associated losses are $\alpha_c = 16 \text{ cm}^{-1}$ for the coated facet and $\alpha_m = 0.5 \text{ cm}^{-1}$ for the cleaved facet. The threshold current would then be doubled compared to a standard laser with the same length.

In this appendix we worked with short cavities of 1 mm to increase the influence of the facets on the total losses. To date no THz anti-reflection coating is accessible, reliable and suitable to THz-QCLs. This development would be essential for the reduction of the free-spectral range as well as the tunability of THz lasers.

A.1 Anti-Reflection Coatings

Finding the good material for anti-reflection coating in the THz is still a challenge. In this section we will first discuss the deposition of polymer films and propose an alternative using thin metal films.

A.1.1 Coatings Based on Transparent and Insulator Materials

The reflectivity at an interface of a material of index n_0 coated with a film of thickness t_{film} and index n_{film} is described by the Fresnel's law [125]:

$$R = 1 - 4 \left[\frac{n_{film}^2}{n_0} + \frac{n_0}{n_{film}^2} + 2 + \left(\frac{1}{n_0} + n_0 - \frac{n_{film}^2}{n_0} - \frac{n_0}{n_{film}^2} \right) \cos^2 \left(\frac{2\pi n_{film} t_{film}}{\lambda} \right) \right]^{-1} \quad (\text{A.2})$$

The reflectivity is minimized if

$$\begin{cases} n_{film} = \sqrt{n_0} \\ t_{film} = \frac{(2m+1)\lambda}{4n_{film}} \quad (m = 0, 1, 2, \dots) \end{cases} \quad (\text{A.3})$$

The thickness of the anti-reflection film can be any odd number of quarter wavelengths, and typically is $\lambda/4n_{film}$ thick to minimize effects of electromagnetic losses. This type of anti-reflection coating has been successfully implemented in the Mid-IR [126].

In the THz range such approaches have been studied for Silicon ($n_{Si} \approx 3.416$) and Germanium ($n_{Ge} \approx 4$). The bulk GaAs has an index $n_{GaAs} \approx 3.3$ close to Silicon, however the index of the biased QC heterostructure is more complex. Polymers with indexes between 1.5 and 1.7, as *Epoxies*, *Mylar*, *Kapton* and *Parylene*, are good candidates for THz anti-reflection coatings on Si or Ge. The major issue in the THz is the thickness of the anti-reflection coating ($t_{film} > 10 \mu m$), that imposes long and precise depositions. In fact, depositing such a film with high homogeneity, reproducibility, on curved optics and resistant to thermal cycles is challenging.

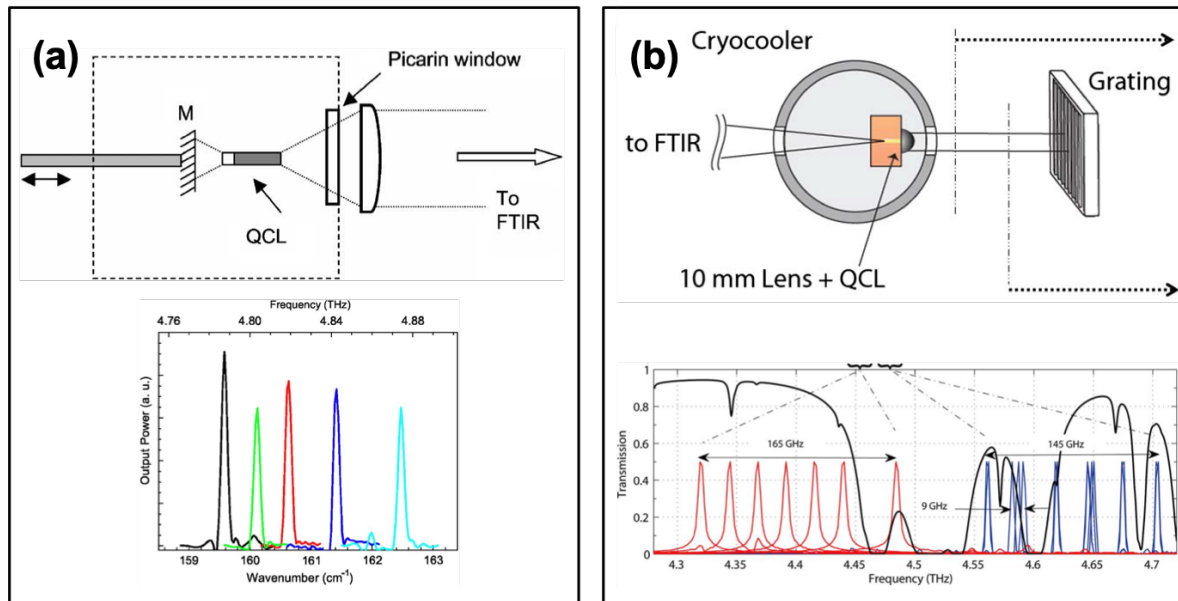


Figure A.1: Developments of two external cavities on single-plasmon THz-QCLs using different anti-reflection coatings: (a) the facet of a 4.76 THz QCL was coated with 8.3 μm -thick SiO_2 film [125], (b) HRSi lens coated with 13 μm -thick low-density polyethylene or 10 μm -thick Parylene positioned on the facet of the QCL with gain central frequencies at 4.35 THz and 4.6 THz [127].

In the range around 2 THz Parylene has been successfully implemented on Si [128]. The thermoplastic properties of Parylene (thermal stability, good adhesion, chemical inertness and low water absorption) make it a good candidate for our study.

Material	THz refractive index	Absorption coefficient (cm^{-1})	Remarks
Parylene C	1.62	$0.006*f-0.7$	Applied on Silicon [129] and on single-plasmon QCLs [130]
Parylene D	1.62	$0.0004*f-0.8$	Applied only on Silicon [129]
Mylar	1.57-1.58		difficult to apply
Kapton	1.7		difficult to apply
SiO ₂	1.9-2.1		Applied on GaAs QCL but not Broadband [125]

Table A.1: Different possible materials for AR coating in the THz for Si or GaAs

The major problems to implement this technique on THz-QCLs are to adapt the thickness of the material to the optical properties of each active region and deposit it on the small facet surface of the active region ($20 \times 60 \mu m^2$). A pioneering work on THz AR coating was performed in 2007 in the group of D.A.Ritchie [125]. They succeeded to produce an external cavity from a single plasmon QCL [131] emitting around 4.76 THz. The anti-reflection coating was composed by a 8.3 μm SiO₂ film and deposited directly on the facet. The laser tunability was from 4.79 THz to 4.87 THz (Figure A.1, (a)).

However, this approach had two major limitations for our application: first the operating AR coating window of 90 GHz is too narrow to be adapted on broadband THz QCLs. Second the far-field is not well behaved.

To broaden the spectral window of the anti-reflection coating other materials have been tested. In 2010 Ref. [130] reported a successful application of a 17 μm -thick film of parylene C on the facet of a single plasmon THz-QC laser with a spectral gain from 2.4 to 3 THz. The reflectivity of the facet dropped from 32% to 5.3% and the threshold current density of the THz-QC laser increased from 90 A/cm² to 124 A/cm². Nevertheless, the anti-reflection coating was not sufficiently low to completely suppress laser oscillations.

The same year in the group of Q.Hu, a high resistivity silicon lens (technique presented in Figure A.2, (b)) - coated with 13- μm -thick low density polyethylene (LDPE) - was abutted with a spring retaining clip to the facet of a single plasmon laser [127]. The residual reflectivity was decreased down to 0.6(± 0.1)%. Laser oscillations were completely suppressed and an external cavity with a single mode tuning over 165 GHz has been demonstrated (Figure A.1, (b)). The major difficulty of this technique is the homogeneous coating in the spherical Si-lens and the alignment of the HRSi lens with the laser facet.

The application of coated Si lenses on M-I-M THz-QC lasers Ref. [132] showed significant improvement of the out-put power, the slope efficiency (Figure A.2, (b)) and of the beam pattern (Figure A.2, (c)).

Furthermore adapting oxide or polymer AR coatings is even more challenging onto a metal-metal waveguide because the laser facet is smaller than single plasmon ones and the

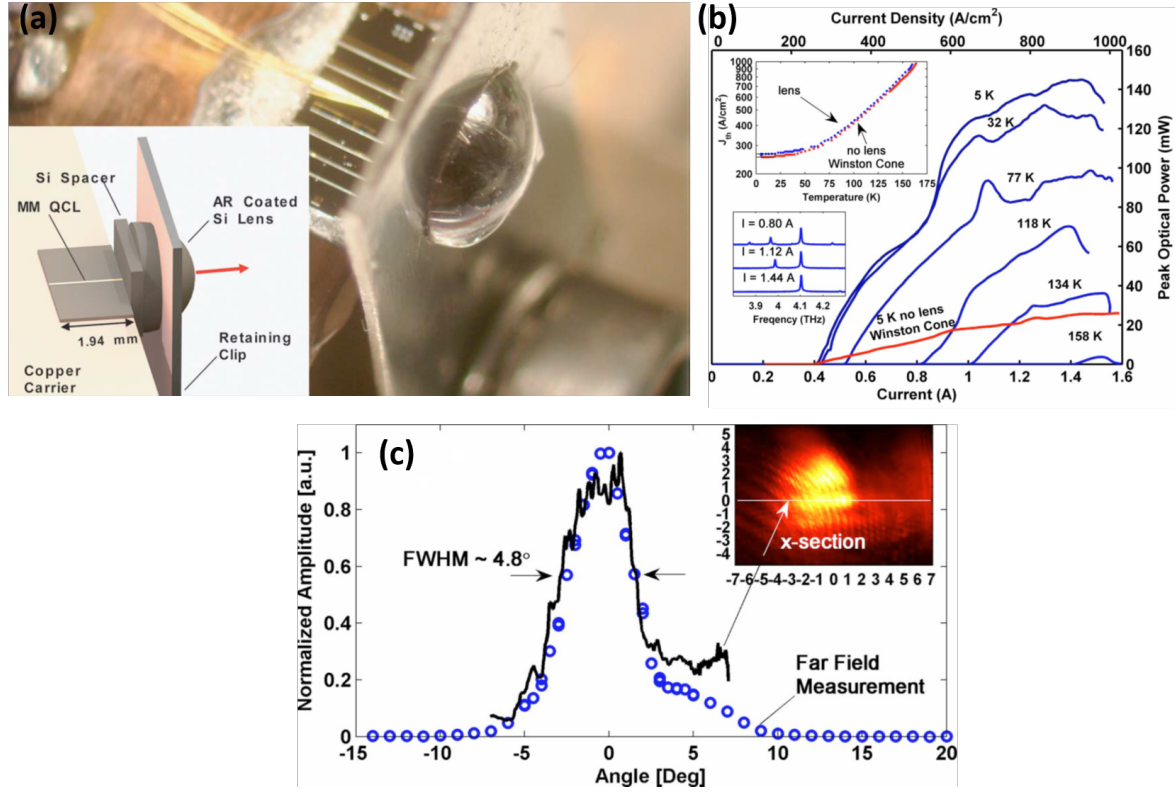


Figure A.2: (a) M-I-M THz QC laser with abutted HRSi spacer and lens. (b) Light versus current: lens-coupled and Winston cone-coupled devices. Insets: top, J_{th} versus temperature; bottom, typical spectra of a device with a lens. (c) M-I-M THz laser with Si lens far-fields at 30 cm (blue circles) and cross section of the image at 6 cm (black line) [132].

facet reflectivity is higher. Consequently, we decided to investigate metallic AR coatings, that have a broader transmission window and are potentially easily applicable on a laser facet.

A.1.2 Coatings Based on Thin Metallic Layers

Thin film of metals deposited by the team of K.Unterrainer [133, 134, 135] on a Si wafer exploit impedance matching to reduce the reflection at the interface with air.

Theoretically the system is equivalent to a transmission line circuit (Figure A.3). n_1 and n_2 represent respectively the indices of the Si and the air. The impedances of these two materials are given by the ratio of the tangential components of the electric and magnetic fields

$$Z = \frac{E_t}{H_t} = \frac{Z_0}{n} \quad (\text{A.4})$$

where $Z_0 = \sqrt{\mu_0/\epsilon_0} = 377 \Omega$ is the impedance of the free space and $n = \sqrt{\epsilon}$. In the thin metallic film (d is thinner than the skin depth) the electric transverse electric field -equal on both sides on the interface- generates a current $j = \sigma E$ assumed to be uniform in the layer. The magnetic field is discontinuous on each side of the interface due to the surface current (H_1 and H_2). Therefore, the impedance of the metallic film is

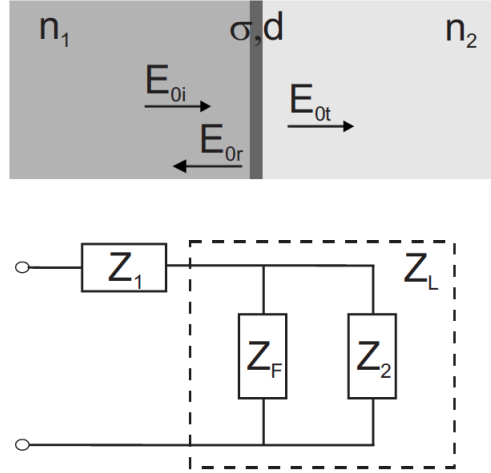


Figure A.3: Two dielectric media with refractive indices n_1 and n_2 separated by a thin film with conductivity σ and thickness d . E_{0i} denotes the incident electric field, E_{0r} denotes the reflected and E_{0t} denotes the transmitted field. The wave propagation in the optical system is represented by signal propagation in an equivalent transmission line circuit with Z_1 and Z_2 the impedances of the slab materials and Z_F the impedance of the film [136].

$$Z_F = \frac{E}{H_1 - H_2} \approx \frac{E}{dj} = \frac{1}{\sigma d} \quad (\text{A.5})$$

In the equivalent circuit, the conducting layer acts as an additional impedance shunting the line. In this case the surface current corresponds to an impedance Z_F in parallel with Z_2 . Both impedances contribute to the load impedance $\frac{1}{Z_L} = \frac{1}{Z_2} + \frac{1}{Z_F}$. The impedance matching condition is defined by the equation $Z_L = Z_1$ that leads to the following equation

$$n_{Si} - n_{air} = Z_0 \sigma(\omega) d \quad (\text{A.6})$$

In this equation we can see that the optimal thickness of the film depends on the metal used. In addition the metal conductivity below the skin depth can not be modeled with the Drude model. Thus for each metal the conductivity has to be measured by TDS.

In our case we used an empirical approach choosing one metal and trying different thicknesses. Chromium has a good adhesion on Si as well as on GaAs and it is an affordable material. On undoped silicon we observed that the amplitude of the echo crossing the slab (25 ps) decreases with the thickness of the metal (Figure A.4) until disappearing at 40 nm (value displayed on the quartz balance, 16 nm at the AFM). Above this thickness the echo comes back, but with the opposite phase, which proves that the echo disappearing is not due to the increase of the losses, but to the reduction of the reflectivity.

Because the metallic coating could not be directly applied on the laser risking a short-cut of the QCL, we first glued the metalized silicon slab on GaAs. From the Fresnel's law we expect the reflectivity of the stacked structure $R = \left(\frac{n_{GaAs} - n_{Si}}{n_{GaAs} + n_{Si}} \right)^2 = 0.0016$ to be small compares to the maximum of reflectivity of an anti-reflection coating for a metal-metal THz laser (4%). Experimentally the result was similar to the anti-reflection coating on Si. This encouraging broadband antireflection coating has then been implemented on the facet of a single plasmon THz-QCL.

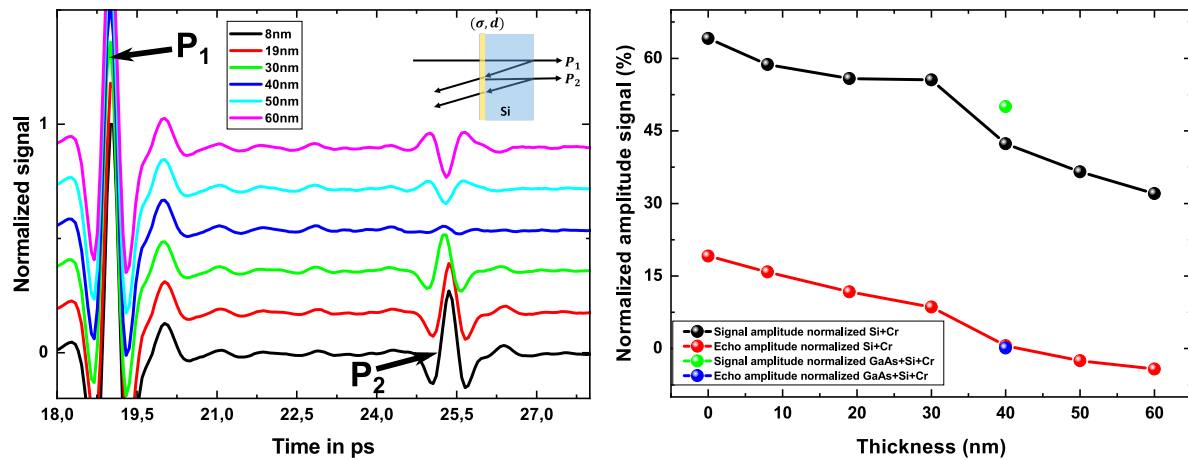


Figure A.4: TDS transmission on undoped Si wafer covered with different thicknesses of Chromium. On the left the time-domain measurement that shows the echo (25.3 ps) as a function of the normalized impulsion (around 19 ps). The echo vanishes for a thickness of chromium of 40 nm and reappears for a higher thickness of Cr, but with the opposite phase. On the right, the signal is normalized by the amplitude of the THz pulse in free space. At 40 nm, the transmitted pulse is 40% of the free space pulse. The negative percentage corresponds to the phase inversion. The metallic Si slab has then been glued to a wafer of GaAs and the transmission (green) and echo (blue) properties were unchanged.

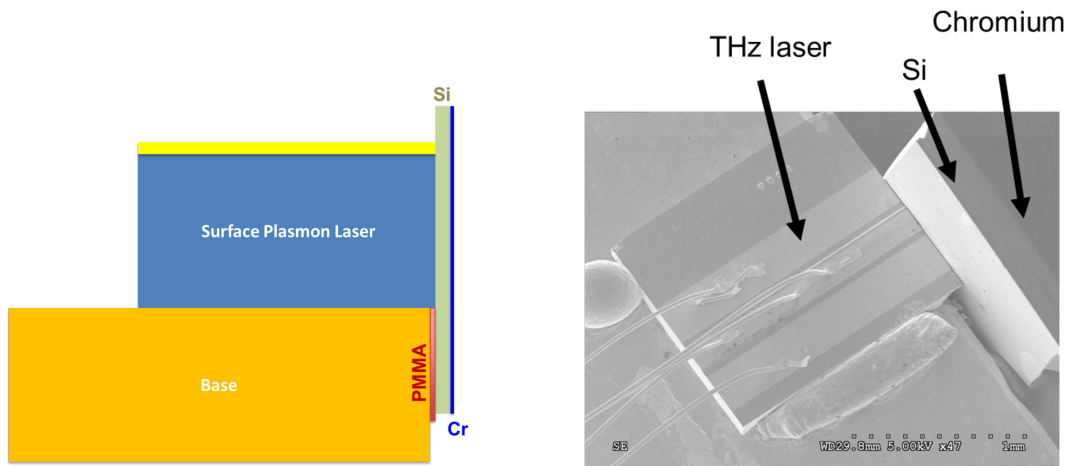


Figure A.5: Positioning of the anti-reflection coating system on the facet of a surface plasmon THz-QC laser (width $100 \mu m$, and length $1 mm$).

Consequently, the metalized Si slab has been manually stuck to the facet of a single plasmon laser (lower facet reflectivity than the metal-metal cavity, Figure A.5). The distance between the facet and the slab was inferior to $5 \mu m$, i.e. highly subwavelength.

The L-I-V characteristics of the laser with and without metalized Si slab are presented in Figure A.6. The electrical properties are similar, the threshold is higher and the output power lower for the laser with metalized Si slab than the standard single plasmon. The decrease by a factor two is coherent with the measurement of the absorption of the metalized Si slab with 40-nm-thick metalization (Figure A.4 shows an absorption of 55%). Consequently, the major effect of the metalized Si slab is to increase the absorption more than reducing the reflectivity.

This result shows that the results on bulk GaAs are not directly transposable to a THz-QCL.

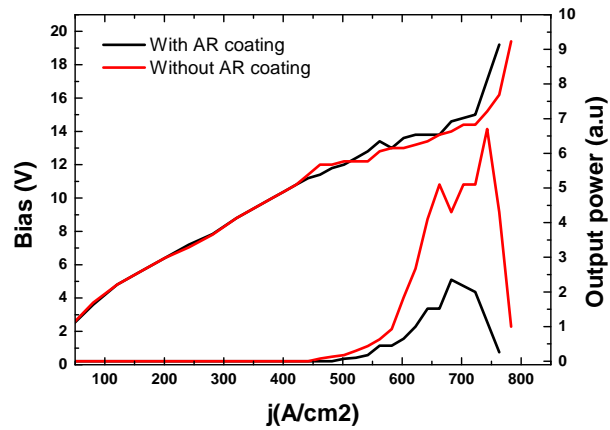


Figure A.6: LIV of the single plasmon THz-QCL (G0058) with and without anti-reflection coating.

The origin of the problem is unclear. The air gap between the laser facet and the metalized silicon slab might be critical for the laser performances. This air gap might increase the reflectivity up to 4% which is enough to reach laser amplification.

Polariton Active Regions: Growth Sheets

B.1 THz Polariton

Material	Thickness (nm)	Doping (cm^{-2})	Remarks
GaAs	250		
$Al_{50}Ga_{50}As$	500		Stop layer
GaAs	800		
Start of 53 repeat periods			
$Al_{25}Ga_{75}As$	15		
Delta doping		×	
$Al_{25}Ga_{75}As$	5		
GaAs	36		
End of the repeat periods			
Delta doping		1×10^{11}	
$Al_{25}Ga_{75}As$	15		
GaAs	50	4×10^{18}	Cap Layer

Table B.1: Growth sheet of the THz-polariton active regions with $\times = 1 \times 10^{11}$ for L1362 and $\times = 2 \times 10^{11}$.

B.2 Mid-IR Polaritons

Material	Thickness (nm)	Doping (cm^{-3})	Remarks
GaAs	250		
$Al_{60}Ga_{40}As$	400		Stop layer
GaAs	50	4×10^{18}	
Start of 31 repeat			
$Al_{20}Ga_{80}As$	20		
GaAs	0.6		
GaAs	5.3	\times	
GaAs	0.6		
End of the repeat periods			
$Al_{20}Ga_{80}As$	20		
GaAs	100	4×10^{18}	Cap Layer

Table B.2: Growth sheet of the bound-to-quasi-continuum structures HM4058 ($\times = 0.8 \times 10^{18}$) and HM4059 ($\times = 1.6 \times 10^{18}$).

Material	Thickness (nm)	Doping (cm^{-3})	Remarks
GaAs	250		
$Al_{60}Ga_{40}As$	400		Stop layer
GaAs	50	4×10^{18}	
Start of 31 repeat			
$Al_{25}Ga_{75}As$	20		
GaAs	0.6		
GaAs	5.3	1.6×10^{18}	
GaAs	0.6		
End of the repeat periods			
$Al_{25}Ga_{75}As$	20		
GaAs	100	4×10^{18}	Cap Layer

Table B.3: Growth sheet of the bound-to-quasi-continuum structure HM4065.

Bibliography

- [1] L. Esaki and R. Tsu, “Superlattice and negative differential conductivity in semiconductors,” *IBM Journal of Research and Development*, vol. 14, no. 1, pp. 61–65, Jan 1970.
- [2] D. Dini, R. Köhler, A. Tredicucci, G. Biasiol, and L. Sorba, “Microcavity polariton splitting of intersubband transitions,” *Physical Review Letters*, vol. 90, p. 116401, Mar 2003.
- [3] A. Liu, “Rabi splitting of the optical intersubband absorption line of multiple quantum wells inside a Fabry-Pérot microcavity,” *Physical Review B*, vol. 55, no. 11, p. 7101, 1997.
- [4] L. Sapienza, A. Vasanelli, R. Colombelli, C. Ciuti, Y. Chassagneux, C. Manquest, U. Gennser, and C. Sirtori, “Electrically injected cavity polaritons,” *Physical Review Letters*, vol. 100, no. 13, p. 136806, 2008.
- [5] P. Jouy, A. Vasanelli, Y. Todorov, L. Sapienza, R. Colombelli, U. Gennser, and C. Sirtori, “Intersubband electroluminescent devices operating in the strong-coupling regime,” *Physical Review B - Condensed Matter and Materials Physics*, vol. 82, no. 4, pp. 1–11, 2010.
- [6] E. Dupont, H. C. Liu, A. J. SpringThorpe, W. Lai, and M. Extavour, “Vacuum-field Rabi splitting in quantum-well infrared photodetectors,” *Physical Review B - Condensed Matter and Materials Physics*, vol. 68, no. 24, pp. 1–9, 2003.
- [7] L. Sapienza, A. Vasanelli, C. Ciuti, C. Manquest, C. Sirtori, R. Colombelli, and U. Gennser, “Photovoltaic probe of cavity polaritons in a quantum cascade structure,” *Applied Physics Letters*, vol. 90, no. 20, p. 201101, 2007.
- [8] G. Günter, A. A. Anappara, J. Hees, A. Sell, G. Biasiol, L. Sorba, S. De Liberato, C. Ciuti, A. Tredicucci, A. Leitenstorfer *et al.*, “Sub-cycle switch-on of ultrastrong light-matter interaction,” *Nature*, vol. 458, no. 7235, p. 178, 2009.
- [9] C. Ciuti, G. Bastard, and I. Carusotto, “Quantum vacuum properties of the intersubband cavity polariton field,” *Physical Review B*, vol. 72, p. 115303, Sep 2005.

-
- [10] Y. Todorov, A. M. Andrews, R. Colombelli, S. De Liberato, C. Ciuti, P. Klang, G. Strasser, and C. Sirtori, “Ultrastrong light-matter coupling regime with polariton dots,” *Physical Review Letters*, vol. 105, no. 19, p. 196402, 2010.
- [11] S. Zanotto, G. Biasiol, R. Degl’Innocenti, L. Sorba, and A. Tredicucci, “Intersubband polaritons in a one-dimensional surface plasmon photonic crystal,” *Applied Physics Letters*, vol. 97, no. 23, p. 231123, 2010.
- [12] J.-M. Manceau, S. Zanotto, T. Ongarello, L. Sorba, A. Tredicucci, G. Biasiol, and R. Colombelli, “Mid-infrared intersubband polaritons in dispersive metal-insulator-metal resonators,” *Applied Physics Letters*, vol. 105, no. 8, p. 081105, 2014.
- [13] P. Laffaille, J.-M. Manceau, T. Laurent, A. Bousseksou, L. Le Gratiet, R. Teissier, A. Baranov, and R. Colombelli, “Intersubband polaritons at $\lambda \approx 2 \mu\text{m}$ in the InAs/AlSb system,” *Applied Physics Letters*, vol. 112, no. 20, p. 201113, 2018.
- [14] J.-M. Manceau, N.-L. Tran, G. Biasiol, T. Laurent, I. Sagnes, G. Beaudoin, S. De Liberato, I. Carusotto, and R. Colombelli, “Resonant intersubband polariton-lo phonon scattering in an optically pumped polaritonic device,” *Applied Physics Letters*, vol. 112, no. 19, p. 191106, 2018.
- [15] P.-B. Vigneron, N.-L. Tran, S. Pirodda, J.-M. Manceau, A. Bousseksou, G. Biasol, I. Carusotto, and R. Colombelli, “Quantum well infrared photo-detectors operating in the strong light-matter coupling regime,” *Applied Physics Letters (in press)*, 2019.
- [16] M. Tonouchi, “Cutting-edge terahertz technology,” *Nature Photonics*, vol. 1, no. 2, p. 97, 2007.
- [17] L. Li, L. Chen, J. Zhu, J. Freeman, P. Dean, A. Valavanis, A. Davies, and E. Linfield, “Terahertz quantum cascade lasers with >1 W output powers,” *Electronics Letters*, vol. 50, no. 4, pp. 309–311, 2014.
- [18] B. Paulillo, S. Pirodda, H. Nong, P. Crozat, S. Guilet, G. Xu, S. Dhillon, L. H. Li, A. Davies, E. Linfield *et al.*, “Ultrafast terahertz detectors based on three-dimensional meta-atoms,” *Optica*, vol. 4, no. 12, pp. 1451–1456, 2017.
- [19] M. Geiser, G. Scalari, F. Castellano, M. Beck, and J. Faist, “Room temperature terahertz polariton emitter,” *Applied Physics Letters*, vol. 101, no. 14, 2012.
- [20] B. Paulillo, J. M. Manceau, L. H. Li, A. G. Davies, E. H. Linfield, and R. Colombelli, “Room temperature strong light-matter coupling in three dimensional terahertz meta-atoms,” *Applied Physics Letters*, vol. 108, no. 10, 2016.
- [21] S. De Liberato, C. Ciuti, and C. C. Phillips, “Terahertz lasing from intersubband polariton-polariton scattering in asymmetric quantum wells,” *Physical Review B - Condensed Matter and Materials Physics*, vol. 87, no. 24, pp. 1–5, 2013.
- [22] J. Faist, F. Capasso, D. L. Sivco, C. Sirtori, A. L. Hutchinson, and A. Y. Cho, “Quantum cascade laser,” *Science*, vol. 264, no. 5158, pp. 553–556, 1994.

- [23] R. Köhler, A. Tredicucci, F. Beltram, H. E. Beere, E. H. Linfield, A. G. Davies, D. A. Ritchie, R. C. Iotti, and F. Rossi, “Terahertz semiconductor-heterostructure laser,” *Nature*, vol. 417, no. 6885, p. 156, 2002.
- [24] M. Brandstetter, C. Deutsch, M. Krall, H. Detz, D. C. MacFarland, T. Zederbauer, A. M. Andrews, W. Schrenk, G. Strasser, and K. Unterrainer, “High power terahertz quantum cascade lasers with symmetric wafer bonded active regions,” *Applied Physics Letters*, vol. 103, no. 17, p. 171113, 2013.
- [25] A. Mottaghizadeh, D. Gacemi, P. Laffaille, H. Li, M. Amanti, C. Sirtori, G. Santarelli, W. Hänsel, L. L. H. Holzgart, Ronald, E. H. Linfield, and S. Barbieri, “5-ps-long terahertz pulses from an active-mode-locked quantum cascade laser,” *Optica*, vol. 4, no. 1, pp. 168–171, 2017.
- [26] F. Wang, H. Nong, T. Fobbe, V. Pistore, S. Houver, S. Markmann, N. Jukam, M. Amanti, C. Sirtori, S. Moumdji *et al.*, “Short terahertz pulse generation from a dispersion compensated modelocked semiconductor laser,” *Laser & Photonics Reviews*, vol. 11, no. 4, p. 1700013, 2017.
- [27] F. Wang, H. Nong, T. Fobbe, V. Pistore, S. Houver, S. Markmann, N. Jukam, M. Amanti, C. Sirtori, S. Moumdji, R. Colombelli, L. Li, E. Linfield, G. Davies, J. Mangeney, J. Tignon, and S. Dhillon, “Short Terahertz Pulse Generation from a Dispersion Compensated Modelocked Semiconductor Laser,” *Laser and Photonics Reviews*, vol. 11, no. 4, pp. 1–9, 2017.
- [28] P. Vigneron, F. Joint, N. Isac, R. Colombelli, and E. Herth, “Advanced and reliable GaAs/AlGaAs ICP-DRIE etching for optoelectronic, microelectronic and microsystem applications,” *Microelectronic Engineering*, vol. 202, pp. 42–50, 2018.
- [29] E. O. Kane, “The semi-empirical approach to band structure,” *Journal of Physics and Chemistry of Solids*, vol. 8, pp. 38–44, 1959.
- [30] L. West and S. Eglash, “First observation of an extremely large-dipole infrared transition within the conduction band of a GaAs quantum well,” *Applied Physics Letters*, vol. 46, no. 12, pp. 1156–1158, 1985.
- [31] H. Liu and F. Capasso, *Intersubband transitions in quantum wells: Physics and device applications*. Academic press, vol. 5, 1999.
- [32] A. Delteil, “Many-body enhancement of the light-matter interaction,” Thesis, Université Paris-Diderot - Paris VII, Dec. 2012. [Online]. Available: <https://tel.archives-ouvertes.fr/tel-00793607>
- [33] M. Helm, *Long wavelength infrared emitters based on quantum wells and superlattices*. CRC Press, vol. 6, 2000.
- [34] M. Fox, *Optical properties of solids*. Oxford University Press, 2002.
- [35] E. D. Palik, *Handbook of Optical Constants of Solids, Author and Subject Indices for Volumes I, II, and III*. Elsevier, 1998.

- [36] M. Zaluzny and C. Nalewajko, “Coupling of infrared radiation to intersubband transitions in multiple quantum wells: The effective-medium approach,” *Physical Review B*, vol. 59, pp. 13 043–13 053, 1999.
- [37] T. Ando, A. B. Fowler, and F. Stern, “Electronic properties of two-dimensional systems,” *Rev. Mod. Phys.*, vol. 54, pp. 437–672, Apr 1982.
- [38] D. M. Pozar, *Microwave engineering*. John Wiley & Sons, 2009.
- [39] F. Marsault, “Manipulation optique de condensats de polaritons des microstructures semiconductrices,” *Université Pierre et Marie Curie*, 2017.
- [40] J. D. Joannopoulos, S. G. Johnson, J. N. Winn, and R. D. Meade, *Photonic crystals: molding the flow of light*. Princeton university press, 2011.
- [41] Y. Todorov, L. Tosetto, J. Teissier, A. M. Andrews, P. Klang, R. Colombelli, I. Sagnes, G. Strasser, and C. Sirtori, “Optical properties of metal-dielectric-metal microcavities in the THz frequency range,” *Optics Express*, vol. 18, no. 13, pp. 13 886–13 907, 2010.
- [42] R. C. Rumpf, “Mooc: Formulation of rigorous coupled-wave analysis,” <http://emlab.utep.edu/ee5390cem.htm>.
- [43] D. Whittaker and I. Culshaw, “Scattering-matrix treatment of patterned multilayer photonic structures,” *Physical Review B*, vol. 60, no. 4, p. 2610, 1999.
- [44] L. Li, “Use of fourier series in the analysis of discontinuous periodic structures,” *JOSA A*, vol. 13, no. 9, pp. 1870–1876, 1996.
- [45] S. Zanutto, “Mathlab: Periodically patterned multi layer.” [Online]. Available: https://www.mathworks.com/matlabcentral/fileexchange/55401-ppml-periodically-patterned-multi-layer?s_tid=prof_contriblnk
- [46] E. T. Jaynes and F. W. Cummings, “Comparison of quantum and semiclassical radiation theories with application to the beam maser,” *Proceedings of the IEEE*, vol. 51, no. 1, pp. 89–109, Jan 1963.
- [47] V. Savona, C. Piermarocchi, A. Quattropani, P. Schwendimann, and F. Tassone, “Optical properties of microcavity polaritons,” *Phase Transitions*, vol. 68, no. 1, pp. 169–279, 1999.
- [48] J. J. Hopfield, “Theory of the contribution of excitons to the complex dielectric constant of crystals,” *Physical Review*, vol. 112, pp. 1555–1567, Dec 1958.
- [49] J. M. Raimond, M. Brune, and S. Haroche, “Manipulating quantum entanglement with atoms and photons in a cavity,” *Rev. Mod. Phys.*, vol. 73, pp. 565–582, Aug 2001.
- [50] S. De Liberato and C. Ciuti, “Quantum theory of electron tunneling into intersubband cavity polariton states,” *Physical Review B*, vol. 79, no. 7, p. 075317, 2009.
- [51] D. Chastanet, J. M. Manceau, T. Laurent, A. Bousseksou, G. Beaudoin, I. Sagnes, and R. Colombelli, “Surface emitting thermally assisted polaritonic light-emitting device,” *Applied Physics Letters*, vol. 110, no. 8, 2017.

- [52] S. Zanotto, “Intersubband polaritons in photonic crystal cavities,” Thesis, Scuola Normale Superiore, 2014. [Online]. Available: <http://metapublishing.org/index.php/MP/catalog/book/45>
- [53] H. A. Haus, *Waves and Fields in Optoelectronics*. Prentice Hall, 1984.
- [54] M. Cai, O. Painter, and K. J. Vahala, “Observation of critical coupling in a fiber taper to a silica-microsphere whispering-gallery mode system,” *Physical review letters*, vol. 85, no. 1, p. 74, 2000.
- [55] E. Purcell, “Spontaneous emission probabilities at radio frequencies,” *Phys. Rev.*, vol. 69, p. 681, 1946.
- [56] P. Jouy, Y. Todorov, A. Vasanelli, R. Colombelli, I. Sagnes, and C. Sirtori, “Coupling of a surface plasmon with localized subwavelength microcavity modes,” *Applied Physics Letters*, vol. 98, no. 2, p. 021105, Jan. 2011.
- [57] C. Sirtori, S. Barbieri, and R. Colombelli, “Wave engineering with thz quantum cascade lasers,” *Nature Photonics*, vol. 7, no. 9, p. 691, 2013.
- [58] S. De Liberato and C. Ciuti, “Stimulated scattering and lasing of intersubband cavity polaritons,” *Physical Review Letters*, vol. 102, no. 13, pp. 1–4, 2009.
- [59] H. Deng, G. Weihs, C. Santori, J. Bloch, and Y. Yamamoto, “Condensation of semiconductor microcavity exciton polaritons,” *Science*, vol. 298, no. 5591, pp. 199–202, 2002.
- [60] R. Colombelli and J.-M. Manceau, “Perspectives for intersubband polariton lasers,” *Physical Review X*, vol. 5, no. 1, p. 011031, 2015.
- [61] J. Manceau, G. Biasiol, N. Tran, I. Carusotto, and R. Colombelli, “Immunity of intersubband polaritons to inhomogeneous broadening,” *Physical Review B*, vol. 96, no. 23, p. 235301, 2017.
- [62] Y. Todorov, L. Tosetto, A. Delteil, A. Vasanelli, C. Sirtori, A. Andrews, and G. Strasser, “Polaritonic spectroscopy of intersubband transitions,” *Physical Review B*, vol. 86, no. 12, p. 125314, 2012.
- [63] B. C. Smith, *Fundamentals of Fourier transform infrared spectroscopy*. CRC press, 2011.
- [64] E. Hecht *et al.*, *Optics*. Addison-Wesley, 2002.
- [65] P. Savvidis, J. Baumberg, R. Stevenson, M. Skolnick, D. Whittaker, and J. Roberts, “Angle-resonant stimulated polariton amplifier,” *Physical review letters*, vol. 84, no. 7, p. 1547, 2000.
- [66] C. Ciuti, P. Schwendimann, and A. Quattropani, “Theory of polariton parametric interactions in semiconductor microcavities,” *Semiconductor Science and Technology*, vol. 18, no. 10, p. S279, 2003.

- [67] L. Nguyen-thê, S. De Liberato, M. Bamba, and C. Ciuti, “Effective polariton-polariton interactions of cavity-embedded two-dimensional electron gases,” *Physical Review B*, vol. 87, p. 235322, Jun 2013.
- [68] J. Nespolo and I. Carusotto, “A generalized gross-pitaevskii model for intersubband polariton lasing,” *arXiv preprint arXiv:1903.10213*, 2019.
- [69] M. Massaouti, J.-M. Manceau, A. Selimis, and S. Tzortzakis, “An intense tunable femtosecond gas-plasma THz source: Application in spectroscopic studies of polycyclic aromatic hydrocarbons,” *Journal of Molecular Structure*, vol. 1006, no. 1-3, pp. 28–33, 2011.
- [70] A. Bonvalet, M. Joffre, J. Martin, and A. Migus, “Generation of ultrabroadband femtosecond pulses in the mid-infrared by optical rectification of 15 fs light pulses at 100 MHz repetition rate,” *Applied Physics Letters*, vol. 67, no. 20, pp. 2907–2909, 1995.
- [71] Y. Shen, P. Upadhyaya, E. Linfield, H. Beere, and A. Davies, “Terahertz generation from coherent optical phonons in a biased GaAs photoconductive emitter,” *Physical Review B*, vol. 69, no. 23, p. 235325, 2004.
- [72] F. Wang, “Ultrafast terahertz pulse generation from quantum cascade lasers,” Thesis, Laboratoire Pierre Aigrain - ENS PARIS ; Paris VI, 2016. [Online]. Available: <https://hal.archives-ouvertes.fr/tel-01530907>
- [73] Y.-S. Lee, *Principles of terahertz science and technology*. Springer Science & Business Media, 2009, vol. 170.
- [74] J.-L. Coutaz, *Optoélectronique térahertz*. EDP Sciences, 2012.
- [75] E. Rosencher and B. Vinter, *Optoelectronics*. Cambridge University Press, 2002.
- [76] S. Zanotto, F. Bianco, L. Sorba, G. Biasiol, and A. Tredicucci, “Saturation and bistability of defect-mode intersubband polaritons,” *Physical Review B*, vol. 91, no. 8, p. 085308, 2015.
- [77] D. Oustinov, N. Jukam, R. Rungsawang, J. Madéo, S. Barbieri, P. Filloux, C. Sirtori, X. Marcadet, J. Tignon, and S. Dhillon, “Phase seeding of a terahertz quantum cascade laser,” *Nature Communications*, vol. 1, p. 69, 2010.
- [78] O. Svelto and D. C. Hanna, *Principles of lasers*. Springer, vol. 4, 1998.
- [79] D. Bachmann, M. Rösch, G. Scalari, M. Beck, J. Faist, K. Unterrainer, and J. Darmo, “Dispersion in a broadband terahertz quantum cascade laser,” *Applied Physics Letters*, vol. 109, no. 22, p. 221107, 2016.
- [80] G. Villares, S. Riedi, J. Wolf, D. Kazakov, M. J. Süess, P. Jouy, M. Beck, and J. Faist, “Dispersion engineering of quantum cascade laser frequency combs,” *Optica*, vol. 3, no. 3, pp. 252–258, 2016.

- [81] M. Amanti, M. Fischer, G. Scalari, M. Beck, and J. Faist, “Low-divergence single-mode terahertz quantum cascade laser,” *Nature Photonics*, vol. 3, no. 10, p. 586, 2009.
- [82] Y. Chassagneux, J. Palomo, R. Colombelli, S. Barbieri, S. Dhillon, C. Sirtori, H. Beere, J. Alton, and D. Ritchie, “Low threshold THz QC lasers with thin core regions,” *Electronics Letters*, vol. 43, no. 5, pp. 41–42, 2007.
- [83] S. J. Pearton, U. K. Chakrabarti, W. S. Hobson, and A. P. Kinsella, “Reactive ion etching of GaAs, AlGaAs, and GaSb in Cl_2 and SiCl_4 ,” *Journal of Vacuum Science & Technology B: Microelectronics Processing and Phenomena*, vol. 8, no. 4, pp. 607–617, Jul. 1990.
- [84] S. J. Pearton, U. K. Chakrabarti, and W. S. Hobson, “Reactive ion etching induced damage in GaAs and AlGaAs using $\text{C}_2\text{H}_6/\text{H}_2/\text{Ar}$ or $\text{CCl}_2\text{F}_2/\text{O}_2$ gas mixtures,” *Journal of Applied Physics*, vol. 66, no. 5, pp. 2061–2064, Sep. 1989.
- [85] S. W. Pang, G. A. Lincoln, R. W. McClelland, P. D. DeGraff, M. W. Geis, and W. J. Piacentini, “Effects of dry etching on GaAs,” *Journal of Vacuum Science & Technology B: Microelectronics Processing and Phenomena*, vol. 1, no. 4, pp. 1334–1337, Oct. 1983.
- [86] G. Franz, W. Hösler, and R. Treichler, “Sidewall passivation of GaAs in BCl_3 -containing atmospheres,” *Journal of Vacuum Science & Technology B: Microelectronics and Nanometer Structures Processing, Measurement, and Phenomena*, vol. 19, no. 2, pp. 415–419, Mar. 2001.
- [87] L. Jalabert, P. Dubreuil, F. Carcenac, S. Pinaud, L. Salvagnac, H. Granier, and C. Fontaine, “High aspect ratio GaAs nanowires made by ICP-RIE etching using Cl_2/N_2 chemistry,” *Microelectronic Engineering*, vol. 85, no. 5, pp. 1173–1178, May 2008.
- [88] A. Larrue, D. Belharet, P. Dubreuil, S. Bonnefont, O. Gauthier-Lafaye, A. Monmayrant, F. Lozes-Dupuy, and S. Moudji, “Inductively coupled plasma etching of high aspect ratio two-dimensional photonic crystals in Al-rich AlGaAs and AlGaAsSb,” *Journal of Vacuum Science & Technology B, Nanotechnology and Microelectronics: Materials, Processing, Measurement, and Phenomena*, vol. 29, no. 2, p. 021006, Jan. 2011.
- [89] G. Xu, L. Li, N. Isac, Y. Halioua, A. Giles Davies, E. H. Linfield, and R. Colombelli, “Surface-emitting terahertz quantum cascade lasers with continuous-wave power in the tens of milliwatt range,” *Applied Physics Letters*, vol. 104, no. 9, p. 091112, Mar. 2014.
- [90] K. A. Atlasov, P. Gallo, A. Rudra, B. Dwir, and E. Kapon, “Effect of sidewall passivation in BCl_3/n_2 inductively coupled plasma etching of two-dimensional gas photonic crystals,” *Journal of Vacuum Science & Technology B: Microelectronics and Nanometer Structures*, vol. 27, no. 5, p. L21, 2009.

- [91] Y. Chen, B. S. Ooi, G. I. Ng, C. L. Tan, and Y. C. Chan, "Dry plasma etching of GaAs vias using BCl_3/Ar and Cl_2/Ar plasmas," *International Society for Optics and Photonics*, vol. 3896, pp. 199–207, Nov. 1999.
- [92] G. T. Edwards, A. Sobiesierski, D. I. Westwood, and P. M. Smowton, "Fabrication of high-aspect-ratio, sub-micron gratings in AlGaInP/GaAs laser structures using a $\text{BCl}_3/\text{Cl}_2/\text{Ar}$ inductively coupled plasma," *Semiconductor Science and Technology*, vol. 22, no. 9, p. 1010, 2007.
- [93] S. Fatholouloumi, E. Dupont, C. Chan, Z. Wasilewski, S. Laframboise, D. Ban, A. Mátyás, C. Jirauschek, Q. Hu, and H. Liu, "Terahertz quantum cascade lasers operating up to ~ 200 K with optimized oscillator strength and improved injection tunneling," *Optics express*, vol. 20, no. 4, pp. 3866–3876, 2012.
- [94] M. Wienold, L. Schrottke, M. Giehler, R. Hey, W. Anders, and H. Grahn, "Low-voltage terahertz quantum-cascade lasers based on LO-phonon-assisted interminiband transitions," *Electronics Letters*, vol. 45, no. 20, pp. 1030–1031, 2009.
- [95] J. A. Fan, M. A. Belkin, F. Capasso, S. P. Khanna, M. Lachab, A. G. Davies, and E. H. Linfield, "Wide-ridge metal-metal terahertz quantum cascade lasers with high-order lateral mode suppression," *Applied Physics Letters*, vol. 92, no. 3, pp. 2006–2009, 2008.
- [96] D. Bachmann, M. Rösch, M. J. Süess, M. Beck, K. Unterrainer, J. Darmo, J. Faist, and G. Scalari, "Short pulse generation and mode control of broadband terahertz quantum cascade lasers," *Optica*, vol. 3, no. 10, pp. 1087–1094, 2016.
- [97] Y. Chassagneux, R. Colombelli, W. Maineult, S. Barbieri, H. Beere, D. Ritchie, S. Khanna, E. Linfield, and A. Davies, "Electrically pumped photonic-crystal terahertz lasers controlled by boundary conditions," *Nature*, vol. 457, no. 7226, p. 174, 2009.
- [98] D. Bachmann, M. Rösch, G. Scalari, M. J. Süess, M. Beck, J. Faist, K. Unterrainer, and J. Darmo, "Pulse generation and spectral optimization of broadband terahertz quantum cascade lasers," *41st International Conference on Infrared, Millimeter, and Terahertz waves (IRMMW-THz)*, pp. 1–2, Sept 2016.
- [99] R. E. Williams, *Modern GaAs processing methods*. Artech House Publishers, 1990.
- [100] A. Gordon, C. Y. Wang, L. Diehl, F. X. Kärtner, A. Belyanin, D. Bour, S. Corzine, G. Höfler, H. Liu, H. Schneider *et al.*, "Multimode regimes in quantum cascade lasers: From coherent instabilities to spatial hole burning," *Physical Review A*, vol. 77, no. 5, p. 053804, 2008.
- [101] H. Schneider and H. Liu, *Quantum Well Infrared Photodetectors*, Springer, Ed., Heidelberg, 2007.
- [102] M. Kane, S. Millidge, M. Emeny, D. Lee, D. Guy, and C. Whitehouse, "Intersubband transitions in quantum wells," pp. 31–41, 1992.
- [103] E. Lhuillier, I. Ribet-Mohamed, M. Tauvy, A. Nedelcu, V. Berger, and E. Rosencher, "Ultimate performance of quantum well infrared photodetectors in the tunneling regime," *Infrared Physics & Technology*, vol. 52, no. 4, pp. 132–137, 2009.

- [104] R. H. Kingston, *Detection of optical and infrared radiation*. Springer, vol. 10, 2013.
- [105] A. Rose, *Concepts in photoconductivity and allied problems*. Interscience publishers, 1963.
- [106] N. Sclar, “Properties of doped silicon and germanium infrared detectors,” *Progress in Quantum Electronics*, vol. 9, no. 3, pp. 149 – 257, 1984.
- [107] W. Schottky, “Über spontane Stromschwankungen in verschiedenen elektrizitätsleitern,” *Annalen der Physik*, vol. 362, no. 23, pp. 541–567, 1918.
- [108] H. Liu, “Noise gain and operating temperature of quantum well infrared photodetectors,” *Applied physics letters*, vol. 61, no. 22, pp. 2703–2705, 1992.
- [109] A. Rogalski, *Infrared Detectors*. CRC press, 2010.
- [110] S. Shen, “Comparison and competition between MCT and QW structure material for use in IR detectors,” *Microelectronics Journal*, vol. 25, no. 8, pp. 713–739, 1994.
- [111] B. F. Levine, K. K. Choi, C. G. Bethea, J. Walker, and R. J. Malik, “New 10 μm infrared detector using intersubband absorption in resonant tunneling GaAlAs superlattices,” *Applied Physics Letters*, vol. 50, no. 16, pp. 1092–1094, 1987.
- [112] S. D. Gunapala, S. V. Bandara, J. K. Liu, C. J. Hill, S. B. Rafol, J. M. Mumolo, J. T. Trinh, M. Z. Tidrow, and P. D. Levan, “Development of mid-wavelength and long-wavelength megapixel portable QWIP imaging cameras,” *Infrared Physics and Technology*, vol. 47, no. 1-2, pp. 67–75, 2005.
- [113] H. Liu, J. Li, E. Brown, K. McIntosh, K. Nichols, and M. Manfra, “Quantum well intersubband heterodyne infrared detection up to 82 GHz,” *Applied Physics Letters*, vol. 67, no. 11, pp. 1594–1596, 1995.
- [114] D. Palaferri, Y. Todorov, A. Bigioli, A. Mottaghizadeh, D. Gacemi, A. Calabrese, A. Vasanelli, L. Li, A. G. Davies, E. H. Linfield, F. Kapsalidis, M. Beck, J. Faist, and C. Sirtori, “Room-temperature nine- μm -wavelength photodetectors and GHz-frequency heterodyne receivers,” *Nature*, vol. 556, no. 7699, pp. 85–88, 2018.
- [115] D. Brewster, “On the laws which regulate the polarisation of light by reflexion from transparent bodies,” *Philosophical Transaction of the Royal Society*, vol. 105, pp. 125–130, 1815.
- [116] E. Eizner, J. Brodeur, F. Barachati, A. Sridharan, and S. Kéna-Cohen, “Organic Photodiodes with an Extended Responsivity using Ultrastrong Light-Matter Coupling,” *ACS Photonics*, 2018.
- [117] K. Choi, B. Levine, R. Malik, J. Walker, and C. Bethea, “Periodic negative conductance by sequential resonant tunneling through an expanding high-field superlattice domain,” *Physical Review B*, vol. 35, no. 8, p. 4172, 1987.
- [118] H. Schneider, P. Koidl, M. Walther, J. Fleissner, R. Rehm, E. Diwo, K. Schwarz, and G. Weimann, “Ten years of QWIP development at Fraunhofer IAF,” *Infrared Physics & Technology*, vol. 42, no. 3-5, pp. 283–289, 2001.

- [119] D. G. Ivey, S. Eicher, S. Wingar, and T. Lester, "Performance of Pd-Ge based ohmic contacts to n-type GaAs," *Journal of Materials Science: Materials in Electronics*, vol. 8, no. 2, pp. 63–68, 1997.
- [120] J. Thompson, S. Beaumont, A. Kean, and C. Stanley, "Germanium-palladium ohmic contacts to n-type GaAs," *Semiconductor Science and Technology*, vol. 5, no. 6, p. 596, 1990.
- [121] Y. G. Wang, D. Wang, and D. G. Ivey, "Thermal stability of Pd/Ge-based ohmic contacts to n-type GaAs," *Journal of Applied Physics*, vol. 84, no. 3, pp. 1310–1315, 1998.
- [122] R. H. Fowler and L. Nordheim, "Electron emission in intense electric fields," *Proceedings of the Royal Society of London. Series A, Containing Papers of a Mathematical and Physical Character*, vol. 119, no. 781, pp. 173–181, 1928.
- [123] Y. Chassagneux, "Photonique pour les lasers à cascade quantique térahertz," Ph.D. dissertation, IEF Paris XI, 2009. [Online]. Available: <http://www.theses.fr/2009PA112147>
- [124] J. Faist, *Quantum cascade lasers*. Oxford University Press, 2013.
- [125] J. Xu, J. M. Hensley, D. Fenner, R. P. Green, L. Mahler, A. Tredicucci, M. G. Allen, F. Beltram, H. E. Beere, and D. A. Ritchie, "Tunable terahertz quantum cascade lasers with an external cavity," *Applied Physics Letters*, vol. 91, no. 12, p. 121104, 2007.
- [126] A. Hugi, R. Terazzi, Y. Bonetti, A. Wittmann, M. Fischer, M. Beck, J. Faist, and E. Gini, "External cavity quantum cascade laser tunable from 7.6 to 11.4 μm ," *Applied Physics Letters*, vol. 95, no. 6, p. 061103, 2009.
- [127] A. W. M. Lee, B. S. Williams, S. Kumar, Q. Hu, and J. L. Reno, "Tunable terahertz quantum cascade lasers with external gratings," *Optics letters*, vol. 35, no. 7, pp. 910–912, 2010.
- [128] A. Gatesman, J. Waldman, M. Ji, C. Musante, and S. Yagvesson, "An anti-reflection coating for silicon optics at terahertz frequencies," *IEEE microwave and guided wave letters*, vol. 10, no. 7, pp. 264–266, 2000.
- [129] M. Ji, C. Musante, S. Yngvesson, A. Gatesman, and J. Waldman, "Study of parylene as anti-reflection coating for silicon optics at THz frequencies," *International Symposium Space THz Technology, University of Michigan*, p. 407, 2000.
- [130] R. Rungsawang, N. Jukam, J. Maysonnave, P. Cavalié, J. Madéo, D. Oustinov, S. Dhillon, J. Tignon, P. Gellie, C. Sirtori *et al.*, "Gain enhancement in a terahertz quantum cascade laser with parylene antireflection coatings," *Applied Physics Letters*, vol. 98, no. 10, p. 101102, 2011.
- [131] R. Köhler, A. Tredicucci, F. Beltram, H. E. Beere, E. H. Linfield, A. G. Davies, D. A. Ritchie, S. S. Dhillon, and C. Sirtori, "High-performance continuous-wave operation of superlattice terahertz quantum-cascade lasers," *Applied Physics Letters*, vol. 82, no. 10, pp. 1518–1520, 2003.

- [132] A. W. M. Lee, Q. Qin, S. Kumar, B. S. Williams, Q. Hu, and J. L. Reno, “High-power and high-temperature THz quantum-cascade lasers based on lens-coupled metal-metal waveguides,” *Optics letters*, vol. 32, no. 19, pp. 2840–2842, 2007.
- [133] J. Kroll, J. Darmo, and K. Unterrainer, “Ultra-thin metallic layers studied by broadband terahertz time-domain spectroscopy,” in *Infrared and Millimeter Waves, 12th International Conference on Terahertz Electronics*, pp. 465–466, 2004.
- [134] J. Kröll, J. Darmo, and K. Unterrainer, “Metallic wave-impedance matching layers for broadband terahertz optical systems,” *Optics Express*, vol. 15, no. 11, pp. 6552–6560, 2007.
- [135] L. Ding, X. Wang, N. S. S. Ang, C. Lu, V. Suresh, S.-J. Chua, and J. Teng, “Ultrathin film broadband terahertz antireflection coating based on impedance matching method,” *IEEE Journal of Selected Topics in Quantum Electronics*, vol. 23, no. 4, p. 8, 2017.
- [136] A. Thoman, A. Kern, H. Helm, and M. Walther, “Nanostructured gold films as broadband terahertz antireflection coatings,” *Physical Review B*, vol. 77, no. 19, p. 195405, 2008.

Titre : Détecteurs moyen infrarouge et dispositifs THz en régime de couplage fort entre lumière et matière.

Mots clés : THz-QCL, photo-détecteurs, couplage fort, polaritons inter-sous-bande

Résumé :

Les polaritons inter-sous-bandes, observés pour la première fois il y a une quinzaine d'années, sont des quasi-particules dont de nombreuses propriétés restent encore à découvrir. La recherche dans ce domaine se focalise actuellement sur la réalisation de condensats de Bose-Einstein. Une telle découverte pourrait révolutionner l'optoélectronique du moyen infra-rouge jusqu'au THz ouvrant la voie à l'instauration de nouveaux concepts de sources lumineuses, de détecteurs ou de systèmes logiques en couplage fort. Dans cette quête, le choix de la cavité résonnante est critique.

Dans ce manuscrit nous proposons d'utiliser des cavités métal-isolant-métal (M-I-M) avec un réseau dispersif sur le métal supérieur. Ce type de cavité, conservant un confinement élevé entre les deux plans métalliques, offre de nombreuses possibilités d'ajustement de la résonance de cavité : via la géométrie de la cavité (épaisseur de la cavité, période et recouvrement du réseau) ainsi que par le couplage de la lumière avec la cavité (vecteur d'onde incident).

Les cavités M-I-M dispersives ouvrent donc un nouveau champ d'exploration des polaritons inter-sous-bande. Dans un premier temps nous avons introduit ces cavités dans le domaine du THz afin d'étudier les phénomènes de relaxation polariton-polariton. Un système expérimental dédié à cette exploration a été conçu pour mesurer la réflectivité des polaritons THz avec une fine résolution en angle.

Dans un second temps, des capteurs moyen infrarouge en couplage fort avec une cavité M-I-M dispersive ont été conçus, fabriqués et mesurés dans le but d'explorer la génération de photo-courant à partir de polaritons et d'utiliser le couplage fort pour dissocier l'énergie de détection de l'énergie d'activation. Cette seconde étude s'inscrit dans l'objectif de pompage électrique des polaritons ISB.

Parallèlement à l'étude des polaritons, nous avons également participé au développement de techniques (interféromètre Gires-Tournois et revêtement anti-réflexion) pour compresser les impulsions optiques de lasers à cascade quantique THz.

Title : Mid-Infrared Detectors and THz Devices Operating in the Strong Light-Matter Coupling Regime.

Keywords : THz-QCL, QWIP, Strong-Coupling, Intersubband

Abstract :

After fifteen years of intersubband polaritons development some of the peculiar properties of these quasi-particles are still unexplored. A deeper comprehension of the polaritons is needed to access their fundamental properties and assess their applicative potential as efficient emitters or detectors in the mid-infrared and THz.

In this manuscript we used Metal-Insulator-Metal (M-I-M) cavities with a top metal periodic grating as a platform to deepen the understanding of ISB polaritons. The advantages of M-I-M are twofold : first they confine the TM_{00} mode, second the dispersion of the cavity -over a large set of in-plane wave-vectors- offers various experimental configurations to observe the polaritons in both reflection and photo-current. We reexamined the properties of ISB polaritons in the mid-infrared and in the THz using these resonators.

In the first part, we explore the implementation of dispersive M-I-M cavities with THz intersubband transitions. In the THz domain, the scattering mechanisms of the THz ISB polaritons need to be understood. The

dispersive cavity is a major asset to study these mechanisms because it provides more degrees of freedom to the system. For this purpose, we fabricated a new experimental set-up to measure the polariton dispersion at liquid Helium temperature. After the characterization of the polaritons in reflectivity, a pump-probe experiment was performed on the polaritonic devices. The second part of this manuscript presents the implementation of M-I-M dispersive cavities with a bound-to-quasi-bound quantum well infrared photo-detector designed to detect in strong coupling. Beyond electrical probing of the polaritons, the strong coupling can disentangle the frequency of detection from the thermal activation energy and reduce the dark current at a given frequency.

In parallel to the exploration of THz polaritons, we developed two techniques (Gires-Tournois Interferometer and Anti-reflection coating) in order to shorten the pulses of THz quantum cascade lasers with metal-metal waveguides.

